



UNIVERSITEIT VAN PRETORIA
UNIVERSITY OF PRETORIA
YUNIBESITHI YA PRETORIA

**DEVELOPMENT AND APPLICATION OF A PHOTOGRAMMETRY
BASED STATISTICAL SHAPE ANALYSIS TECHNIQUE FOR
CONDITION MONITORING OF ROTATING STRUCTURES**

by
Benjamin Katerere Gwashavanhu

Submitted in partial fulfilment of the requirements for the degree

Philosophiae Doctor (Mechanical Engineering)

In the Faculty of

Engineering, Built Environment and Information Technology

University of Pretoria, Pretoria

2024

© University of Pretoria

DEVELOPMENT AND APPLICATION OF A PHOTOGRAMMETRY BASED STATISTICAL SHAPE ANALYSIS TECHNIQUE FOR CONDITION MONITORING OF ROTATING STRUCTURES

Benjamin Katerere Gwashavanhu

Supervisors: Dr A.J. Oberholster and Professor P.S. Heyns

University of Pretoria

Department of Mechanical and Aeronautical Engineering

Degree: Philosophiae Doctor (Mechanical Engineering)

Abstract

Large rotating structures such as wind turbine blades require specialized measurement techniques for the purpose of online condition monitoring and assessment. Contact transducers such as accelerometers and strain gauges are traditionally used to capture vibrational data that can be analysed to understand the dynamics of a system. These are however intrusive in the sense that they must be physically attached to the structure under investigation. In addition, they are point-wise in nature, implying that measurements are only captured for those specific locations where the transducer is attached. They may also alter the local structural properties at the point of attachment, including additional mass loading effects of the sensor on light structures. Optical techniques such as photogrammetry and laser vibrometry are promising alternatives that have been receiving much attention.

3D Point Tracking (3DPT) and Digital Image Correlation (DIC) constitute photogrammetric-based optical measurement techniques that have proven to be efficient for the vibration analysis of rotating machinery. In addition to complex image processing software and tracking algorithms, these two approaches typically require surface preparation in the form of markers and speckle patterns. The surface preparation typically requires a system shutdown which can be complicated and costly. Applied surface treatments also do not last throughout the lifespan of the structure and often must be reapplied. In order to track specific pixels for 3DPT and DIC, the lighting on the surface of the structure needs to be closely monitored since the tracking is based on pixel gray scale values. These requirements limit the applicability of photogrammetry as a condition monitoring tool, especially when it comes to field or outdoor full-scale testing.

Photogrammetric shape-based analysis is an alternative approach that does not require prior surface preparation. By focusing on the boundary outline of a structure, the technique is a suitable candidate for outdoor investigations where consistent uniform lighting on an entire structural surface may be impossible. It can also be applied to large structures with significant levels of rigid body motions. To date, this approach has not yet been employed for dynamic analysis of machines. The concept of shape analysis is typically applied for object recognition or shape matching in applications such as Content Based Image Retrieval (CBIR). Thus a

single image is captured and then analysed to be matched to another image stored in a database, for instance.

This research focuses on the development and application of a shape based photogrammetric technique that can be used to capture dynamics of rotating structures without the requirement for surface preparation. The goal of the study is to develop an approach that can be used to distinguish faults in the system and classify machine behaviour for condition monitoring purposes. In this type of application, sequences of images of a structure in operation are captured, and boundary contours of an object in the images extracted. Through defining parameters that characterise contours extracted from each of these images, and then monitoring the variation of these parameters in time, the idea of shape analysis can be adopted for condition monitoring of machines as an optical non-contact measurement technique. Shape Principal Component Descriptors (SPCDs) determined by performing Shape Principal Component Analysis (SPCA) of Fourier descriptors calculated from shape signatures of the extracted contours are the parameters investigated in this study.

Condition monitoring strategies for rotating structures are discussed in a literature review that highlights the importance of structural health maintenance and the shortcomings and limitations of conventional measurement techniques. Advanced optical measurement techniques that include photogrammetry and laser vibrometry are discussed to describe and illustrate the evolution of recent noncontact technologies as viable tools for condition monitoring purposes. Typical applications of photogrammetric techniques such as surface strain measurement are highlighted. Instances that demonstrate the successful use of optical approaches to capture dynamics of rotating structures are discussed. This lays out a foundation onto which the necessity of advancing optical based strategies into more suited techniques for industrial application purposes is built.

The concept of shape analysis is introduced and its SPCDs investigated for a 2D shape that has in-plane form variations associated with it. On application to a physical rotor system, it is illustrated that different dynamics of the rotor resulting from different faults of unbalance, rotor-stator rub and hydrodynamic bearing oil instabilities can be detected and classified using the shape-based approach. It is clearly illustrated that the multi-dimensional measurement technique provides insights into the behaviour of a rotor system, as confirmed by uniaxial conventional proximity probe measurements. The proposed approach complemented the widely used proximity probe sensing technique in terms of investigating rotor systems.

An extension of the approach from 2D to 3D is also presented, starting with analysing how different shape descriptors influence the form of contours representing blade shapes in 3D. A detailed numerical investigation in which a Finite Element (FE) model of a physical rotor is analysed for changes in dynamic behaviour resulting from introduced damage in the blades, is conducted. The FE environment provides a platform in which the procedures for 3D shape analysis can be developed and tested before the proposed approach can be implemented experimentally. An experimental study that involves the use of a calibrated system of high-speed cameras to synchronously capture stereoscopic images of a rotating turbomachine is then presented. Variations in the dynamics of rotating blades are investigated and through a revolution based Principal Component Analysis (PCA) of SPCDs, the feasibility of a shape-based condition monitoring approach for turbine blades is illustrated.

A comparative study to investigate the performance of PCA of SPCDs in relation to Kernel Principal Component Analysis (KPCA) is also conducted, and it is shown that KPCA outperforms PCA in terms of classifying different blade faults. The feasibility of using Multi-domain Statistical Features (MSFs) as feature vectors to which PCA or KPCA is applied for classification purposes is also presented. Results indicating how well different blade damage modes can be distinguished are provided, and it is clearly illustrated that MSFs are more robust to noise contamination in the signals compared to using the raw SPCDs time data.

Dedication

This work is dedicated to my father, the late Mr Robert Robson Katerere, my mother, Mrs Ratidzo Mandava, my wife Tshepang (Khahlu Gwashavanhu) Katerere, and my siblings Saniso, Agatha, Linda, Clarence, Sharon, Lorraine and Chipso.

ACKNOWLEDGEMENTS

I would like to thank the following people for their help in the completion of this work:

- My supervisors, Dr A.J. Oberholster and Professor P.S. Heyns, for presenting me with an opportunity to do this work, and for their guidance and assistance throughout the duration of my postgraduate studies.
- Mr Breitenbach, Mr Booysen and colleagues at the University of Pretoria Sasol laboratories, for their assistance in experimental setting up and testing.
- Dr S. Schmidt, for the many office discussions which contributed significantly to the success of this study.
- My wife Tshepang for her unwavering faith in me, her unconditional support and understanding, and for standing by me throughout the duration of this study.
- My family and my dear friends, Mr Gautam Ranjit, Mr Winston T Jimu and Mr Richard Mukandiro, for the continued support and encouragements.

LIST OF PUBLICATIONS BASED ON CANDIDATE'S RESEARCH

1. Gwashavanhu, B, Heyns, PS & Oberholster, AJ. (2017). Statistical shape analysis as a noncontact method for condition monitoring of turbomachines. In: *IOMAC 2017 - 7th International Operational Modal Analysis Conference*.

Content presented in Chapter 2.

2. Gwashavanhu, B, Heyns, PS & Oberholster, AJ. (2017). Statistical shape analysis as a non-contact method for condition monitoring of turbomachines - sensitivity analysis. In: *Proceedings of 2nd International Conference on Maintenance Engineering*. J.K. Sinha, Ed. Manchester.

Content presented in Chapter 2.

3. Gwashavanhu, B, Heyns, PS & Oberholster, AJ. (2018). Shape principal component analysis as a targetless photogrammetric technique for condition monitoring of rotating machines. *Measurement*, 132, pp.408-422

Content presented in Chapter 3.

4. Gwashavanhu, B, Oberholster, AJ & Heyns, PS. (Submitted). Turbomachinery blade condition monitoring using a photogrammetric stereovision 3D based shape analysis approach. *Manuscript submitted for publication*.

Content presented in Chapter 4.

5. Gwashavanhu, B, Oberholster, AJ & Heyns, PS. (Submitted). A comparative study of principal component analysis and kernel principal component analysis for photogrammetric shape-based turbine blade damage analysis. *Manuscript submitted for publication*.

Content presented in Chapter 5.

TABLE OF CONTENTS

ACKNOWLEDGEMENTS	v
LIST OF PUBLICATIONS BASED ON CANDIDATE'S RESEARCH	vi
GLOSSARY.....	x
ABBREVIATIONS	x
SYMBOLS	xii
GREEK SYMBOLS	xiii
CHAPTER 1: INTRODUCTION	1
1.1 Problem statement.....	1
1.2 Literature study.....	2
1.2.1 Structural Health Monitoring and Condition Monitoring – Rotating Structures.....	2
1.2.1.1 Wind turbines	3
1.2.1.2 Wind turbine failures	4
1.2.1.3 Conventional condition monitoring of wind turbines	7
1.2.2 Optical Measurement Techniques	9
1.2.2.1 Thermography and LDV.....	9
1.2.2.2 Photogrammetry.....	10
1.2.3 Statistical shape analysis.....	17
1.2.3.1 The Freeman's chain code Fourier descriptors.....	20
1.2.4 Statistical data reduction.....	24
1.2.4.1 Principal component analysis.....	24
1.2.4.2 Kernel Principal Component Analysis (KPCA)	25
1.2.5 Statistical and circular domain features.....	26
1.3 Scope of research.....	27
1.4 Document overview	29
CHAPTER 2: FEASIBILITY OF CONDITION MONITORING USING SHAPE ANALYSIS ...	31
2.1 Introduction	31
2.2 2D shape analysis procedure	32
2.3 Relationship between different principal components (V) and the form of a 2D shape	34
2.4 Feasibility of condition monitoring using 2D shape analysis.....	35
2.5 Shape principal components descriptors basic sensitivity analysis.....	39
2.5.1 Effect of camera positioning on the extracted shape principal components	41
2.5.2 Vibration amplitude resolution requirements for 2D shape analysis	43

2.5.3	Camera frame rate requirements for 2D shape analysis	45
2.6	Chapter conclusion.....	47
CHAPTER 3: 2D SHAPE ANALYSIS EXPERIMENTAL INVESTIGATION.....		49
3.1	Introduction	49
3.2	Bently system experimental setup	49
3.3	System analysis using proximity probes	50
3.4	System analysis using shape analysis	53
3.5	Investigating rotor-stator rub and oil instabilities using proximity probes and 2D shape analysis.....	57
3.6	Chapter conclusion.....	61
CHAPTER 4: 3D SHAPE ANALYSIS NUMERICAL AND EXPERIMENTAL INVESTIGATION APPLIED TO MODEL ROTATING TURBINE BLADES.....		62
4.1	Introduction	62
4.2	3D SPCDs determination.....	62
4.3	Geometric modes for a 3D rectangular shaped contour.....	64
4.4	FE based numerical investigation of blade shape analysis behaviour.....	67
4.4.1	Model simplification.....	68
4.4.2	Natural modal analysis of the blades	69
4.4.3	FEA shape based dynamic analysis.....	71
4.5	Setting up and calibrating a stereo-photography system	86
4.6	3D system experimental setup description and specifications	89
4.7	Experimental investigations.....	93
4.7.1	Single point responses using 3DPT	93
4.7.2	Shape based dynamic analysis.....	94
4.8	Application to wind turbines.....	98
4.9	Chapter conclusion.....	99
CHAPTER 5: A COMPARATIVE STUDY OF THE PERFORMANCE OF PCA AND KPCA.....		101
5.1	Introduction	101
5.2	Data classification performance evaluation	101
5.2.1	PCA vs KPCA	102
5.2.2	Multi-domain Statistical Features (MSF) based evaluation	107
5.2.3	Robustness to noise.....	114
5.3	Chapter conclusion.....	117
CHAPTER 6: CONCLUSIONS AND RECOMMENDATIONS.....		118
6.1	Conclusions	118

6.2	Recommendations and future work	120
	REFERENCES	122

GLOSSARY

ABBREVIATIONS

<i>Abbreviation</i>	<i>Description</i>
3DPT	Three-Dimensional Point Tracking
AAM	Active Appearance Models
AGMD	Adaptive Geometric Moment Descriptor
AI	Artificial Intelligence
ART	Angular Radial Transform
ASM	Active Shape Models
CAD	Computer Aided Drawing
CBIR	Content Based Image Retrieval
CBM	Condition Based Monitoring
CCD	Charged Coupled Devices
CSLDV	Continuous Scanning Laser Doppler Vibrometry
CSSD	Curvature Scale Space Descriptor
DCNN	Deep Convolution Neural Networks
DF	Damage Factor
DIC	Digital Image Correlation
FBG	Fibre Bragg Grating
FD	Fourier Descriptor
FE	Finite Elements
FEA	Finite Element Analysis
FEM	Finite Element Model
FEMU	Finite Element Model Updating
FFT	Fast Fourier Transform
FOV	Field of View
FPS	Frames per Second
FRF	Frequency Response Function
ICA	Independent Component Analysis
IEFD	Invariant Elliptical Feature Descriptor

IMU	Inertial Measurement Unit
KPCA	Kernel Principal Component Analysis
LIDAR	Light Detection and Ranging
LDV	Laser Doppler Vibrometry
MIF	Magnitude Increase Factor
MPC	Multipoint constraint
MSF	Multi-domain Statistical Feature
ODS	Operational Deflection Shape
NFV	Normalized Feature Value
PAA	Piecewise Aggregate Approximation
PCA	Principal Component Analysis
QBIR	Query By Image Content
RBE	Rigid Body Elements
RMS	Root Mean Square
RPM	Revolutions Per Minute
SCD	Shape Context Descriptor
SF	Scaling Factor
SHM	Structural Health Monitoring
SIFT	Scale Invariant Feature Transform
SLDV	Scanning Laser Doppler Vibrometry
SNR	Signal to Noise Ratio
SPC	Shape Principal Components
SPCA	Shape Principal Component Analysis
SPCD	Shape Principal Component Descriptor
STFT	Short Time Fourier Transform
TLDV	Tracking Laser Doppler Vibrometry
UAVs	Unmanned Aerial Vehicles
WD	Wavelet Descriptor
ZCMD	Zernike and Chebyshev Moment Descriptor

SYMBOLS

Symbol	Description
$a_n, b_n, c_n, d_n, e_n, f_n$	Elliptical Fourier coefficients
b	Baseline distance
c	Camera optical centre
C	Camera optical centre
C	Covariance matrix
Cc	Chain-code
C_f	Crest factor
C_i	Cluster class
d	Standoff distance
D	Disparity
D_x	Variance
f	Focal length
f_k	PCA or KPCA extracted features
$\mathcal{H}\{t\}$	Hilbert transform
I	Eigenvalues
K	Kernel function
R	Cluster centroid distance from the origin
R_m	Calibration rotation matrix
S_b	Between-class scatter value
S_f	Shape factor
S_w	Within-class scatter value
T	Time
T_m	Calibration translation matrix
u_L	Left camera point projection
u_R	Right camera point projection
V	Shape principal components or geometric modes matrix
\vec{V}_i	i^{th} geometric mode
(x, y, z)	Contour point coordinates

(x_k, y_k)	xy-plane projections of the k^{th} chain-code link
x_p	Maximum peak value
x_r	Square root value
x_{rms}	Root mean square value
$\mathbf{X}_{2D}, \mathbf{X}_{3D}$	2D and 3D normalized truncated Fourier coefficients matrices
\mathbf{X}^{new}	Principal component scores matrix
\mathbf{Y}	Sampled vibration data
Z	Pixel depth

GREEK SYMBOLS

Symbol	Description
α	Cluster centroid counterclockwise xy-plane angle
β	Cluster centroid elevation angle from the xy-plane
γ	Skewness
δ_s	Vibration response features
ϵ	Contour transformation angle
κ	Kurtosis
κ_T	Time domain kurtosis
$\theta(t)$	Hilbert transform instantaneous phase
μ	Cluster class average
μ_p	p^{th} -order sample trigonometric moment
v_i	i^{th} -chain-code link
$\phi(x_i)$	Higher dimensional mapping of (x_i)
σ	Standard deviation
τ	Piecewise aggregate approximation reduced data set
$\psi(t)$	Hilbert transform instantaneous amplitude

CHAPTER 1: INTRODUCTION

This chapter opens with a problem statement that paints a picture of where exactly the research presented in this document fits in. An outline of why there is a need for developing a non-contact measurement technique more suitable for rotating structures is given. A literature review that discusses condition monitoring of structures using conventional contact techniques and the more recent non-contact techniques follows. Limitations of the current approaches being used for analysing rotating machines are highlighted. Concepts pertaining to shape analysis that are either investigated or utilized in investigations presented in the following chapters are discussed. A document overview is then given at the end of the chapter.

1.1 Problem statement

Damage detection, characterization, and classification in rotating structures for Structural Health Monitoring (SHM) or Condition Based Maintenance (CBM) purposes require the use of transducers to capture vibrational information. The dynamic behaviour of a structure is directly associated with the condition of the machine, and a full understanding of this behaviour provides valuable insight into the health condition of the structure. Through understanding the state of the machine, condition monitoring strategies that ensure scheduling of maintenance at the precise moments in the machine's life can be put in place. The maintenance must be conducted not too early that functioning components are disposed of, or too late that catastrophic failures occur. This limits the maintenance costs and reduces downtime related losses as well. Wind turbines represent such typical mechanical structures for which these maintenance strategies are quite important. With the increasing need for renewable clean energy, the wind energy industry is growing significantly, meaning that wind turbines are getting even bigger and more sophisticated.

Vibrational information for CBM purposes is typically captured whilst a machine is in operation. This requires installation of transducers, the most common of which are the traditional accelerometers and strain gauges. Whilst these have been successfully used and are more popularly considered, they are limited especially when it comes to rotating structures such as fan and wind turbine blades. Being contact in nature, these transducers are intrusive and they can potentially influence the dynamics or local properties of the structure at the point of transducer attachment. By being point-wise, measurements are captured only for that specific point where the transducer is attached. Therefore multiple sensors need to be installed to capture the entire dynamics of the structure. Thus the data acquisition and logging system can easily become too complex and costly when analysing large structures. A system shutdown is also typically required for installing the contact sensors, unless if they are attached prior to assembling the full system. Attached transducers also do not generally last for the entire lifespan of the machines owing to the harsh conditions these machines operate in.

The most popular alternative to these contact sensors is photogrammetry, an image processing based approach in which cameras are used to capture images of operating machines and the images are processed to extract vibrational information. Advances in high-speed imaging technologies have produced cameras capable of astonishingly high frame rates at decent resolutions (McFadden, 2018), making it possible to capture even high frequency responses of structures superimposed with significant rigid body motions. For

example, the Phantom TMX 7510 manufactured by Vision Research can capture 76 000 frames per second at 1280×800 full resolution setting, and up to 1 750 000 frames per second at 1280×32 resolution. Being optical and non-contact in nature, this technique is not associated with all the disadvantages that come with an intrusive contact-based measurement approach. The full-field nature of the technique implies that dynamics of entire components can be captured, and data transfer from sensor to data logging systems is also much more easily accomplished.

The problem with current photogrammetric approaches being used to analyse rotating structures is that they are essentially based on specific pixel tracking algorithms. This means that some form of surface preparation or attachment of distinct markers on the surface of the structure under investigation must be done before practical information can be extracted from the captured images. Successful tracking of pixels is largely affected by the image quality and lighting in the environment, since each pixel is identified by its grey-scale value (a number between 0 and 255 assigned based on the brightness of the pixel for 8-bit images). This becomes a significant problem when analysing structures with significant rigid body motions. Performing these tests outdoors adds even more tracking problems, when one considers variations in the lighting with changes in the time of the day and possibly the weather. Thus there is need for better more suitable techniques for capturing vibrational information of large mechanical structures.

Image processing in which boundaries of objects in a captured image are extracted is a common practice used in object identification or matching. No tracking of specific pixels is required, and provided that the object can be distinguished from its background, a contour defining the boundary can be obtained. This type of image processing has not been adopted yet for dynamic analysis of structures for SHM purposes. Considering monitoring of wind turbine blades, developing a robust more industrially applicable optical non-contact measurement technique will add significant value to the future of wind energy harnessing.

1.2 Literature study

1.2.1 Structural Health Monitoring and Condition Monitoring – Rotating Structures

Basic online machine behaviour analysis constitutes a significant part of structural condition monitoring. CBM is a predictive maintenance strategy that identifies changes in the functionality of a machine, and detects irregularities in measured data. Condition monitoring strategies ensure that components are replaced at the right moment in a machine's life to avoid catastrophic system failures. This saves companies significant amounts of money through limited, scheduled downtime. Unlike preventive maintenance strategies which are implemented at specific time intervals, predictive condition monitoring ensures that maintenance is conducted when failure is likely to occur, and when the system performance is decreasing. Several techniques can be applied for condition monitoring purposes. These include vibration analysis, thermography, ultrasound, temperature monitoring, acoustics and lubricant analysis. When considering online machines' behaviour, analysing the vibrations associated with different components of a system can provide significant information that can be used to assess the condition in which the machine is operating.

To capture the vibrational information of these machines, conventional transducers such as accelerometers, strain gauges and proximity probes have been successfully utilized. In a

practical field implementation on rotating structures, these are typically attached at the non-moving components such as a wind turbine hub or a shaft bearing. They can also be installed on the rotating components as well, the shaft or turbines for instance. Whilst practical information about the behaviour of the system components can be gathered, that information is generally limited owing to the discrete nature of contact transducers. When attached to the rotating components, telemetry systems that allow data transfer from the transducer to the data logging system are typically used. These are however notorious for lowering the quality of the captured measurements in terms of the Signal-to-Noise Ratio (SNR). Wireless tri-axial accelerometers do exist, and these have been successfully used for condition monitoring purposes. These devices use microelectromechanical systems for sensing, and as such suffer from limited measurement ranges and frequency bandwidth. They also have low sensitivity and are generally large, making them unsuitable for some applications.

Whilst this study addresses optical noncontact measurement techniques being applied to rotating structures in general, wind turbines have been adopted as the structures of interest to motivate the study. Illustrated in Figure 1 are some of the aspects of wind turbines that make them appealing as the structures of interest to which development of a novel condition monitoring technique can be aimed at. How these aspects contribute to the need for the development of advanced optical measurement techniques is discussed in the sections that follow.

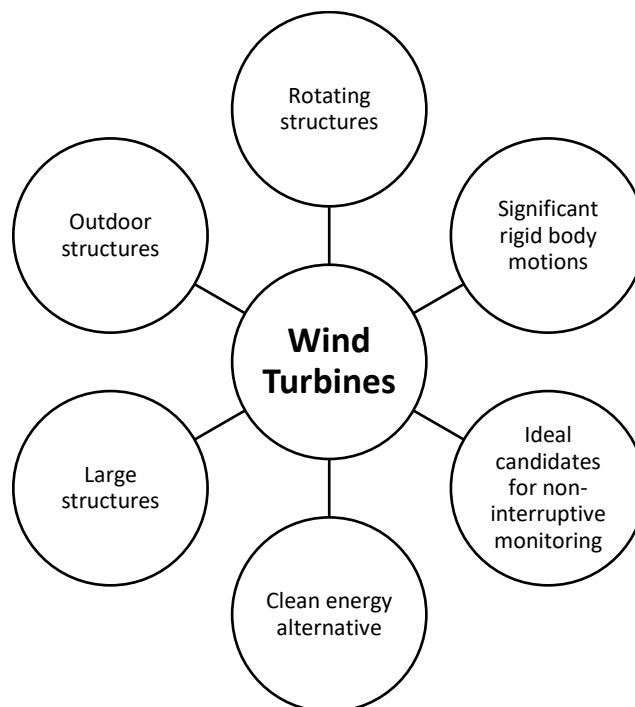


Figure 1: Motivation for choice of wind turbines as the model structures of interest

1.2.1.1 Wind turbines

Wind turbines are examples of large rotating machines which require specialized tools and strategies for condition monitoring. With the enormous drive to develop clean alternative sustainable renewable energy sources, the sizes of wind turbines being built are continuously increasing to harness more power from the wind. According to the 2023 Global Wind Energy Council report (GWEC, 2023), 680 GW of wind capacity are expected to be added globally between the years 2023 and 2027. This type of growth creates a great need for measurement

strategies that are better suited to easy capturing of usable operational data that can be used for designing structurally sound systems, and maintaining of turbines in operation. Owing to the harsh environments these structures operate in, failures typically resulting from strong winds, fatigue, moisture, lightning and fire are a present threat according to Zhou et al. (2014).

1.2.1.2 Wind turbine failures

Quite a significant amount of work has been done by Scotland Against Spin, an organization which campaign towards reforming the wind energy policy in Scotland. Some of the information they document relates to the accidents associated with wind turbines. In this case, accidents refer to incidents in a wind turbine life cycle that can potentially result in injuries or deaths of humans either directly working on the turbines or in the vicinity of the turbines when structural failures occur. Global yearly reported accidents highlighted in Figure 2 were found and confirmed through press reports or official information releases up to 30 June 2023.

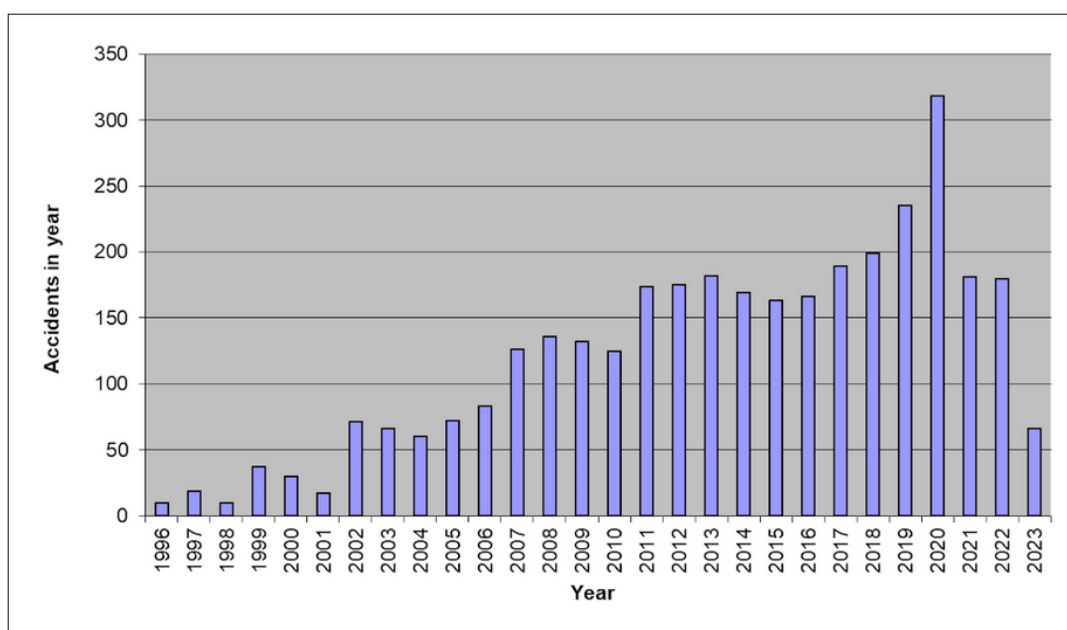


Figure 2: Documented yearly reported general wind turbine accidents (Scotland Against Spin, 2023)

In Figure 2, an increase in incidents owing to an increasing number of built wind turbines is clearly apparent. These numbers however seem to be generally flattening out. In addition to the general understanding that the public can be protected by ensuring safer distances between new turbine developments and settlements, sound engineering practices in handling and operating these structures will go a long way in reducing these numbers.

Most of the information relating to accidents caused by wind turbines is reported by advocacy groups. This means that the data can be difficult to verify, and its reliability might be questionable. Peer reviewed research such as the one conducted by (Ertek & Kailas, 2021) do provide insights in terms of the distribution of the number of accidents and fatalities associated with wind turbines during transportation of components, installation, operation and maintenance of wind turbines. Using information collected for a decade spanning from 2010 to 2019 in which a data set of 721 reports was considered, research done by these authors indicates that most accidents occur during the operation and transportation phases. These results are shown in Figure 3. Top twelve countries in the wind energy industry were considered in this case.

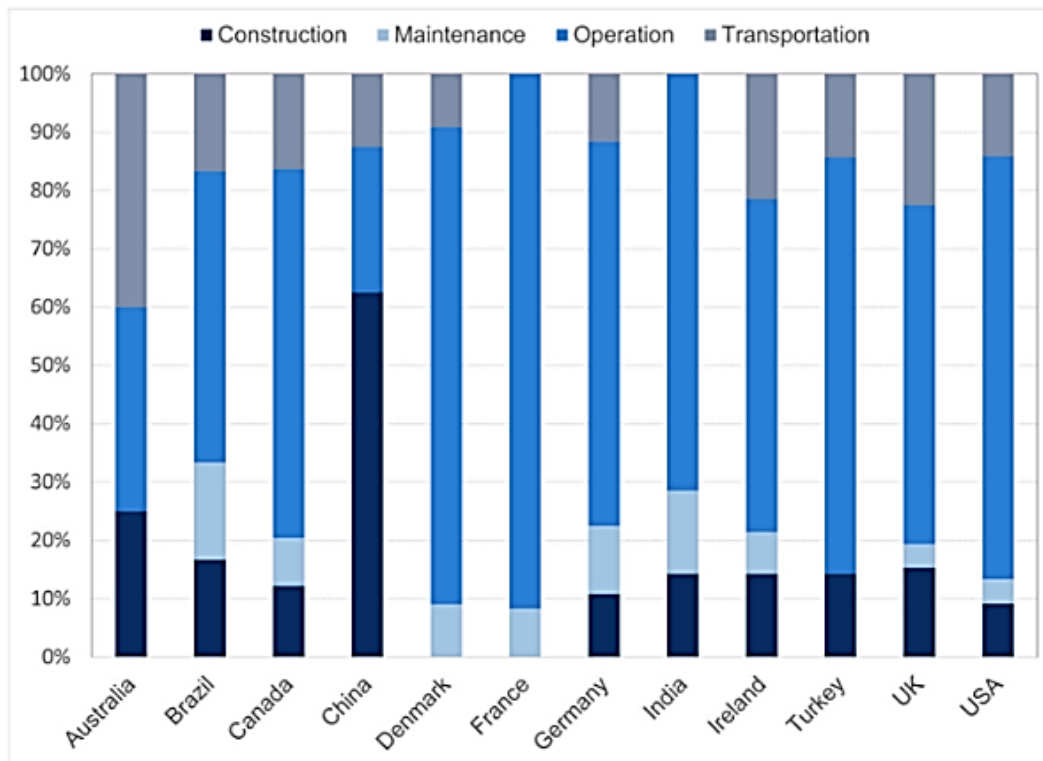


Figure 3: Frequency of accidents in different phases of a wind turbine's life cycle (Ertek & Kailas, 2021)

Figure 4 illustrates the percentages of wind turbine malfunctions, as collected for a period of over 15 years at a German wind farm. The information was collected from a total of 34582 recorded fault incidents. As can be noted, 7% of the faults are related to rotor blades. Although this is the case, it has been determined that about 15-20% of all costs related to a wind turbine are associated with the blades.

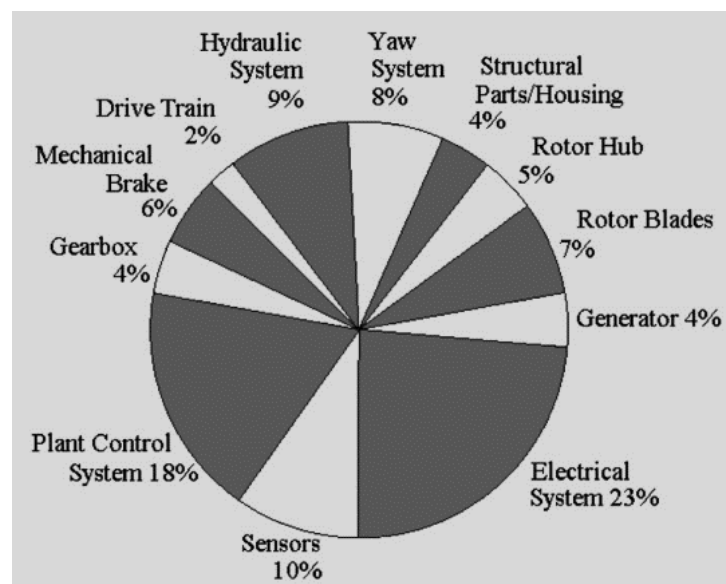


Figure 4: Component percentage contributions to wind turbine malfunctions (Ciang et al., 2008)

Additionally, they are also the most expensive to repair and the repair process is time consuming, based on the type and extent of the fault. A blade failure typically induces very

large rotor mass unbalances which can ultimately result in the collapse of the entire tower. As indicated by (Zhou et al., 2014), high wind failures resulting from malfunctioning rotor braking systems have been known to result in entire nacelles flying off towers, with one nacelle being thrown as far as half a kilometre. A typical case the authors indicated was recorded in a China wind farm (the Hedingshan Wind Farm) at which Typhoon Saomai swept turbines with wind speeds as high as 140 km/h, during 2006.

Figure 5 illustrates wind turbine failures resulting in total tower collapse. At the initiation stages of these failures, it is essential that engineers can detect changes in the system dynamics from captured vibration data. This will reduce the frequency at which dangerous expensive visual inspections have to be conducted, and avoid these catastrophic system failures.



Figure 5: Total tower collapse (Ciang et al., 2008)

The different damage modes that can result in turbine failure can be categorized as indicated in Table 1, as highlighted by Ciang et al. (2008). Figure 6, shows some of these damage modes.

In terms of the downtime and frequency of failures associated with different wind turbine components, Figure 7 adopted from (Turnbull et al., 2022) indicates that turbine blades failures are among the significant contributors to stop rates and downtime.

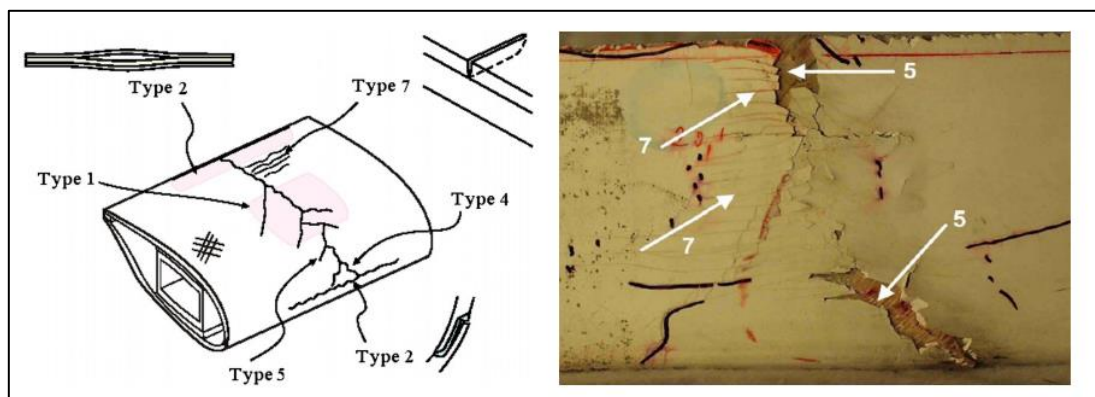


Figure 6: Illustration of wind turbine blade damage types (Ciang et al., 2008)

Table 1: Damage types for a wind turbine blade (Ciang et al., 2008)

Damage type	Description
1	Damage formation and growth in the adhesive layer joining skin and main spar flanges (skin/adhesive debonding and/or main spar/adhesive layer debonding)
2	Damage formation and growth in the adhesive layer joining the up- and downwind skins along leading and/or trailing edges (adhesive joint failure between skins)
3	Damage formation and growth at the interface between face and core in sandwich panels in skins and main spar web (sandwich panel face/core debonding)
4	Internal damage formation and growth in laminates in skin and/or main spar flanges, under a tensile or compression load (delamination driven by a tensional or a buckling load)
5	Splitting and fracture of separate fibres in laminates of the skin and main spar (fibre failure in tension; laminate failure in compression)
6	Buckling of the skin due to damage formation and growth in the bond between skin and main spar under compressive load (skin/adhesive debonding induced by buckling, a specific type 1 case)
7	Formation and growth of cracks in the gel-coat; debonding of the gel-coat from the skin (gel-coat cracking and gel-coat/skin debonding)

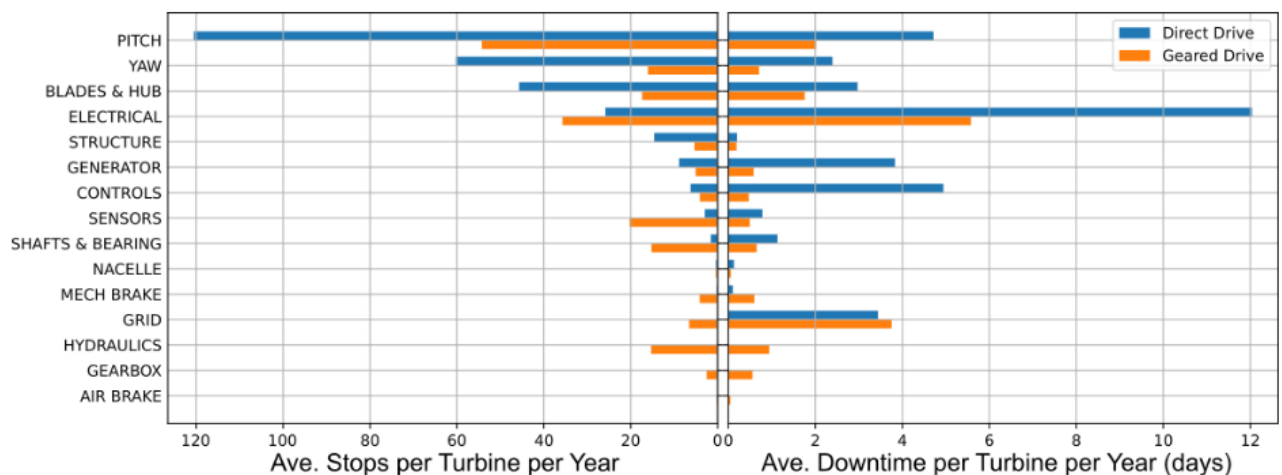


Figure 7: Average stop rates and downtimes due to different component failures for direct and geared drive wind turbines (Turnbull et al., 2022)

1.2.1.3 Conventional condition monitoring of wind turbines

The issues discussed above illustrate the need for sound condition monitoring strategies. Condition monitoring relies on the ability to acquire vibration data that can be analysed to gain information reflecting the dynamic behaviour of the blades. As reported by Antoniadou et al. (2015), wind turbine responses have a non-stationarity component associated with them. This

is because the responses are influenced by varying loads and environmental conditions. Whilst a number of damage detection strategies have been developed on scaled-down rotor sizes in controlled environments, it is difficult to accurately solve the damage detection issue in real world situations using basic signal processing techniques.

Time-domain approaches in which statistical parameters or moments such as the peak-to-peak value, peak amplitude, crest factor, kurtosis and skewness have been used as general vibration levels to capture wind turbine operational conditions. These are however mostly related to condition monitoring of other wind turbine components, the gearbox for instance. When considering turbine blades, the biggest obstacle to overcome is the issue of finding a practical and reliable sensing technology to capture the vibration data. Antoniadou et al. (2015) highlighted some of the different methods that have been used to analyse turbine blades for condition monitoring purposes. These are listed below:

- accelerometers
- piezo or microelectromechanical systems
- strain measuring devices (strain gauges or fibre optic cables)
- Fibre Bragg Grating (FBG) strain gauges
- piezoelectric transducers for measuring ultrasonic waves in composite structures
- smart paint in the form of fluorescent particles
- acoustic emissions using barrel sensors
- impedance techniques using a piezoelectric transducer
- scanning laser Doppler vibrometry
- impedance tomography using carbon nanotubes
- thermography using infrared cameras
- laser ultrasound
- nanosensors
- buckling health monitoring devices

The authors highlight that even though wireless sensors are more suitable for analysing the remotely situated turbine blades, their need for high power supplies tend to steer operators towards telemetry systems-based data acquisition techniques for damage detection purposes. These contact-based approaches can be very accurate when installed correctly, but they however suffer from a number of disadvantages highlighted by Zhou et al. (2014). In addition to hysteresis related errors and measurement non-linearities, strain gauges can be affected by changes in temperature. The degradation implies that they cannot be used over many years. Carrier material viscoelastic effects also influence the performance of these transducers, with the foil material cold working causing possible zero shifting in measurements as well.

For displacement measurements, discrete conventional transducers that have been adopted include micrometer gauges and linear variable differential transducers. These do have very limited measurement ranges, and if data must be captured at multiple locations on the structure, the system can easily become very complex and expensive. Contact sensors installed on the blades will typically not last for the estimated 20-year life span of a wind turbine whilst being exposed to the harsh environment and cyclic loading. Reinstalling these sensors is quite complicated on account of the size of these structures (Mistras Group, 2019). A fatal accident involving a collapsing tower whilst a person was still on top has been highlighted by

Ciang et al. (2008). In Wasco USA at Klondike III wind farm, a maintenance worker fell to death after a not-yet operational wind turbine snapped and broke about halfway up the tower. Other incidents of collapsing turbines have been reported as well.

Optical measurement techniques have thus been receiving significant attention as alternative approaches for acquiring vibrational information for condition monitoring of these rotating structures. The non-contact and full-field nature of some of these techniques make them better suited for these types of applications.

1.2.2 Optical Measurement Techniques

The optical techniques currently being used for capturing dynamic behaviour of rotating structures include the use of digital cameras (photogrammetry), Laser Doppler Vibrometry (LDV) and thermography. These are referred to as non-contact techniques in the sense that they do not interfere with the structure under investigation, something which can be significantly important when analysing light structures susceptible to mass loading related measurement errors. Whilst contact sensors capture discrete measurements for the location where the sensor is attached, photogrammetry for instance is capable of simultaneously capturing responses over an entire surface of a structure.

1.2.2.1 Thermography and LDV

Infrared thermography is an optical non-contact method in which surface thermal images captured using an infrared camera are analysed to detect subsurface defects in composite materials. These defects typically alter temperature distributions. According to Sanati & Wood (2018), thermographic inspections can be categorized as either active or passive thermography. Flash and halogen lamps heating sources are used to heat the structure under analysis in active thermography, making the approach less ideal for rotating wind turbines. Static laboratory tests can be successfully conducted using this approach, as indicated by the authors. In that investigation, defects such as cracks and delamination could be detected.

Laser vibrometry has been successfully used for capturing dynamics of rotating structures. Time domain and non-harmonic Fourier analysis techniques have been proposed in applying Eulerian LDV. In this approach the turbine blades sweep through a fixed laser beam as they rotate (Oberholster & Heyns, 2011). Several investigations have been conducted in which the laser beam actually rotates with the blades to capture full revolution blade out-of-plane responses. A self-tracking technique that employs a vertex mirror attached to the rotating hub and a fold mirror that reflects the laser beam onto the required blade was introduced by Lomenzo (1998). This approach is however not practical for large wind turbine blades since the laser vibrometer needs to be aligned with the wind turbine axis for it to work. Tracking systems that involve scanning laser vibrometers tracking blades based on the shaft angular position have been developed and successfully used to capture measurements (Gwashavanhu et al., 2016; Halkon & Rothberg, 2006). More advanced systems in which a video captured using a camera system is used to track full-scale wind turbine blades and then position the laser beam accordingly do exist, and they have been successfully adopted by Ebert et al. (2014).

Continuous Scanning Laser Doppler Vibrometry (CSLDV) which involves capturing both temporal and spatial information as a laser beam is continuously swept over a structure, has been successfully employed for structural analysis. Yang & Allen (2012) performed output-only modal analysis of a free-free beam under random excitation and a stationary 20 kW wind

turbine. Qualitatively reasonable results were reported. For a scanner synchronized with a rotating target, Di Maio & Ewins (2010) presented line and area scanning. Complicated deflection shape patterns were successfully captured using area scanning. Martarelli & Ewins (2006) investigated the effect of speckle noise on captured CSLDV data when the approach was being used to analyse an arbitrary shape. In the investigation, it was deduced that the speckle noise typically associated with CSLDV (as the coherent laser beam scatters on an optically rough surface) is concentrated at the laser scanning frequency and its harmonics.

1.2.2.2 Photogrammetry

Photogrammetry is a non-contact measurement technique that utilizes digital cameras to capture sequences of images of a vibrating structure. These images are then processed to extract displacements resulting from changes in position, or strains resulting from structural deformation. Whilst in-plane vibrations can be captured using a single camera, practical applications typically employ two cameras that ensure synchronized capturing of two stereoscopic images of the same structure at a particular time instant. These sequences of images of a dynamic structure can then be processed to obtain 3D structural responses.

The algorithms used in photogrammetry rely on identifying different pixels in the captured digital images, based on the pixel grey-scale values. Image matching techniques use the grey-scale values to identify corresponding pixels in images from different cameras. As a specimen moves or deforms, the pixels also need to be identified in the sequence of captured image pairs so their locations can be tracked from one image pair to the next. A reference or source image, typically the first image captured before a structure is loaded, is required. Based on its grey-scale intensity variations for a particular subset on the image, tracking of subsequent image subsets is done by means of establishing maximum similarity between them (Pan, 2010).

As described by Sutton et al. (2009), it is not always possible to establish pixel correspondence in images from different cameras. A pixel gray-scale value in one image can be identical to the gray-scale values of pixels in a thousand other locations in the other image. Thus successful pixel tracking is significantly influenced by the quality of gray-scale variation among pixels in a selected subset of the full image. A speckle pattern is usually applied on the surface of the specimen to address this correspondence problem. These random patterns deform or move with the structure.

Investigations to address how the quality of the speckle pattern affects the accuracy of the captured measurements have been conducted. Lecompte et al. (2006) investigated how three different speckle patterns perform in terms of the correlation between photogrammetry and imposed displacements in a finite element environment. It was established that the speckle size and the pixel correspondence subset/window size used during image matching clearly influence the accuracy of the results. Whilst a larger subset seemed to yield more accurate results, it was concluded that the subset size should be chosen according to the expected deformations, as inaccurate measurements were registered for displacements or strains with steep gradient variations. This was attributed to the smoothing effect large subsets tend to have on the real deformation behaviour.

In a different study, Crammond et al. (2013) did a quality assessment of the speckle pattern for the purposes of strain measurement using photogrammetry. In that investigation, it was realised that small densely populated speckles in a pattern decreased the measurement error.

Bigger speckles in a pattern produced more accurate results than smaller ones, owing to the greater speckle shape variation they provide.

Surface preparation is therefore a crucial part of accurate data acquisition using photogrammetry. Not only does it require careful considerations in terms of the magnitudes of the displacements or deformations to be captured, a system shutdown will be necessary for the pattern to be applied. For large structures such as wind turbines, the process will be complicated and time consuming. The type of environment in which the structure is operated can also limit the applicability of the approach as harsh conditions can easily damage applied speckle patterns.

On the other hand, even though limited to surface defect detection, visual inspection of captured images is a popular non-destructive inspection approach that does not require surface preparation. Fault identification through detection of cracks and discontinuities on a turbine blade surface via visual inspection was conducted by Kim et al. (2013). The authors developed a system for damage detection that incorporates a pan-tilt zoom camera to detect cracks on a blade. 2 cm cracks were detected at a standoff distance of 200 m. One of the problems associated with blade defect identification originates from the lack of defect images that can be used to limit variances in defects when considering manual inspections. Yu et al. (2020) proposed a method in which a Deep Convolution Neural Network (DCNN) is created and trained on an ImageNet Large Scale Visual Recognition Challenge dataset. According to Russakovsky et al. (2015), the ImageNet Large Scale Visual Recognition Challenge is a benchmark in object category classification and detection based on hundreds of object categories and millions of images. Yu et al. (2020) extracted deep hierarchical features of the training blade images using the trained DCNN and used these for classification. This then allowed blade defect classification to be conducted. Further applications of visual based inspections of wind turbines are discussed in the review by García Márquez & Peco Chacón, (2020), which highlights various strengths and weakness of some of these techniques.

Two main forms of photogrammetry that rely heavily on prior surface preparation are Digital Image Correlation (DIC) and 3D Point Tracking (3DPT). These have been successfully employed to analyse dynamics of structures as discussed below.

1.2.2.2.1 DIC and 3DPT

DIC is typically used to refer to photogrammetric strain measurements in deforming structures. Because this approach relies heavily on tracking subsets of a speckle patterned image, DIC is usually employed for analysis of structures that do not have significant rigid body motions. The technique is especially popular for measuring strains in statically loaded specimens, and crack growth analysis in applications involving fatigue life investigations.

Being a full-field measurement technique, DIC can be an invaluable tool in Finite Element Model Updating (FEMU). Whilst conventional contact transducers capture discrete measurements of mode shape responses, DIC can capture entire surface responses. Wang et al. (2011) used a comparison made between shape features extracted from full-field DIC data to those from a FE model, to identify that modelling bolted joints as springs instead of bolted joints, resulted in a more accurate model of an L-beam. Helfrick et al. (2011) stated that the significant mismatch in the degrees of freedom between experimental data and the FE model hindered effective and efficient analytical model correlating and updating. To address

this, the DIC approach they utilized provided numerous data points which could be geometrically correlated to nodes in a FE model.

Through investigating functionally graded materials crack growth using DIC, Abanto-Bueno & Lambros (2002) also demonstrated how optical full-field techniques are better suited for strain analysis. Understanding strain variations in the K-dominance regions where theoretical asymptotic fields capture deformations at the tip of a crack accurately, is not possible using conventional measurement techniques that only capture boundary measurements. This was successfully done using DIC. Vanlanduit et al. (2009) dynamically loaded a test sample to investigate fatigue induced crack growth in a sample. A sub-sampling image acquisition approach adopted with the understanding that the fatigue cyclic loading is periodic, allowed for sinusoidal displacement curve fitting. In that investigation, displacements could be calculated with accuracies within a few hundredths of a pixel.

Static analysis of turbine blades using photogrammetry has been conducted. In one investigation, LeBlanc et al. (2013) statically loaded a 9-m turbine blade at one end, whilst a set of cameras were being used to measure strains at different sections on the blade. These captured images were joined together using a stitching technique, allowing strains over the entire blade surface to be visualised. Damage localisation through identification of high strain areas on the blades was achieved. As highlighted by these authors, the load testing full-field strain measurements over the entire blade surface can be used for quality assurance purposes, in which anomalies in blades can be detected using 3D DIC.

In another static application Baqersad et al. (2015) used a mechanical shaker to excite turbine blades. High speed cameras were used to track markers attached on the surface of the blades. A modal expansion approach was then used to transform these 3D measurements captured to all the nodes' degrees of freedom in a finite element model, and full-field dynamic strains were extracted. Strain gauge measurements were also captured to validate the 3DPT data. The modal expansion of data captured using a discrete point photogrammetric technique proved to accurately predict the strains on the entire surface of the blades. Unlike DIC which requires more complicated permanent speckle pattern surface preparation for full-field dynamic strains, 3DPT, which requires discrete markers that are more easily attached, can thus be coupled with a modal expansion algorithm to obtain these strain measurements in a FE model environment.

Hasanen et al. (2013) successfully captured torsional vibrations in a shaft using a single camera and several mirrors carefully positioned to ensure that the 2-m separated two sets of spots on different locations on the shaft, could be recorded in a single picture simultaneously. This was done with the help of a pulsed diode laser illumination. Local displacements of the two spots were successfully used to determine the shaft torsional vibrations, which were then analysed in both the time and the frequency domains. The correlation between a theoretical model and photogrammetry measurements captured using this proposed experimental setup is quite promising in terms of avoiding the use of contact transducers on rotating components. These contact installations are considered high risk and the use of telemetry data transfer systems is generally undesirable on the account of the signal contamination by noise.

Blast loading of specimens to characterize their material properties is obviously better investigated using optical non-contact measurement approaches. Tiwari et al. (2009) successfully coupled high speed stereovision with 3D DIC to accurately capture high rate

surface deformations and also quantify the specimen responses. Spranghers et al. (2012) analysed aluminium plates under free air blast loading conditions using DIC. A good correlation between the captured DIC measurements and an explicit FE method was obtained, and the two sets of measurements were successfully used to calculate the elasto-plastic material properties. In that study, an inverse approach in which a tuning process to adjust parameters so that numerical observations are matched to the experimental data, was employed, this then allowing realization of the unknown material parameters.

Helfrick et al. (2009) exploited the dense measurement capabilities of Scanning Laser Doppler Vibrometry (SLDV) and DIC to successfully detect, localize and quantify the damage in a simple cantilever beam. The damage detection technique utilized was based on the fact that there is a local curvature variation of a structure under excitation at the region where a crack is located. Measurements captured over the entire span of the structure are therefore required. This has the potential of being successful as a structural health monitoring approach for a structure that also has rotational rigid body motion (wind turbine blades).

Data reduction of the full-field displacement data captured using DIC, through the use of the multivariate data analysis Principal Component Analysis (PCA), has been done to illustrate how the dimensionality of the displacement fields can be significantly reduced (Grama & Subramanian, 2014). These authors were able to extract excellent measurements for displacement fields that varied smoothly. Whilst 2D Savitzky-Golay is typically used to process noisy measurements before strains are calculated, the proposed PCA coupled with 1D filtering resulted in better estimated strain measurements.

In another investigation, Wang et al. (2012) used shape features to extract only the succinct noise robust parameters from the highly redundant DIC full-field measurements. These shape features extracted from 2D Adaptive Geometric Moment Descriptor (AGMD) were then successfully used for modal testing. From DIC raw measurements comprised of more than 14000 spatial data points per time step, 20 AGMD terms could be determined to accurately represent the DIC data. This proved to be an efficient way to represent the measurements, making it much easier to estimate frequency response functions at various points on the structure. Similarly, Pasialis & Lampeas (2015) utilized Zernike and Chebyshev Moment Descriptors (ZCMDs) to drastically reduce the computational effort in terms of data sizes to be analysed in a different investigation.

Najafi & Vesth (2018) developed a robust 3DPT approach for analysing a 1.64 m horizontal axis wind turbine, at a stand-off distance of 7.5 m from two high speed-cameras. In the investigation, the authors found that an alternative measurement technique to the conventional accelerometers existed. In addition to being intrusive, the installation of accelerometers typically includes wiring, which can be expensive and time consuming when measurements are to be captured on a large scale. Due to practicalities around 2D calibration of a full-scale wind turbine FOV using a calibration grid, a 3D calibration approach is suggested. At least a 120×120 m² grid size is required for a modern day wind turbine according to Najafi & Vesth (2018). 3D calibration uses exact point locations on a structure captured using a Leica surveillance device with a laser range finder as the calibration coordinates. To define the entire rotor area, the blades will have to be rotated by a specific angle in steps so that a collection of known coordinates can be developed for the camera calibration. The investigations done illustrated that this type of calibration proved to be more accurate. Blade out-of-plane displacements were then successfully captured using this approach.

In terms of wind turbine analysis using a pair of high-speed cameras, Winstroth et al. (2014) applied DIC on a full-scale 3.2 MW wind turbine. Surface preparations were done on four radial locations on the blades, and captured data was compared to aero-elastic simulations. The measurements obtained illustrate the applicability of using a photogrammetric approach to analyse a full-scale wind turbine in which the cameras are separated by 105 m and situated about 205 m in front of the turbine blades. In addition to demonstrating feasibility of the approach, in-plane, out-of-plane and torsional blade responses were also measured whilst the turbine was in operation. For an experiment of this magnitude, the preparations required are quite elaborate. Self-adhesive foils are used to apply the speckle pattern to the blade prior to blade mounting. This obviously limits/restricts the practicality of the proposed technique, something which the work presented here wishes to address. For a pitch angle step input, the small variations in the torsion, in-plane and out-of-plane blade responses detected illustrated that the optical system had a high spatial accuracy. The comparison done by the authors between DIC and aero-elastic simulations indicated good agreement of measurements, demonstrating that DIC can be used for aero-elastic simulation code validation.

Ozbek et al. (2010) also analysed a full-scale wind turbine (2.5 MW, 80 m diameter) using four CCD cameras. At a stand-off distance of 220 m, operational deflection shapes of the blades could be captured, and displacements with an accuracy of ± 25 mm identified. Whilst the maximum overall error for markers at the tip of the blade could reach 35 mm, the authors suggested that these systematic errors could be reduced by using more sophisticated camera calibration systems, and also by utilizing hardware and data processing methods more specialized for analysing wind turbines. Since this approach does not require extra cable installations and focuses only on the markers attached on the surface of the blade, it is generally more suited for analysing these large structures when compared to the conventional fibre optics strain gauges and accelerometers. The authors also highlighted the advantages of adopting this measurement approach, which include the fact that a single system can be used to monitor several turbines. Data capturing systems located on the ground can be easily accessed and data analysed to detect any faults. The measurements can also be stored to develop proper condition monitoring archives. Even though the installation costs can be reduced by replacing the markers with retroreflective paints applied in the factory during the manufacturing stages, in-service systems will still be interfered with for the surface preparation.

Lundstrom et al. (2016) used high speed stereo-photogrammetry in the form of 3DPT to analyse the dynamics of rotating helicopter blades in both grounded and hovering conditions. The authors emphasized the advantages of using the approach for structural health monitoring, highlighting that the non-contact nature of the approach imply that no slip rings for data transmission from transducer to data logging systems are necessary. Interference with the structure in the form of mass loading was avoided, and the markers attached for tracking introduced a negligible effect on the blades' aerodynamics as well. The full-field nature of the technique that allows data acquisition at hundreds of measurement locations simultaneously was also highlighted. The flap-wise blade dynamic responses of the centre of rotation were effectively analysed through coordinate transformation. In addition to that, the non-harmonic operational deflection shapes could be successfully captured and analysed.

The use of Unmanned Aerial Vehicles (UAVs) to capture footage (image sequences) of blades has been investigated. Khadka et al. (2020) employed a DIC system installed on a drone to measure deflections of a six bladed 113 cm rotor with a hub height of 154 cm. Using a dynamic

image stitching technique of the DIC measurements, the authors were able to characterize the dynamics of the entire blade with high accuracy. Limitations when it comes to adopting the technique for large wind turbines onsite were also highlighted. These include the need for speckle pattern application, the requirement that the drone flight mode path be programmed for each specific turbine, and the windy conditions of the locations where wind turbines are installed. Ensuring that patterns are applied during manufacturing and equipping the drones with Light Detection and Ranging (LIDAR) to improve drone the control were proposed possible solutions to these issues. Guan et al. (2022) proposed a similar UAV based technique for defect detection of a 94 m diameter wind turbine. In the investigation, a combination of ground cameras at a standoff distance of 248 m and stereo camera system mounted on an UAV was used. Successfully captured were the turbine global dynamic measurements and local blade deformations. Inspection of the blade surfaces using data from the UAV allowed for a complete assessment of the wind turbine.

A number of investigations have been conducted in which photogrammetric results have been correlated to measurements captured using other measurement techniques. Warren et al. (2010) successfully analysed a rotating 1.17-m diameter wind turbine using DIC, 3DPT and accelerometers. The auto-power spectra of the captured measurements showed good agreement, with some discrepancies, however. These were attributed to possible accelerometer cross-axis sensitivity, optical system noise floor and telemetry system slip ring noise. Unlike accelerometers that are point-wise transducers which also potentially mass load a structure, scanning vibrometers can measure large numbers of points in a non-contact manner. In addition, they also have a quite wide measurement frequency range. Being capable of capturing large displacements at very low frequencies, photogrammetry can be used to complement measurements captured using accelerometers and vibrometers. Warren et al. (2011) analysed a base upright specimen using digital image correlation, 3DPT, 3D laser vibrometry and an accelerometer. Even though good correlation was observed around the Frequency Response Function (FRF) peaks, differences in the system noise floors at particular frequencies and varying system SNRs resulted in slightly different observations. An investigation done by Helfrick et al. (2011) provided results that indicated great correlation of measurements captured using high speed cameras, accelerometers and a scanning laser vibrometer. This was for a dryer-cabinet panel being excited by a mechanical shaker.

Illustrated in Table 2 are comparisons of the characteristics of different modal analysis techniques, as indicated by Helfrick & Niezrecki (2011).

Ha et al. (2013) investigated the dynamic characteristics of an artificial wing mimicking the *Allomyrina dichotoma* beetle's hind wing using photogrammetry and scanning laser vibrometry. Results of mode shapes at predetermined natural frequencies illustrated good correlation between the two techniques, with DIC being capable of providing very high resolution mode shapes. Gwashavanhu et al. (2016) analysed rotating blades using 3DPT and Tracking Scanning Laser Doppler Vibrometry (TLDV). Out-of-plane blade responses indicated a maximum of 2.5% difference in magnitude, and a 0.076% difference in frequency at the frequency peaks for percentages calculated with reference to TLDV measurements. These were attributed to differences in the system noise floors for the two measurement approaches.

Table 2: Comparison of contact and non-contact methods for modal analysis (Helfrick et al., 2011)

Impact hammer test	Photogrammetry	Scanning laser vibrometer
Transfer function easily determined	Complex post-processing of results necessary	Transfer function easily determined
Sensitivity depends on the transducers used	Sensitivity inversely proportional to the FOV	Sensitivity related to the laser light wavelength
Broadband excitation of all modes	Mostly suited for excitations at a single frequency	Broadband excitation of all modes
Discrete responses at locations where transducers are attached	Responses on the entire visible surface of a specimen	Responses at pre-defined locations on a specimen
Each point tested separately	Each shape tested separately	Each point tested in a series
No stability requirements	Generally less sensitive to camera rigid body motion	Calibration is highly sensitive to changes in the set-up conditions
Inexpensive equipment	Expensive, depending on the quality of the high-speed cameras	Very expensive
A contact measurement technique, with possible mass loading	Non-contact technique, but requires a clear line of sight to structure	Non-contact technique, but requires a clear line of sight to structure
Low spatial resolution	Very high spatial resolution	High spatial resolution

1.2.2.2.2 Motion magnification

Wadhwa & Rubinstein (2013) describe a video processing and motion magnification technique that allows visualizations of otherwise non-apparent motions in captured video footage. In this approach, termed Eulerian Video Magnification, processing is done by applying frame spatial decomposition and temporal filtering. Amplification of the resulting signal is then implemented. Using this technique, the authors were able to magnify the motion of a seemingly stationary crane being swayed by the wind. Lu et al. (2019) applied the technique to successfully observe the vibration of a tower through amplification of its small motions. Using a similar approach, Wu et al. (2012) magnified temporal colour changes using spatio-temporal processing to amplify motions in ordinary videos. In their investigation, they were able to visualize the human pulse by analysing a video sequence of a human face.

Diamond et al. (2016) applied a complex filter to down-sampled frames, and calculated vibration responses from the phase of selected active pixels. The captured measurements were validated using accelerometer and laser vibrometry data. In the investigation, it was

shown that responses 450 times smaller than the size of a pixel could be captured. Yang et al. (2017) combined a multiscale pyramid decomposition approach, in conjunction with blind source separation, to manipulate image pixel phase information. In the investigation, modal parameters and mode shapes of a beam structure were successfully captured from video measurements. For a 2.3-m long wind turbine blade fixed at one end and excited by a modal hammer, Sarrafi et al. (2018) used phase-based motion estimation and motion magnification to estimate the blade's structural motion for both baseline and damaged test scenarios. Operational deflection shapes and resonant frequencies were used for damage detection, illustrating the feasibility of using non-contact video-based measurements for condition monitoring purposes.

For a more sensitive vibration detection approach on a sub-pixel level, Lado-Roigé et al. (2023) explored the use of learning-based video motion magnification instead of hand-designed or manually tuned filters. The synthetically trained learning-based model was created using a non-related image dataset, and then successfully applied to verify and validate the approach on a structural system to detect different vibration scenarios. Further reviews on the different applications of motion magnification-based techniques are detailed in the work done by Śmieja et al. (2021).

This type of video analysis to magnify the motion of objects in captured footage can become very useful when a shape analysis approach similar to the one described in this research is to be implemented. Amplified motions imply improved SNR of shape variations in captured data, which has significant influence on the accuracy and validity of the conducted analysis. Molina-Viedma et al. (2018) successfully coupled DIC and motion magnification to analyse magnified videos. Characterisation of DIC mode shapes at high frequencies through displacement amplification could be performed. Whilst initial video magnification techniques focused on analysis of specific selected 'active' pixels (Diamond et al., 2016) and on non-rotating structures where rigid body motions were not a factor to consider (Wu et al., 2012), more research is being done to improve the applicability of the technique. With regards to structures undergoing significant rigid-body motions, Yang et al. (2020) successfully identified full-field vibration modes and the rigid motions of a bench-scale building structure using an output-only video analysis approach. Both the subtle full-field deformation modes of the structure and its dominant rigid-body motions could be captured. Thus, motion magnification coupled with a statistical shape analysis for condition monitoring of rotating structures is definitely an interesting possible area of research with significant potential impact on the applicability of optical non-contact measurement techniques.

1.2.3 Statistical shape analysis

One of the limiting factors of photogrammetry is the need for prior surface preparation in the form of a speckle pattern (DIC) and distinct markers (3DPT). As discussed earlier on, a speckle pattern for DIC cannot be randomly applied on the surface of the structure if accurate consistent results are to be obtained. This especially becomes problematic when one is tasked with analysing large outdoor structures. In addition to getting the ideal speckle density and size right, the less control one has on the overall lighting on the structure presents its own problems for DIC and 3DPT, especially for DIC.

Structural boundary shape analysis is an alternative photogrammetric measurement technique that has not been considered as a condition monitoring approach. It is typically used for shape recognition and matching purposes. For instance, handwritten digits by different

people can appear similar to an observer but have very different pixel arrangements. If these digits are to be captured using an automated system, some form of shape recognition and matching will have to be applied.

Shape analysis is widely used in Content Based Image Retrieval (CBIR), which entails the use of shape descriptors for extracting visual features from a shape boundary and/or interior (Kazmi et al., 2013). The authors define a shape descriptor as a vectorial representation of a 2D or 3D shape. The vector is composed of a set of numerical values or a graphical structure that describe the geometrical and topological features of the shape. These features include unique shape signatures, boundary contour curves, shape context and histogram, and shape spectral features. The most visually similar image to a query image of interest, described in the form of these shape features, is then extracted from a database of images. Thus, CBIR is also referred to as Query By Image Content (QBIC). With the abundance of cameras capturing digital images in everyday lives, quite a few applications have been emerging to exploit the advantages of image-based search algorithms. According to Zhou et al. (2017), titles and tags have been used as the image surrounding meta data information indexed on the web in traditional image search engines. However, the inconsistencies between textual information and visual content have been the driving force for advancing CBIR. Typical different query schemes and their significantly distinguishable outcomes as presented by Zhou et al. (2017) are given in Figure 8.

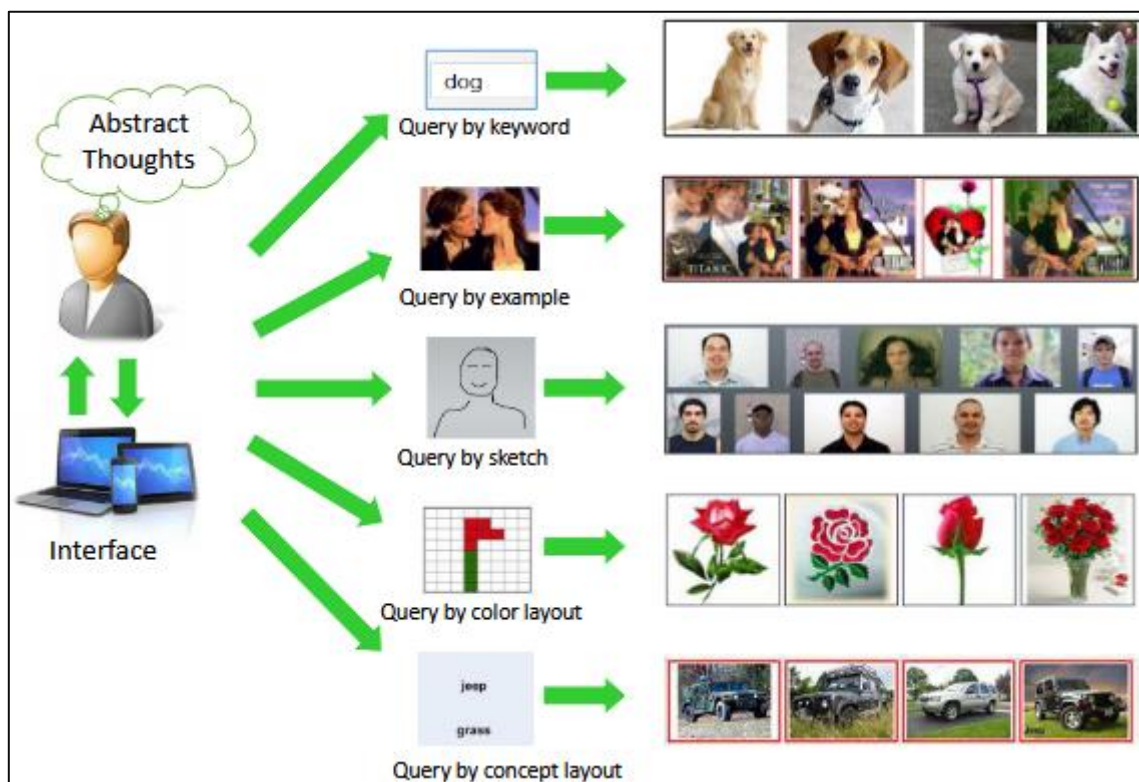


Figure 8: Typical CBIR query schemes and their outcomes (Zhou et al., 2017)

Kazmi et al. (2013) conducted a survey on 2D and 3D shape descriptors in which they reviewed widely used descriptors. Descriptors are typically evaluated in terms of a number of qualities that represent how well they can define a shape. These characteristics, as highlighted by Kazmi et al. (2013), are stated below.

- Descriptor invariance to translation, scaling and rotation transformations
- Descriptor uniqueness for unique or different shapes, with discriminative accuracy based on subtle differences
- Computational complexity and memory efficiency
- Robust shape matching in the case of partially incomplete shapes
- Robust to accurately describe noisy shapes

Simple descriptors that one can monitor include the area, aspect ratio, normalized central moments and perimeter of a shape. These geometric features are however not efficient as shape descriptors, and do not contain much information when compared to shape features, as highlighted by Mebatsion et al. (2012). More sophisticated shape descriptors such as those discussed by Kazmi et al. (2013) have therefore been proposed. These tend to be more sensitive to various shape changes, and can be classified in 2D as contour, region or hybrid-based descriptors. The contour-based descriptors namely Fourier Descriptors (FDs), Wavelet Descriptors (WDs), Curvature Scale Space Descriptors (CSSDs) and the Shape Context Descriptors (SCDs), extract shape features from the boundary of a shape. On the other hand, region-based descriptors such as the Zernike Moment Descriptors (ZMDs), the Scale Invariant Feature Transform (SIFT) and the Angular Radial Transform (ART) obtain features from the whole region of the shape. For strain analysis, region-based descriptors from full-field DIC measurements data reduction implementation are utilized. The data reduction features are less computationally expensive. 3D shape descriptors can be classified as view based, histogram based, transform based, graph based and hybrid descriptors. These are however not investigated further in this study.

When calculating FDs, the contour must first be represented by a shape signature, which is essentially a 1D function which can be the shape centroid distance, complex coordinates, the curvature function or the cumulative angular function according to (Kazmi et al., 2013). Other shape signatures such as the Freeman's chain code adopted in this study are discussed further in the following sections. In typical applications, the discrete Fourier transform is used to calculate the FDs in the form of Fourier coefficients of the shape signature. FDs are generally easier to compute and are quite robust to noise when compared to other 2D descriptors.

Wavelet descriptors involve the use of a multiresolution approach that decomposes the contour into several components in multiple scales. Higher resolution components represent the global shape features, whilst the lower resolution components capture the more detailed local features (Kazmi et al., 2013). They are generally known to represent local features more accurately than the other descriptors.

CSSDs are computed by dividing a shape into convex and concave segments and then identifying a set of points where the shape curvature is zero (inflection points). The curvature values are calculated whilst the curve is being progressively smoothed down, and a CSSD plot consisting of a 2D curve of all the curvatures zero crossing points determined. On the other hand, the SCD is based on finding the correspondence between two shapes through defining a dissimilarity measure between them. Further details on determining these 2D descriptors can be found in the survey conducted by Kazmi et al. (2013) and the work by Zhang & Lu (2004).

Descriptors are usually picked according to the application, and significant work has been done to critically assess how they perform against each other. For instance, Zhang & Lu (2003) did a comprehensive comparison between FDs and CSSDs using standard principles and a standard data base in an image retrieval application. It was concluded that FDs are more robust than CSSDs, in addition to entailing lower computations, better retrieval performance, and hierarchical representation. CSSDs are shown to be robust to only local shape variations, not the global features. Empirical factors influence its performance to retrieve and represent images. These factors include the number of sample points on the boundary considered, the set threshold for a positive peak identification and the peak position matching tolerance.

Most of the focus on shape descriptors for mechanical engineering applications has been on the use of region-based descriptors. Descriptors have been used to handle the massive amounts of data obtained from FEA and full-field measurement techniques prior to structural dynamics analysis. This includes the work done by Wang et al. (2011), in which finite element model updating of a panel is done through the use of the Tchebichef moment descriptor applied to DIC measurements. In that investigation, the region-based descriptor's formulation incorporating parameter orthogonality and therefore uniqueness was exploited to determine shape features described as succinct and effective in representing mode shapes. The already mentioned work by Wang et al. (2012) and Pasialis & Lampeas (2015) also entail data analysis using region-based shape descriptors.

Patterson & Patki (2012) utilized an image decomposition approach through the use of geometric moments to represent strain data. Different descriptors associated with different levels of damage in a specimen were then compared using Euclidean distance, and a good correlation between these distances and the level of damage was observed. A quantitative evaluation of damage in composite materials was therefore successfully done.

To date, not much work has been done in terms of employing contour-based descriptors to investigate mechanical structures for condition monitoring purposes. Studies conducted typically involve shape classification and identification in the biological and medical field. Bhonsle et al. (2009) used the centroid distance function as a shape signature for FDs in an application involving clustering of cancer cells. *k*-means clustering with FDs made it possible to distinguish different cells shapes, something which is important when quantifying tumor cells. Mebatsion et al. (2012) classified cereal grains based on grain kernel shapes using the Invariant Elliptic Fourier descriptors (IEFDs). In the investigation, it was shown that the first three to five IEFDs could classify the grains with accuracies of more than 99%.

1.2.3.1 The Freeman's chain code Fourier descriptors

Contour based FDs are considered in this study. The descriptors have the following listed advantages, as described by Zhang & Lu (2004).

- They are developed from the sufficiently understood Fourier theory
- They are simple to compute
- They can be easily normalized, making them ideal for shape matching applications
- They can capture both the local and global features of a shape

In addition, and a significant factor why FDs are considered, each computed descriptor has a unique and specific physical meaning associated with it. This is further discussed and illustrated in the following chapters.

FDs can be determined for a closed contour describing a shape of interest. The closed contour representation can be obtained by the use of Freeman's chain code (Freeman, 1974). As described by Jusoh & Zain (2009), a chain code represents a boundary of interest based on either 4-connectivity or 8-connectivity of segments. It is a 1D function (shape signature) created by tracing the mid-points of the boundary pixels in a counter-clockwise direction. For the 8-directional chain-code, each integer in the code will be assigned a value between 0 and 7 depending on its orientation relative to the previous pixel. This is illustrated in Figure 9, where the starting point is the red pixel.

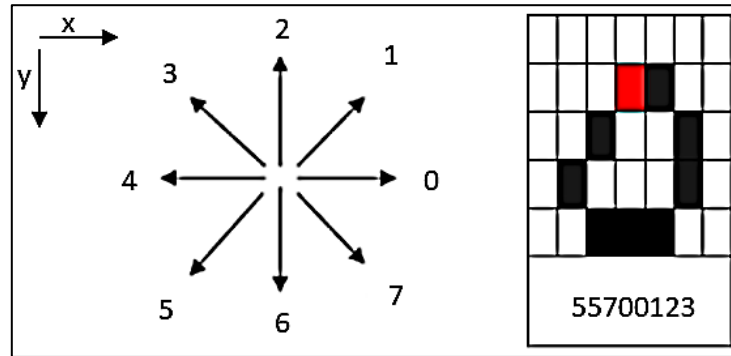


Figure 9: 8 directional chain-code (counter-clockwise, starting point red pixel)

As discussed by Kuhl & Giardina (1982), a Fourier series representation of the code can be used for extracting shape descriptors, since the code repeats itself on successive traversals of a closed contour. The Fourier coefficients of the chain-coded contour form the FDs for that particular shape. A description of the representation of a chain-code using a Fourier series is given below.

Consider a chain-code $Cc = v_1, v_2, \dots, v_k$ whereby $v_i \in [0:7]$. According to Kuhl & Giardina (1982), a continuous boundary contour can be approximated by a sequence of piecewise linear fits. Each fit or link v_i is an integer between 0 and 7, oriented in the direction $(\pi/4)v_i$, and of length 1 (if v_i even) or $\sqrt{2}$ (if v_i odd). In phasor notation, each link can thus be represented as a vector using Equation (1):

$$\left(1 + \left(\frac{\sqrt{2}-1}{2}\right)(1 - (-1)^{v_i})\right) \angle \frac{\pi}{4} v_i \quad (1)$$

The contour's chain-code is then projected onto the xy-plane. Variations in the x- and y-projections of the chain code as the link v_i is traversed, can then be calculated using Equation (2) and Equation (3).

$$\Delta x_i = \text{sgn}(6 - v_i) \text{sgn}(2 - v_i) \quad (2)$$

$$\Delta y_i = \text{sgn}(4 - v_i) \text{sgn}(v_i) \quad (3)$$

In the above equations, $\text{sgn}(\zeta)$ corresponds to the sign of a value, ζ , as defined by Equation (4).

$$\text{sgn}(\zeta) = \begin{cases} 1, & \text{if } \zeta > 0 \\ 0, & \text{if } \zeta = 0 \\ -1, & \text{if } \zeta < 0 \end{cases} \quad (4)$$

Equations (5) and (6) are adopted to calculate projections onto the xy-plane of the k links of the determined chain-code.

$$x_k = \sum_i^k \Delta x_i \quad (5)$$

$$y_k = \sum_i^k \Delta y_i \quad (6)$$

For a closed chain-coded contour projected on the xy-plane, the elliptical Fourier series approximating the contour can be defined using Equations (7) and (8) below, (Mebatsion et al., 2012a).

$$x_n(q) = A_0 + \sum_{n=1}^N a_n \cos\left(\frac{2n\pi q}{Q}\right) + b_n \sin\left(\frac{2n\pi q}{Q}\right) \quad (7)$$

$$y_n(q) = C_0 + \sum_{n=1}^N c_n \cos\left(\frac{2n\pi q}{Q}\right) + d_n \sin\left(\frac{2n\pi q}{Q}\right) \quad (8)$$

In the above expressions, the geometric step to move from one pixel to the next is given by q . Q is the geometrical period for traversing through the k links of the chain code, and N gives the number of Fourier harmonics considered. Detailed descriptions on the derivations of these coefficients can be found in Mebatsion et al. (2012a); Kuhl & Giardina (1982). The Fourier power of a harmonic, which indicates the amount of shape information described by that particular harmonic (Mebatsion et al., 2012), can be used to estimate the number of harmonics required.

$$\text{Fourier power} = \frac{\sum_{n=1}^N (a_n^2 + b_n^2 + c_n^2 + d_n^2)}{2} \quad (9)$$

The average cumulative Fourier power percentage increases with the number of considered Fourier harmonics. The number of harmonics required for the truncated Fourier coefficients can thus be determined based on the preferred average cumulative power percentage. A high average cumulative power percentage ensures that the local shape features are captured more accurately. According to Mebatsion et al. (2012), for N equal to half the number of contour boundary points, a cumulative power more than 99% can be obtained, which will guarantee an accurate representation of the contour.

In the case of a 3D shape analysis, the 26-connectivity chain code must be adopted. Each pixel of the discretized contour is assigned a value based on its direction relative to the previous pixel. Figure 10 below illustrates how the different pixel directions are assigned to a pixel whose previous neighbour is positioned at the centroid of the cuboid. A description of the procedure used to transform the 26-connectivity chain code of a contour to shape descriptors, in the form of Fourier coefficients, that uniquely describe the contour, follows.

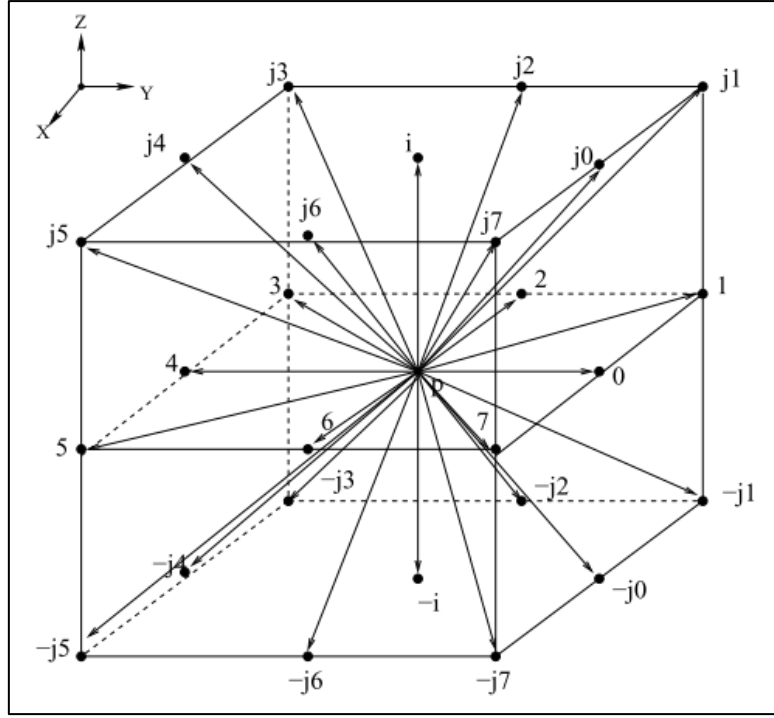


Figure 10: Direction based code assignment for the 26-connectivity chain code (Bose, 2000)

As reported by Bose (2000), for a 26-connectivity chain code shape signature in which each link v_l is one of the directions, the length l of that link for a chain code $Cc = v_1, v_2, \dots, v_k$ is given by Equation (10).

$$l(v_l) = \begin{cases} 1, & \text{if } v_l \in \{0, 2, 4, 6, i, -i\} \\ \sqrt{2}, & \text{if } v_l \in \{1, 3, 5, 7, j_0, j_2, j_4, j_6, -j_0, -j_2, -j_4, -j_6\} \\ \sqrt{3}, & \text{if } v_l \in \{j_1, j_3, j_5, j_7, -j_1, -j_3, -j_5, -j_7\} \end{cases} \quad (10)$$

As link v_l is traced, successive pixel direction changes in x-, y- and z-projections of the chain can then be represented as given in the equations below.

$$\Delta x_l = \begin{cases} 0, & \text{if } v_l \in \{0, 2, 4, 6, i, -i\} \\ -1, & \text{if } v_l \in \{1, 3, 5, 7, j_0, j_2, j_4, j_6, -j_0, -j_2, -j_4, -j_6\} \\ 0, & \text{if } v_l \in \{j_1, j_3, j_5, j_7, -j_1, -j_3, -j_5, -j_7\} \end{cases} \quad (11)$$

$$\Delta y_l = \begin{cases} 1, & \text{if } v_l \in \{0, 2, 4, 6, i, -i\} \\ -1, & \text{if } v_l \in \{1, 3, 5, 7, j_0, j_2, j_4, j_6, -j_0, -j_2, -j_4, -j_6\} \\ 0, & \text{if } v_l \in \{j_1, j_3, j_5, j_7, -j_1, -j_3, -j_5, -j_7\} \end{cases} \quad (12)$$

$$\Delta z_l = \begin{cases} 1, & \text{if } v_l \in \{0, 2, 4, 6, i, -i\} \\ -1, & \text{if } v_l \in \{1, 3, 5, 7, j_0, j_2, j_4, j_6, -j_0, -j_2, -j_4, -j_6\} \\ 0, & \text{if } v_l \in \{j_1, j_3, j_5, j_7, -j_1, -j_3, -j_5, -j_7\} \end{cases} \quad (13)$$

It is for these projections that the Fourier series approximation of the entire contour for N considered harmonics are calculated using the equations below, to determine coefficients that are considered the shape descriptors.

$$x_n(q) = A_0 + \sum_{n=1}^N a_n \cos\left(\frac{2n\pi q}{Q}\right) + b_n \sin\left(\frac{2n\pi q}{Q}\right) \quad (14)$$

$$y_n(q) = C_0 + \sum_{n=1}^N c_n \cos\left(\frac{2n\pi q}{Q}\right) + d_n \sin\left(\frac{2n\pi q}{Q}\right) \quad (15)$$

$$z_n(q) = E_0 + \sum_{n=1}^N e_n \cos\left(\frac{2n\pi q}{Q}\right) + f_n \sin\left(\frac{2n\pi q}{Q}\right) \quad (16)$$

Coefficients a_n, b_n, c_n, d_n, e_n and f_n for a closed contour for a particular captured image constitute the contour's Fourier shape descriptors. A number of sources outline detailed derivations of these coefficients (Mebatsion et al., 2012; Kuhl & Giardina, 1982; Bose, 2000).

The way these Fourier shape descriptors are then further processed to ultimately capture dynamic shape variations is described in the following section.

1.2.4 Statistical data reduction

The concept of data reduction using statistical methods such as PCA and Independent Component Analysis (ICA) is widely used as a post-processing tool in SHM. This is done to extract features of reduced dimensionality that retain most of the variations present in the original data. The technique allows classification of dynamic behaviours of machines that have different forms or levels of damage to be done more efficiently and accurately.

1.2.4.1 Principal component analysis

Using PCA in a machine learning application, dimensionality reduction and visualization of measurements is achieved by linearly projecting the possibly correlated data into a lower dimensional feature space of uncorrelated data using a linear transformation (Tippmann et al., 2015). When performing 2D or 3D shape analysis, it is not the data reduction that is of importance, but rather the uncorrelated nature of the computed principal components. Normalized truncated Fourier coefficients determined as described in the previous section are considered as the multivariate vector (X_{2D} for 2D shape analysis and X_{3D} for 3D shape analysis) to which a standard PCA is applied. This multivariate vector is given in the equation below for 3D analysis. In terms of a 2D analysis, X_{2D} is a $4 \times N$ matrix comprising only of coefficients a_n, b_n, c_n, d_n as given by Equations 7 and 8. X_{3D} for 3D analysis is a $6 \times N$ matrix of coefficients $a_n, b_n, c_n, d_n, e_n, f_n$ as given by Equations 14, 15 and 16.

$$X_{3D} = \begin{bmatrix} a_1 & a_2 & \dots & a_N \\ b_1 & b_2 & \dots & b_N \\ c_1 & c_2 & \dots & c_N \\ d_1 & d_2 & \dots & d_N \\ e_1 & e_2 & \dots & e_N \\ f_1 & f_2 & \dots & f_N \end{bmatrix} \quad (17)$$

Principal Component Analysis (PCA) of the $6 \times N$ multivariate vector (X_{3D}), henceforth referred to as simply X , can then be conducted by first computing the 6×6 covariance matrix C of X according to Equation 18. In Equation 18, \bar{X} corresponds to the mean and \bar{X}_i the i^{th} column of X .

$$\mathbf{C} = \frac{1}{N-1} \sum_{i=1}^N (\vec{X}_i - \bar{\mathbf{X}})(\vec{X}_i - \bar{\mathbf{X}})^T \quad (18)$$

For \mathbf{C} , eigenvector \mathbf{V} and eigenvalues \mathbf{I} that satisfy Equation 19 are determined, from which a new uncorrelated multivariate vector \mathbf{X}^{new} can be computed according to Equation 20.

$$\mathbf{C}\vec{V}_i = \mathbf{I}_i\vec{V}_i, \quad i = 1:6 \quad (19)$$

$$\mathbf{X}^{new} = \mathbf{V}^T \mathbf{X} \quad (20)$$

Each row of matrix \mathbf{X}^{new} (which contain the principal component scores and denoted as \vec{X}_i^{new} for row i) represents the uncorrelated linear combinations of the original data, accounting for the variance in the data. Each column of matrix \mathbf{V} (i.e., \vec{V}_i) represents a specific shape feature, termed the Shape Principal Component (SPC). \mathbf{V} can be considered to be composed of geometric shape modes. The physical relationships between different \vec{V}_i vectors and the form of a typical shape are investigated further in the following chapters.

The uncorrelated \vec{V}_i s represent unique shape features whose variations can be monitored separately to get an in-depth insight on how the overall shape changes in a dynamic situation. Each \vec{V}_i represents an independent shape feature which allow a quantitative analysis of the shape to be conducted by use of \mathbf{X}^{new} as the ordinary quantitative characters (Mebatsion et al., 2012).

The approach of using \mathbf{V} for shape analysis has been used before. Shape analysis was conducted by Iwata et al. (2002), in which different variations of citrus leaf shape were investigated and quantified using PCA. Variations in the shape of cereal grains were also successfully investigated using PCA. Mebatsion et al. (2012) illustrated that \mathbf{V} of standardized elliptic Fourier descriptors can be used to quantitatively capture grain shape variability. They concluded that this type of analysis is more objective and precise when compared to classification by humans.

For a condition monitoring application, shape analysis is done for all the images captured in a sequence, and their variations investigated to get an insight into how the machine is behaving.

1.2.4.2 Kernel Principal Component Analysis (KPCA)

For data reduction purposes, PCA is based on a linear transformation approach, in which the feature vectors considered are assumed to be extracted from data that has a Gaussian distribution. In an application where nonlinear relationships may exist among variables or time intervals, the use of PCA may result in a loss of the nonlinear features (Yao & Wang, 2015). This nonlinearity is quite common in complex industrial systems which have responses that are nonstationary. A linearly behaving structure can exhibit nonlinear dynamics in its vibrational responses as damage develops. This introduces another machine behaviour characteristic that is important when monitoring the health of a structure.

KPCA addresses this issue by first transforming the original data in a nonlinear fashion into a different feature space using various kernels. The kernels used are typically polynomial, sigmoid and Gaussian kernels. PCA is then conducted in the new feature space on the data with nonlinear dependencies between variables. Consider a dynamic system described by a

set of vibration response features in the form of an n -dimensional vector δ_s ($j = 1, \dots, M$). In this case, n corresponds to the number of sensors, and M the number of samples. According to Nguyen & Golinval (2010), the concept of KPCA boils down to the nonlinear mapping $\delta_s \mapsto \phi(\delta_s)$ using the kernel ϕ , with $\delta_s \in \mathfrak{R}^n$, ($s = 1, \dots, M$) which represents a higher dimensional space. For centred data ($\sum_{s=1}^M \phi(\delta_s) = 0$), the covariance matrix used in the PCA eigenvalue problem can then be calculated using Equation (21).

$$C = \frac{1}{M} \sum_{s=1}^M \phi(\delta_s) \phi(\delta_s)^T \quad (21)$$

The Gaussian kernel function, defined by Equation (22), with σ the width of the kernel, is most frequently used for KPCA investigations.

$$K(\delta_i, \delta_j) = \exp\left(\frac{-\|\delta_i - \delta_j\|^2}{2\sigma^2}\right) \quad (22)$$

Compared to the linear PCA, KPCA can essentially extract the higher order nonlinear relationships between data, retaining a greater degree of the complex information between the data (Shao et al., 2014). With the appropriate choice of parameters, different kernel functions produce very similar results (Nguyen & Golinval, 2010). In classification applications such as optical character recognition, KPCA has been shown to outperform PCA in terms of feature extraction (He et al., 2007).

1.2.5 Statistical and circular domain features

According to He et al. (2007), mechanical systems are generally complex and difficult to analyse owing to the stochastic processes that essentially contribute to the measured structural responses. This makes deterministic time function-based investigations insufficient to analyse the machines. It is often difficult to capture the behaviour of a machine from the raw data time series directly. Feature extraction from the raw time data must be conducted and the 'hidden' patterns identified from these features.

When analysing rotating structures, a set of angular domain features can be extracted. In some applications, these features can actually contain information more descriptive of the machine behaviour compared to their time domain counterparts. These features include the angular mean, angular variance, angular skewness and the angular kurtosis.

Caesarendra et al. (2014) proposed an angular domain analysis approach based on a Piecewise Aggregate Approximation (PAA) data reduction process, in which the following listed steps are followed:

- (i) Reduction of the vibration data using PAA and construction of neighbourhood correlation plot of the reduced data
- (ii) Neighbourhood correlation plot ellipse least-square fitting for pattern classification
- (iii) Plotting the distribution of the ellipse shape in angular domain, and calculation of the circular domain features

PAA is a data reduction technique applied to large time series data in which a sequence of sampled data $Y = (Y_1, Y_2, \dots, Y_N)$ is divided into w windows of equal size (Caesarendra et al. 2014). These windows are termed frames, and for each frame the reduced data representation

is then taken as the mean value of the data in that frame. Equation (23) is used for this calculation, in which the vector $\boldsymbol{\tau} = (\tau_1, \tau_2, \dots, \tau_n)$ represents the PAA reduced data set, or the running average of the original signal Y .

$$\tau_n = \frac{1}{w} \sum_{j=w_{n-1}+1}^{w_n} Y_j \quad (23)$$

A neighbourhood correlation plot is then simply τ_{n+1} against τ_n . Caesarendra et al. (2014) illustrated how the orientation of an ellipse fitted onto the neighbourhood correlation plot data points, is frequency dependent. This becomes very useful when analysing non-stationary signals of a machine captured over an extended period of time. Onset of damage in a structure is typically associated with a change in the frequency of the vibrational responses. If neighbourhood correlation plots are developed for different time segments in measurement sequence, a change in the ellipse orientation will thus be an indication of dynamic behavioural changes in the machine system. Properties of the fitted ellipse such as its orientation, size and aspect ratio can be considered as angular domain features for the time signal of interest.

Other angular domain features can be obtained through representing signals by features extracted from their random circular variables. Hilbert transformation of time signals can be utilized to determine the instantaneous phase angles of the time series. This is well documented in the work done by Martin et al. (2010). Real valued signals are represented as complex signals using the Hilbert transform. For a time domain signal $Y(t)$, an analytical signal $Y_a(t)$ can be determined using Equation (24).

$$Y_a(t) = Y(t) + j\mathcal{H}\{t\}(t) \quad (24)$$

In the equation above, $\mathcal{H}\{t\}$ is the Hilbert transform of $Y(t)$. The analytical signal can then be expressed as:

$$Y_a(t) = \psi(t)e^{j\theta(t)} \quad (25)$$

$\psi(t) = |Y_a(t)|$ is the amplitude envelope of the analytical signal, and $\theta(t) = \arg(Y_a(t))$ the instantaneous phase with $\theta(t) \in [0, 2\pi]$.

1.3 Scope of research

This research focuses on extending the applicability of photogrammetry as an optical non-contact measurement technique for rotating structures. The concept of shape analysis, commonly used for object identification and shape matching, is used in developing a dynamic analysis procedure suitable for CBM of machines. The proposed approach entails an analysis of a sequence of images captured using high-speed cameras of a machine in operation. Shape boundary extraction of the components or regions of interest is conducted. Variations in the shape of extracted contours are then monitored to get details on the dynamic behaviour of the machine.

Damage detection, characterization and classification for condition monitoring purposes is conventionally conducted through the use of contact transducers. The point-wise nature of contact transducers mean that multiple sensors are typically required to capture the full dynamics of a structure under investigation. Being contact in nature, these transducers are intrusive, can interfere with the structure, and often introduce complexities in terms of

mounting and data acquisition especially when applied to large rotating structures such as wind turbines. Non-contact photogrammetric techniques such as 3DPT and DIC can address these limitations of conventional sensing, introducing an alternative approach to SHM of rotating machines. Whilst technological advancements in the field of imaging have resulted in increased availability of high-speed cameras, use of 3DPT and DIC require surface preparation in the form of markers and speckle patterns. Pixel-targeted algorithms are typically used to extract dynamic behaviour measurements of the machines, which means that the robustness and applicability of the techniques can become limited for certain applications where the structures are large, and measurements are being captured in out-door settings. On the other hand, contour-based analysis techniques incorporating statistical shape analysis have been adopted in other scientific fields of study such as object classification. However, these techniques are yet to be incorporated in the dynamic analysis of rotating structures for condition monitoring purposes. The research presented is aimed at the development of a statistical shape analysis technique in a controlled laboratory environment. The aim is to establish an approach that can be ultimately scaled and refined to be adopted for analysing industrial structures such as wind turbines.

A systematic way of investigation is adopted in this research. An investigation into how defined shape descriptors are related to variations in the form of a shape is conducted, and a numerical analysis performed to evaluate the typically required camera minimum frame rate, the smallest shape variation displacements detectable, and also the optimum camera positioning. The approach is then applied to a 2D scenario, where a single camera is used to capture in-plane shape variations and detect different forms of out of normal operation. An extension into 3D is conducted by using a pair of stereoscopic cameras on a rotating blade system. Investigations are then done to refine the results post-processing approach used, to develop a more reliable and robust behaviour classification system.

For the 2D analysis, a portable Bently Nevada rotor system is used for the investigation. Shape variations imposed by different shaft ODSs are analysed. The most common forms of faults that are associated with turbomachines composed of long shafts and flywheels are imposed and investigated. These include the different forms of rotor unbalance, rotor-stator rub, and hydrodynamic bearing oil instabilities. Shaft misalignment is not analysed as the system used was not designed for such a set up. This 2D investigation focuses mainly on establishing the possibility and applicability of condition monitoring using a non-contact shape-based SHM technique. Results obtained were verified and compared to measurements captured using the conventional proximity probes.

In the 3D investigation on rotating blades of a turbomachine test setup, three rotational speeds are considered. Two of the rotational speeds (650 rpm and 1000 rpm) were chosen based on the blades' first bending mode natural frequencies. Having the rotational speeds harmonics coincide with the blade natural frequency meant that the out-of-plane blade responses were going to be significant enough to be easily captured by the system (improved SNRs). The third rotational speed (1460 rpm) was considered to test the applicability of the approach when the system is running at an arbitrary speed. At 1460 rpm, the blades are expected to exhibit behaviour associated with basic ODSs, instead of the natural frequency influenced mode shapes. Operating away from the natural frequencies will not only be the desirable setting, but also the most probable operational state of a rotating structure. Data acquisition was conducted at a frame rate of 4000 FPS, the maximum possible for the cameras used at full resolution. Only at full resolution is the full bladed system in the camera FOV.

The development of this shape analysis procedure is conducted in a laboratory setting where environmental conditions, especially the room lighting, could be readily controlled. In developing the measurement technique, it was decided that the initial investigations be conducted in a setting that best approximates ideal conditions. This was done to make it easier to identify sources of errors in measurements and to recognise aspects that may result in the malfunctioning of the approach. Considering a wind turbine as an example of a rotating structure to focus on, the literature study conducted illustrated the possibility of full-scale rotor system outdoor analysis using high speed cameras through complex pixel tracking. In this research, a smaller system is adopted as the test set up on which the investigations are conducted. The data analysis and results processing procedure developed here can be scaled up in further work aimed at investigating a full-scale system such as an operating wind turbine.

The research conducted introduces the idea of coupling shape analysis with rotating machine condition monitoring. In this context, the idea of shape variation analysis-based condition monitoring is developed, implemented and verified to be an effective approach for identifying and classifying different damage modes in a system. This is achieved through introduction and definition of novel unique shape characteristics in the form of Shape Principal Component Descriptors (SPCDs). For purposes of condition monitoring, the research extends optical noncontact image processing approaches from being either speckle pattern (DIC) based or target marker (3DPT) based, to being boundary shape-based as well. This goes a step further in terms of exploring and establishing more applicable measurement techniques suitable especially for rotating structures. The research is presented in such a way to highlight the potential of the proposed technique. Starting with a 2D shape-based application, the flexibility of the approach is demonstrated through extension to a 3D application. Investigations focusing on the evaluation of the performance of various SPCDs analysis and processing procedures illustrate room for further research in terms improving the accuracy and robustness of the approach.

The dissertation contributes to the field of structural health monitoring by proposing a novel photogrammetric methodology for analysing rotating structures for condition monitoring purposes. Through a comprehensive literature review, the study identifies the limitations of current optical measurement techniques such as DIC and 3DPT with regards to prior surface preparation of structures under investigation. Using numerical simulations and empirical analyses, a shape-based technique is developed that advances the applicability of image-based optical condition monitoring techniques. The research findings illustrate that in cases where surface preparation is not practical or where machine shutdowns are not possible, a shape analysis approach that focuses on boundary edge extraction and statistical shape analysis through PCA can be adopted to provide insights on the dynamic behaviour and condition of a rotating machine. This work further advances the current state of knowledge in structural health monitoring using optical non-contact measurement techniques in terms of surface preparation and shaped-based image analysis.

1.4 Document overview

Chapter 1 contains a literature review that discusses condition monitoring of structures using conventional contact techniques and the more recent non-contact techniques follows. Limitations of the current approaches being used for analysing rotating machines are highlighted. Concepts pertaining to shape analysis that are either investigated or utilized in

investigations presented in the following chapters are discussed. A document overview is given at the end of the chapter.

Chapter 2 introduces the concept of 2D shape analysis. The idea of principal component-based shape descriptors is introduced, and the link between these descriptors and shape variations investigated. Also investigated is the feasibility of condition monitoring using shape analysis. Some simulation-based investigations to better understand the functionality of the proposed target-less photogrammetric measurement technique are also presented in Chapter 2.

Application of 2D shape analysis on an actual physical system is done in Chapter 3. Different operating states of a Bently Nevada rotor system are analysed using the shape analysis approach and the conventional proximity probes. Performances of the two approaches in terms of distinguishing and identifying faults are compared.

Chapter 4 discusses the extension of shape analysis from 2D to 3D applications. A FE based analysis of a rotor system in which variations in the dynamic behaviour of blades as a result of increasing root damage is introduced as the initial step. These variations are monitored by first considering conventional parameters (natural frequencies), before moving on to the SPCDs. The feasibility of monitoring progressing damage is illustrated in a FE environment, and an experimental study is subsequently conducted. The experimental investigation introduces the determination of 3D shape principal component descriptors from stereoscopically captured images of rotating blades. Variations in the dynamics of different damage modes for rotating axial blades are investigated, and the feasibility of a condition monitoring shape-based approach for turbine blades is illustrated.

An investigation into how blade damage modes can be better classified is conducted in Chapter 5. Full-scale turbine blade analysis requires a more robust system that can still perform in cases where there are many errors resulting from noise for instance. The concept of kernel principal component analysis is evaluated and applied to the time domain shape descriptors data. The performance of the system when multi-domain statistical features are considered instead of the typical time domain data is also evaluated. Conclusions and recommendations for future work are then presented in Chapter 6.

CHAPTER 2: FEASIBILITY OF CONDITION MONITORING USING SHAPE ANALYSIS

2.1 Introduction

This chapter investigates the feasibility of using a statistical shape analysis approach for investigating the dynamics of a rotating machine. In this study, it is considered that a closed contour of a particular section of the machine can be extracted from images captured whilst the machine is online. The closed contour, whose shape form varies due to the dynamic behaviour of the rotating machine, is the object of interest.

The feasibility study is conducted to verify the existence of a relationship between the dynamic behaviour of a system and the statistical parameters extracted for the typical shape of interest. With a verified correlation between shape features and the dynamics of a system, minimum requirements and critical constraints required to capture useful data on the behaviour of the machine using shape analysis can be determined.

Similar to any other typical approach, implementation of a shape analysis-based condition monitoring approach can be considered to be a two stage process.

1. Data acquisition and pre-processing
 - capturing images of a component or section of interest on a rotating structure
 - camera positioning
 - camera frame rate
 - extraction of contours from captured images
2. Data post-processing
 - transformation of closed contours into shape principal components (V)
 - analysis of variations in V from one image to the next in a sequence of captured images
 - machine dynamic behaviour investigation

Since the data post-processing component can be investigated theoretically, this chapter starts off by outlining theoretical descriptions of the determination of shape form parameters (V columns) for a given typical 2D shape of interest. An investigation is then conducted to better understand the correlation between the determined geometric modes V and the form of the shape. This highlights the relationships between different shape principal components and the shape of interest, illustrating the physical meaning of the various V terms. To bridge the gap between shape analysis and condition monitoring, variations in V when known forced displacements are utilized to alter the form of the shapes are analysed.

In a numerical sensitivity investigation, a FEA based approach is employed to better understand application constraints in condition monitoring through shape analysis. Data acquisition related constraints are investigated using a FE model of an actual rotating structure. An analysis of the physical rotor system in terms of image processing for shape extraction is also presented to authenticate the adopted shape of interest analysed in the theoretical and numerical study sections of the chapter.

2.2 2D shape analysis procedure

A generic horseshoe shape typically enclosed between a shaft and a bearing/probe holder housing (presented in Figure 20 and Figure 23) was considered as the shape of interest for the 2D shape analysis. This is shown in Figure 11.

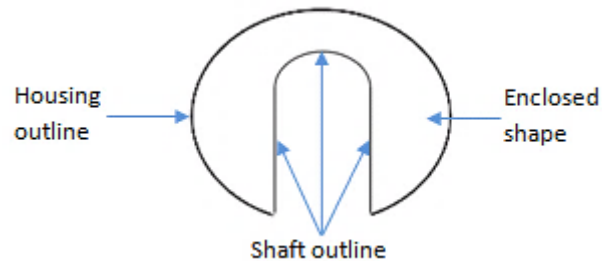


Figure 11: Feasibility study shape of interest

In this investigation, the 8-connectivity chain-code (Kuhl & Giardina, 1982) was employed as the shape signature of the extracted contour. As highlighted in Section 1.2.3.1, Fourier coefficients of the shape signatures can be calculated and four Fourier descriptors used as the multivariate vector for Shape Principal Component Analysis (SPCA). In this case, four parameters are obtained for this 2D shape analysis, according to Equations 7 and 8. Figure 12 illustrates the determination of SPCDs.

$$\begin{array}{c}
 \vec{V}_1(t) \quad \vec{V}_2(t) \\
 \downarrow \quad \downarrow \\
 \mathbf{V}(t) = \begin{bmatrix} V_{1,1} & V_{2,1} & V_{3,1} & V_{4,1} \\ V_{1,2} & V_{2,2} & V_{3,2} & V_{4,2} \\ V_{1,3} & V_{2,3} & V_{3,3} & V_{4,3} \\ V_{1,4} & V_{2,4} & V_{3,4} & V_{4,4} \end{bmatrix} \\
 \downarrow \quad \downarrow \\
 \text{SPCD}_1(t) = \|\vec{V}_1(t)\|_2 = \left\{ \sum_e^4 V_{1,e}^2 \right\}^{\frac{1}{2}} \quad \text{SPCD}_2(t)
 \end{array}$$

Figure 12: Calculation of Shape Principal Component Descriptors

The four parameters in the form of column vectors contained in matrix \mathbf{V} (Equations 19 and 20) are calculated for the boundary shape extracted from a single image. For a time sequence of captured images, variations of the four parameters from one image to the next can then be analysed, in the frequency domain for instance, to extract information descriptive of the manner in which a machine is operating. In essence, shape principal components \mathbf{V} are associated with a shape at a specific time instant, whereas SPCDs constitute the time series obtained by combining descriptors extracted from the individual \mathbf{V} of each shape from a sequence of captured shapes. These SPCDs are calculated by way of the Euclidean vector norms of columns \vec{V}_i in matrix \mathbf{V} , according to Equation 26. Thus for a column vector \vec{V}_i at time instance t , given by $\vec{V}_i(t) = [V_{i,1}, V_{i,2}, V_{i,3}, V_{i,4}]^T$, the SPCD associated with that shape principal component at time stamp t is defined as follows:

$$SPCD_i(t) = \|\vec{V}_i(t)\|_2 = \left\{ \sum_e^4 V_{i,e}^2 \right\}^{\frac{1}{2}} \quad (26)$$

The full procedure of the analysis implemented to determine the components V for the shape of interest, and the subsequent calculation of SPCDs is summarised in the flow diagram given in Figure 13. The equations included in the flow diagram were introduced in Section 1.2.3.1.

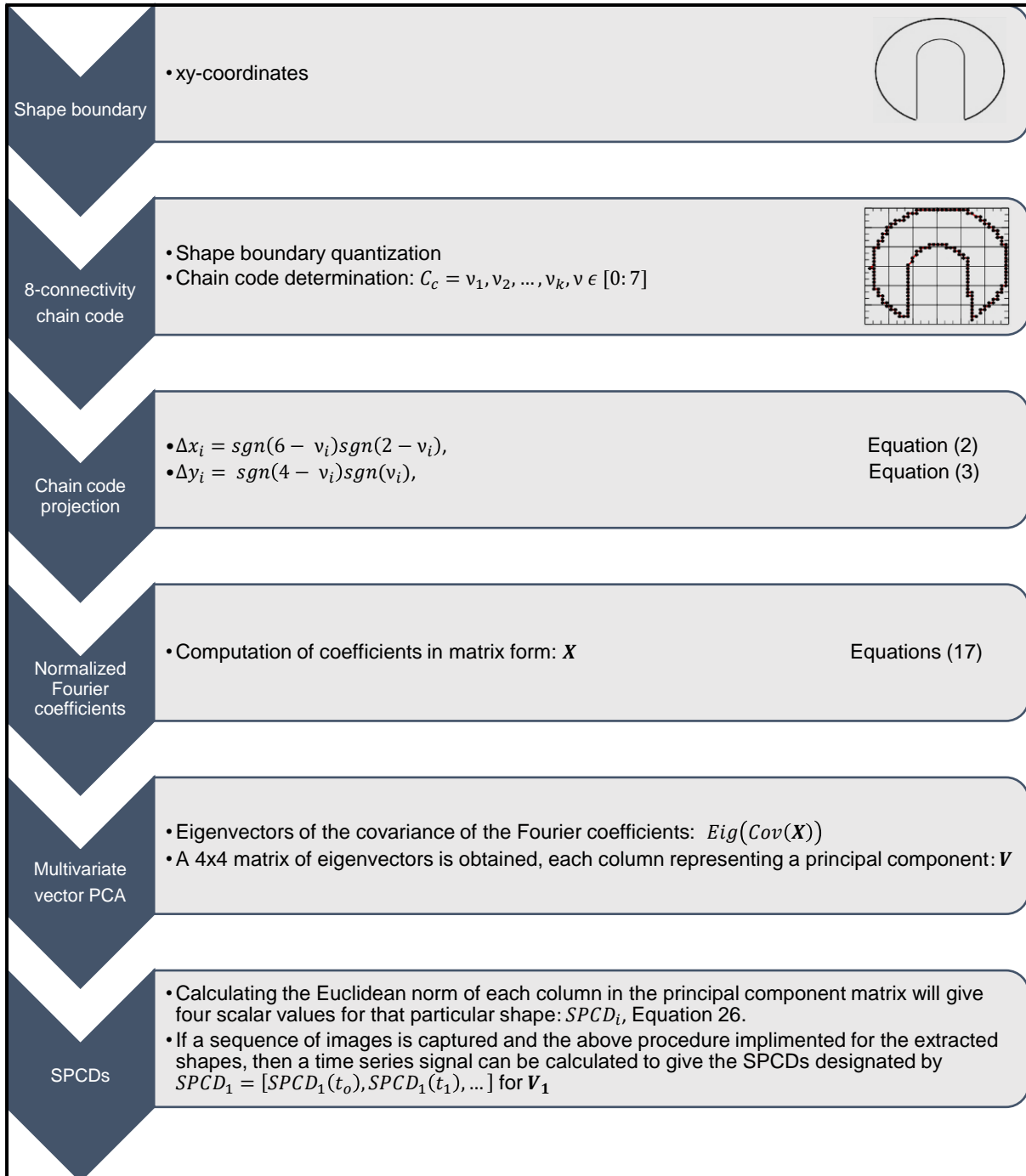


Figure 13: Shape principal components determination flow chart for 2D shape analysis

2.3 Relationship between different principal components (\vec{V}) and the form of a 2D shape

A numerical analysis of the shape of interest was conducted. This was done to better understand the relationship between the principal components and the form of the shape of interest. The four V columns of a shape were determined and then their scores X^{new} scaled one at a time before reconstruction of the shape. The procedure for shape reconstruction using scaled principal component scores is illustrated in Figure 14, where a Scaling Factor (SF) scalar of 0.5 was used to test the relationship between \vec{V}_1 and the form of the shape.

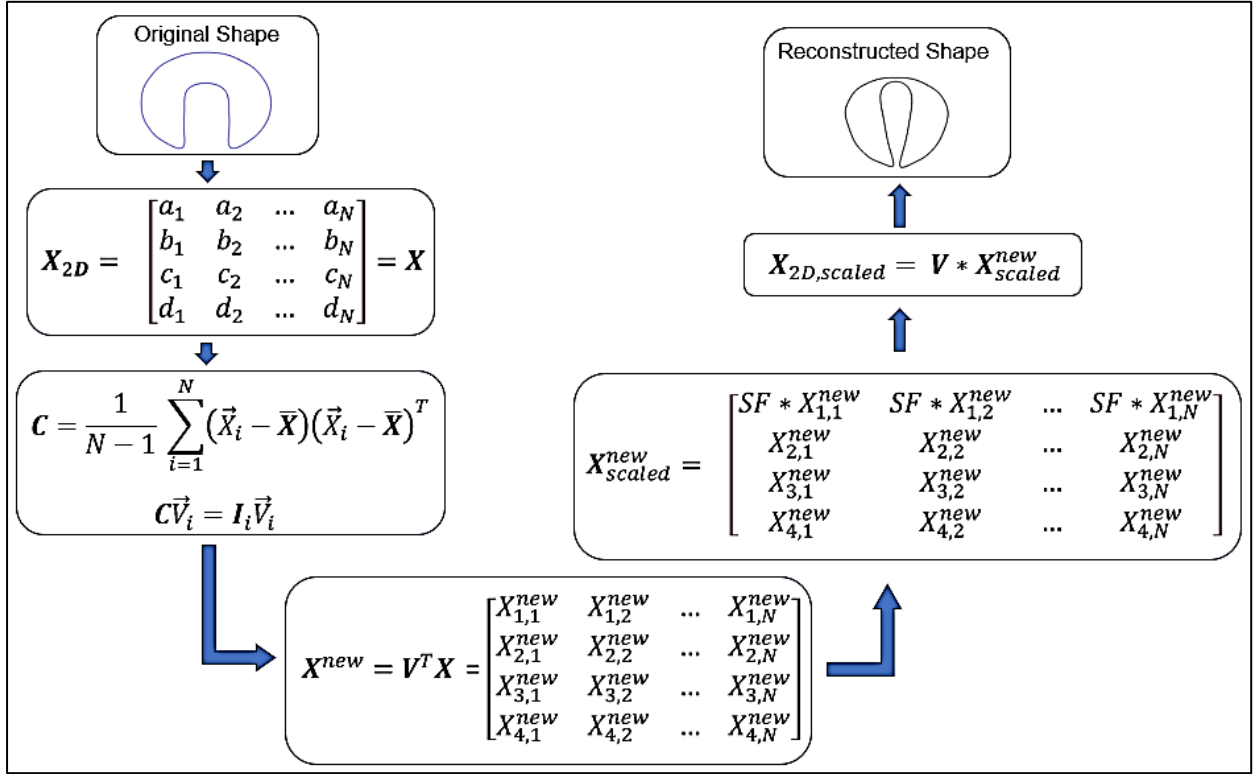


Figure 14: Principal component score scaling and shape reconstruction flowchart for visualization of different geometric modes

As highlighted in Section 1.2.4.1, each row of X^{new} , denoted as \vec{X}_i^{new} , is associated with a corresponding \vec{V}_i , a column vector in the SPCA matrix V . Each \vec{V}_i represents a specific shape feature, considered as a geometric mode in this study. Thus to investigate the nature of the first geometric mode, or to understand the relationship between \vec{V}_1 and the form of the shape, only \vec{X}_1^{new} is multiplied by an SF and Equation 20 used to calculate a new set of scaled Fourier coefficients $X_{2D,scaled}$ that can then be used to recreate the shape. To allow for better visualization of the nature of each \vec{V}_i , different SFs were applied to different X^{new} . Figure 15 illustrates the results obtained.

From Figure 15, \vec{V}_1 is associated with the overall size of the shape, without addition of any lobes. \vec{V}_2 is mostly associated with a shape variation that conserves the distance between the two horizontal vertices whilst the overall shape size changes. \vec{V}_3 is associated with the shape skewness, resulting in a three-lobe characterized shape. \vec{V}_4 conserves the distance between the horizontal vertices, whilst the vertical vertices move to create a four-lobe geometric mode.

This investigation identifies the relationships between geometric modes or principal components and the form of the shape, by way of scaling various principal components scores. It is evident that each \vec{V}_i has influence on more than a single degree of freedom. Additionally, the extent to which each principal component influences various shape forms differs, as is evident from the different SFs that must be applied to obtain noticeable shape changes for \vec{V}_3 and \vec{V}_4 . Shape principal components 3 and 4 have a significantly reduced effect on the shape form as compared to \vec{V}_1 and \vec{V}_2 .

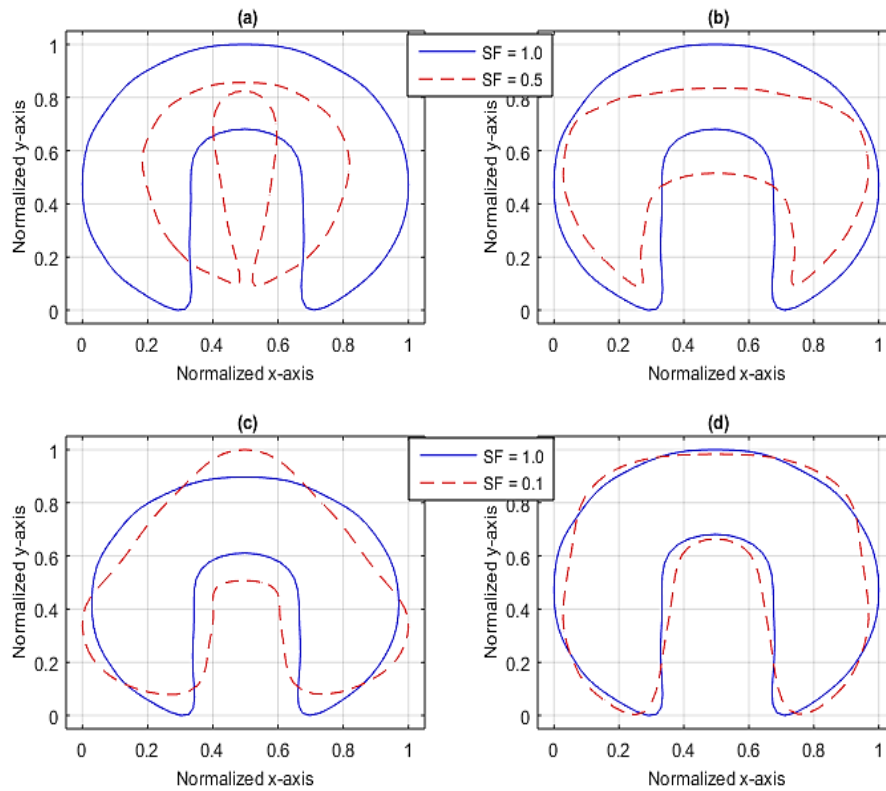


Figure 15: Nature of the different geometric modes (a) \vec{V}_1 , (b) \vec{V}_2 , (c) \vec{V}_3 , (d) \vec{V}_4 ,

2.4 Feasibility of condition monitoring using 2D shape analysis

The applicability of a 2D shape analysis for condition monitoring of a rotating machine is subsequently investigated using the adopted horseshoe shape. The outer contour of the shape can be assumed to represent the probe holder housing and the inner contour the shaft. The position of the shaft contour is varied using sinusoidal displacements to simulate shaft motion. For the in-plane motion, the virtual shaft can be moved in either a single direction or in both x- and y-directions. By using sine and cosine signals of unit amplitude to move the shaft in the x- and y-directions respectively, shaft whirl motion can be simulated. Three different shaft forced motions are simulated. These are forced displacements in the x-direction, y-direction, and a combination of both x- and y-direction. This is conducted to investigate the variation in the shape principal components descriptors calculated from \mathbf{V} of the 2D shape when forced displacements are applied. Figure 16 illustrates these enforced shaft displacements.

For forced displacements at a frequency of 20 Hz, the following SPCDs (variations in the Euclidean norms of \vec{V}) are obtained in the frequency domain. The properties of forcing

displacement signals were set as a unit amplitude, 400 Hz sampling rate and with a signal sample length of 10s. The parameters were selected to ensure that artefacts resulting from signal discontinuities for instance do not contaminate the observed spectra.

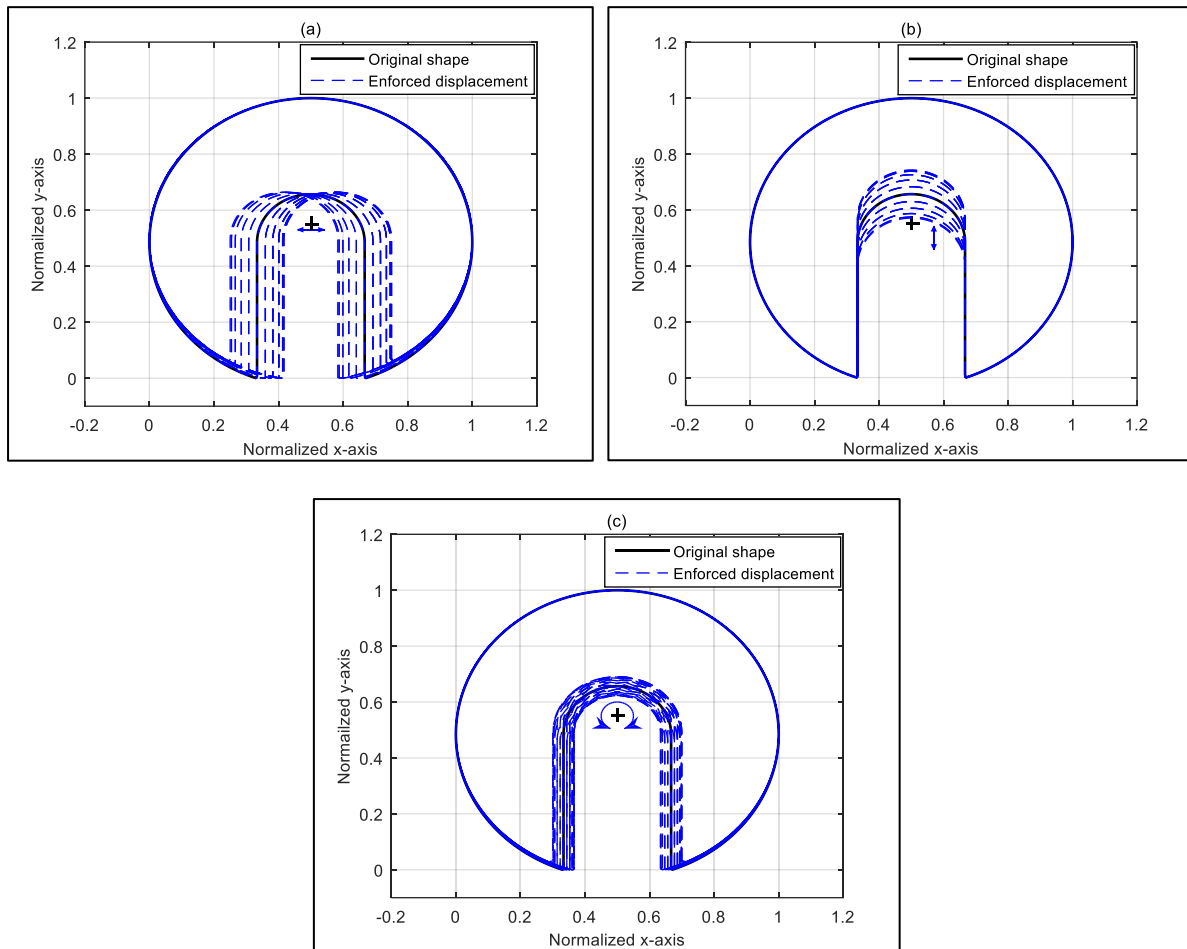


Figure 16: Enforced shape variation, (a) horizontal shaft excitation, (b) vertical shaft excitation, (c) circular shaft excitation (whirl)

As can be noted in Figure 17, all the SPCDs have peaks at the excitation frequency of 20 Hz, as well as the 2x, 3x and 4x harmonics.

For $SPCD_1$, the vertical and whirl motions have the same magnitudes at the fundamental frequency, with the horizontal motion having the least influence on the SPCD. It is evident that pure shaft vertical motion has the least influence on the shape's second, third and fourth SPCDs. Linking the obtained results to the relationships between \vec{V} and shape form illustrated in Figure 15, a correlation exists in the sense that higher SPCD magnitudes are obtained for $SPCD_1$ vertical excitation in Figure 17. The shape variation illustrated in Figure 15(a) very much resembles shaft up and down motion. Scaled principal scores associated with \vec{V}_2 , \vec{V}_3 and \vec{V}_4 result in shape variations that do not resemble vertical shaft motions.

The harmonics present in Figure 17 are expected since none of the forced motions correspond identically to the shape variations associated with the principal components illustrated in Figure 15. In the same way that sine signals are considered to be pure tones from which other periodic signals such as square and saw tooth waves can be created, the shape forms illustrated in Figure 15 can be considered as pure \vec{V} shape modes. When performing 2D shape

analysis in the frequency domain, general shape variations such as shaft whirling motion that deviate from the pure V shape modes are approximated by sums of pure V modes with frequencies corresponding to the harmonics of fundamental forcing frequency (Fourier analysis application). Owing to the significant differences that can exist between the pure shape forms and shape variations due to the forced shaft whirling motions, it is possible that sometimes the harmonics contain more energy than the fundamental frequency, as observed in some of the SPCD results presented later in this chapter.

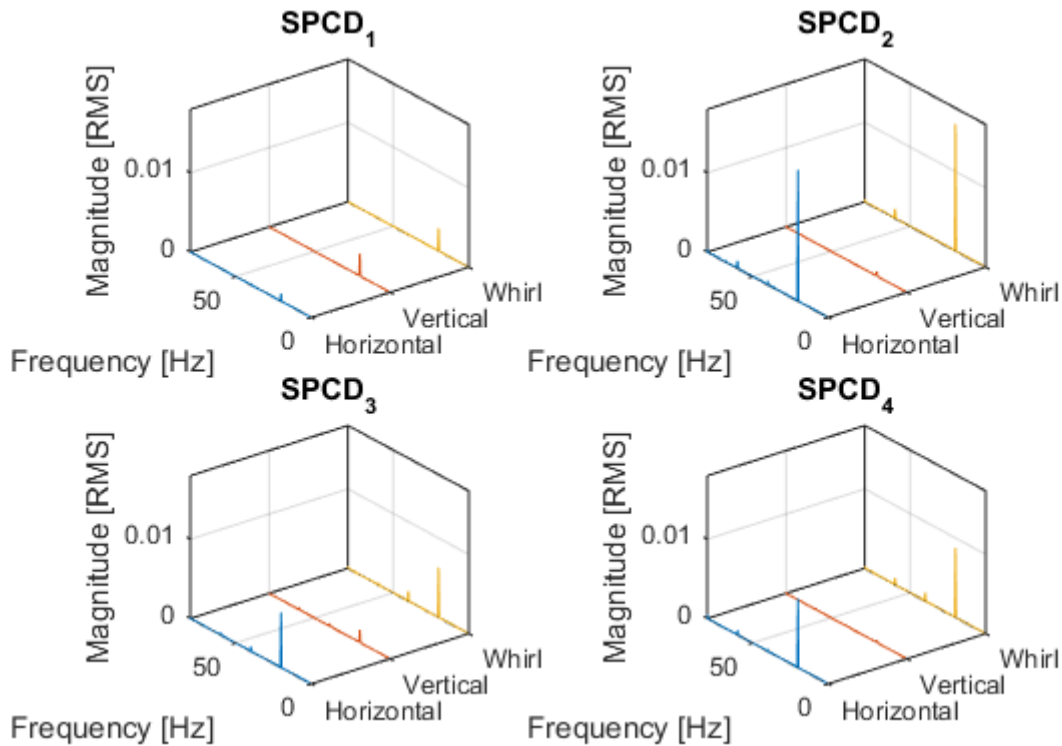


Figure 17: Principal components descriptors frequency responses

As an illustration, forced shape variations given in Figure 18 are identical to one cycle variations associated with principal component 4 (similar to Figure 15(d), \vec{V}_4 shape). In this case one would expect frequency responses with a single peak at the forcing frequency for SPCD₄ and different results for the other SPCDs.



Figure 18: Typical one cycle forced shape variation associated with a single PC (PC 4 in this case)

Results obtained for forced shape variations identical to each of the four \vec{V}_i s are given in Figure 19 for forcing frequency of 20 Hz.

For enforced geometric modes (different \vec{V}_i s), Figure 19 shows that the \vec{V}_i of interest tends to show significant peaks at the fundamental frequency of the SPCD it is associated with, whilst the rest of the \vec{V}_i s have significant peaks at higher harmonics. Peaks at the fundamental frequency of the \vec{V}_i of interest also have higher magnitudes than the remaining \vec{V}_i s, with the exception of \vec{V}_1 . As mentioned earlier, \vec{V}_1 is associated with overall size variation. When forced explicitly, \vec{V}_1 type of shape variation tends to effect shape changes that influence the other principal components more. This is a result of cross sensitivity between the \vec{V}_1 type of shape variation and shape variations associated with the other shape principal components. Considering the behaviour of \vec{V}_1 to forced shape variations representative of all the other principal component descriptors, it can be observed that \vec{V}_1 always has its most significant peak at the fundamental frequency, but with lower magnitudes.

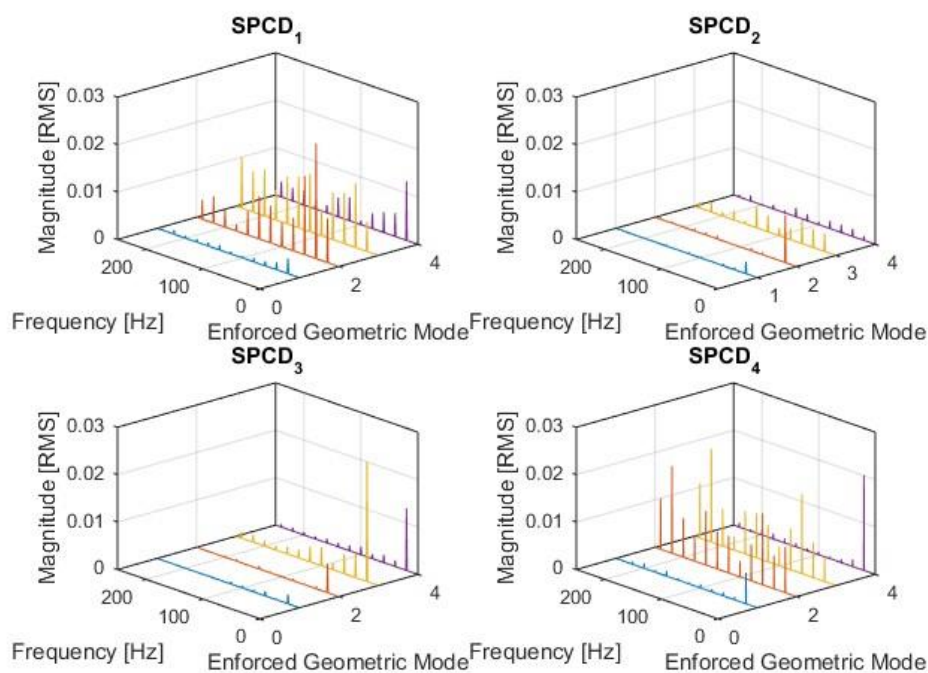


Figure 19: SPCD responses to specific enforced geometric modes

Thus when considering shaft whirling motion, the harmonics observed in the SPCD results do indicate presence of information that is associated with how the forced shape variation differs from the shape variation associated with a particular shape principal component. Whilst the physical (in this case forced) shape variation might not be identical to any of the predicted shape principal component forms, it is possible to obtain unique SPCDs for every physical shape variation. The results obtained will give an indication of how the physical variation relates to the predicted \vec{V}_i shape forms. Determined results can then be used to complement conventional single point sensor measurements.

The above investigation shows that for a 2D analysis, Fourier shape descriptors can be used to extract four different parameters in the form of shape principal components. These evidently vary with various changes in the shape, implying that they can be monitored to characterize dynamics of rotating structures.

2.5 Shape principal components descriptors basic sensitivity analysis

A sensitivity analysis of the system was conducted through evaluation of a FE model of a Bently Nevada rotor kit. A FE model presents a better controlled environment in which setup configurations can be more accurately adjusted and measurements accurately extracted for post-processing analysis purposes.

The physical model of the rotor kit is shown in Figure 20. The kit consists of two flywheels on a shaft supported between a hydrodynamic bearing and a bush bearing. A coupling connects the shaft to a motor capable of running up to a maximum of 10 000 rpm.

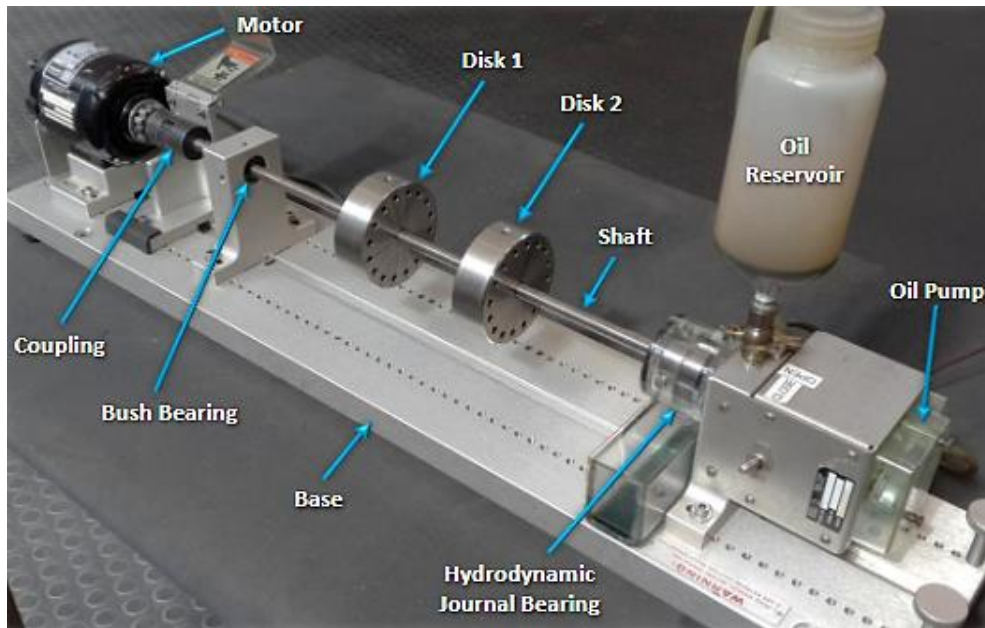


Figure 20: Bently Nevada rotor system (Krüger, 2012)

A FE model of the Bently system can be created from parasolids developed in Solidworks. These can be imported into MSC/Patran pre-processor to approximate the system. The system coupling can be considered to be a cylindrical hollow disk press fitted onto the shaft, and meshing conducted using Hex 6 elements. Material properties assigned can be assumed to be those of steel for the shaft, disks and journal bearing, and bronze for the coupling. Figure 21 shows a model created this way.

Investigations conducted by Krüger (2012) were used to estimate the material properties and boundary conditions for the rotor model. At this point of the study, a proper validation of the assumed FE model through modal updating was not necessary since none of the actual nodal displacements were being evaluated further or employed for further analysis. The aim of the investigation was solely to investigate how the shape of interest can be analysed to understand the sensitivity of detected V_s to various experimental setup configurations.

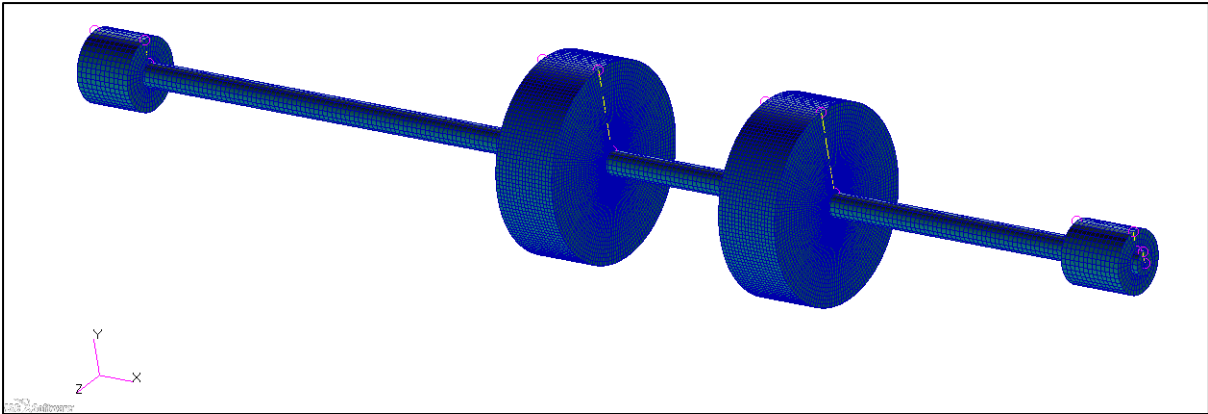


Figure 21: Rotor system full model

Rotor dynamic analysis using MSC Patran/Nastran usually requires a significant amount of processing resources for a model such as the one in Figure 21, since it is composed of a significantly large number of defined elements. For the sensitivity analysis investigation, it was decided to simplify the model by replacing the two disks, coupling and journal bearing with point masses at their respective centres on the shaft. Figure 22 shows the simplified system model, in which the bearing housing was assumed to be a plate at the appropriate location. This plate was fixed not to allow rotations and translations in any direction.

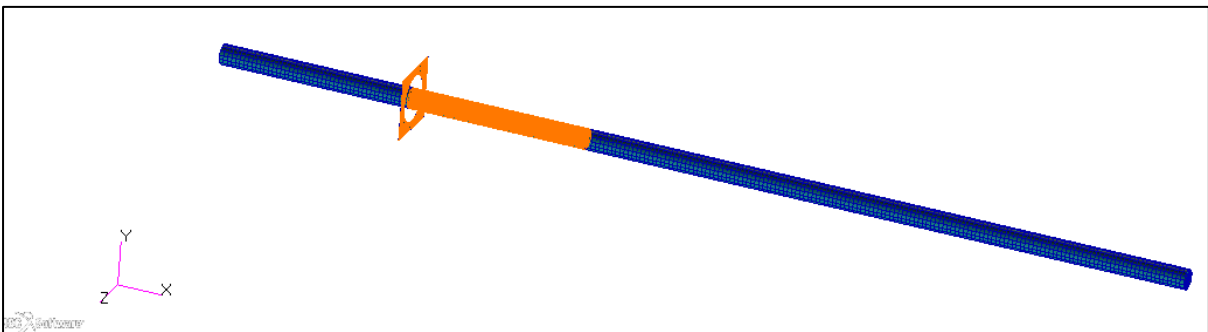


Figure 22: Rotor system reduced model

To simplify the dynamic analysis process and also make it possible to extract a shape similar to the one under investigation, FE groups to only focus on nodes of interest were created in MSC Patran/Nastran. The group of interest was composed of the elements highlighted in the figure above. Figure 23 shows the FEM extracted image. For contour extraction using LabVIEW's Vision Assistant Toolkit, the image on the right was obtained by extracting only the red colour plane of the original RGB image.

The horseshoe shaped contour that was considered for the theoretical analysis presented at the beginning of the chapter can be observed in the figure as the enclosed region between the shaft and the bearing housing. This particular 2D closed contour can actually be analysed for shaft translational vibrations to capture dynamics typically captured using sensors such as proximity probes positioned along specific shaft locations.

Analysis of this 2D shape has the potential to allow acquisition of information representative of the variation in the shaft Operational Deflection Shape (ODS). This is expected because variation of an enclosed shape at a bearing housing is directly influenced by the shaft deflection shape resulting from the rotating shaft whirling motion. The shape of interest chosen

for theoretical investigations was therefore based on the representation of the rotor system illustrated in Figure 23. As illustrated in Figure 23, a virtual camera can be considered to be positioned in such a way that its FOV captures images from which the appropriate contours of interest can be extracted.

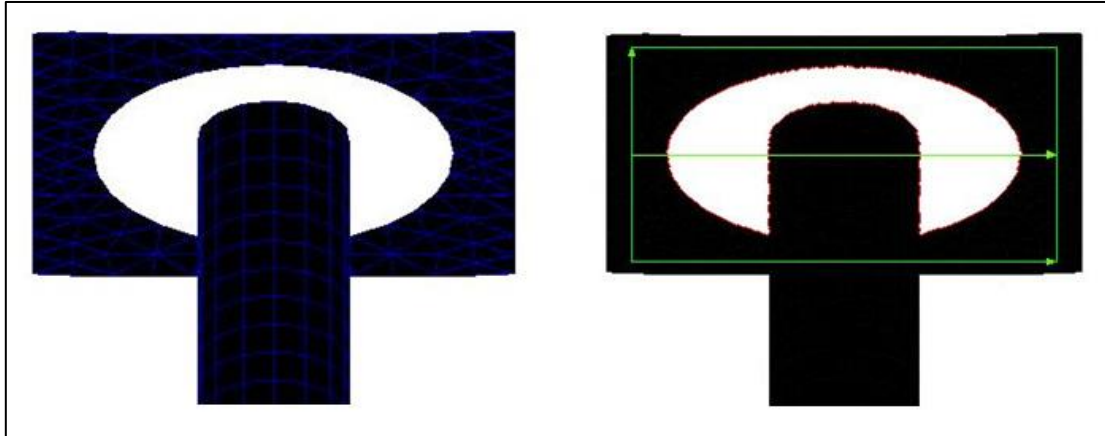


Figure 23: Typical FE extracted images

In a rotor dynamic analysis of a system in which system responses have been determined using Nastran, MPEG video files composed of a specified number of images can easily be exported. Image processing using a procedure more or less similar to the one presented later in Section 2.5.3 can be conducted to extract the shape of interest. The sensitivity analysis investigations described for the camera positioning and vibration amplitude resolution in the sections below were accomplished using the FEM described above, in which a statically unbalanced rotor dynamic system was being investigated at 1200 rpm rotational speed.

2.5.1 Effect of camera positioning on the extracted shape principal components

When employing shape analysis as a condition monitoring tool, the way the cameras are positioned play an important role in the extracted contours. It is expected that the larger the relative angle at which an observer is viewing a 2D shape, the easier it will be to realize shape variations associated with the shape. This however applies to changes in simple shape descriptors such as area and aspect ratio. When dealing with geometric modes in V , variations of a shape are 2D based and specific to a particular orientation, meaning that positioning the cameras at angles way off the normal FOV may not be the best approach.

To investigate this, virtual camera positions in an FE updated model of the Bently Nevada rotor system were varied and SPCA performed to determine V . The variations introduced about the horizontal axis are shown in Figure 24. Angles were varied from 10° to 70° .

Figure 25 illustrates the results obtained for the camera angle variation about the horizontal axis. As can be noted, $SPCD_1$ increases to a maximum at 50° pitch angle, then starts decreasing. A general increase in the magnitude is observed for $SPCD_2$ and $SPCD_3$, whilst $SPCD_4$ generally decreases. $SPCD_4$ second harmonic increases with pitch angle, illustrating how the ability of the SPCD to capture local shape variations improves.

Yaw angle variations were also introduced for a set camera pitch angle of 60° . These variations are shown in Figure 26. As can be noted from Figure 27, yaw angle variation does not significantly affect the SPCD magnitudes. However, an increase in the noise levels of the extracted data is observed, especially for $SPCD_1$ and $SPCD_4$. The increase in noise stems

from shape variations related to V_1 and V_4 not being easily identifiable at high yaw angle camera orientations. This in turn results in low SNR of $SPCD_1$ and $SPCD_4$. From Figure 25, the higher magnitude of $SPCD_5$ appears to be an anomaly, for a generally decreasing trend. One can therefore consider the best pitch angle as the one where all SPCDs are still increasing in magnitude. From Figure 25 and Figure 27, it can be concluded that shape principal components are better captured from a plane normal to the shape of interest (0° yaw angle) and at 30° shaft pitch angle. This conclusion is specific to this particular case as different shapes will have different geometric modes, and also because the variations to which these different shapes will be subjected to is dependent on the dynamics of the structure under investigation.

That essentially applies to this particular investigation. When utilizing SPCA in other applications, it will be necessary to establish the form of V that relates closely to the expected physical shape variation. Through conducting an investigation similar to this one, it can then be established which camera positions result in the maximum SPCD magnitude for the established V of interest.

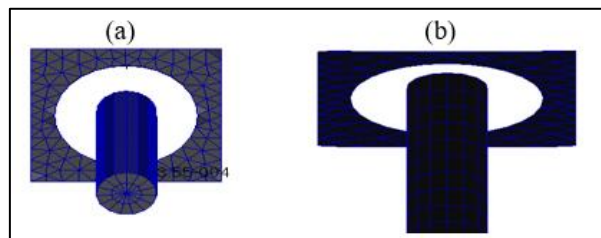


Figure 24: Pitch angle variation (a) 10° and (b) 70°

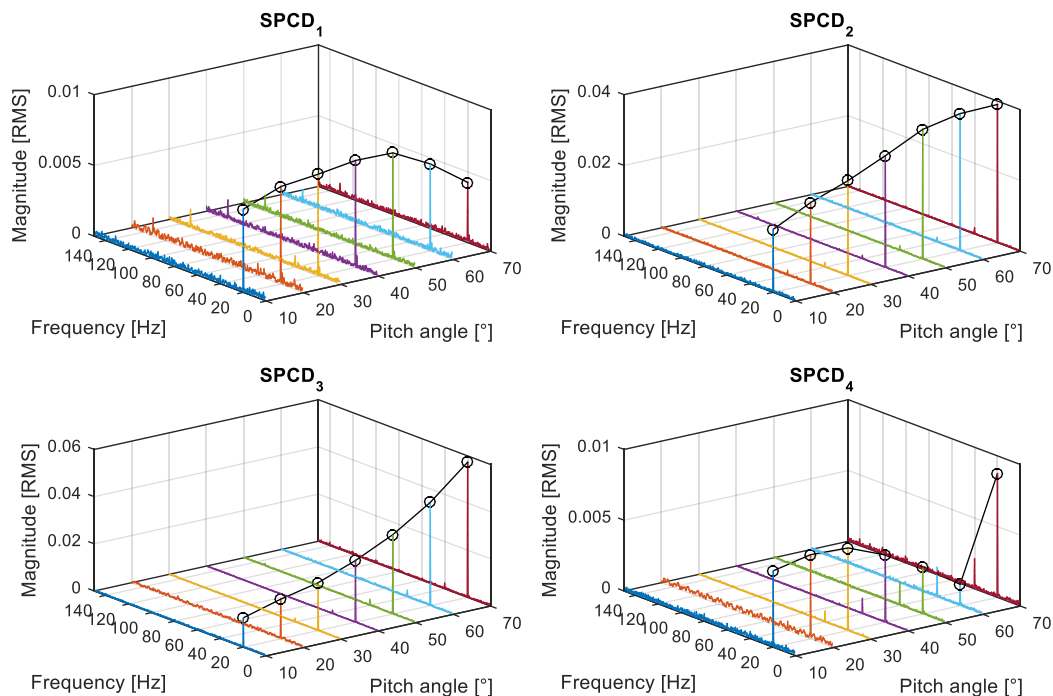


Figure 25: SPCDs variation with increasing camera pitch angle



Figure 26: Yaw angle variation (a) 0° and (b) 40°

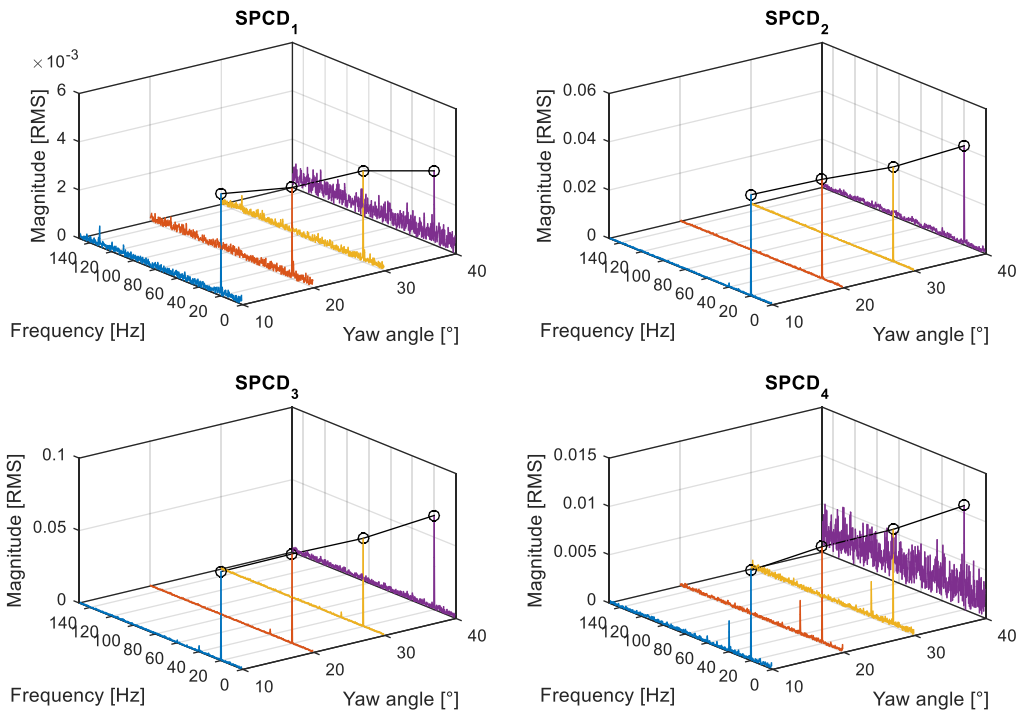


Figure 27: SPCDs variation with increasing camera yaw angle

2.5.2 Vibration amplitude resolution requirements for 2D shape analysis

As with any measurement technique, it is important to have an idea of the limitations in terms of accurately detectable measurements. To determine the minimum shape variation that can be detected using 2D shape analysis, shaft deflections in FEA extracted image sequences were scaled by different factors before the 2D shape analysis was conducted. The radial displacements of the node located on the centre of the shaft at the plane of interest (where the 2D shape was being extracted from) were used as reference for linking V variation to actual physical measurements.

In a typical FEA rotor dynamic run at 1200 rpm in which no magnification of the system response results was imposed to allow visualization of the rotor dynamics, the peak-to-peak vibrational amplitude response of the node of interest was observed to be 0.48 μm (Figure 28).

No apparent shape variations can be detected for shape analysis at such small responses. Amplification factors (50, 100, 200 and 500) were then applied to the system responses to detect the minimum shaft radial displacement that results in shape variations significant enough to be detectable using a shape principal component-based analysis.

It can be observed from Figure 29 that the fundamental frequencies become apparent with increasing scaling factors applied to the image sequences. A scaling factor of 100 is shown to give results clear enough to capture the 20 Hz frequency of interest. Considering the actual displacements given in Figure 28, it can be concluded that one can extract practical information in terms of the shaft whirling frequencies using SPCA for vibrational amplitudes as small as approximately $50\ \mu\text{m}$ (from $100 \times 0.48\ \mu\text{m}$).

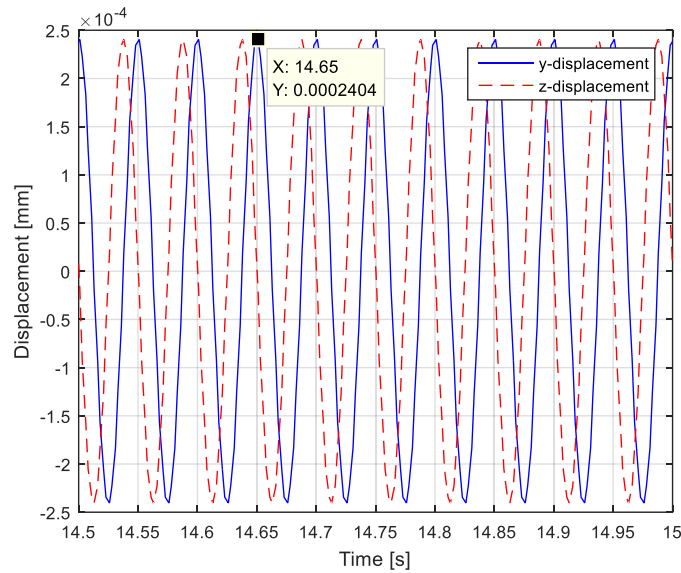


Figure 28: FEA vibration amplitude responses

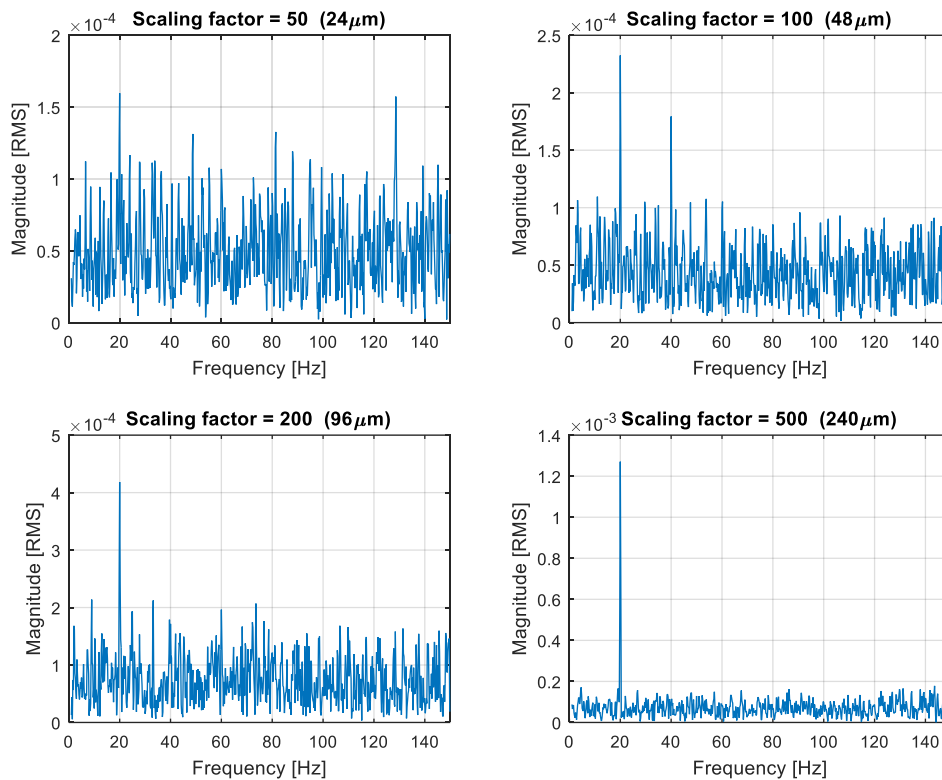


Figure 29: SPCD₁ frequency data for different scaling factors applied to the response

Very small single axis responses in the range of 50 μm can compound to overall shape variations significant enough to be detected using a shape analysis-based approach. For this particular investigation, 50 μm corresponds to 0.036 of a pixel (1/27 pixel size). This means that in order to employ shape analysis as a condition monitoring tool, the expected responses should be no less than about 0.036 of the pixel size of the images captured by the cameras being used. For different applications, the quality of the images (in terms of lighting for instance) and the accuracy of the contour extraction process can introduce noise in the data. This can potentially increase the minimum detectable response.

The variation of SPCD_1 fundamental frequency magnitude with increasing scaling factor is illustrated in Figure 30.

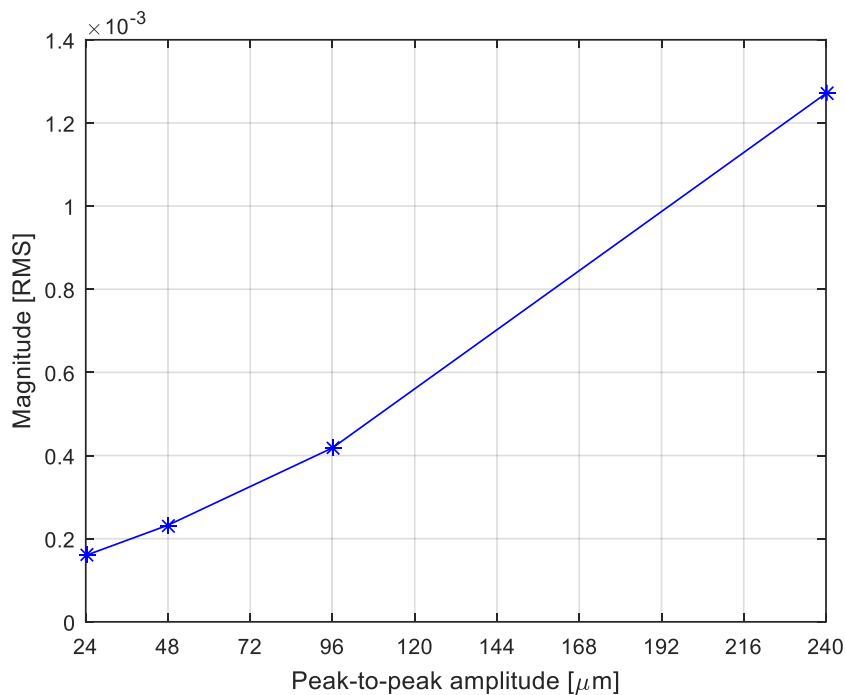


Figure 30: SPCD_1 fundamental frequency magnitude variation with scaling factor

2.5.3 Camera frame rate requirements for 2D shape analysis

To investigate how the set camera frame rate affects the quality of the extracted V_s , the setup shown in Figure 31 was used. In the setup, a single GOM 4M camera was used to capture images of the shape enclosed between the shaft and probe holder housing. The image in Figure 31(b) can then be processed to extract 2D contours. Figure 32 shows the captured and processed images from which a typical contour for analysis is obtained. The image processing stages were implemented in LabVIEW using the National Instruments Vision Assistant Toolkit.

Starting with an original image, a colour plane extraction is implemented to obtain a grayscale image. A smoothing filter is then applied to isolate the region enclosed between the shaft and probe holder housing. After performing brightness, contrast and gamma corrections to improve the picture luminance, masking of pixels (whose intensities differ significantly from the rest) is performed to allow for the extraction of a smooth continuous contour of the boundary pixels. Pixel masking is performed by drawing polygons enclosing the regions of interest, and then assigning a grayscale value of zero to the covered pixels. It is not a requirement to mask out the probe noticeable on the top left corner of the isolated region

between the shaft and probe holder housing. For this analysis all that is required is a continuous contour. In a dynamic analysis, the shape variation is actually of more importance than the initial shape form.

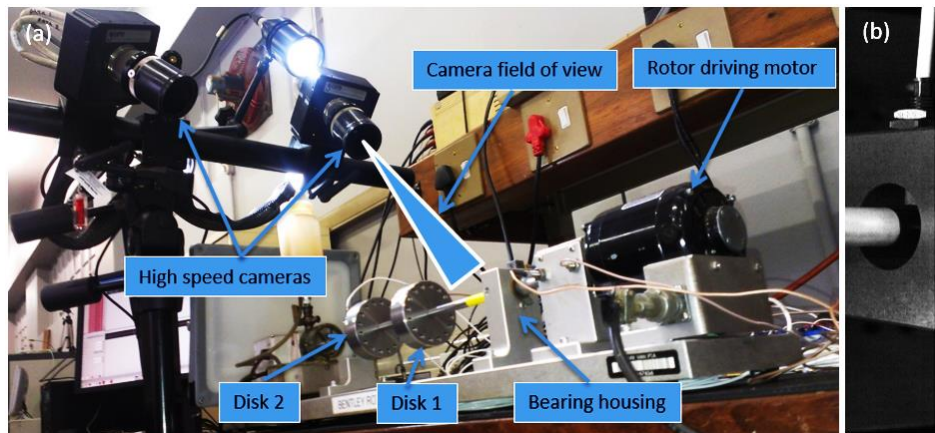


Figure 31: (a) System setup for a Bently Nevada rotor system, (b) single camera FOV

The image processing presented here understandably depends on the quality of the images captured as determined by the camera resolution and the lighting conditions. Once the contour has been captured, a shape form investigation can then be conducted to analyse different properties of that contour.

To investigate the frame rate requirements, the camera was set to record at 420 FPS, and the captured image sequence decimated to reduce the sampling frequency (FPS) for each analysis. The system was set to rotate at 1200 rpm. The results obtained for $SPCD_1$ at different sampling frequencies are given in Figure 33.

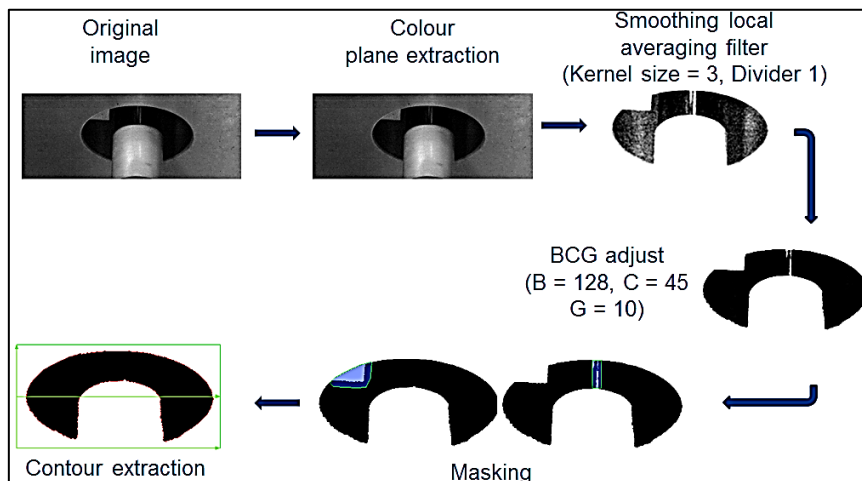


Figure 32: Contour extraction steps

For data acquisition, it is required that measurements be captured at least twice the frequency of interest to avoid signal aliasing (Nyquist sampling criteria). When analysing shape principal components however, Figure 33 indicates that sampling rates of no less than four times the frequency of interest are required for practical information to be extracted. The harmonics at higher frequencies are particularly useful when diagnosing machines using vibrational analysis. Because of this, camera frame rates need to be high enough to allow for accurate capture of at least the first three frequency harmonic components. Low sampling rates result

in very noisy SPCD values from which usable information cannot be extracted. Generally, improved frequency resolution from longer measurement time can help mitigate the effects of a low sampling rate in cases where responses with low frequency components are involved. For this particular investigation where low frequency components (20 Hz and its harmonics) are expected, longer measurement times at low FPS are expected to improve the SNRs. It is worth highlighting that when it comes to high speed imaging, measurement durations are typically dictated by the image storage capacity of the cameras used.

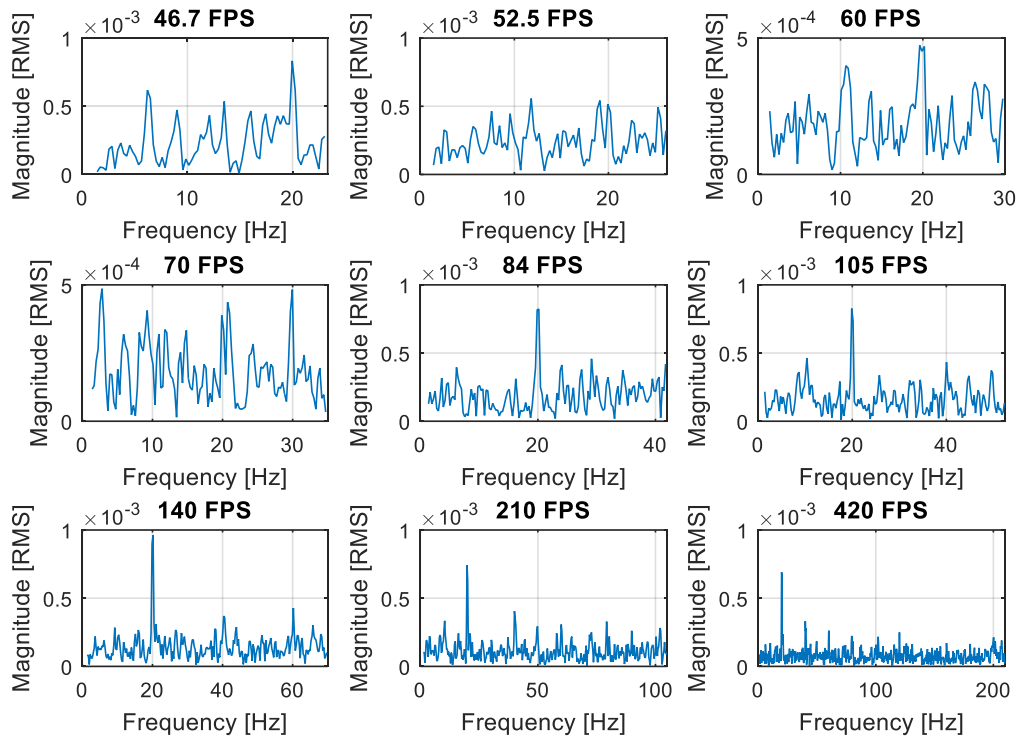


Figure 33: SPCD₁ frequency data for different camera frame rates

In this particular investigation where measurements are captured using the camera setup in Figure 31, peak-to-peak displacements in the range of about 120 μm were captured (this is presented later in Section 3.3 where proximity probes are employed). These values are much higher than the detectable simulation measurements (about 50 μm peak-to-peak) presented in the previous section. To comment on the performance of the shape-based analysis, the accuracy and sensitivity of the technique in a simulation-based environment is expected to be significantly better owing to the improved SNR of extracted data. Accurate shapes are extracted from a simulation video as opposed to shapes extracted from camera captured images.

2.6 Chapter conclusion

This chapter introduces the concept of a shape analysis approach for condition monitoring of turbomachines. A typical image processing procedure that can be followed to extract 2D contours from an image is presented. Specific shape characteristics in the way of principal components are defined, and an investigation in the manner in which each of these \vec{V}_i geometric modes are uniquely related to the form of the shape illustrated. It is illustrated that changes in the four computed shape principal components (2D analysis) can be monitored to

indicate the way imposed shape variations are related to \vec{V} . Thus, from an image captured with a single camera, four determined unique shape characteristics that are uniquely affected by enforced shape changes can be monitored. In a sensitivity investigation, it is shown that the perspective at which images are captured by the camera affect the apparent shape variation that can be observed. It is also illustrated that a camera sampling rate of at least four times the frequency of interest is required to obtain shape principal component variations smooth enough to be monitored for accurate shape variation analysis.

CHAPTER 3: 2D SHAPE ANALYSIS EXPERIMENTAL INVESTIGATION

3.1 Introduction

In this chapter a Bently Nevada rotor system operating at different states of static and couple unbalance is analyzed using the conventional proximity probes. The measurements obtained are then correlated to 2D based shape analysis measurements to establish the applicability of shape analysis as a condition monitoring tool in a practical environment. The dynamics of the system when rotor-stator rub is introduced are investigated using the two techniques, and oil instabilities also analyzed.

3.2 Bently system experimental setup

The setup considered for this investigation consists of a 455 mm long, 9.5 mm diameter steel shaft onto which are mounted two 25 mm thick, 75.5 mm diameter flywheels. The system is driven by a 75 W DC motor through a flexible coupling, and the other end of the shaft is supported by a fluid film journal bearing. The maximum speed of the system is 10 000 rpm, with a maximum ramp rate of about 15 000 rpm/min. A bush bearing supports the system at the driven end of the shaft. Meggitt proximity transducers with sensitivities of 8 V/mm and measuring ranges of 2 mm were positioned as indicated in Figure 34(a).

The system was balanced at a rotational speed of 1200 rpm. Six investigations were conducted to capture variations in shape principal components resulting from different machine faults. These faults include rotor unbalance, hydrodynamic bearing oil instabilities and rotor-stator rub. Rotor unbalances were introduced at disk 1 and disk 2, and shaft rub condition applied at the mid-point of the two disks by screwing a bronze stud onto the shaft (Figure 34(b)).

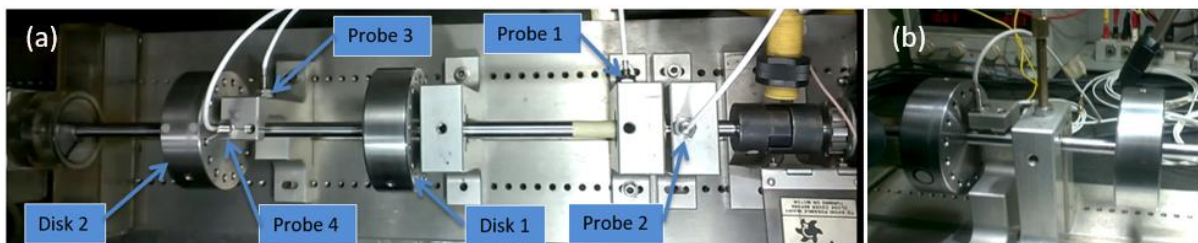


Figure 34: (a) Positioning of proximity probes, (b) rotor-stator rub application

Unbalance in a rotor results from an uneven mass distribution about the axis of rotation, causing vibration as a result of the interaction between the unbalancing mass and the rotational radial acceleration. Thus a centrifugal force that is ultimately transmitted to the bearings once every revolution is generated (MacCamhaoil, 1989). A point mass attached at a particular radius from the axis of rotation centre that results in eccentricity of the centre of gravity produces static unbalance. Couple unbalance on the other hand results from symmetrically attached two equal masses at 180° from each other about the centre of gravity. This causes the rotor inertial axis to shift from the rotation axis, also resulting in severe vibrations that the bearings will have to endure. A combination of the static and couple unbalance is what is termed dynamic unbalance. The different forms of unbalance are illustrated in Figure 35.

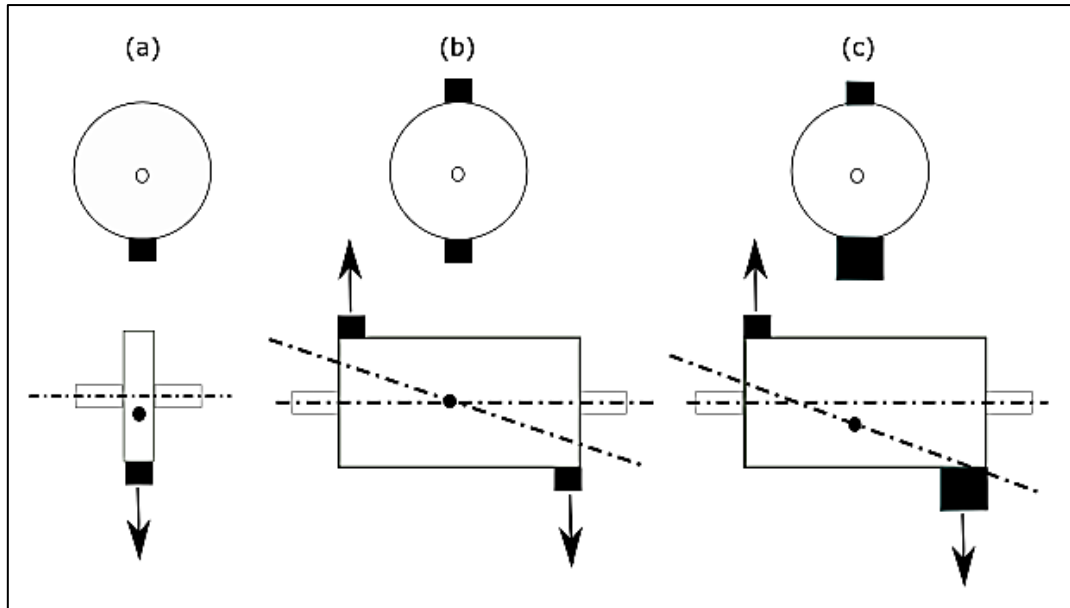


Figure 35: Rotor unbalance (a) static unbalance, (b) couple unbalance and (c) dynamic unbalance

Four different unbalance cases were investigated. These are given in Table 3.

Table 3: Unbalance cases

Case	Unbalance on Disk 1	Unbalance on Disk 2	Unbalance Type
1	5.62 gram at 0°	0	static
2	0	5.62 gram at 0°	static
3	4.85 gram at 0°	4.85 gram at 0°	couple
4	4.85 gram at 0°	4.85 gram at 180°	couple

3.3 System analysis using proximity probes

Time domain measurements from the proximity transducers were analysed first to get an idea of how the system was behaving. Captured measurements in mV were converted to displacements (mm) using the sensor sensitivity values. These measurements are usually contaminated with possible mechanical run-out (non-uniform shaft radius) and electrical run-out (variations in shaft electrical properties), as described by Littrell (2005). A slow roll compensation was therefore implemented for each sensor to ensure that the considered measurements reflected only the rotor dynamic response (Bently & Hatch, 2003).

Orbit plots from probe 3 and 4 measurements (Figure 34(a)) indicate differences in the shaft whirling vibrations for the different operating conditions. It is these differences in vibrations that we aim to detect and distinguish using shape analysis for condition monitoring purposes.

In Figure 36, the shaft whirling motion for the cases with unbalance can be recognized from the close to circular orbit plots. Oil instabilities result in a tilted elliptical orbit. The shaft is prevented from motion in the upward direction in the rotor-stator rub investigation, which can be clearly noticed from the flat-topped orbit plot.

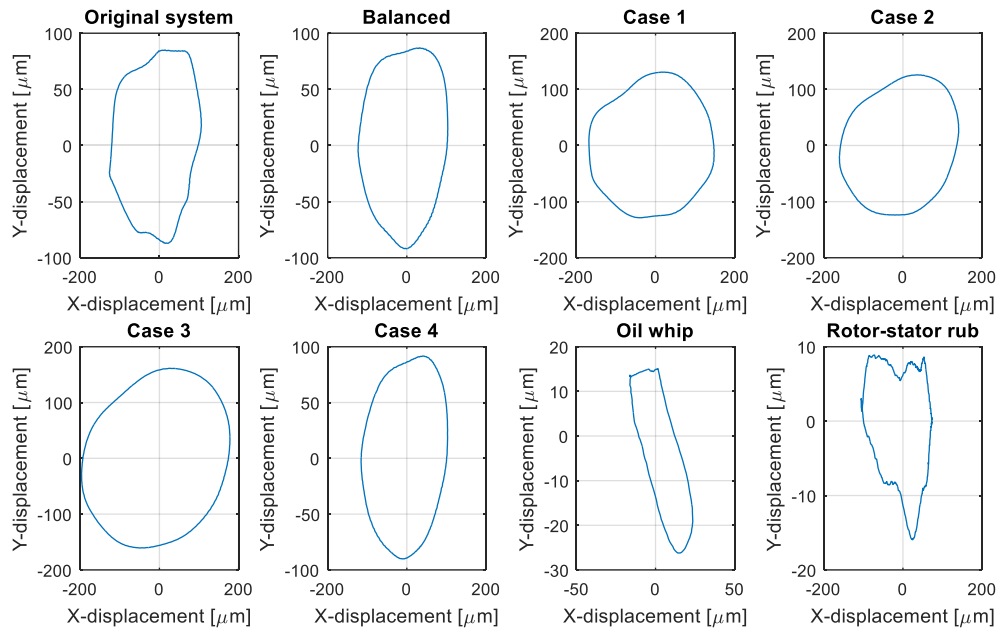


Figure 36: Orbit plots for probes 3 and 4

Frequency domain proximity sensor measurements are given in Figure 37 and Figure 38. Probes 1 and 2 are located at the bush bearing supported end of the shaft, where the coupling to the driving motor is also attached. At this end of the shaft, the constraints restrict shaft vibrations more relative to constraints at the hydrodynamic bearing end (probes 3 and 4). Due to that interference, the resulting dynamic nonlinearity and the low SNR of the measurements from probe 1 and 2 result in the more significant sub-harmonic frequency components observed in Figure 37 and Figure 38. Synchronous frequency integer harmonics (probe 1 and 2) are typically associated with electrical runout as described by Adams (2010). These harmonics can still be observed even with runout compensation implemented, something which can be attributed to the low SNRs of measurements captured using probes 1 and 2.

Focusing on probes 3 and 4, a frequency domain proximity sensor measurement analysis does not yield significant information in terms of classification of system unbalance. This can be observed by comparing Figure 37 and Figure 38. Whilst the introduction of unbalance clearly results in a general increase of fundamental frequency magnitudes for the probes, variations between different static and couple unbalance operating conditions cannot be detected.

The conventional phase analysis approach, which involves determining the fundamental frequency phase differences between various probes, was employed to detect, classify and distinguish the different forms of unbalance using measurements from the proximity probes. A value of $90^\circ (\pm 30^\circ)$ to account for mechanical variance (SKF, 2018)) between the vertical and horizontal probes at any particular bearing indicates the presence of unbalance. This is expected regardless of the type of unbalance present in the system.

Distinguishing unbalances entails the analysis of phase measurements for probes measuring in the same direction but at different bearings. For a statically unbalanced system, a phase difference of $0^\circ (\pm 30^\circ)$ is expected. This phase difference will be approximately 180° for a

couple-unbalanced system. Dynamic unbalance, which is a combination of both static and uncouple unbalance, can be identified by a phase difference between 0° and 180° .

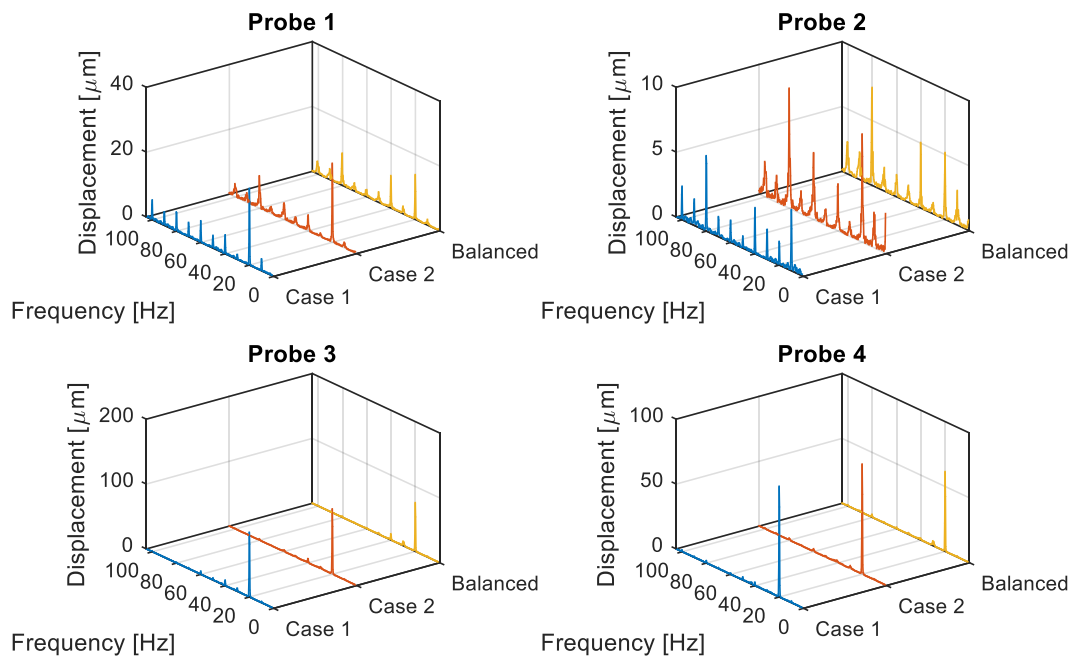


Figure 37: Proximity probes based static unbalance

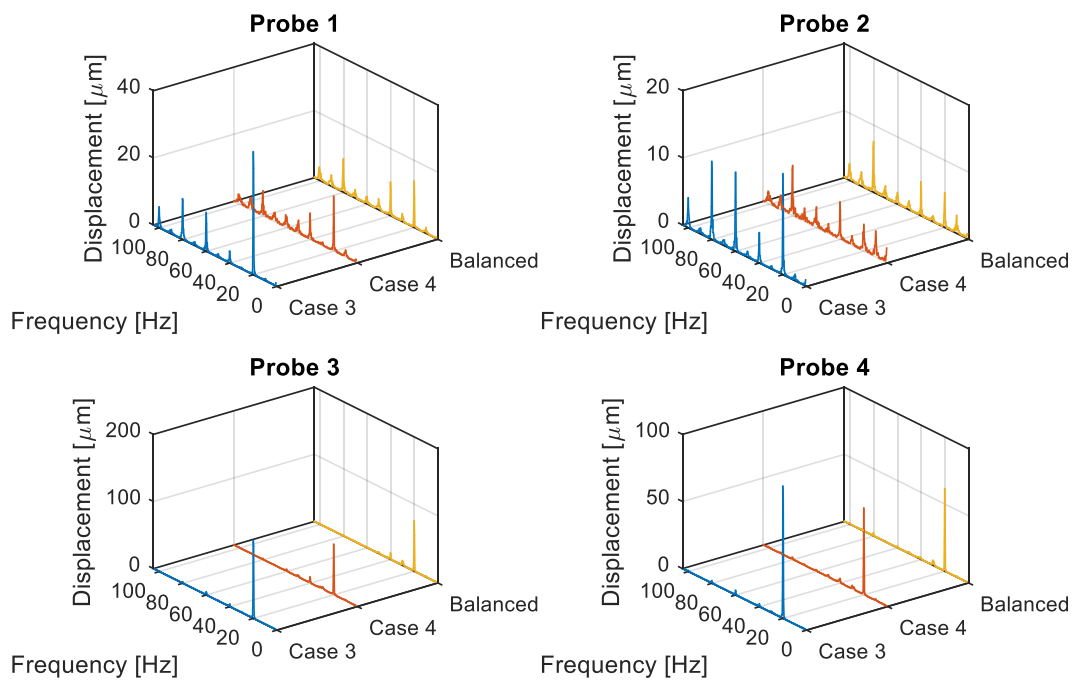


Figure 38: Proximity probes based couple unbalance

Shown in Table 4 are the phase analysis results. Probes 1 and 3 were measuring the horizontal shaft position at different bearings, and probes 2 and 4 the vertical shaft position (refer to Figure 34).

Table 4: Proximity probes phase analysis

System state	Phase difference (Probes 1 and 2)	Phase difference (Probes 3 and 4)	Phase difference (Probes 1 and 3)	Phase difference (Probes 2 and 4)
Balanced	289.6°	275°	12.8°	1.8°
Case 1	180.7°	273.2°	0.3°	92°
Case 2	89.6°	80.6°	8.5°	0.5°
Case 3	174.5°	82.9°	2.6°	89°
Case 4	46.3°	85.2°	2.6°	134°

Considering signals from proximity probes 3 and 4, Table 4 indicates the presence of unbalance in the system, with the exception of Case 1 (static unbalance at disk 1). The effect of unbalance at disk 1 is not apparent enough in these results. Probes 1 and 2 only indicate the presence of unbalance for Case 2, something that can be attributed to the probes being located quite close to the journal bearing. Shaft vibration amplitudes are very low, and the SNR is also low. Analysing phase values for probes at different bearings, Table 4 indicates the presence of dynamic unbalance in the system for all the cases investigated. This was expected as some form of residual unbalance always remains after a system has been balanced, with the unbalance effect being more significant for small systems.

3.4 System analysis using shape analysis

An investigation using shape analyses was then employed to check if the different system operating conditions could be better distinguished. From the results presented above, this could not be conclusively done using data from the proximity probes. A GOM 4M stereo-videography system was used to capture images of the rotor at 420 FPS, and 2D shape extraction and analysis conducted as discussed in the previous chapter.

Figure 39 illustrates the SPCD results obtained for static unbalance. It should be noted that SPCD results from captured images tend to have a significant noise floor. The roughness of the extracted shape at the local boundary pixels varies from image to image, and this tends to influence the determined SPCDs to some extent. The “roughness” in this case is not referring to the physical profile of the shaft, but rather the quality of the extracted contour based on the camera resolution and shaft orientation at various angular positions. If the shaft centroid is along the vertical axis for instance, the pixels of the shaft profile are aligned vertically, with no change in the direction (along the horizontal axis) implying a smooth extracted profile. If the centroid is along the 45° line, then a noisy or rough extracted shaft profile is expected.

Application of static unbalance at either disk 1 or disk 2 increases the forced rotor whirling motion, thus resulting in more significant shape variations. This is evident from the increased PC magnitudes observed in Figure 39 especially for SPCD₁ and SPCD₄ relative to the balanced case. The additional unbalancing masses added produces larger shape variations compared to the ones resulting from the residual unbalance in a ‘balanced’ system. Case 2 involves addition of unbalance on disk 2, which is located closer to the shaft central location and furthest from the two bearing supports. It is expected that the energy introduced to the

system in Case 2 be greater than that introduced in Case 1. This is evident from the SPCD magnitude differences in Figure 39.

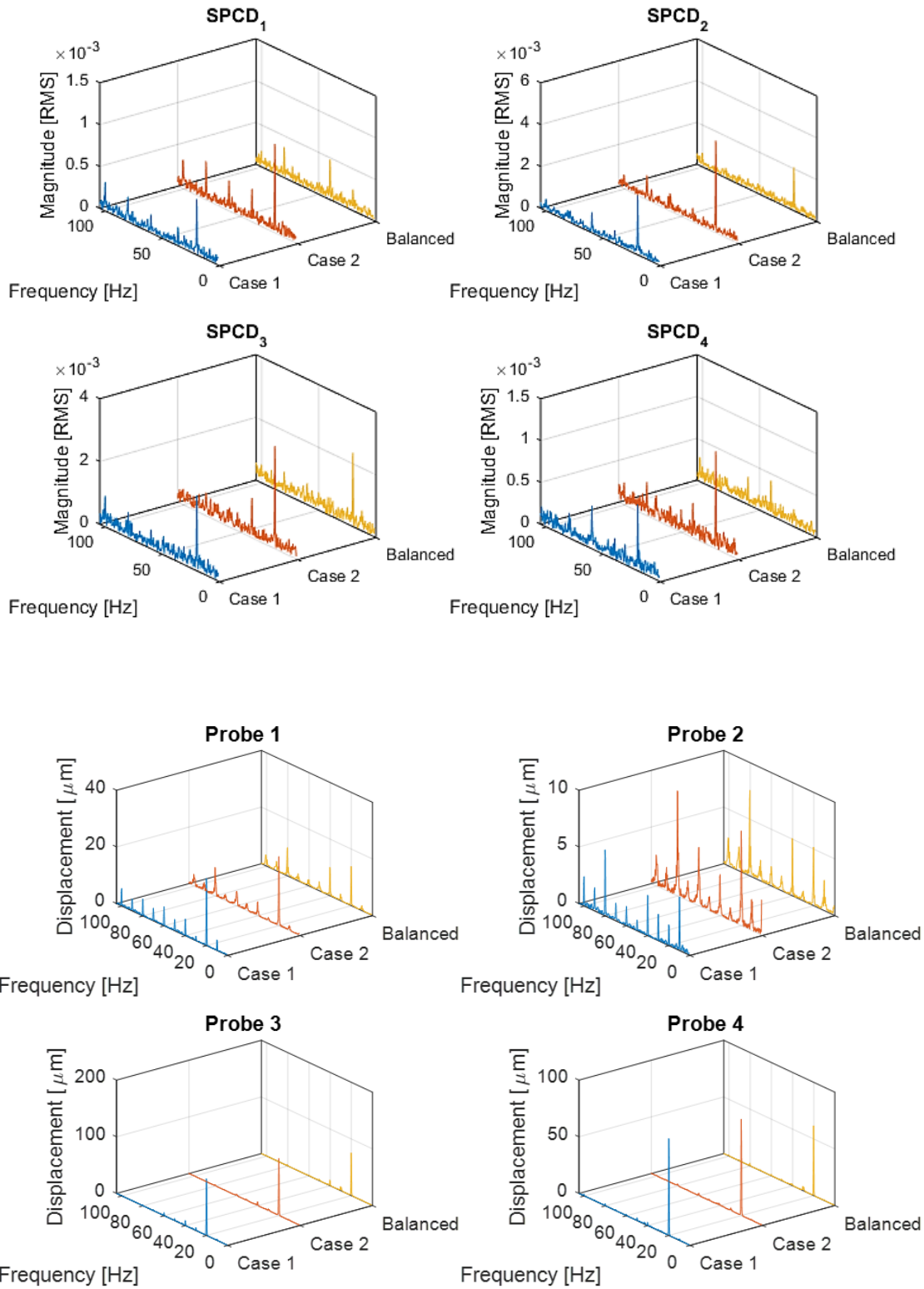


Figure 37: Proximity probes based static unbalance

Figure 39: Shape principal component based frequency responses for static unbalance

Compared to proximity probe measurements, static unbalance results in a very different frequency structure for SPCDs measurements (Figure 37 and Figure 39). Energy introduced into the system by a static unbalance results in a shape variation that is predominantly associated with the rotational speed. This difference between a balanced and the two statically unbalanced system cases is not that apparent when considering probe-based measurements (Figure 37), as illustrated in Table 5. The harmonic Magnitude Increase Factors (MIFs) for each case are calculated relative to the balanced system values using Equation (27). A zero value indicates the absence of a peak at a particular harmonic for the unbalance case of interest. An asterisk (*) indicates absence of a peak for the balanced system, and a peak present for the unbalance case.

$$MIF = \frac{\text{Unbalance system magnitude} - \text{Balanced system magnitude}}{\text{Balanced system magnitude}} \quad (27)$$

The first harmonic SPCD MIFs from Table 5 clearly indicate an increase in the system response magnitudes as a result of the static unbalance. Case 2 MIFs for the SPCDs are significantly higher than those for case 1 as expected, making a distinction between the two unbalance cases possible. This can be adopted for quantifying the extent of static unbalance in a system. Measurements from the proximity probes do not capture the differences in static unbalance in this case. For static unbalance, MIFs at the higher harmonics do not yield significant fault classification information except for SPCD₂. Higher harmonics are noticed in the system the moment static unbalance is introduced.

Table 5: Harmonic magnitude increase factors for static unbalance

	1× harmonic MIF		2× harmonic MIF		3× harmonic MIF	
	Case 1	Case 2	Case 1	Case 2	Case 1	Case 2
SPCD₁	1.62	3.18	0	-0.18	*	*
SPCD₂	0.37	1.13	*	*	*	*
SPCD₃	0.02	0.39	0	*	0	0
SPCD₄	*	*	0	0.01	0.54	0
Probe 3	0.33	0.34	0	0	0	0
Probe 4	0.39	0.38	0	0	0	0

Figure 40 shows the PC results obtained after introducing couple unbalance into the system (Case 3 and 4).

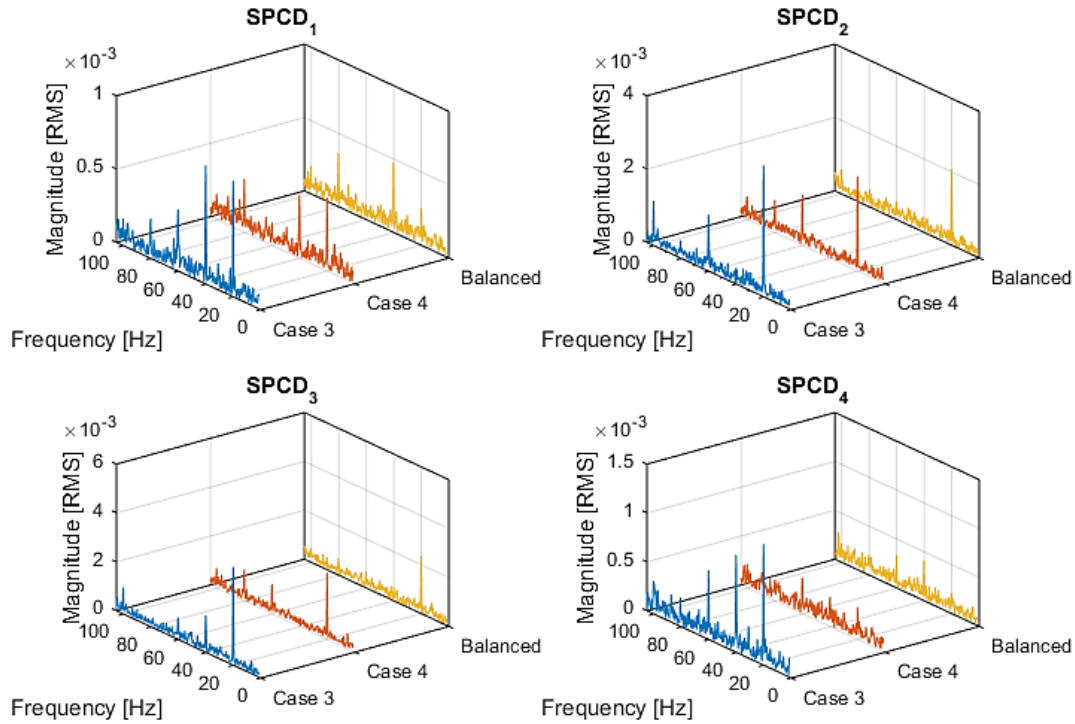


Figure 40: Shape principal component based frequency responses for couple unbalance

Comparing Figure 39 to Figure 40, it can be clearly noted that there are significant differences in shape variations introduced by the presence of either static or couple unbalance in the system (SPCD₁ and SPCD₄). Static unbalance imposes rotor whirling that results in a bent Operational Deflection Shape (ODS) around the shaft reference axis. The ODS has a form similar to the first bending mode. This results in a general increase in the magnitude of the fundamental frequency component for all the SPCDs, when analysed relative to a balanced system with some residual unbalance in it. On the other hand, depending on the positioning of the unbalance weights, the ODS associated with couple unbalance can be more complex taking forms similar to how the shaft higher bending modes would appear. Thus, the shaft whirling motion will result in complex shape variations, which do not correlate directly with the basic principal component shape variations discussed in the previous chapter, resulting in the higher harmonics receiving even more energy in a frequency domain analysis. This explains the higher frequency component magnitudes at 40 Hz for SPCD₁ and SPCD₄. This can be used as a condition monitoring tool to differentiate between static and couple unbalance in a system.

To illustrate this further, Table 6 shows the MIFs determined for the rotor system. Couple unbalance introduced at the same angle on different shaft locations (case 3) clearly results in increased system energy as indicated by the higher case 3 first harmonic MIFs. Comparing Table 5 results to Table 6, the SPCD₁ and SPCD₄ second harmonic MIFs illustrate a difference between static and couple unbalance. Couple unbalance clearly results in a significant increase (case 3) or significant decrease (case 4) of the second harmonic SPCDs magnitudes. This is not the case with static unbalance. In addition all SPCDs show an increase in the third harmonic magnitudes in the presence of couple unbalance.

Comparing the proximity probe measurements (both phase analysis and single probe frequency domain measurements) to SPCA in terms of unbalance investigations, it is evident that the proposed shape analysis approach offers results that easily illustrate different system operating conditions. This applies to this specific investigation. Variations in system dynamics that are too small to be clearly captured using uniaxial transducers are much more easily identified by using a 2D based data capturing scheme. The low SNR of signals captured by the proximity probes too close to the bearings may limit the robustness of uniaxial transducers. Shape analysis makes it possible to look further away from the bearings where rotor responses are significant enough to be detected for condition monitoring purposes.

Table 6: Harmonic magnitude increase factors for couple unbalance

	1x harmonic MIF		2x harmonic MIF		3x harmonic MIF	
	Case 3	Case 4	Case 3	Case 4	Case 3	Case 4
PC 1	2.12	0.96	0.69	-0.99	*	*
PC 2	0.73	0.24	0	0	*	*
PC 3	0.71	0.16	*	0	*	*
PC 4	*	*	1.42	-0.27	1.12	0.10
Probe 3	0.54	0.003	0	0	0	0
Probe 4	0.60	0.05	0	0	0	0

Based on how the MIFs are calculated (Equation 27), unbalance magnitudes less than the balanced system magnitude can result in negative values that can be noticed in Table 6. Conventionally, one would expect the unbalance response magnitudes to be always higher than the balanced responses. However, in the case of SPCDs where the values are calculated based on the relationship between the specific geometric modes and the response shape variation, the unbalanced magnitude (in this case for the 2X harmonic) can be lower than the balanced response magnitude.

3.5 Investigating rotor-stator rub and oil instabilities using proximity probes and 2D shape analysis

The advantages of incorporating a 2D based analysis in detecting system operating changes are further illustrated in the case of rotor-stator rub. The rotor-stator rub was introduced by screwing the stud in the probe holder housing between the two flywheels further down until it interfered with the rotating shaft (Figure 34(b)).

Figure 41 indicates that rotor-stator rub results in a decrease in fundamental frequency magnitude for the proximity probes. This is expected since the amplitude of vibration response in a particular direction is reduced if a component is interfering with the shaft in that direction. Advanced probes sensitive enough to capture signals with high SNRs might need to be employed to diagnose a system operating in these conditions, if the probe measurements are to be considered as independent signals, and not as 2D orthogonal pairs. This is however

different when considering SPCDs. The 2D analysis approach focuses on shape variation, an occurrence which can be amplified by the presence of rotor-stator rub. This is evident in $SPCD_1$, $SPCD_2$, and $SPCD_4$ of Figure 42. In this case the decrease in the magnitudes of individual axis responses did not decrease the quality of the measurements captured. The shape variation influence on the principal components was substantially significant, even though the variation magnitudes were small. The multi-dimensional shape analysis approach proposed can therefore be used to complement proximity probe measurements when investigating changes in the overall behaviour of a system.

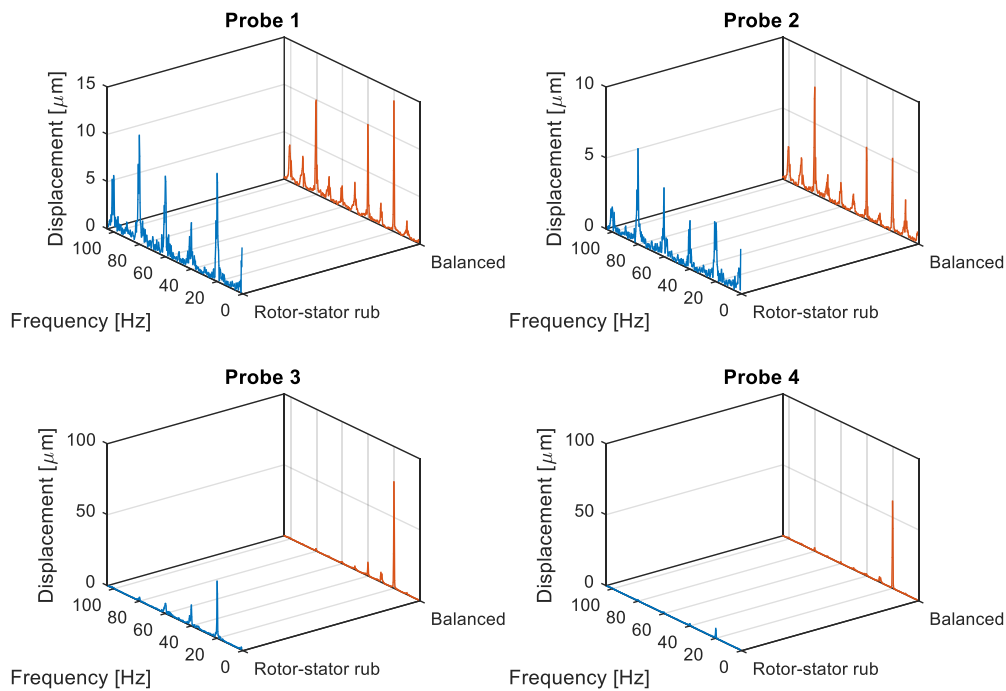


Figure 41: Proximity probes rotor-stator rub

Hydrodynamic bearing oil instabilities tend to be one of the most dangerous faults in rotating machines owing to the fact that the damage of a structure exhibiting oil whip characteristics progresses to failure in a very short period of time. Therefore hydrodynamic bearing oil instabilities were also investigated to check if the proposed approach can capture information that can allow for easier identification of bearing oil instabilities.

When a rotor system is running at a particular speed, the fluid flows around the bearing at a speed that is approximately half the journal surface speed. This will then introduce oil whirl motion into the system, of which the sub-synchronous frequency will be slightly less than 50% of the shaft rotational frequency. If the shaft rotational speed is then set to twice the first critical speed, then the oil whirl motion will then coincide with the critical speed. Energy from the oil whirl instability will now be exciting the first bending mode resulting in a system instability (Liu et al., 2018). The vibratory responses associated with the instability often cause failure in a short period of time (Nelson, 2007).

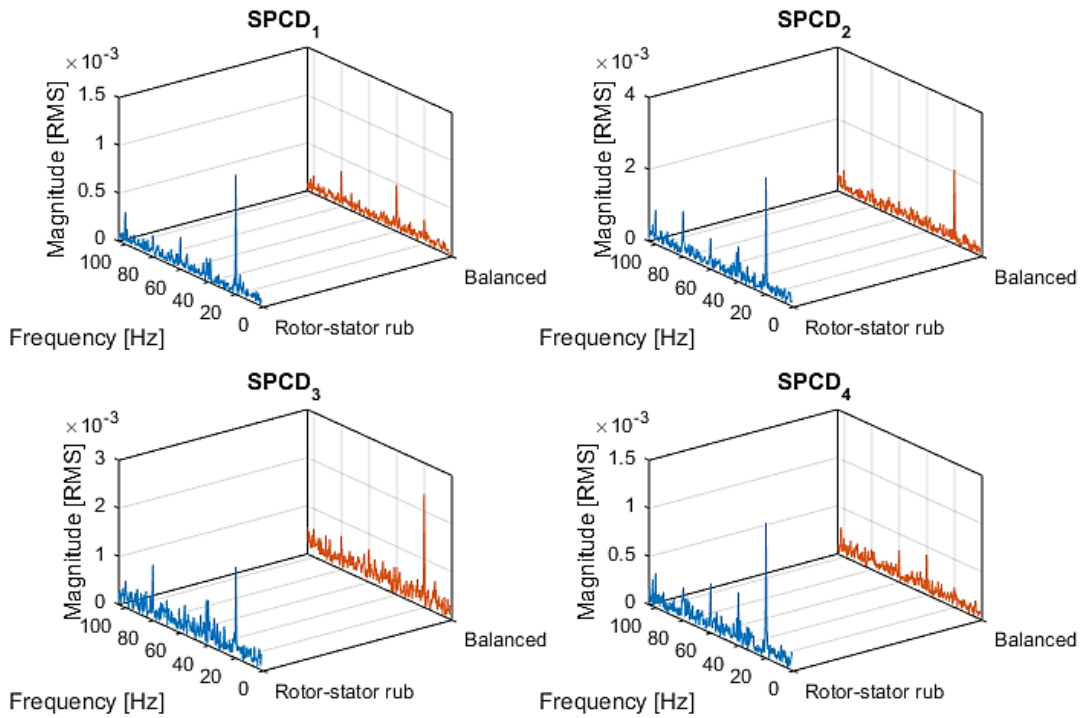


Figure 42: Shape principal component based frequency responses for rotor-stator rub

To experimentally determine the rotor system critical speeds, a system run up and run down was conducted, and the in-plane shaft positions from proximity probes 3 and 4 extracted. Increased shaft vibrations are expected when the rotor spin speed coincides with a critical speed. The speed was increased from about 175 rpm to 5420 rpm.

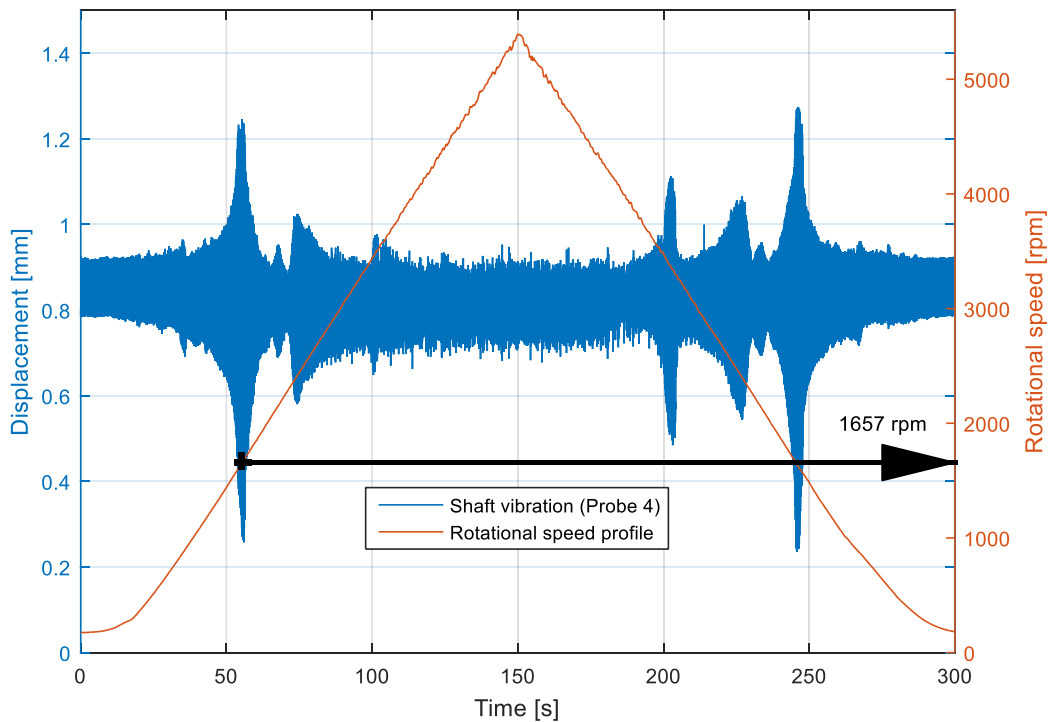


Figure 43: Rotational speed ramp up and down system response

It can be noted from Figure 43 that the first critical speed of the system is 1657 rpm (27.6 Hz). Thus setting a rotational speed to 3314 rpm (55.2 Hz), which is twice the critical speed, will induce oil whirl. Figure 44 shows the responses obtained from the proximity probes when the rotor was being rotated at 3314 rpm. Except for probe 2, the probes reflect the highest vibratory frequency magnitudes to be located at the shaft critical speed, with significant peaks at the system rotational speed as well.

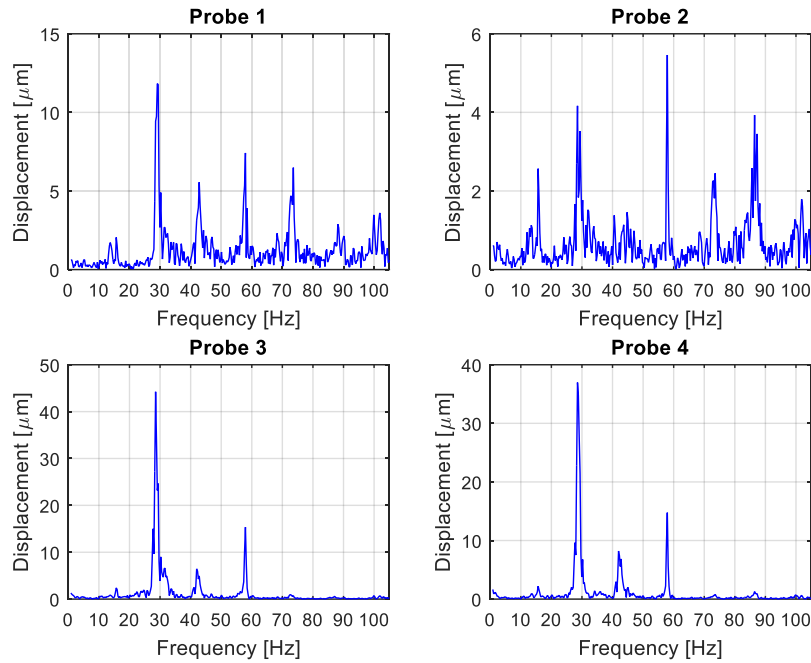


Figure 44: Proximity probes oil instability effects

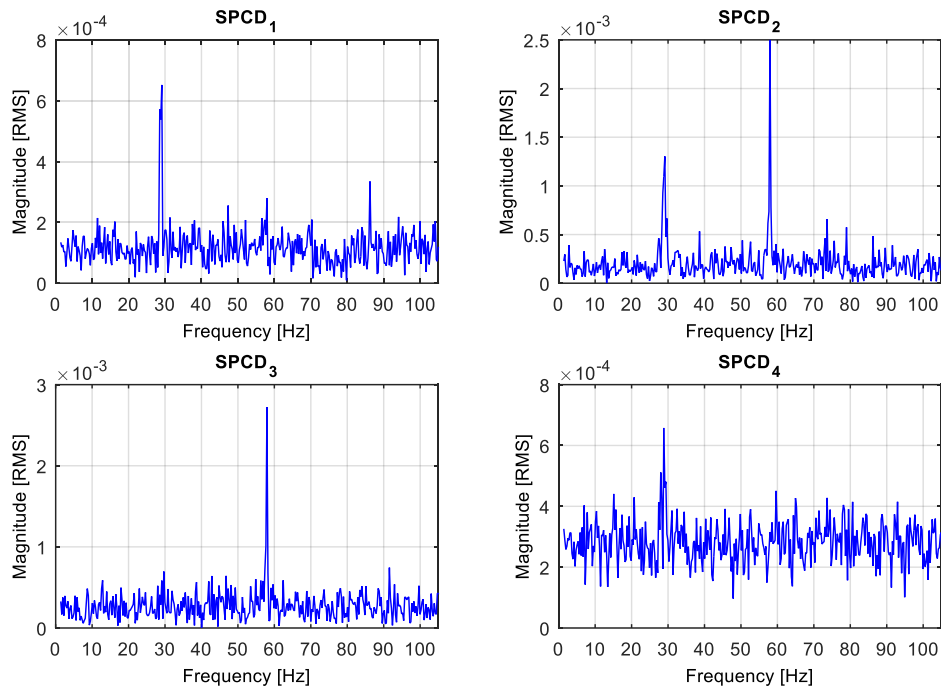


Figure 45: Shape principal components-based oil instability effects for a system rotational frequency of 55.2 Hz

A different behaviour is however observed for the SPCDs, as shown by Figure 45. Whilst $SPCD_1$ and $SPCD_4$ clearly show peaks at the shaft critical frequency (27.6 Hz), $SPCD_2$ and $SPCD_3$ show peaks at the set system rotational frequency. This indicates that the system dynamics introduced by oil instabilities have less influence on shape variations associated with $SPCD_2$ and $SPCD_3$. In this case, the general shaft whirling due to the set rotational speed has more influence on these shape variations. These distinct differences in the form of the four SPCDs analysed for the same system condition are noticed only for a system where oil instabilities are present. Currently, there is no concrete physical explanation for this observation, and further investigations will have to be conducted to fully understand how the oil instability induced shaft whirl behaviour relates to shape variations at the bearing location where the images are being captured.

The 2D shape analysis variability of four different parameters extracted from an image captured using a single non-contact sensor can therefore be used to complement single axis sensor measurements from probes to fully understand the dynamics of a rotating machine.

3.6 Chapter conclusion

This chapter focused on the application of a 2D shape analysis approach for condition monitoring of a rotating machine. The distinction between different forms of system unbalance could be performed using this approach, complementing proximity probe measurements in instances where conventional phase analysis results were not conclusive.

Even though not explicitly investigated experimentally, condition degradation monitoring due to increasing unbalance for instance will typically be characterized by increased shaft whirling amplitudes. The increasing unbalance forcing more significant shape variations would simply result in increasing SPCDs peak amplitudes as demonstrated in the FEM analysis in Section 2.5.2, allowing for condition degradation monitoring. Considering Figure 39 in which a higher static unbalancing effect to the system (Case 2) resulted in higher SPCDs peaks relative to lower system unbalancing effect (Case 1), it can be concluded that the technique has the potential to successfully quantify damage in an experimental setting. However, establishing and quantifying the relationship between the level of unbalance and changes in the SPCDs peaks for condition degradation monitoring purposes is something that will have to be considered in future studies.

From the rotor-stator rub investigation, it could be clearly shown that the multi-dimensional nature of shape analysis allows easier detection of changes in a system even in cases where the uniaxial point vibrations are very small. In these cases, conventional contact transducers tend to have very low SNRs, something which usually complicates accurate fault classification. The distinct uncorrelated nature of the computed shape principal components illustrated that the four parameters can be very differently influenced by the way a system behaves, making it much easier to distinguish between different system operating conditions. This was observed in the case of rotor hydrodynamic bearing oil instabilities. This makes the proposed approach an ideal tool for damage progression monitoring in structures. The 2D nature of the approach and the decomposed form of the monitored parameters ensures significant sensitivity to changes in the behaviour of the system.

CHAPTER 4: 3D SHAPE ANALYSIS NUMERICAL AND EXPERIMENTAL INVESTIGATION APPLIED TO MODEL ROTATING TURBINE BLADES

4.1 Introduction

This chapter focuses on the extension of a shape-based condition monitoring approach from 2D to 3D applications. After the introduction of 3D SPCDs, an analysis into the type of geometric modes associated with the generic rectangular shape of an axially rotating blade in 3D is conducted.

A numerical investigation of 3D SPCDs using a FE model of a rotor system is introduced. This investigation is conducted to better understand the relationship between the 3D shape descriptors and the behaviour of a rotor system under various operating conditions of different levels of blade damage. In addition to the verification of expected system behaviours such as a decrease in natural frequency with increasing blade root damage, the FE investigation is also adopted to investigate how the proposed shape analysis approach compares and relates to conventional techniques. Monitoring changes in the modal analysis parameters is considered in this case. Through PCA of determined SPCDs, a clustering technique for easier identification of different damage modes is introduced and implemented. To investigate the applicability of the technique as a condition monitoring tool, variations of shape analysis results with changing system operating conditions are analysed.

In an experimental study, the determination of 3D SPCDs from stereoscopic images of rotating blades is presented. Variations in the dynamics of different damage modes for actual rotating axial blades are investigated by monitoring these SPCDs. The developed and numerically investigated order based PCA of the SPCDs, is employed to verify the feasibility of a condition monitoring shape-based approach for turbine blades in an experimental setting. The applicability of the proposed shape analysis technique in a laboratory-controlled environment is successfully demonstrated.

The last section of the chapter discusses the applicability of the proposed approach for condition monitoring of out-door full scale wind turbines. The size of a typical out-door wind turbine and its maximum out-of-plane deflections is considered, and that information is correlated to the rotor size and measurements captured in the laboratory based experimental investigation. The feasibility of using shape analysis to capture the dynamics of actual wind turbines for condition monitoring purposes is illustrated.

4.2 3D SPCDs determination

As highlighted in Section 1.2.4.1, four Fourier coefficients (a_n, b_n, c_n, d_n) can be calculated for a 2D shape, whilst six ($a_n, b_n, c_n, d_n, e_n, f_n$) can be determined for a 3D shape. Similar to what was conducted in the 2D analysis, a PCA of the multivariate vector composed of six Fourier shape descriptors (Equation 17) of a 3D contour was employed to extract linearly uncorrelated variables. Each of these principal components (columns of V) represent a specific shape feature form, and the procedure for characterizing a shape using these principal components is summarized in Figure 46.

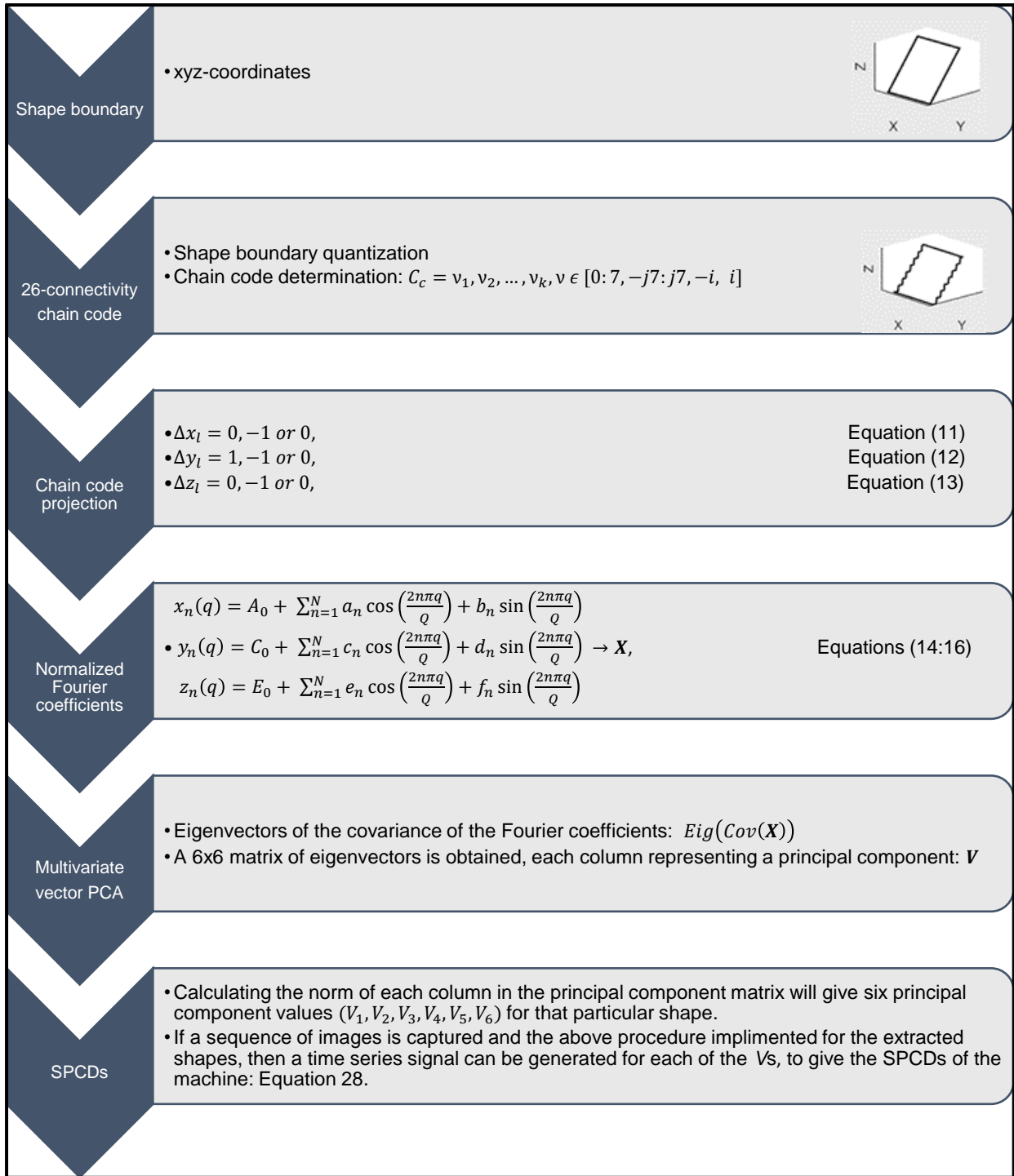


Figure 46: Shape principal components determination procedure for 3D shape analysis

Thus for two consecutive image contours from two frames f and $f + 1$, each described by a 6×6 multivariate matrix \mathbf{V} , the i^{th} measure of variation between two consecutive frames (Shape Principal Component Descriptor, SPCD _{i}) can be considered as the difference between the consecutive \vec{V}_i Euclidean norm values, as given by Equation 28. The difference between the two frames was considered for an improved SNR in this case.

$$\Delta SPCD_i(t) = \|\vec{V}_i(f)\|_2 - \|\vec{V}_i(f + 1)\|_2 \quad (28)$$

Thus for a set of captured images, 3D contour variations can be characterized by six time varying SPCDs, [SPCD₁(t) SPCD₂(t) SPCD₃(t) SPCD₄(t) SPCD₅(t) SPCD₆(t)].

4.3 Geometric modes for a 3D rectangular shaped contour

Similar to what was highlighted in Chapter 2 for a 2D analysis, each column in V is associated with a very specific shape feature, termed a geometric mode in this study. For a typical blade contour, the specific shape characteristics each \vec{V}_i captures can be investigated visually by scaling its corresponding scores X_i^{new} individually before reconstructing the original shape using the Fourier sums. This type of scaling and shape reconstruction is illustrated in the flow diagram in Figure 47 for a Scaling Factor (SF) of 0.5 applied to the scores associated with the first geometric mode.

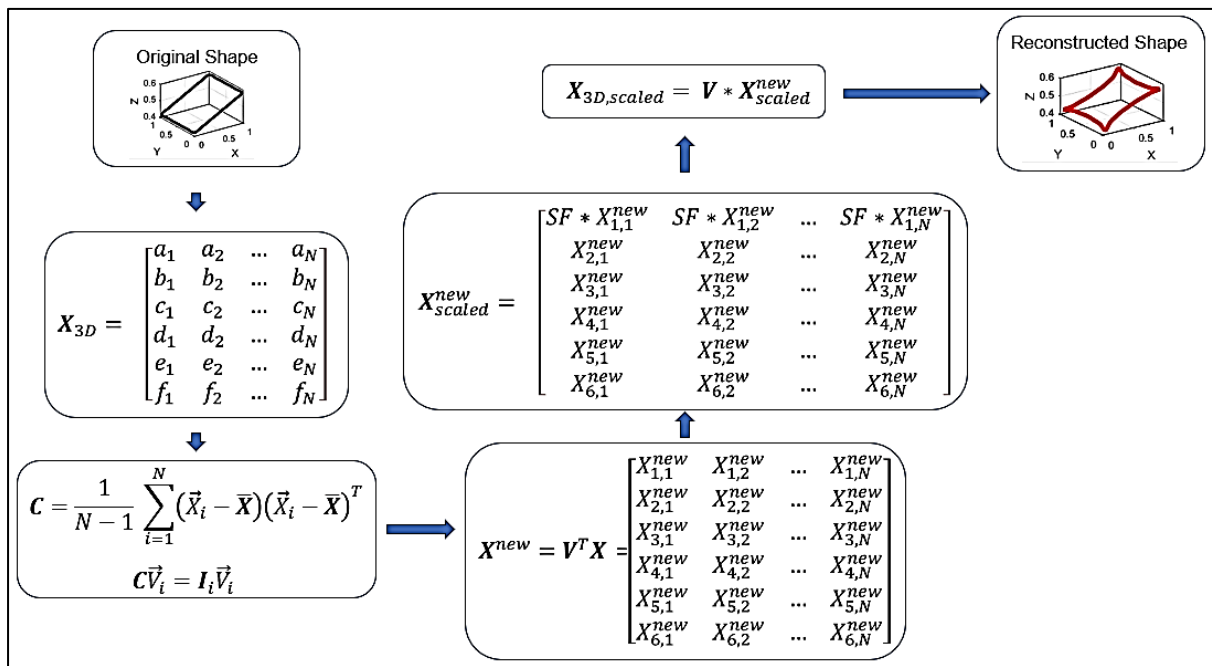


Figure 47: Principal component score scaling and shape reconstruction flowchart for visualization of different geometric modes

These variations are illustrated in Figure 48 for a 3D contour described by six principal components. The shape variations illustrated in Figure 48 are dictated by the principal component scores (X^{new}) calculated for the specific rectangular shape. This means that if a complex shape representative of a twisted blade is considered, then different shape variations unique to that particular shape will be obtained. In accordance with Figure 48 observations, the following discussion considers 'in-plane' geometric modes as those modes affecting the rectangularity of the shape, and 'out-of-plane' geometric modes to refer to modes associated with the smoothness of the shape.

When performing shape analysis, it is necessary that one identifies the necessary SPCDs to monitor based on the direction of the response (in-plane or out-of-plane response). In that regard, Figure 48 points to SPCD₅ and SPCD₆ for an out-of-plane response. In addition to the direction of the response, it is also important to consider how the shape variation of the response relates to the geometric modes V illustrated in Figure 48. The sensitivity of a particular SPCD to a specific response under investigation is directly influenced by how well

the response shape variation correlates to the shape changes obtained by scaling X^{new} (correlation to the geometric modes).

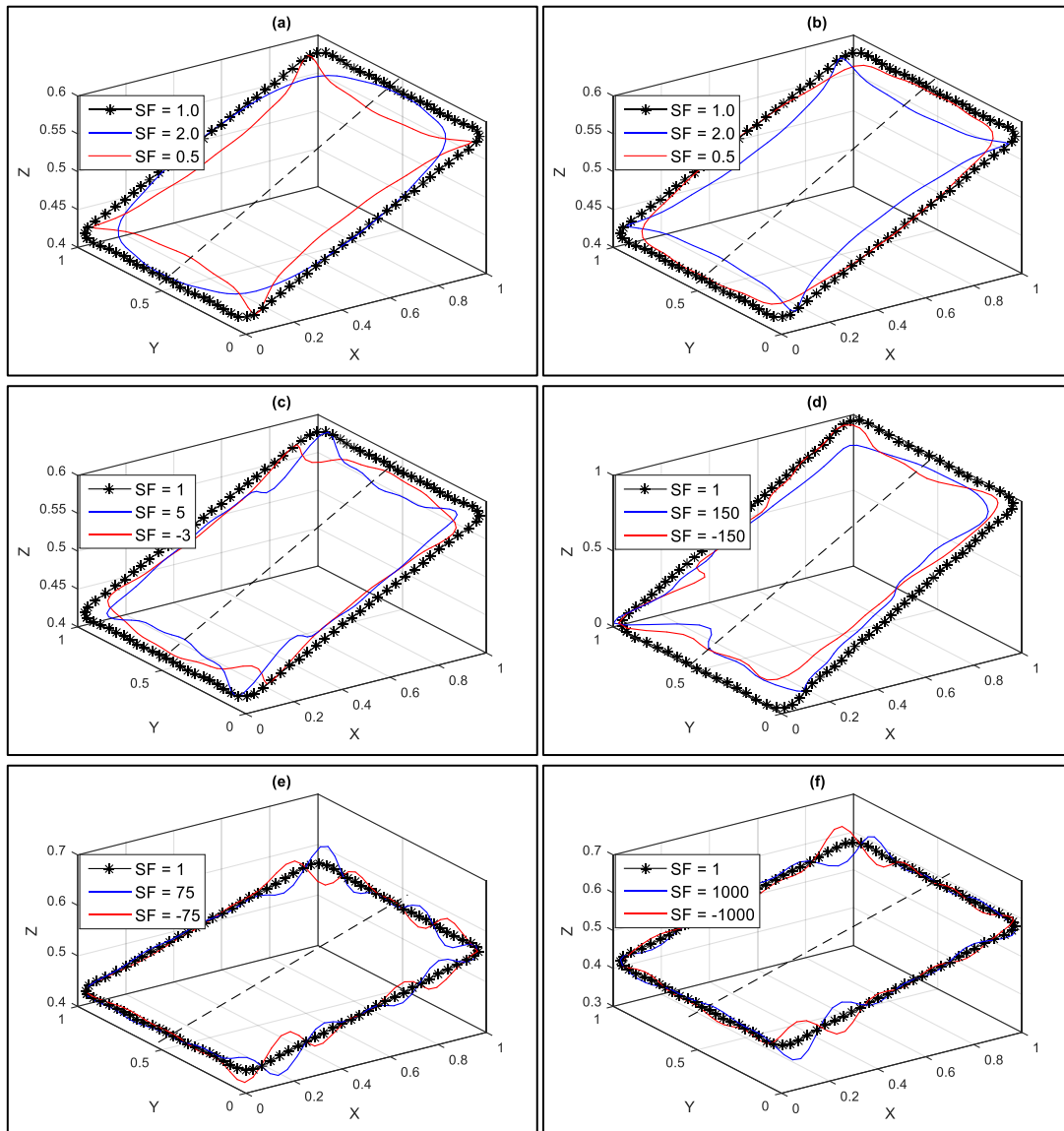


Figure 48: Nature of geometrical modes for a 3D rectangular shape (a) \vec{V}_1 , (b) \vec{V}_2 , (c) \vec{V}_3 , (d) \vec{V}_4 , (e) \vec{V}_5 and (f) \vec{V}_6

As can be observed from Figure 48, \vec{V}_1 to \vec{V}_4 are essentially associated with in-plane contour variations. \vec{V}_1 and \vec{V}_2 geometric modes are very similar to each other and they influence the rectangularity form of the contour. \vec{V}_5 and \vec{V}_6 are associated with the out-of-plane blade responses, which make them the most important to monitor in a case where the blade damage mode is expected to have a more significant effect on the out-of-plane vibrations. Whilst the shape variations associated with the shape principal components might not be similar to expected blade physical or practical responses in terms of symmetry (\vec{V}_4 to \vec{V}_6), the obtained descriptors can still be used to monitor condition. This is because calculated SPCDs are composed of information regarding the relation between the geometric modes and the actual blade responses for a particular test. It has been demonstrated in Section 2.4 that for a particular ultimately calculated SPCD, the quality of the measurements in terms of signal-to-

noise ratios improves according to how well the physical response shape variation resembles a certain X^{new} variation.

In the case of axial blades vibrating out-of-plane, the expected shape variations are predominantly associated with the rectangularity nature of a shape (first bending mode ODS). As can be observed in Figure 48, scaling \vec{V}_5 and \vec{V}_6 are related to the local form (smoothness) of the shape. On account of the out-of-plane ODS responses being different from these geometric modes, one can therefore expect a low sensitivity of \vec{X}_5^{new} and \vec{X}_6^{new} to the response. By association, this low sensitivity behaviour extends to the calculated $SPCD_5$ and $SPCD_6$ as well. If one intends on focusing on the $SPCDs$ whose corresponding X^{new} are closely related to the type of response, the multi-dimensional nature of 3D shape principal component analysis presents further opportunities in the form of possible shape rotation and transformation. This is discussed further in the following sections.

The captured blade profiles can be rotated or transformed about the blade longitudinal axis indicated as dotted lines in Figure 48. This coordinate transformation from an initially pure out-of-plane shape variation to shape variations in the xy-plane will ensure that in-plane geometric modes components (\vec{X}_1^{new} and \vec{X}_2^{new}) are directly influenced by the response as well. In turn, this will allow for easier detection of the shape variation resulting from the blade response. This transformation is illustrated in Figure 49.

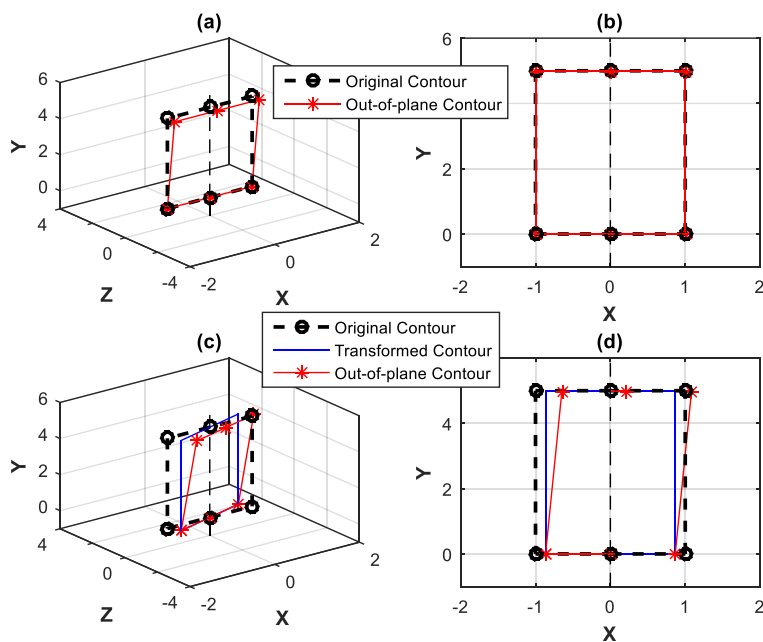


Figure 49: Shape transformation illustration

For an arbitrarily chosen rectangular original contour, Figure 49(a) shows the contour's out-of-plane (z-axis) deflection (30°), resembling a typical blade response. Figure 49(b) is the xy-plane view of the same figure, which shows that the out-of-plane contour does not reflect any in-plane shape variation for geometric modes V_1 and V_2 to be influenced. On the other hand, consider Figure 49(c), where the original contour is first transformed by a 5° rotation about the longitudinal axis before the 30° deflection is imposed. Figure 49(d) which shows the same figure viewed in the xy-plane clearly shows how the exact same deflection imposed in Figure

49(a) is now very apparent in terms of in-plane shape variation. This makes it possible to use $SPCD_1$ and $SPCD_2$ for dynamic characterization through shape analysis in this case. The contour transformation can be achieved by using the rotation matrix given in Equation 29, for transformation of contour point (x, y, z) into new coordinates $(x_{new}, y_{new}, z_{new})$ by ε angular rotation about the longitudinal y-axis.

$$\begin{bmatrix} x_{new} \\ y_{new} \\ z_{new} \end{bmatrix} = \begin{bmatrix} \cos(\varepsilon) & 0 & \sin(\varepsilon) \\ 0 & 1 & 0 \\ -\sin(\varepsilon) & 0 & \cos(\varepsilon) \end{bmatrix} \begin{bmatrix} x \\ y \\ z \end{bmatrix} \quad (29)$$

This is illustrated in the analysis presented in the following section of this chapter, where an FE based investigation to determine the applicability of the proposed approach is conducted.

4.4 FE based numerical investigation of blade shape analysis behaviour

FE based numerical studies offer a reliable controlled environment in which uncertainties and possible measurement errors can be eliminated. The FE model employed for this investigation was developed based on the experimental setup (five 2 mm thick, 40 mm width and 112 mm long blades) introduced later in Section 4.5. To reduce the size of the model and minimize the computational requirements, only the blades were considered in the analysis. Since only the behavioural trends and no direct correlation between the FE model and experimental set up were going to be investigated in this study, modal updating was therefore not conducted.

Illustrated in Figure 50 are the single blade and bladed disk models. In some of the blades, slot damage located close to the blade roots (110 mm from the blade tips) was introduced. 6 mm and 12 mm slot lengths from the edge of the blade were considered.

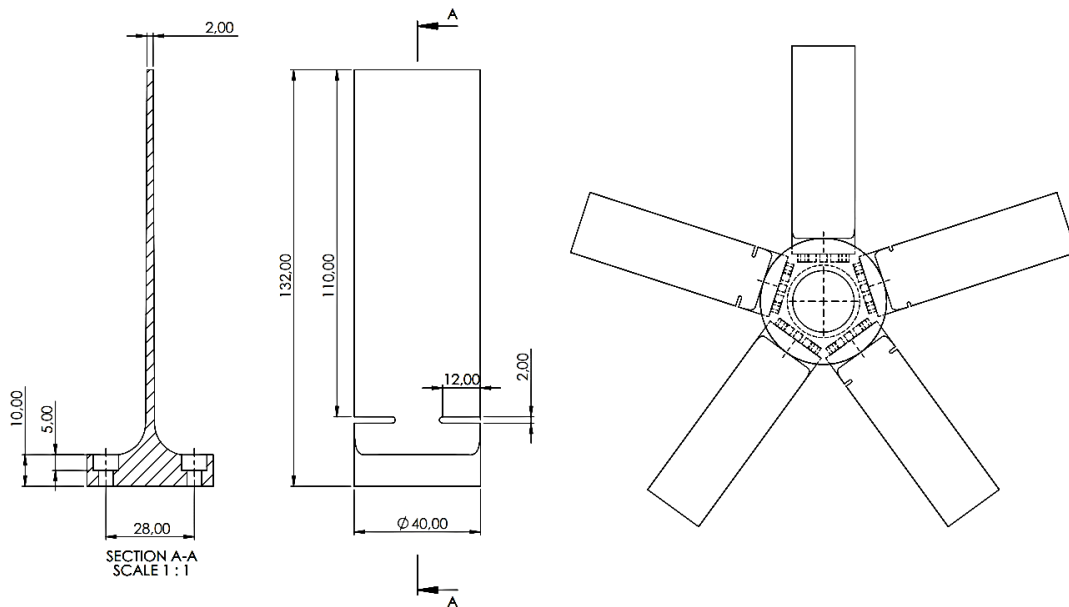


Figure 50: Single blade and bladed disk models

For the FEA, generic aluminium alloy material properties were used. These are given in Table 7. Tet 10 elements were used to mesh the models in MSC/Patran. The curved nature at the blade roots and the damage slots make the blade geometry somewhat complex, implying that meshing using tetrahedral elements instead of hexahedral elements is more ideal. Whilst

hexahedral elements are generally quicker to solve when using MSC/Nastran, the geometrical model modification to make an imported parasolid compatible to meshing with hexahedral elements can be tedious and time consuming in itself.

Table 7: Aluminium material properties

Property	Density	Young's modulus	Poisson's ratio
Value	2770 kg/m ³	70 GPa	0.33

The following sections outline the different numerical investigations conducted.

4.4.1 Model simplification

To reduce the size of the model and minimize the computational requirements, only the blades were considered in the analysis. The hub onto which the blades are attached was neglected and a multipoint constraint (MPC) boundary condition used to connect the roots of all the blades to an added central node. For the MPC, rigid body elements (RBE2 type) were considered, with the central node defined as the master, and all the nodes at the roots of each blade as slaves. This is illustrated in Figure 51. Modelling the system in this manner, instead of simply grounding the blades individually, ensures that the coupling effect expected as the response of one blade influences the dynamic behaviour of the other blades is conserved.

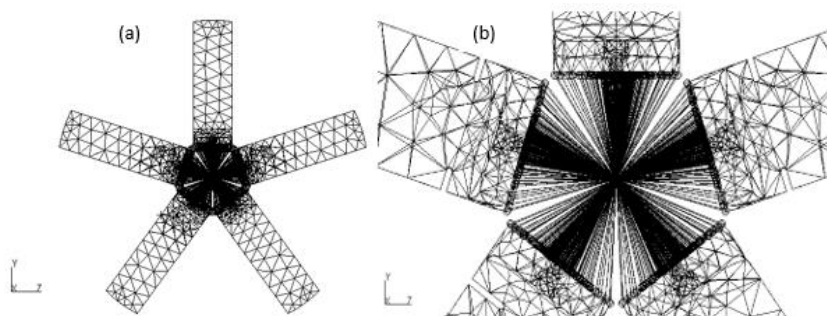


Figure 51: Multipoint constraint definition

To test the validity of replacing the hub with an MPC in terms of preserving the global dynamic behaviour of the system, a frequency response analysis was conducted. With a translationally constrained master node, a single point load was applied to a node on one of the blades for a system comprising of healthy and root damaged blades. Two systems were analysed, the first one consisting of five healthy blades, and the second one with blades arranged in a clockwise order of healthy, 6 mm damaged, healthy, 12 mm damaged and 6 mm damaged. Frequencies were linearly defined for the range 0-1000 Hz, and no damping was specified in the analysis. Figure 52 illustrates the setup for this analysis.

Frequency Response Functions (FRFs) of the system shown in Figure 53(a) illustrate that the healthy blades all respond in a similar manner. Comparing Figure 53(a) to Figure 53(b), it can be noted that the frequency responses of the system change when damaged blades are introduced in the system, confirming that the system global dynamic effects are conserved with the MPC.

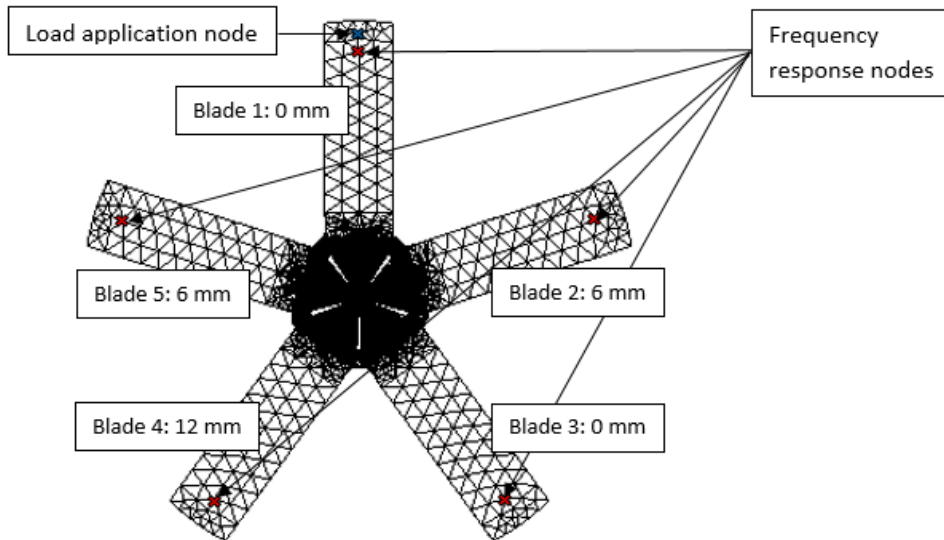


Figure 52: Frequency response analysis setup

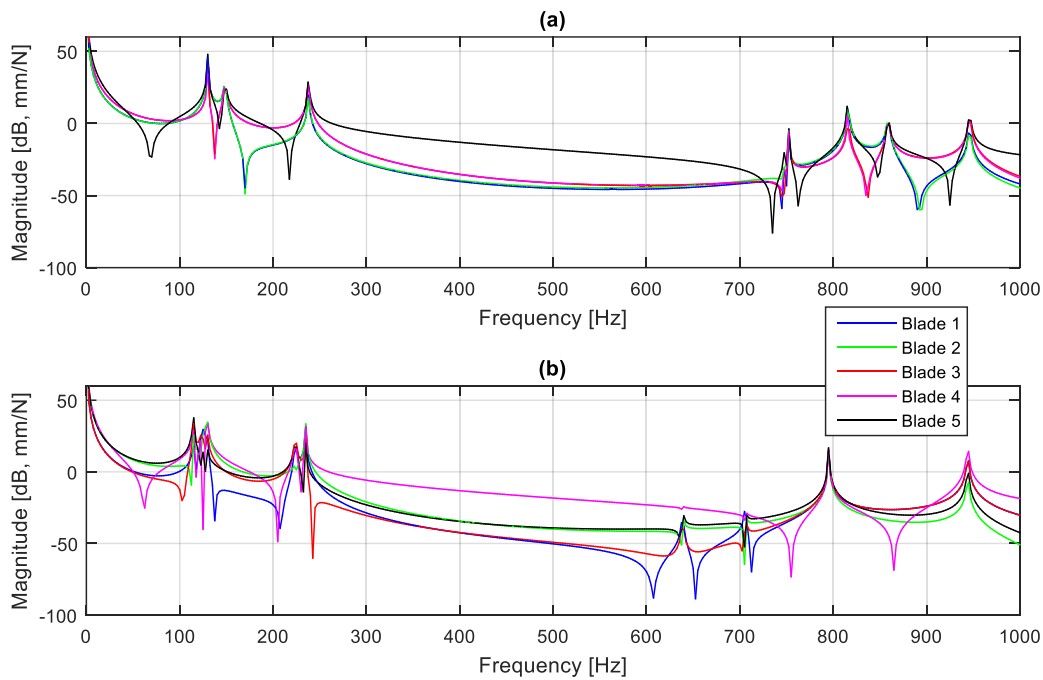


Figure 53: System FRFs (a) healthy blades, (b) combination of healthy and damaged blades

4.4.2 Natural modal analysis of the blades

The static natural frequencies of blades fixed at the root were determined for four damage levels (blade root slot depths of 2 mm, 4 mm, 6 mm and 8 mm). The expected blade dynamic responses in the investigations conducted are essentially similar to the first bending modes (out-of-plane dynamic responses of axial blades), and therefore attention was paid to the first three natural frequencies. The obtained results for the blades are presented in Table 8. As can be observed in Figure 54, the natural frequencies decrease with increasing damage, owing to the decreasing blade root stiffness.

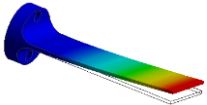
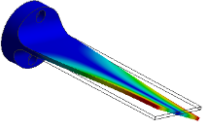
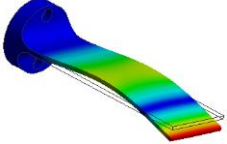
For the full bladed system, the first five modes are essentially bending modes associated with the five blades. The natural frequencies for these modes vary according to the level of damage in the blades. Illustrated in Figure 55 is a typical mode shape for a system with four healthy blades and a single damaged blade. The hub onto which the blades are attached has been replaced by a single centroid node constrained in all translational and rotational degrees of freedom. As highlighted earlier, this is done to limit the size of the model and reduce the required computational time.

In the following discussions, a case presented as H-H-H-H-H consists of five healthy blades, whereas H-6-H-12-6 refers to a system with blades arranged as illustrated in Table 9.

Considering healthy blades, the bending natural frequency for a full system with multiple blades was determined to be 129.5 Hz, which is slightly higher than the individual blade natural frequency (127.5 Hz, from Table 8). A system of multiple blades connected to a central node via a multipoint constraint boundary condition is slightly more rigid than a standalone blade grounded at its root, as expected.

Whilst an increase in natural frequencies is expected for blades undergoing a rotation as a result of rotational stiffening, these stiffening effects were not investigated as they are expected to affect the responses of all the blades in a very similar way. This means that they were not going to influence the captured results in a way that necessarily influence the monitored and presented trends in the findings.

Table 8: Single blade mode shapes and natural frequencies for different damage levels

Mode	Healthy blade	Damage 1 (2 mm slot)	Damage 2 (4 mm slot)	Damage 3 (6 mm slot)	Damage 4 (8 mm slot)
First bending mode 	127.531 Hz	125.777 Hz	123.608 Hz	120.559 Hz	116.748 Hz
First torsional mode 	733.326 Hz	724.327 Hz	712.405 Hz	696.698 Hz	676.870 Hz
Second bending mode 	793.674 Hz	784.482 Hz	774.292 Hz	761.284 Hz	746.070 Hz

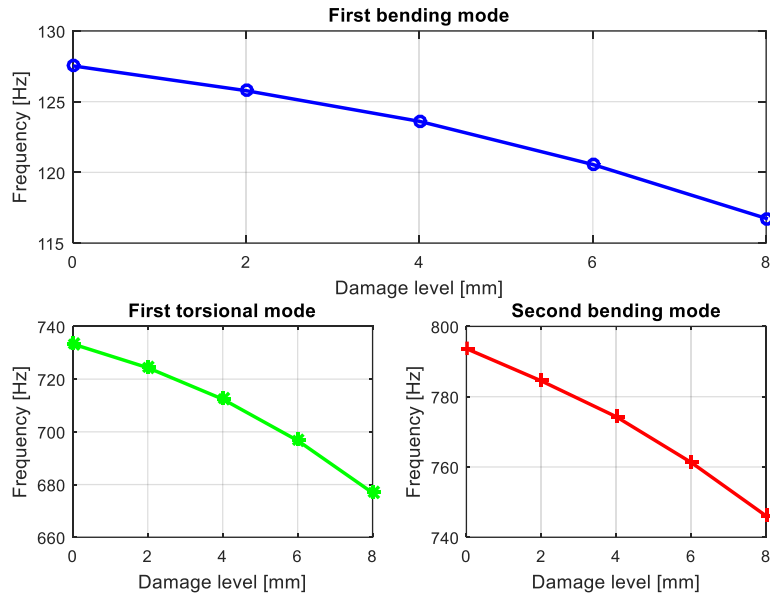


Figure 54: Variation of natural frequency with root damage level

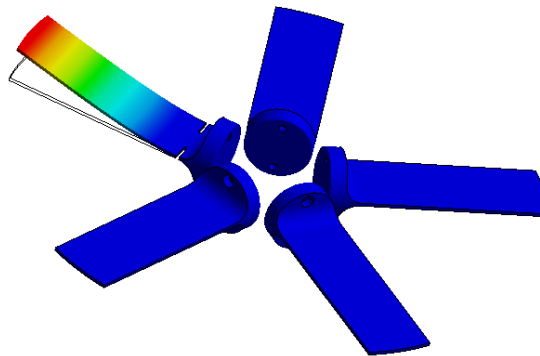


Figure 55: Typical mode shape for a system with four healthy blades and a single damaged blade

Table 9: Rotor system clockwise blade arrangement

Case	Blade 1	Blade 2	Blade 3	Blade 4	Blade 5
1: H-H-H-H-H	Healthy	Healthy	Healthy	Healthy	Healthy
2: H-2-H-H-H	Healthy	2 mm damage	Healthy	Healthy	Healthy
3: H-4-H-H-H	Healthy	4 mm damage	Healthy	Healthy	Healthy
6: H-6-H-12-6	Healthy	6 mm damage	Healthy	12 mm damage	6 mm damage

4.4.3 FEA shape based dynamic analysis

The FE model considered is based on a physical system consisting of blades being excited using two air nozzles positioned 180° apart (Figure 78). The blades are thus exposed to an impulse form pressure load excitation with a frequency twice the set rotational speed. For a

bladed system with five equally spaced blades, a phase difference of 36° exists between the excitations of consecutive blades.

The FE investigation is aimed at analysing the behavioural trends in differently damaged blades. A basic model and excitation approach was considered in the investigation. The dynamic response behaviour of a system rotating at a particular speed, with the blades undergoing periodic excitations, was approximated by imposing an out-of-plane displacement excitation to the added central node. It should be emphasized that whilst this type of excitation is not identical to a physical rotating system operational excitation, the expected bending mode out-of-plane responses the blades exhibit, are still dependent on the nature of blade damage modes in any case. With the out-of-plane responses still directly influenced by the type of damage at the root in the simplified FE model excitation, the only neglected effects are those associated with rotational stiffening. Unlike the type of excitation in which a pulsating pressure load is applied directly to the actual blade surfaces, the considered excitation also ensures that direct interference of the excitation with the blade shape response is avoided. As highlighted earlier on in the chapter, the FE investigation is aimed at analysing the behavioural trends in differently damaged blades, without necessarily directly correlating a physical system to a modally-updated FE model. Thus for purposes of developing and testing the applicability of the proposed condition monitoring approach in a simplified manner, this imposed type of system excitation was considered acceptable.

Imposing an excitation frequency in the range of the system's first bending natural frequencies to the central node means that the blades are expected to respond in a manner corresponding to a resonating first bending mode. The first five natural frequencies of a system with five healthy blades were determined to be in the range [129.326 – 129.496] Hz. Therefore a sinusoidal displacement excitation with a frequency of 129.5 Hz was applied to the central node, to limit the blade vibration responses to the first bending mode.

For this investigation, MSC/Nastran SOL 109 (transient response analysis) was employed. Two thousand time-steps with a time increment of 0.001 s were considered, and xyz-coordinates describing the various blade profiles extracted for 3D shape analysis. Only the boundary nodal points on the face of each blade were considered, as illustrated in Figure 56 for the maximum deflection of a set of healthy blades.

4.4.3.1 Blade tip response analysis

Maximum deflection time domain responses for the five blades are illustrated in Figure 57. For Case 1 where all the blades are identical, the responses are identical as expected. In terms of Cases 2 to 5, the damaged blade clearly shows a response significantly different from that observed for the healthy blades. For Case 6, the two healthy blades show similar behaviour, and the same can be noted for the blades with 6 mm slot damage.

From Figure 57, it can also be observed that interference between two signals whose frequencies are slightly different exists. The low frequency periodic variation in the response magnitudes points to the presence of signal beating. In addition to that, response magnitudes tend to be decreasing with increasing damage size, which contradicts with what one would normally expect in the case of blades whose root stiffness values are decreasing. To investigate these observations, the data was analysed in the frequency domain.

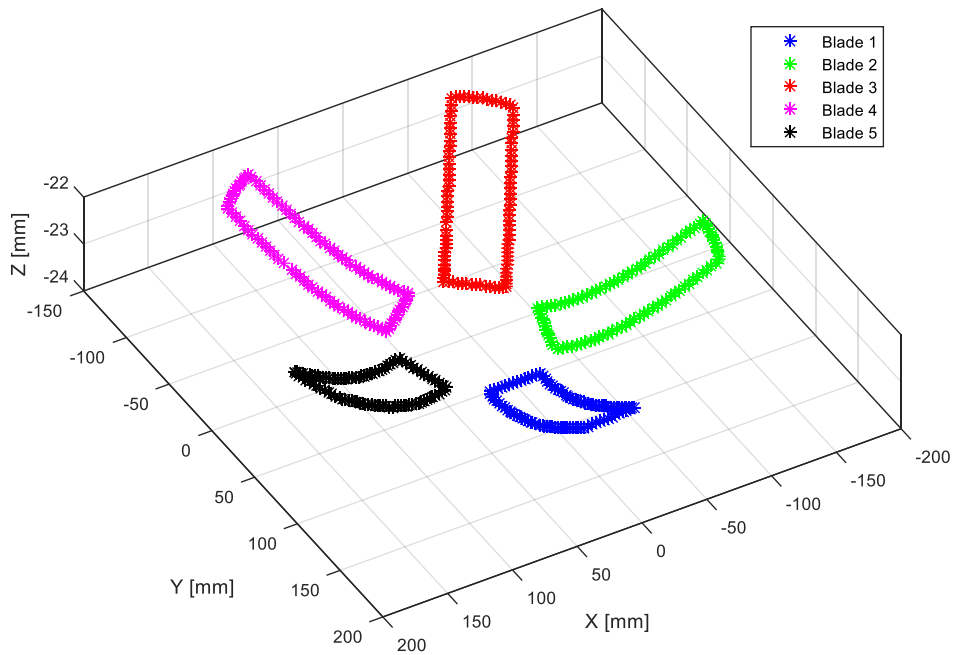


Figure 56: FEA blade shape profiles illustration

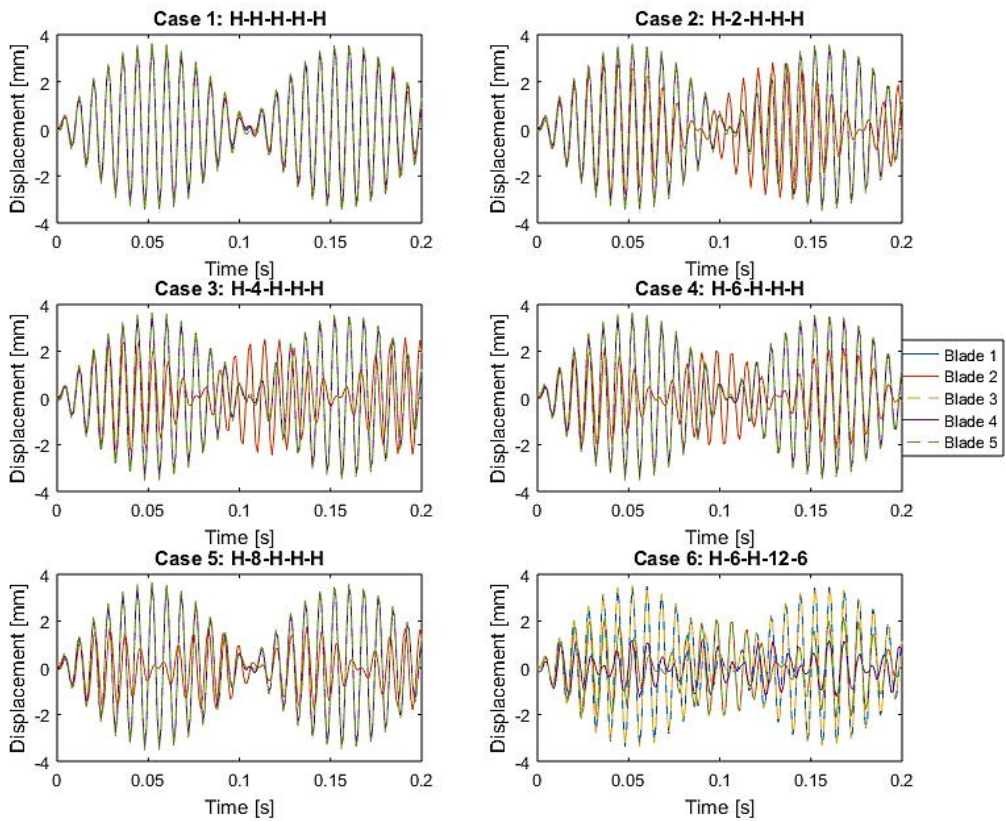


Figure 57: Maximum deflection time domain responses for different blade combinations

Figure 58 illustrates responses in the frequency domain for each of the six cases. For better visualisation, Figure 59 has also been included to show the responses of the blades individually.

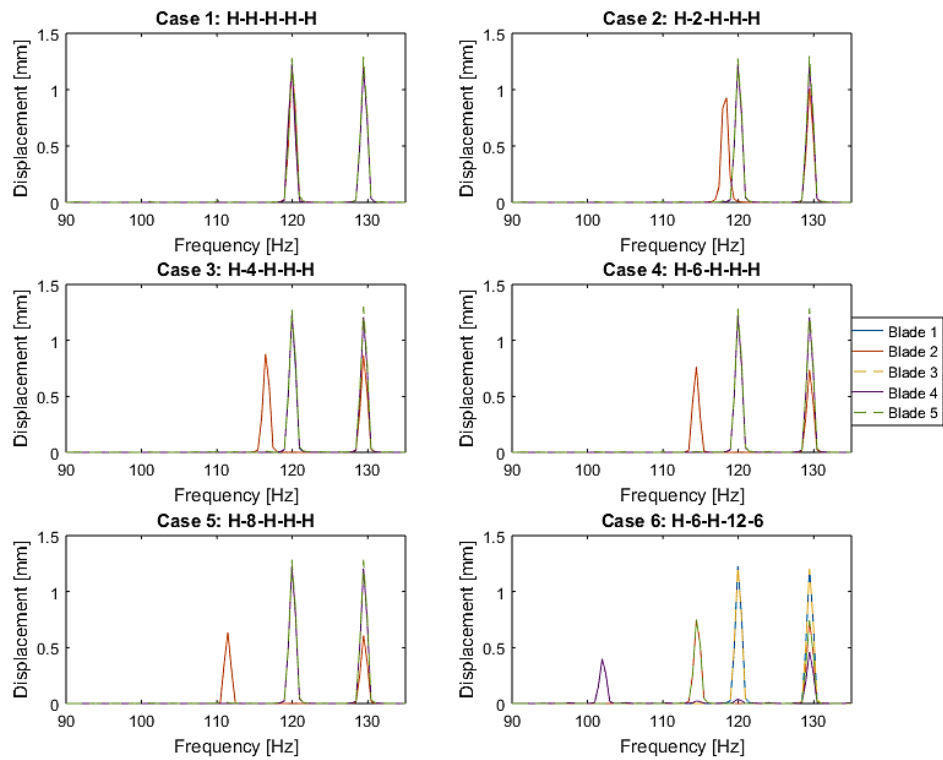


Figure 58: Tip deflection frequency domain responses for different blade combinations

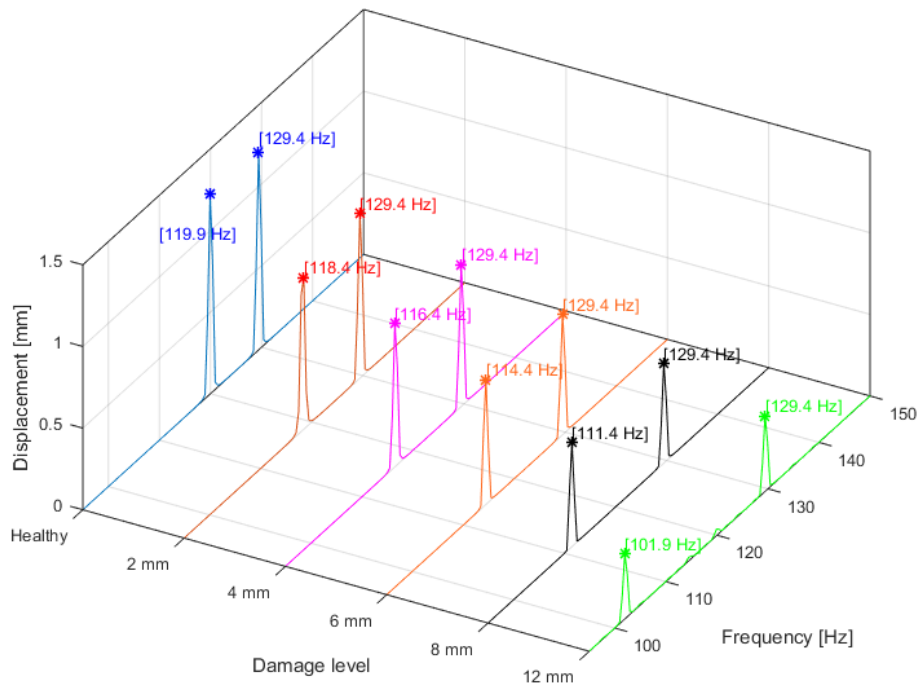


Figure 59: Rotor responses variation for different levels of damage in blade 2

From Figure 58 and Figure 59, a frequency component of 129.4 Hz can be observed. This corresponds to the 129.5 Hz excitation frequency imposed on the centroid node. With this excitation frequency being close to the blade natural frequencies, and the blades' behaviour being very similar to lightly damped cantilever beams, a second component is observed at a frequency less than the natural frequency values. As this second response frequency is close to the excitation frequency, a beating phenomenon is therefore apparent in the time domain measurements presented in Figure 57.

As the damage levels increase for the blades, the individual blade natural frequencies are further away from the excitation frequency, implying that with every damage increment the blades are operating further away from resonance. In this particular case, the magnitudes of response actually decrease regardless of the blades being more flexible at the roots.

4.4.3.2 Blade SPCDs analysis

SPCDs were determined as outlined in Section 4.2 for the blades with different damage modes. A frequency domain analysis of the shape descriptors was conducted, and given in Figure 60 are results for a system with four healthy blades and a 2 mm slotted blade.

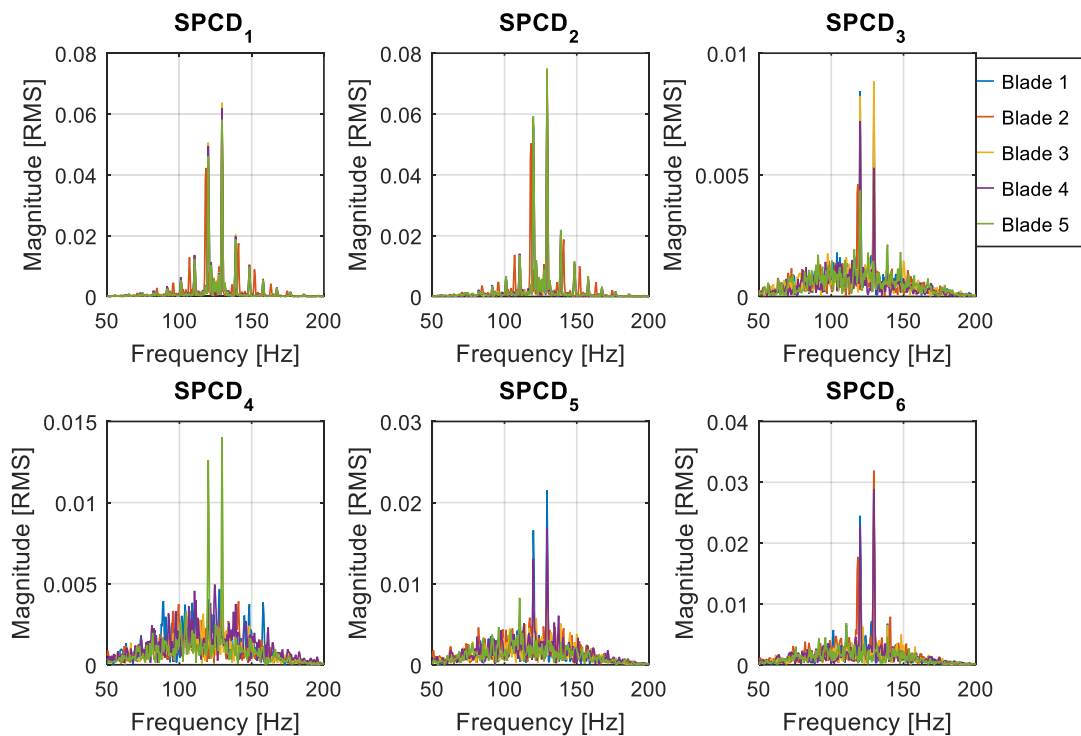


Figure 60: Case 2 SPCDs FFTs

SPCD₅ and SPCD₆ are comprised of the out-of-plane responses, as explained in Section 4.3 and Figure 48. From the results presented in Figure 60, SPCD₅ and SPCD₆ measurements in the frequency domain do not provide sufficient information to isolate the different blades with respect to damage mode. The in-plane related shape varying SPCDs (SPCD₁ and SPCD₂) can be noticed to have higher magnitudes compared to the local shape varying SPCDs. This can be attributed to the fact that similar to in-plane geometric modes that affect the rectangularity of the shape, the out-of-plane responses are essentially shape rectangularity related. The transformation described in Section 4.3 that involves rotation of blades about their

individual longitudinal axes to align responses with specific geometric modes can be employed to improve the quality of the results. Figure 61 shows the frequency domain measurements of Figure 60 transformed in this manner. The measurements are clearly less noisy for the in-plane SPCDs, and for this particular case, the slight shift in the damaged blade (blade 2) frequency peaks for SPCD₁ can be observed. As expected, the amplitudes of the SPCDs also change as the modified response-based shape variations now affect the original shape defining principal component scores differently.

In an FEA setting, the coordinate transformation can be easily implemented. For the following investigation on classification, this transformation was conducted and SPCD₁ measurements were considered. Further discussions on the coordinate transformation are presented in Section 4.4.3.4.

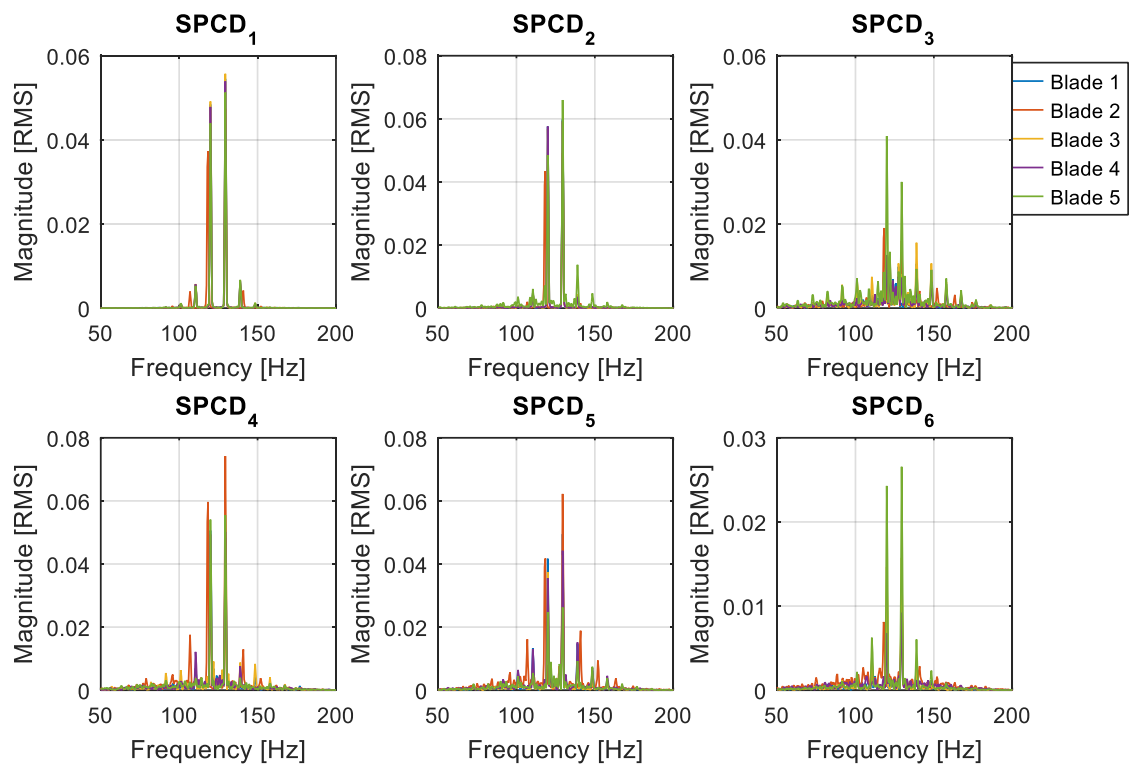


Figure 61: Case 2 SPCDs FFTs for 5° rotated blades

4.4.3.3 Clustering technique for blade classification

For condition monitoring purposes, a clear visually expressive representation of the results is usually desirable. This allows for easier identification of different damage modes, and is especially beneficial for online monitoring applications where the information is required for quick machine diagnosis.

One viable way to accomplish this will be through a data reduction coupled with data projection approach, conducted to implement a variable-based clustering of calculated SPCDs. The SPCDs calculated are temporal parameters composed of information that is dependent on the way response-based shape variations influence specific geometric modes. This means that applying a data reduction approach that defines additional dimensional parameters presents an opportunity for visually grouping or clustering SPCDs, based on any detected coherent patterns. Thus different SPCDs captured for different blades in a system can be distinguished

based on the behaviour of the blades. This can be accomplished through PCA applied as a data reduction tool to a time series data set.

In the investigation conducted earlier on shape principal component analysis, PCA was being applied to a multivariate system of parameters (Fourier coefficients X) descriptive of the shape geometric characteristics. Different to establishing various shape variations associated with parameters in the multivariate system describing the shape, PCA as a data reduction tool focuses on truncating the original data X (which will now be the determined SPCDs in this case) by only keeping a few of the first principal components (X^{new} columns). Since the maximum variance in a data set is captured by these first few principal components, one can plot them against each other in the commonly termed principal component diagrams (PC 1 vs PC 2 or PC 1 vs PC 2 vs PC 3) to create clusters that can be used to ultimately assess similarities in blade responses.

In the case of blade classification using computed SPCDs presented in Figure 61, each SPCD is a univariate time series that will therefore only give a single cluster point for each blade on a principal component diagram. When using principal component diagrams to classify data, clusters consisting of multiple points are usually considered. Multiple points for each blade on the diagram not only result in effective visualization of clusters but contribute to a deeper and enhanced accurate understanding of the data in terms of detecting subtler patterns or structures of the clusters. The stability and robustness of clusters with regards to influence from outliers and fluctuations in the data can also be accurately assessed. This accurate assessment extends to the shape, density and spread of the clusters within the principal component diagram as well. To take advantage of a multiple point cluster analysis, the univariate SPCD time series must therefore be transformed into either a single multivariate series or a set of multiple univariate series. Transforming SPCD₁ for instance into multiple univariate series can be done by cutting the time domain signal into multiple shorter signals before computing the FFTs to which PCA for clustering is ultimately applied.

It is worth highlighting that the FFTs of short duration signals have poor frequency resolution, something which can make it difficult to distinguish between frequency components that are very close to each other. If the signals are too short, clustering results obtained by PCA data reduction of FFTs calculated for these short duration signals might not be able to accurately capture SPCDs response properties. This will in turn result in inaccurate blade damage mode classification using clustering. A compromise must therefore be made between the desired number of points in the principal component diagrams (the more points the clearer the clustering) and the acceptable duration of the signal considered for accurate FFT calculations (shorter signals have a diminished frequency resolution).

To investigate this for a signal that has been cut into several segments, FFTs of the originally 2 s long and 1000 Hz sampled signal were considered. Blade 1 SPCD₁ time response signal was segmented accordingly to analyse four different scenarios – one segment or full-length response, ten segments, twenty segments and forty segments response. In this case, a full-length signal corresponds to the 2 s long signal, and ten segments correspond to ten 0.2 s long segments of the original signal. Illustrated in Figure 62 are FFTs of the first segment of each scenario. Whilst the diminished frequency resolution can be noted for the segmented signals, it can be observed that 0.2 s long signals (10-segmented signal) can still capture the two frequency peaks characteristic of the original signal in the linear scaled plot (Figure 62(a)). The dB scaled plot (Figure 62(b)) is also included to better highlight the differences in the data.

Illustrated in Figure 63 are SPCD₁ principal component diagrams for Case 2, in which clustering was considered for different number of segments for all five blades. For this specific case, it can be observed from Figure 63 that a chosen set of ten segments can clearly capture the differences in SPCD₁ for different blades without the effect of segmenting the signal into shorter samples completely distorting the data. The effect of significantly diminished frequency resolution on clustering performance is evident in the twenty and forty segments' results.

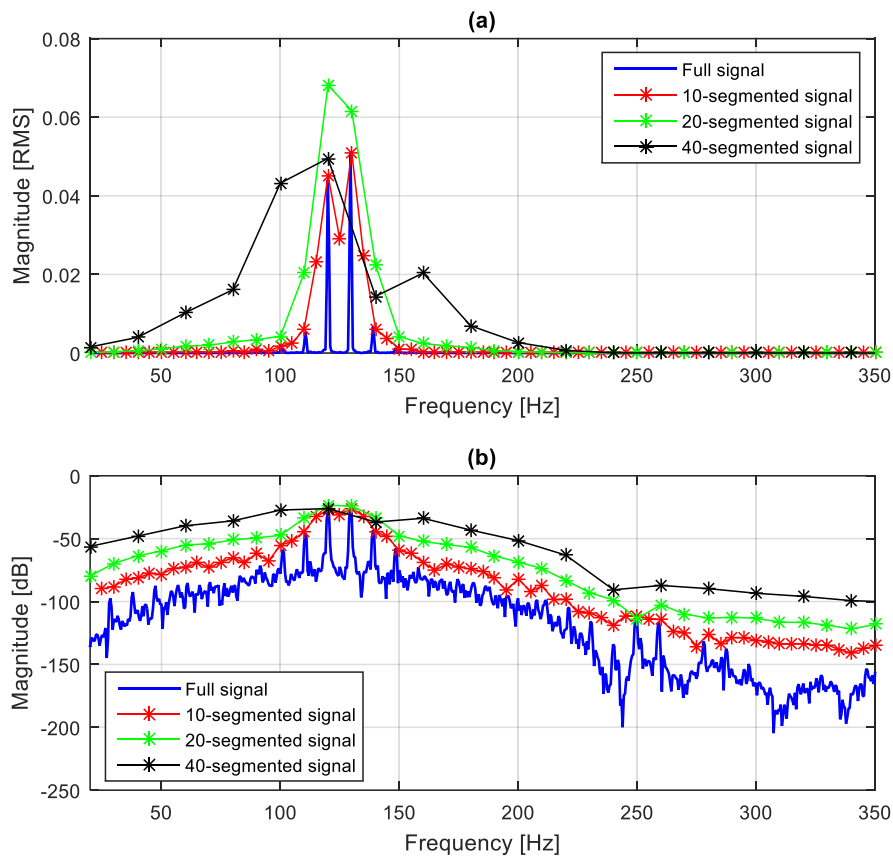


Figure 62: Effect of signal segmentation - 5° rotated blade 1 SPCD₁ FFTs, (a) linear scale, (b) dB scale

It can be observed that for a set of ten segments, the damaged blade (blade 2) is well separated from the healthy blades. Ten segments are subsequently used henceforth for analysis of simulation-based measurements. It should be highlighted that the presented analysis was conducted as a preliminary investigation during the development of the shape analysis-based condition monitoring technique. The viability of a clustering-based classification technique using 0.2 s long signals was done specifically for the simulation-based investigation. Further studies to establish the optimum frequency resolution for the highest quality of clustering can be considered in future work.

Focusing on Figure 63(b), it can be observed that cluster points of the same blade lie in the same vicinity on the principal component diagram, with recognisable within-cluster variations (points for the ten segments are not coincident). This is expected as the periodic variation in amplitude due to the beating effect observed in Figure 57 mean that segmented signals are not identical. This translates to slightly different signal PCA based properties. Regardless,

clusters of segments for differently damaged blades can still be clearly isolated using the proposed approach.

To quantitatively identify the location of the clusters, the distance R of a cluster centroid from the origin can be considered. Figure 64 illustrates these distances.

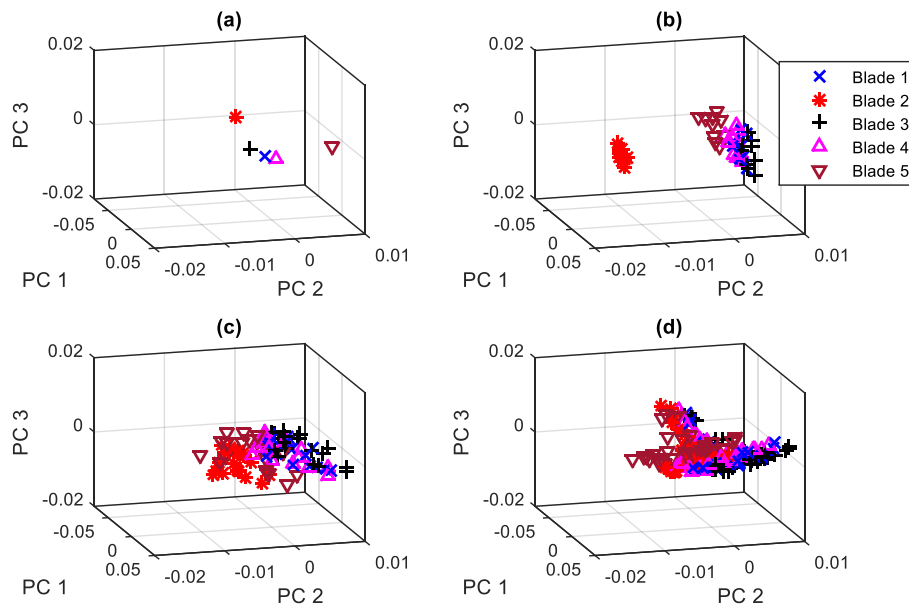


Figure 63: Case 2 SPCD₁ projected in a 3D feature space (a) 1 segment, (b) 10 segments, (c) 20 segments and (d) 40 segments

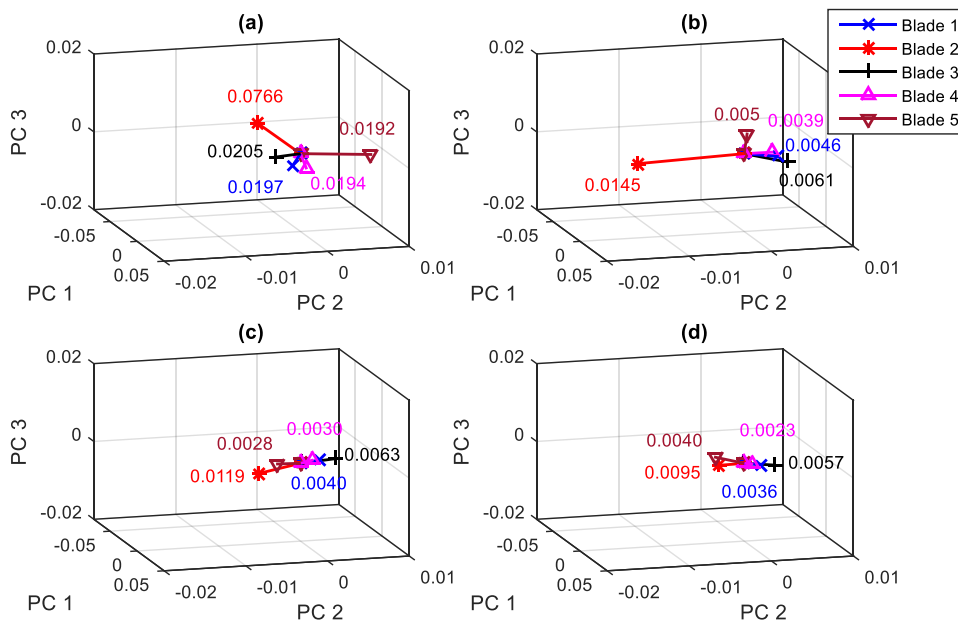


Figure 64: Cluster centroid distances from origin for Case 2 SPCD₁ projected in a 3D feature space (a) 1 segment, (b) 10 segments, (c) 20 segments and (d) 40 segments

4.4.3.4 Sensitivity testing and effects of shape coordinate transformation

As highlighted, geometric modes 5 and 6 are associated with the out-of-plane shape variations. This means that for a blade vibrating out-of-plane, $SPCD_5$ and $SPCD_6$ are the ones directly influenced by the response shape variations. However, \vec{V}_5 and \vec{V}_6 variations are local in nature (blade smoothness), different from the out-of-plane global-natured response shape variation. Thus the sensitivity of $SPCD_5$ and $SPCD_6$ to the expected responses is consequently low, especially for small amplitude responses. To investigate this further, clusters for $SPCD_5$ and $SPCD_6$ were plotted for different scaling factors of the out-of-plane responses. For a system with four healthy blades and a 2 mm damaged blade, Figure 65 illustrates the obtained clustering results.

For this particular system with response amplitudes of about 4 mm, it can be observed from Figure 65 that out-of-plane responses need to be more than 8 mm for the damaged blade to be clearly distinguished from the healthy blades. For purposes of quantitatively visualising the locations of the clusters, Figure 66 illustrating the cluster centroid distances from the origin has been included.

In cases where the out-of-plane SPCDs cannot capture different blade behaviour, one can alternatively transform the blade profiles by rotating them about their longitudinal axes to allow the response to influence other shape variations, as highlighted in Sections 4.3 and 4.4.3.2. The effect of coordinate transformation on the SPCDs is illustrated in Figure 67, and the cluster locations in terms of the centroid distance from the origin given in Figure 68. As can be observed, transformation of blade profiles results in clearly distinctive calculated $SPCD_1$ clusters.

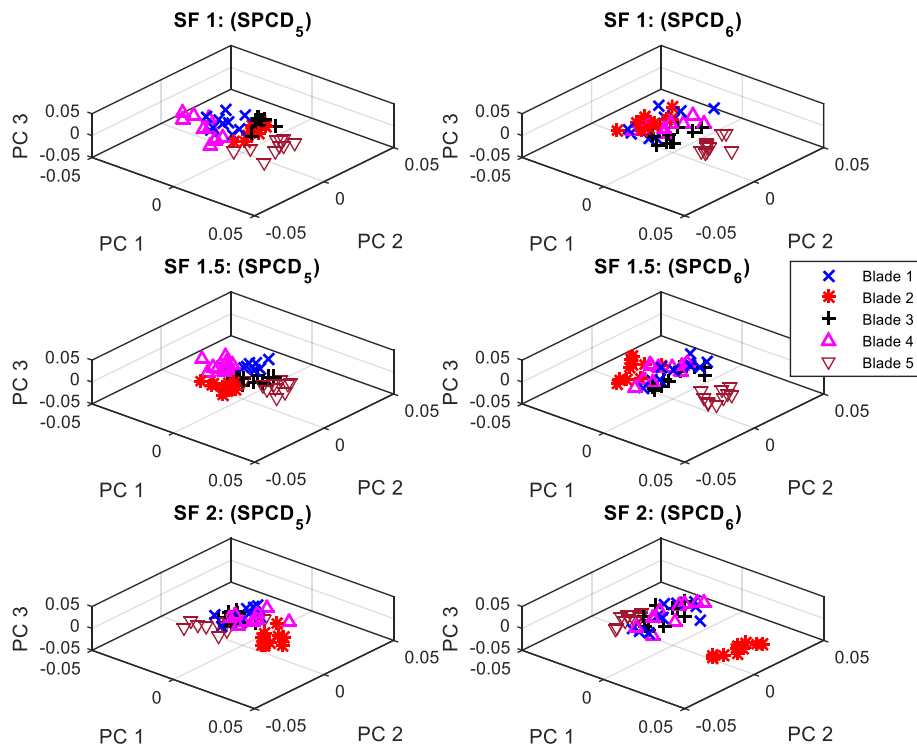


Figure 65: Sensitivity of $SPCD_5$ and $SPCD_6$ with respect to response amplitude

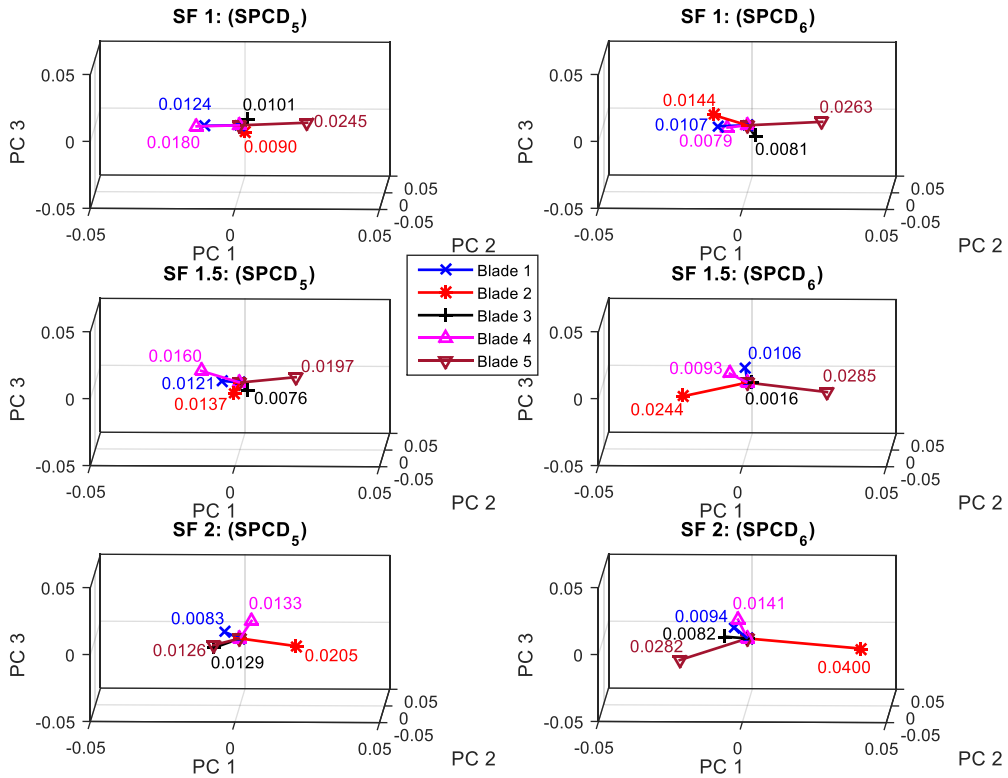


Figure 66: Cluster centroid distances - Sensitivity of SPCD₅ and SPCD₆ with respect to response amplitude

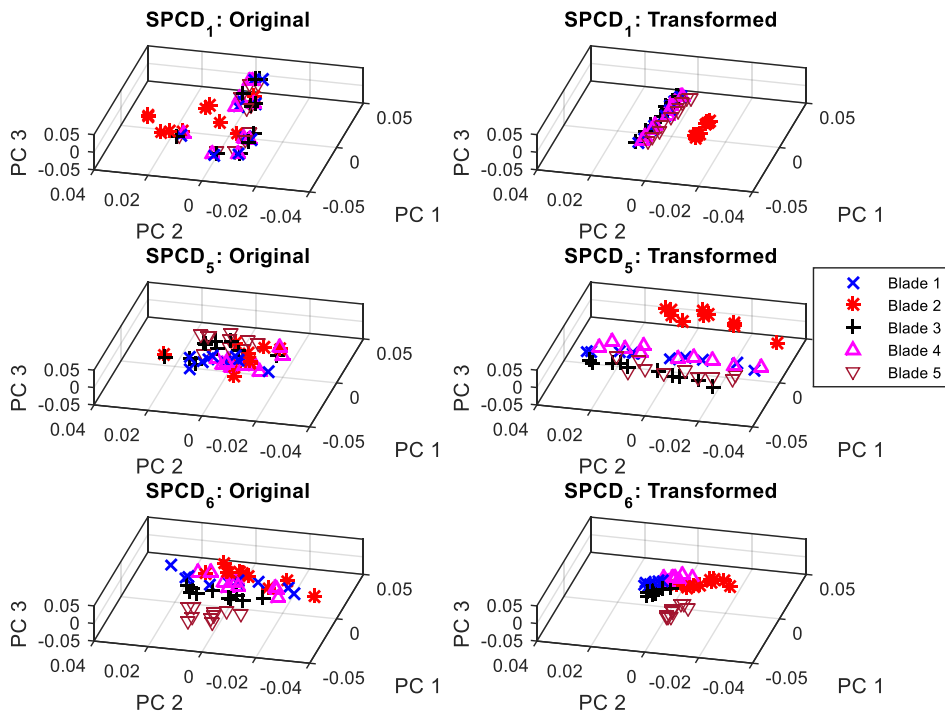


Figure 67: Effect of shape coordinate transformation on clustering classification

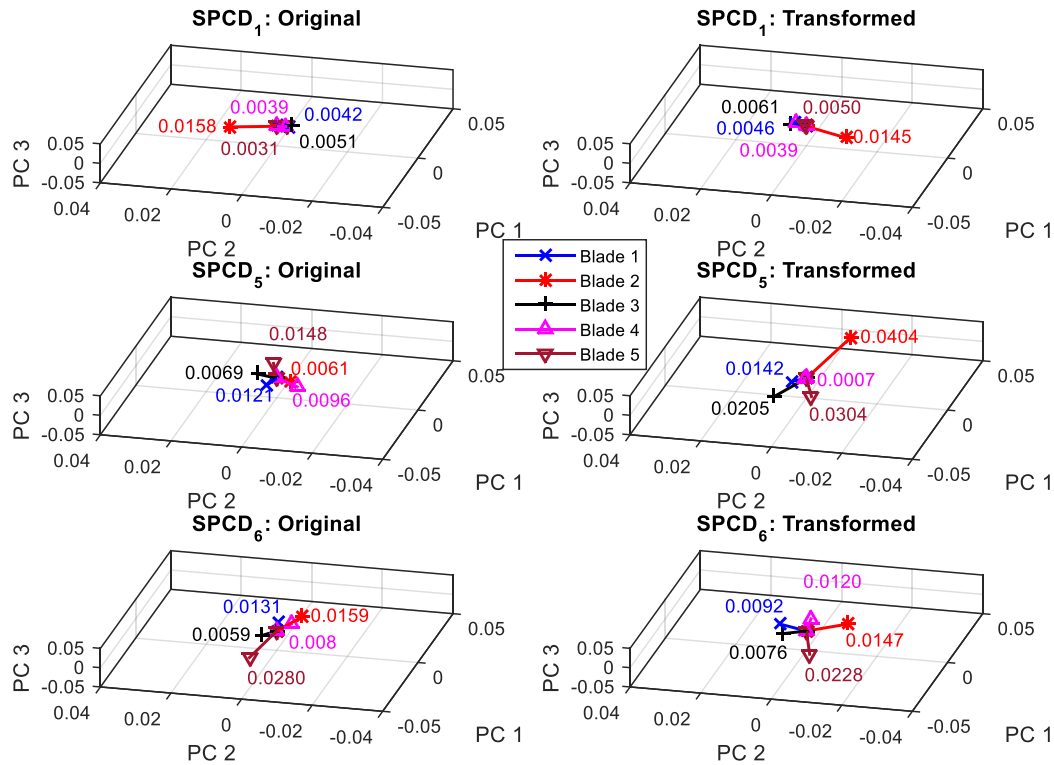


Figure 68: Cluster centroid distances from the origin - Effect of shape coordinate transformation on clustering classification

4.4.3.5 Classification of blades with different levels of damage

For classification of blades, the first investigation conducted was to test cluster inter-variability for blades that nominally have the same fault. Figure 69 shows the cluster formation for a system that has a mixture of differently damaged blades, some of which being similar (Case 6, Table 9). As can be observed, blades of similar damage levels are clustered together, making it simple to identify blades exhibiting similar behaviour. Also illustrated in Figure 69 are the spherical coordinates of each cluster's centroid relative to the origin. These coordinates in the PC 1-2-3 space can be defined as α the counterclockwise angle in the PC 1-2 -plane, β the elevation angle from the PC 1-2 plane and the already introduced R , the distance of the cluster centroid from the origin. Considering R , the blade with the most severe damage (Blade 4, with a 12 mm slot) has its cluster furthest from the origin. The angular locations of the clusters also confirm how closely arranged blades of similar damage levels are clustered.

The trend pointing towards the deterministic nature of damaged blades response observed in Figure 69, whereby the clusters for the damaged blades are compact and different from the spread-out healthy blades' clusters, is something that will have to be further investigated in an analysis focusing on the quality of clustering for this type of system.

Investigations were then conducted to analyse how clusters of similarly arranged blades with different levels of damage appear. As can be observed from Figure 70, the damaged blades (blade 2 for each case) form a cluster separated from the healthy blades. Clusters calculated for healthy blades are located in the same vicinity, but they do not overlap point for point. As the blades respond to the excitation, the existing coupling effect contributes to the blade

dynamics not being essentially identical for similar blades. The clusters can still be clearly identified as being in the same vicinity regardless.

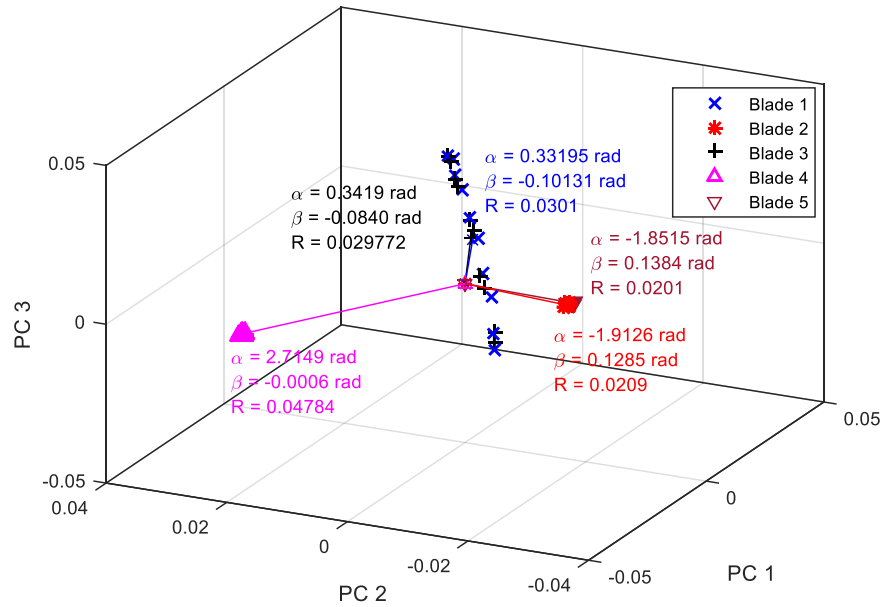


Figure 69: SPCD₁ projected in a 3D feature space for a system with two healthy blades, two 6 mm slotted blades, and a 12 mm slotted blade (H-6-H-12-6)

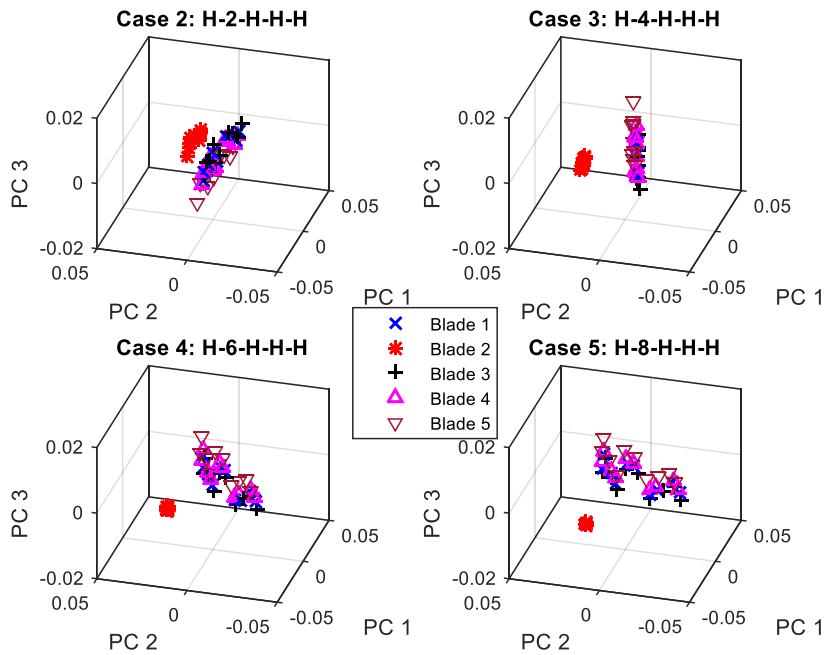


Figure 70: SPCDs projected in a 3D feature space for systems with a single damaged blade

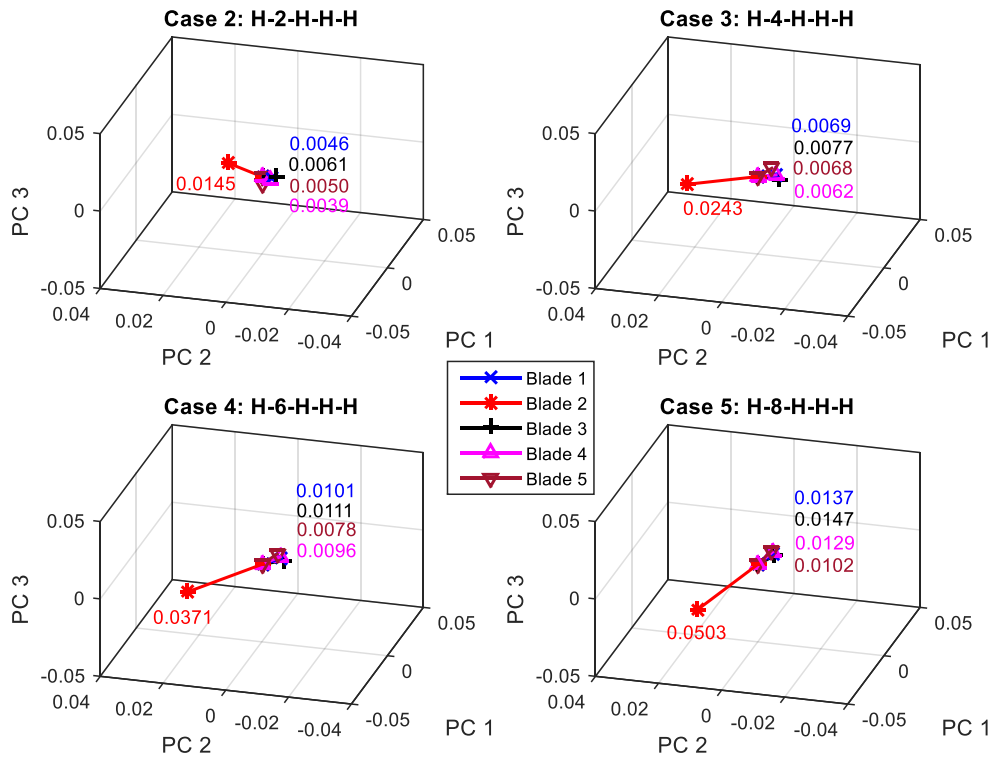


Figure 71: Cluster centroid distances to origin - SPCDs projected in a 3D feature space for systems with a single damaged blade

The damaged blade clusters can also be observed to be shifting away from the healthy blade clusters as the levels of damage increase, as highlighted by the centroid distance changing from 0.0145 for 2 mm damage level to 0.0503 for 8 mm damage level in Figure 71. This is investigated further in Section 4.4.3.6.

In Figure 72, healthy blade clusters (only one for each case) for different cases have been presented on the same plot to further test the existence of global inter-blade interactions in the analysed FEA model. 2D projections for PC 2 vs PC 3 and PC 1 vs PC 2 for the same results have been shown. It can be observed in Figure 72 (a) that the healthy blade clusters for similarly arranged blades (Cases 2 to 5) are essentially in the same location (for PC 2-3 plane) even though the systems' levels of damage are different. Case 6 with a completely different blade arrangement has its healthy blades oriented in a different manner. Figure 72 (b) illustrates that the locations of the clusters for the similarly arranged blades are actually shifted from each other when viewed in a different plane. To sum up these observations, a conclusion can be made that the interaction between blades connected by a MPC is also detectable when a clustering approach is used to classify the SPCDs.

It is worth noting that for a particular case, blades in the same state of damage are still clustered together regardless of the global dynamics of the system (Figure 69 and Figure 70). The shift in the location of healthy clusters as a result of changes in the global dynamic behaviour however highlights that in a practical setting, it might be difficult to anticipate the location of healthy or damaged blade clusters. This can be addressed through the use of supervised classification techniques, in which baseline data for training the system will have to be collected. In those cases, the approach can be implemented on the basis of monitoring

cluster deviation from a pre-captured or predefined stage in the life of a system. Simulations analysing captured response data and FE modal updated models can also be an alternative solution for identifying or classifying blades.

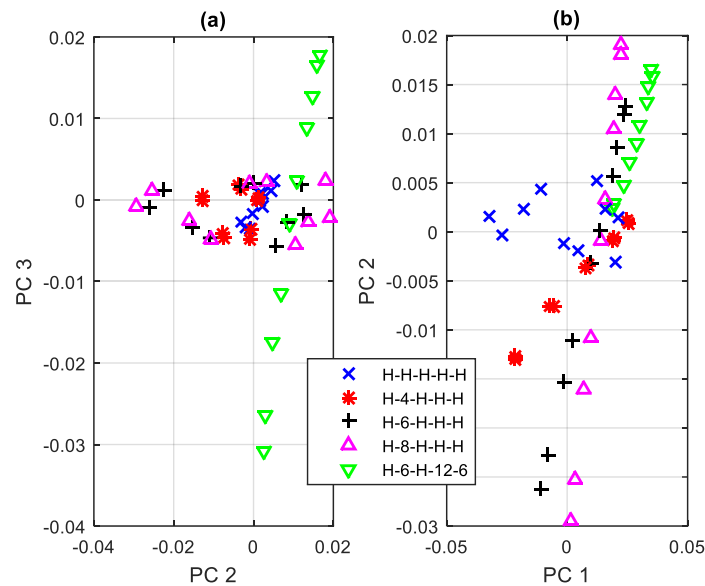


Figure 72: Inter-blade interaction dynamic effects (healthy blade, blade 1, clusters for different cases)

4.4.3.6 FEA based damage progression

In terms of the relationship between damage level and cluster location, Figure 70 showed that clusters get more separated and shift away from the healthy location as the levels of the damage of the blades they correspond to increases. This can be a useful tool for monitoring progressing damage in the blades. To complement the argument on shifting cluster location with increasing damage, Figure 73 considers the location of damaged blade clusters for all the cases presented in Figure 70. Damaged blade 2 clusters (2 mm, 4 mm, 6 mm and 8 mm) are shown on the same plot. For better visualisation, only one single healthy blade cluster for the case H-2-H-H-H is shown. This is also assumed to be the healthy state for all the damage cases considered. In this illustration, the assumption to neglect the variable inter-blade interactions is made based on the results presented in Figure 72, where the cluster centroids of similarly arranged blade cases can be noted to be reasonably close to each other. Figure 73 shows that the blade clusters are separated from the healthy blade location with increasing damage level.

Whilst it is clear that blade clusters are well separated, it is important to be able to quantitatively differentiate the blades for online condition monitoring purposes. The spherical coordinates α , β and R are considered. These coordinates can be used as indicators monitored to track the change in dynamics of blades as damage progresses.

Figure 74 shows that α and the cluster centroid distance from the origin can be used as an indication of the severity of damage in a blade. For a physical system whose finite element model has been successfully updated, simulations and investigations to identify the specific location of a cluster where system failure is expected to occur can provide crucial information necessary for predicting remaining useful life of a blade.

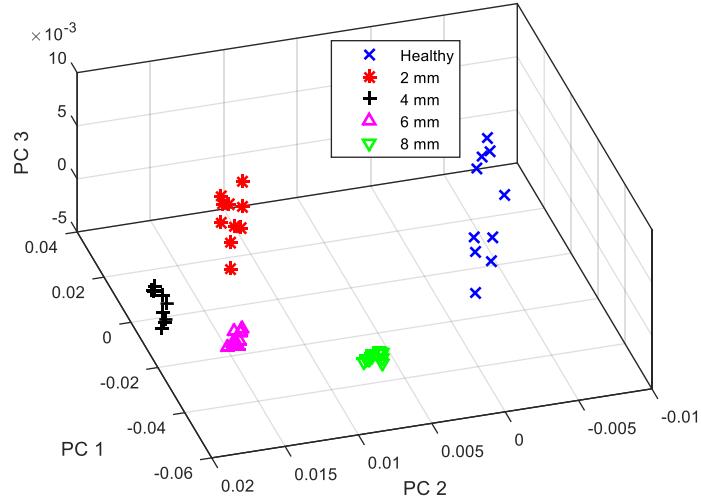


Figure 73: FEA blade 2 progressing damage illustration using SPCDs clustering

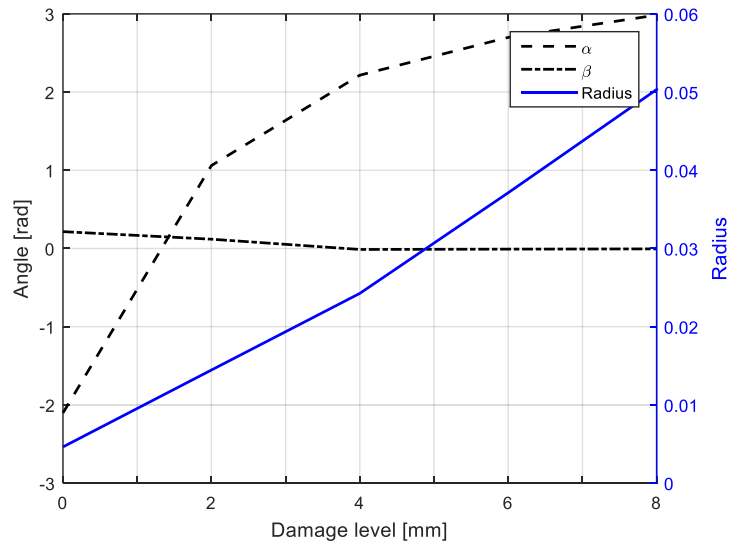


Figure 74: Monitoring blade 2 damage progression by tracking the position of clusters

In a practical setting, image sequences of the blades can be taken at regularly spaced intervals and the identifiers captured and logged for condition monitoring purposes. With numerical investigations conducted in a controlled FEA environment, an experimental study presented in the following section was then conducted to implement the shape analysis approach for a rotating physical system.

4.5 Setting up and calibrating a stereo-photography system

To be able to extract 3D shape information of a physical rotor, a pair of high-speed cameras must be employed. The cameras should be set up at a standoff distance and angle such that the entire test turbine is in the FOV of both cameras. A typical system setup is given in Figure 75.

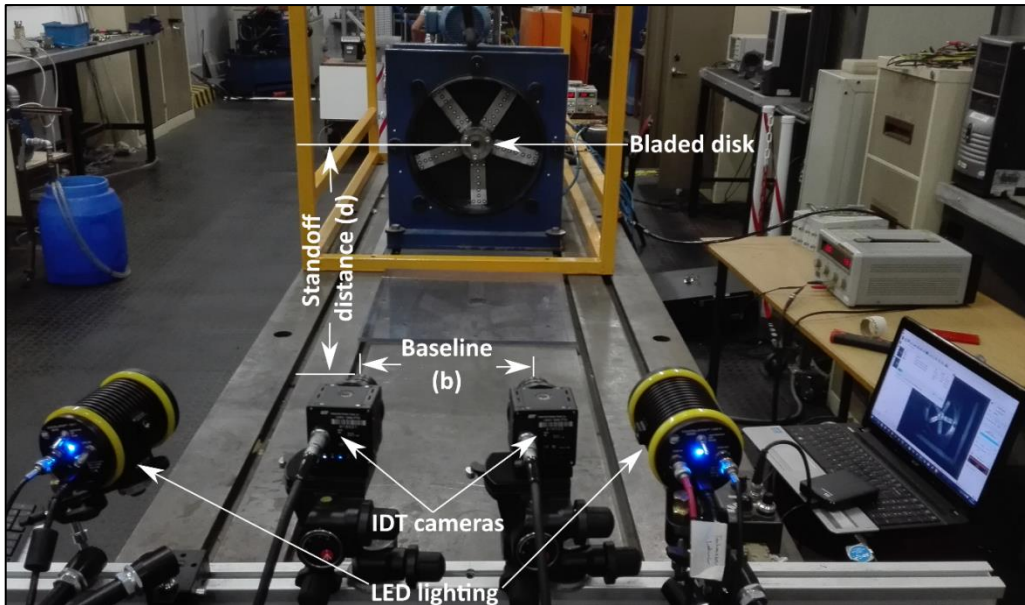


Figure 75: Stereo-photography system setup

The baseline and standoff distance must be chosen accordingly. Not only do they have to allow the test turbine to be in the FOV, but it also affects how effectively depth can be calculated from the stereo images. Generally, a shorter baseline performs better for small standoff distances and vice versa. Whilst correspondence estimation of the location of a point in the different views is easier with a small baseline, the uncertainty is greater. At the same time, a larger baseline allows more accurate depth determination, but with reduced corresponding certainty. This is important in cases where a smooth full field depth with constant depth accuracy over the entire volume must be determined.

After the cameras have been set up properly, the stereo system must be calibrated for both spatial and stereo correction. This can be typically done using a calibration grid consisting of a pattern suitable for the image processing software of choice. Spatial or model calibration focuses on correcting each camera for perspective errors and lens distortion. Internal camera parameters that include the focal length and the optical centre are obtained from this calibration. The camera model information can then be used when stereo calibrating the system.

Stereo calibration is necessary to rectify the images so that the correspondence between similar points in the images captured by the different cameras can be established. Image rectification ensures that the set of images are vertically aligned, which simplifies stereo correspondence of pixels of interest. A disparity value, which indicates the horizontal difference in position of a particular pixel in the camera views, can then be used to calculate the relative depth of that pixel. When using a LabVIEW NI Vision toolkit to calibrate the system, the procedure illustrated in Figure 76 is used.

The left and right images of the target are corrected for distortion using the spatial calibration information. Stereo calibration is then done through rectification, and corresponding points in the different camera views matched. Depth is then computed using the determined disparity values.

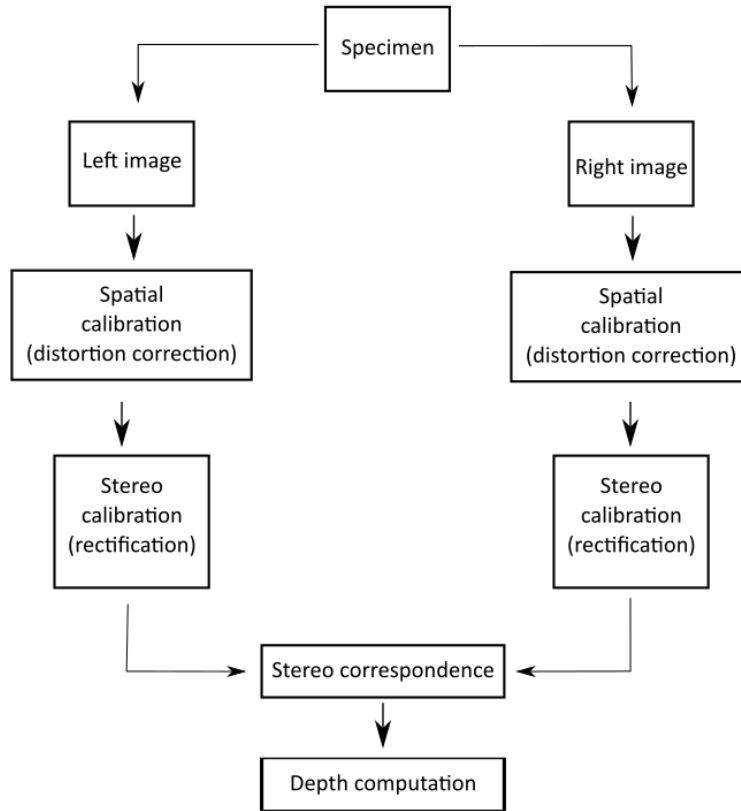


Figure 76: Procedure for depth computation using stereoscopic camera images

Stereo calibration results include the rotation matrix R_m (denoting coordinate system rotation, or rotation transformation between the two cameras) and the translation vector T_m (denoting coordinate system translation between the cameras). These matrices are used to rectify the images to compensate for the camera misalignment.

For a system with a baseline of b , camera focal length f , X_A the x-axis of a camera and Z_A the camera optical axis, a real-world point P at location (X, Y, Z) will be projected at u_L and u_R in the left and right camera respectively. This is illustrated in Figure 77. In the figure, c_x and c_y represent the camera optical centres.

X-coordinates of the points u_L and u_R are calculated using Equations (30) and (31).

$$u_L = \frac{fX}{Z} \quad (30)$$

$$u_R = \frac{f(X - b)}{Z} \quad (31)$$

The depth Z of a pixel at point P of interest can then be determined from the disparity D , focal length f and baseline b using Equations (32) and (33).

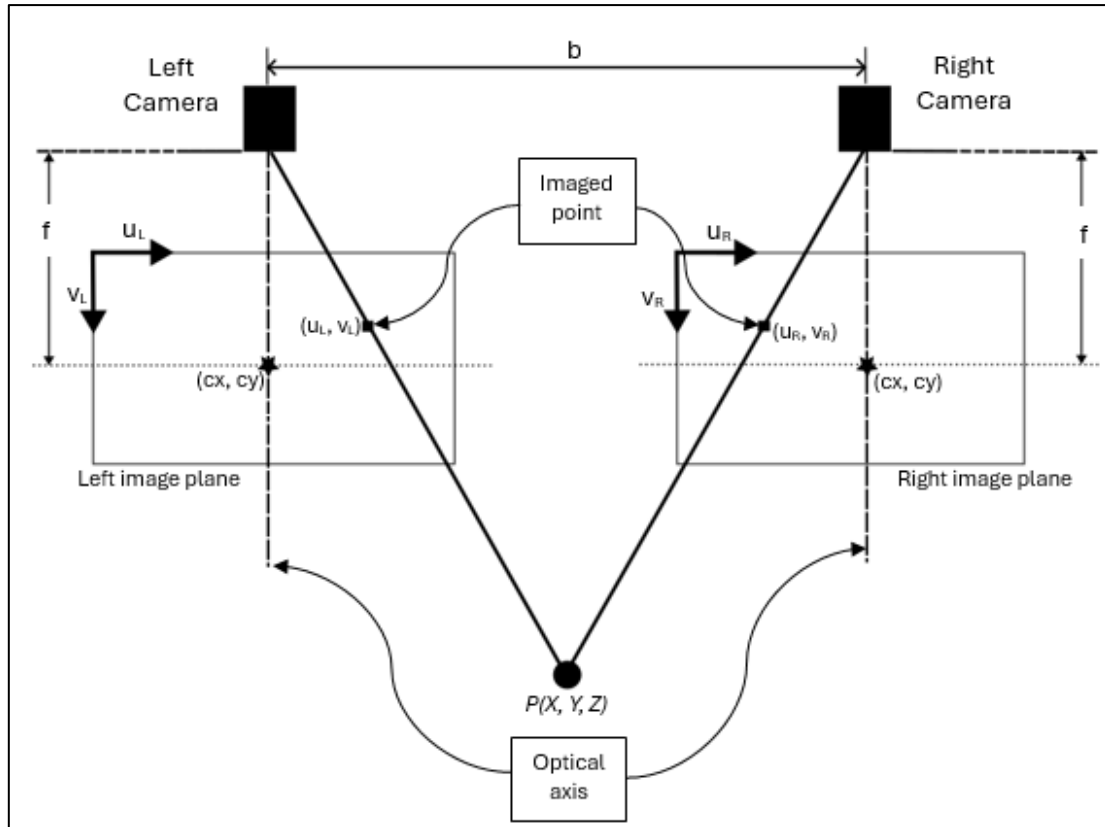


Figure 77: Stereo correspondence of a point observed from two cameras

$$D = u_L - u_R = \frac{fb}{Z} \quad (32)$$

$$Z = \frac{fb}{D} \quad (33)$$

4.6 3D system experimental setup description and specifications

The stereo-photography system was set up as indicated in Figure 75. The camera angle of separation was adjusted to have the centre of the blades located at the centre of each image. A camera standoff distance, $d = 140$ cm, and the baseline distance, $b = 11.5$ cm were used. For the investigation conducted, the baseline and standoff distance were chosen based on space availability on the test bench.

High-speed IDT NX8-S2 cameras were used at their maximum resolution of 1600×1200 , and images captured at a frame rate of 4000 FPS. 25 mm lenses were employed, and the exposure was set at $248 \mu\text{s}$. Table 10 gives the internal parameters for the cameras obtained during spatial calibration, for which f_x and f_y are foci lengths along the horizontal and vertical directions respectively. The parameters in the table are shown in Figure 77.

For stereo calibration and image rectification, the following R_m and T_m matrices were obtained.

$$R_m = \begin{bmatrix} 0.9915 & 0.000619 & 0.087663 \\ -0.00110 & 0.999984 & 0.005498 \\ -0.08765 & -0.00557 & 0.996135 \end{bmatrix}, T_m = \begin{bmatrix} -11.366 \\ -1.233 \\ 0.343 \end{bmatrix}$$

Table 10: Cameras spatial calibration parameters

Left camera focal length (pixels)		Left camera optical centre (pixels)		Right camera focal length (pixels)		Right camera optical centre (pixels)	
fx	fy	cx	cy	fx	fy	cx	cy
2950.0	2948.6	847.9	615.5	2957.6	2956.3	815.4	627.1

The correlation between points from the left and the right images is dictated by these two matrices. For a perfectly aligned system, the rotation matrix R_m will be an identity matrix, and the translation matrix T_m will be zeros except for the first entry (baseline distance, x-axis direction). By multiplying left image xyz-coordinates with R_m and then adding T_m , the two matrices can thus transform the left image to overlap with the right image for instance.

Table 11: Camera calibration quality parameters

Maximum projection error (pixels)	Calibration quality (%)	Maximum rectification error (pixels)	Rectification quality (%)
0.4075	0.9817	0.3910	0.9898

Table 11 indicates the calibration quality information. A calibration is considered valid if the quality is greater than 0.7, making 0.9817 acceptable (National Instruments, 2018). The maximum rectification error indicates how well the rectified images are aligned, and is acceptable when less than 1.5. The maximum projection error is computed as the error between left image grid points projected onto the right image and the original points in the right image. Perfect rectification is obtained when the rectification quality is 1, and a value of 0.9898 was considered as acceptable. Moreover, the physically measured baseline distance was 11.5 cm (standoff distance 140 cm), which is quite close to the translation x-axis distance between the cameras noticed in the translation vector (11.4 cm). Thus the calibrated stereo system was considered accurate enough to use for the investigation.

The bladed system analysed was driven by an electric motor with a maximum rotational speed of 1470 rpm. A Computer Aided Drawing (CAD) rendering of the experimental setup is illustrated in Figure 78(a). Blade excitation was achieved through the use of air jets mounted behind the blades, as indicated in Figure 78(b).

The 5 bladed system analysed was composed of 3 damaged blades and two healthy blades. Of the damaged blades, one of them had two machined slots, and the other two just a single slot on one side of the blade. The machined slots resembled cracks at the root of the blade. The aluminium blade geometries in millimetres as given in Figure 50, and their vibrational characteristics can be obtained from the work by Church (2015).

Two rotational speeds of 650 rpm and 1000 rpm were considered for this investigation. The blades were arranged in an alternating healthy-damaged blade manner. Owing to the small

crack sizes and the fact that they are aluminium, unbalance effects were not considered. For the rest of the document, blade 1 corresponds to a blade with two cracks, blade 2 a healthy blade, and blade 3 a blade with a single crack.

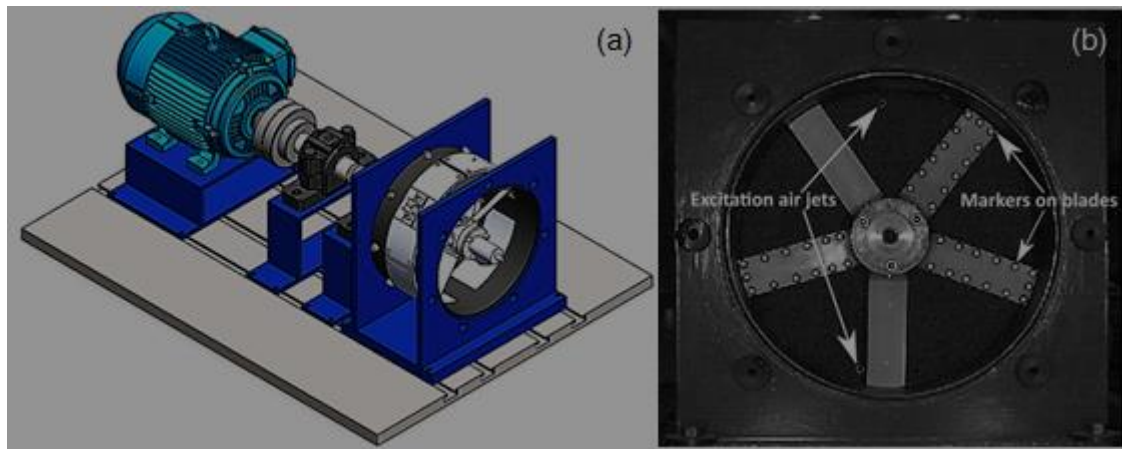


Figure 78: (a) CAD rendering of the experimental setup (Church, 2015), (b) excitation and blade markers setup

When using a disparity-based approach to compute the depth of a particular point as given by u_L and u_R , it is critically important that the same point is considered in both the left and the right images. In a practical setting where image edge detection algorithms are used to extract contours, computational depth errors resulting from imperfectly associating corresponding points in the stereo-captured 2D contours can be expected. The severity of the effect these errors will have on the ultimately computed 3D contour is also expected to increase with decreasing out-of-plane responses. To illustrate this, Figure 79 shows the sequence of steps necessary to conduct typical edge detection for the rotor, performed using National Instruments Vision Assistant image processing software.

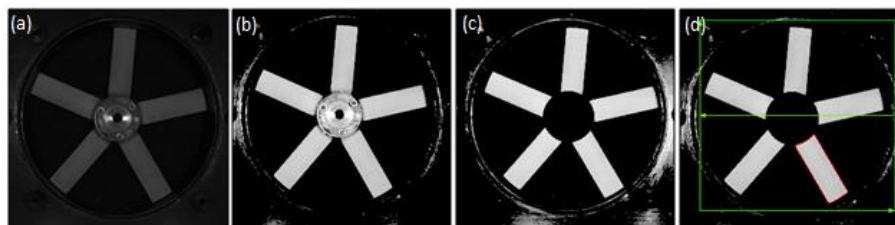


Figure 79: Edge detection procedure (a) raw image, (b) brightness, contrast and gamma adjustment, (c) hub masking, (d) contour extraction

Detected edges for one of the blades can be shown in Figure 80. As can be observed, the resolution of captured images for this particular setup is not fine enough to extract smooth contours for analysis. The rough contours means that the possibility of significant errors resulting from imperfectly associating corresponding points in the stereo-captured images is high. Thus for a system with small out-of-plane responses, the noisy nature of computed 3D contours can easily mask the small shape deformations making it impossible to accurately detect out-of-plane shape variations. The resolution of captured images should at least be high enough for contour corners to be clearly identifiable, so that accurate corresponding point matching can be conducted. In an investigation, the size of the specimen, magnitudes of responses, and set camera resolution will therefore contribute to the quality of computed 3D contours.

As evident in the computed 3D contours illustrated, the blade responses in this particular investigation were actually very small. In efforts to minimize possible depth computational errors when developing and testing the viability of the proposed shape-based condition monitoring approach, only the three blades with markers attached on their edges were considered (Figure 78(b)). By correctly matching and connecting corresponding left and right image markers, improved quality blade contours for three out of the five blades in the system could be constructed for shape variation analysis. This is illustrated in Figure 81. It is worth mentioning that software packages such as TEMA automotive motion analysis for contour and volume analysis already exist, and one can employ these for easier and accurate contour extraction using edge detection from raw images.

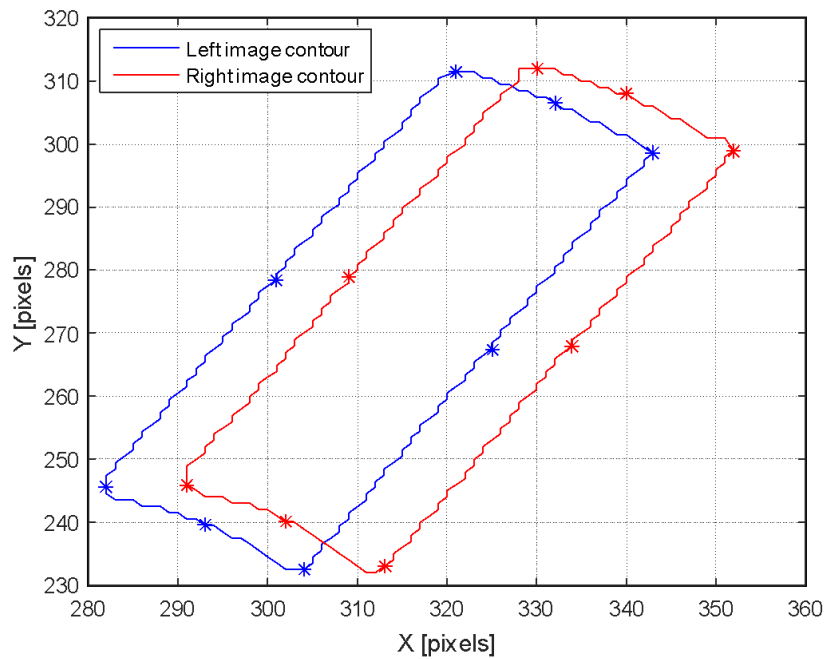


Figure 80: Edge detection based contours

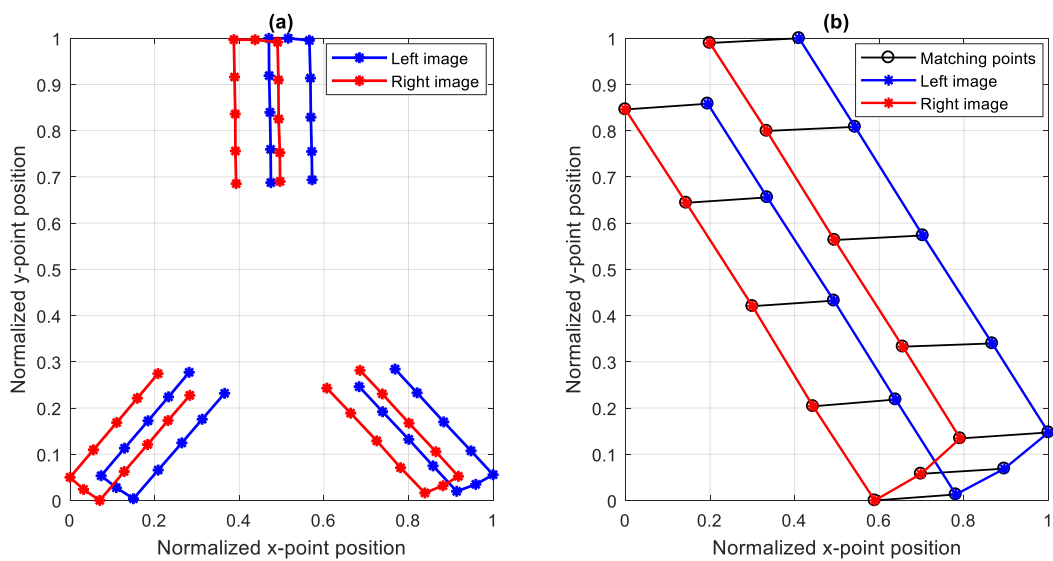


Figure 81: (a) Left and right image contours, (b) Corresponding points matching for a single blade

In using a stereo camera system, two in-plane contours from the left and the right cameras are available at each captured timestamp. Either of these contours can be chosen to be the one onto which the calculated depth values are imposed in constructing a 3D profile of the blade at that particular timestamp. Using Equation 32, the depths of the different contour points were determined, and the depth values imposed on the left image contour. For one typical stage in a sequence of captured images, Figure 82 shows a 3D representation of computed contours for the three blades with markers attached to them. In this investigation, it is expected that the blade operational deflection shapes will be similar to the first bending mode (low rotational speeds considered). Therefore the blade profile can be approximated by a smooth nonlinear quadratic surface fitted using the discrete blade contour points.

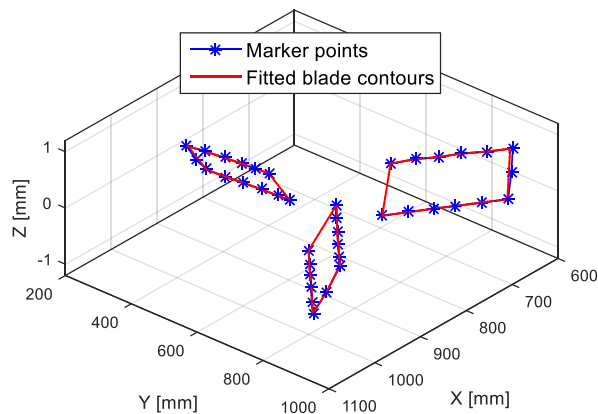


Figure 82: Blades fitted quadratic nonlinear contours

4.7 Experimental investigations

4.7.1 Single point responses using 3DPT

To first identify if there were any differences in the blade responses, data was analysed for a single middle point on the tip of each blade using 3DPT and the results in Figure 83 were obtained.

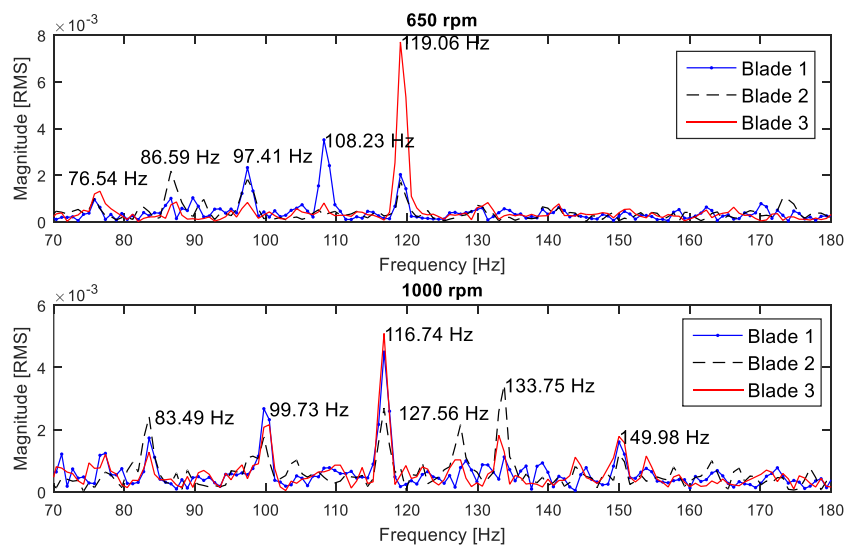


Figure 83: Single point 3DPT blade responses

As observed, the out-of-plane blade responses are significantly composed of the 10.8 Hz and the 16.7 Hz harmonic components corresponding to the 650 rpm and 1000 rpm rotational speeds respectively. The out-of-plane first bending natural frequencies for blades 1, 2 and 3 were determined to be 108 Hz, 127 Hz and 119 Hz respectively (Church, 2015). For each blade, significant peaks are expected when the rotational speed harmonics coincide with these natural frequencies. This can be observed at 650 rpm for blades 1 and 3, and at 1000 rpm for blade 2 (Figure 83). This does illustrate that the blades did have noticeably different out-of-plane responses owing to the different blade damage modes.

4.7.2 Shape based dynamic analysis

Considering the SPCDs determined as outlined in Section 4.2, a frequency domain analysis of the time synchronous averaged responses out-of-plane descriptors (5th and 6th SPCDs) resulted in the measurements given Figure 84. Data cursors for some of the prominent frequency peaks have been added for easier identification.

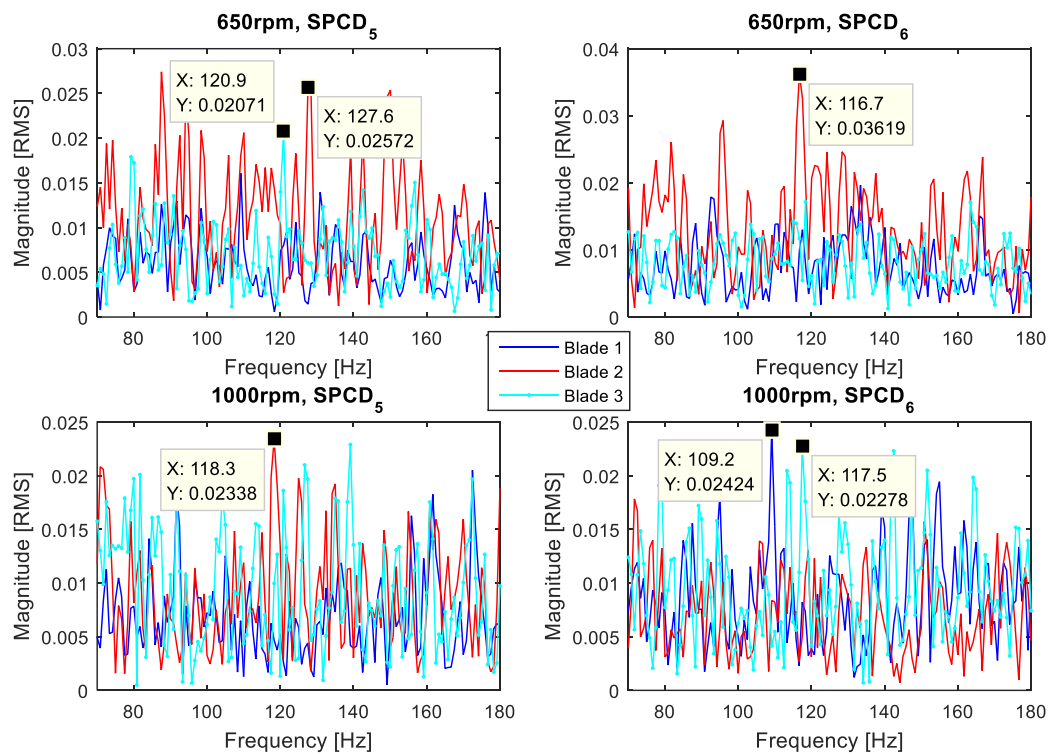


Figure 84: Time synchronous averaged SPCD frequency responses

The expected 108 Hz for blade 1 and the 127 Hz for blade 2 can be identified for some of the 650 rpm and 1000 rpm measurements, and differences are noticeable in the blade responses. However, the small out-of-plane blade vibrations do not result in significant shape variations easily identifiable from the noise-masked responses.

In the case of a rotating structure, a transformation to an angular domain can be used to create multiple univariate SPCD time series, a highlighted requirement for clustering using principal component analysis. By considering each revolution of the blades as a separate signal, one can perform clustering on the data for classification purposes. Transformation of these short duration signals into the frequency domain before clustering can be neglected, analysing the SPCDs directly in the time domain in a way similar to the commonly used spike sorting signal

processing technique described by Ge & Farina (2013), Caro-Martín et al. (2018) and Souza et al. (2019). In spike sorting, spikes generated by various neurons are detected and sorted to differentiate and identify the neurons generating them. A single microelectrode signal from the brain is typically composed of spikes from a number of neurons. After detecting, isolating and aligning the peaks of the spikes in that particular signal, a sorting process that involves PCA data reduction of the spike distribution is conducted. Each spike detected corresponds to a point on the principal component diagram, and distributions of the detected spike sets form the clusters.

Two investigations were conducted, one in which the blades were positioned with faces in the xy-plane, and the other one with blades staggered at 30° . For a given system rotational speed, signal segments for all three blades' SPCDs were combined to form a set of multiple univariate SPCD time series. Thus if there were N revolutions with a period of t s in a particular test, a single blade data set would have $N \cdot t$ seconds time signals, making the combined set a three times N set of signals to which the standard PCA data reduction and clustering described in Section 4.4.3.3 is applied.

As highlighted in the calculation of X^{new} , Fourier coefficients e_n and f_n capture z-plane contour characteristics (Figure 48). Similar to the presented FEA, the experimental investigation where the blade profiles are in the xy-plane with bending operational deflection shapes which essentially comprise of out-of-plane responses are expected. This implies that the blade responses directly influence SPCD₅ and SPCD₆. Results for 650 rpm and 1000 rpm are given in Figure 85 and Figure 86, which show that the positions of clusters differ for different blade damage levels. Unlike the FEA investigation where the out-of-plane response magnitudes were not significant enough for SPCD₅ and SPCD₆ to provide easily distinguishable clusters, the responses in the experimental study clearly capture the differences in behaviour without the need for response amplitude scaling. The differences in the position of clusters for different rotational speeds (for example SPCD₅ for 650 rpm and 1000 rpm) highlights that the system dynamics affect how the clusters are positioned. This is expected, since the rotational speed imposed on the system directly influences the blade operational deflection shapes.

Illustrated in Figure 87 are results for the 3D projections at 1000 rpm for blades with faces aligned with the xy-plane, and for blades staggered at 30° . As can be observed by comparing SPCD₁ and SPCD₂, clusters for blades that are staggered to influence shape variations in the xy-plane are more compact and better isolated. This is in agreement with the claims made in the FE investigation where the applicability of the technique was being investigated in a controlled environment.

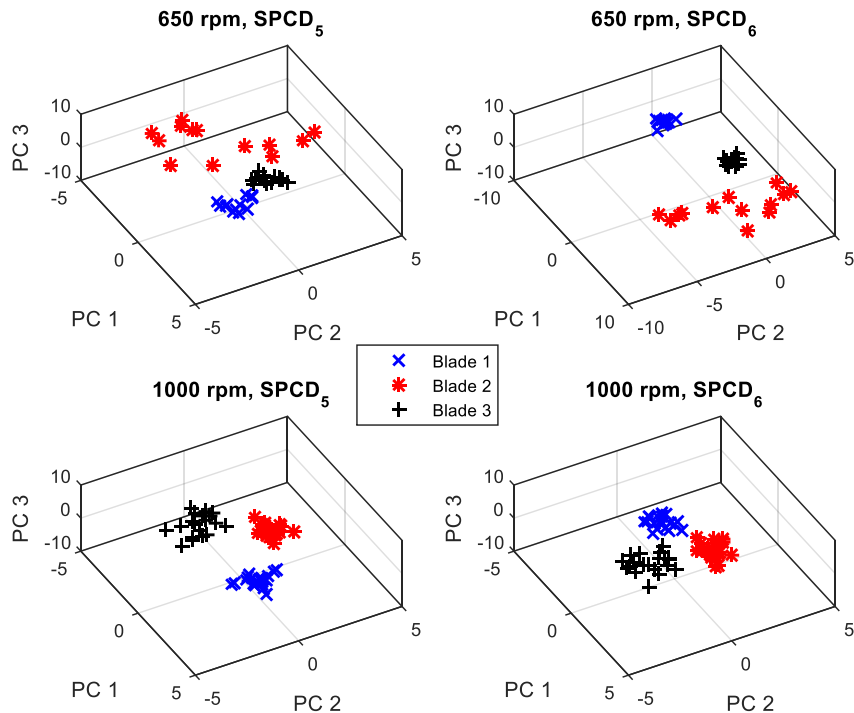


Figure 85: 650 rpm and 1000 rpm SPCDs 5 and 6 projected in a 3D feature space

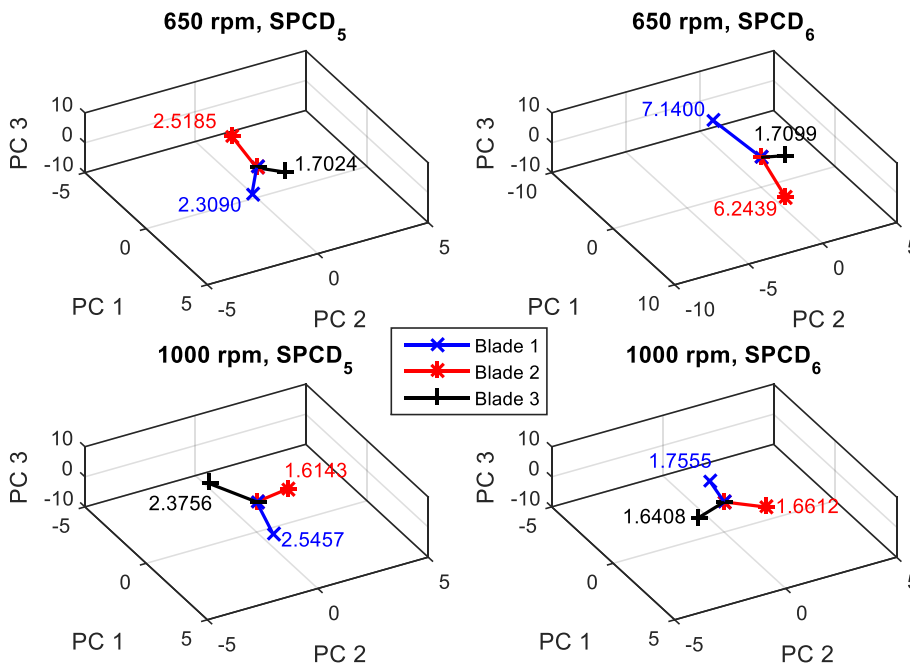


Figure 86: Cluster centroid distances from origin - 650 rpm and 1000 rpm SPCD₅ and SPCD₆ projected in a 3D feature space

As expected, Figure 87 also captures how staggering the blades minimizes the influence blade responses have on the out-of-plane based SPCDs. This is clearly illustrated in the 3D projected data (Figure 88), where the clusters for SPCD₅ and SPCD₆ can be observed to be either closer or even overlapping with each other for the 1000 rpm measurements.

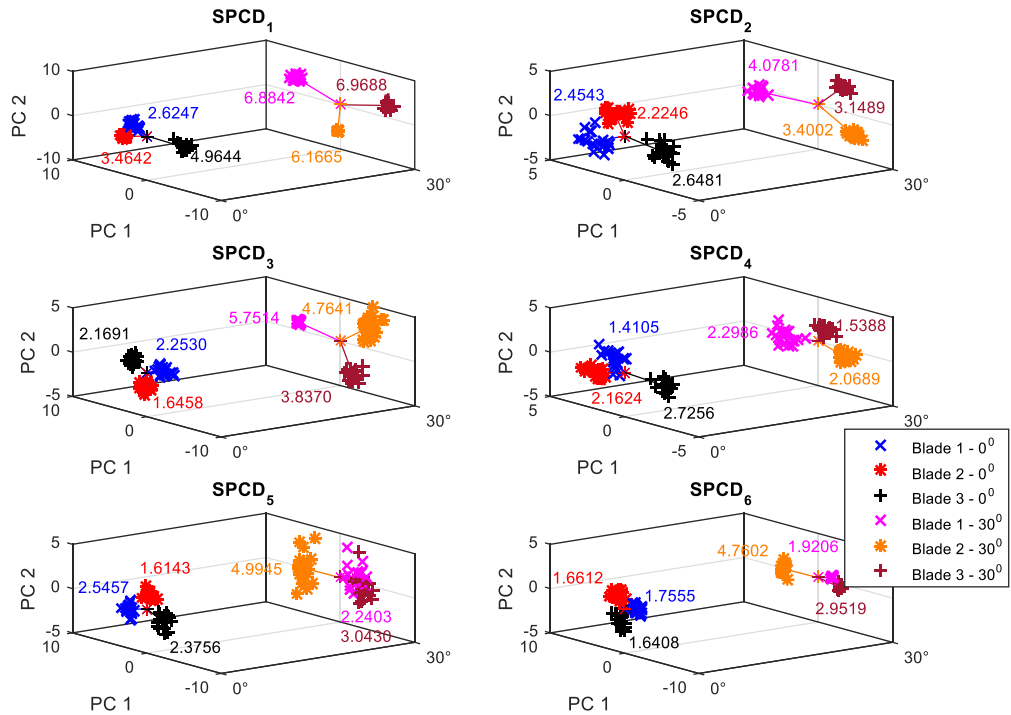


Figure 87: 1000 rpm SPCDs projected in a 2D feature space for 0° and 30° stagger angle

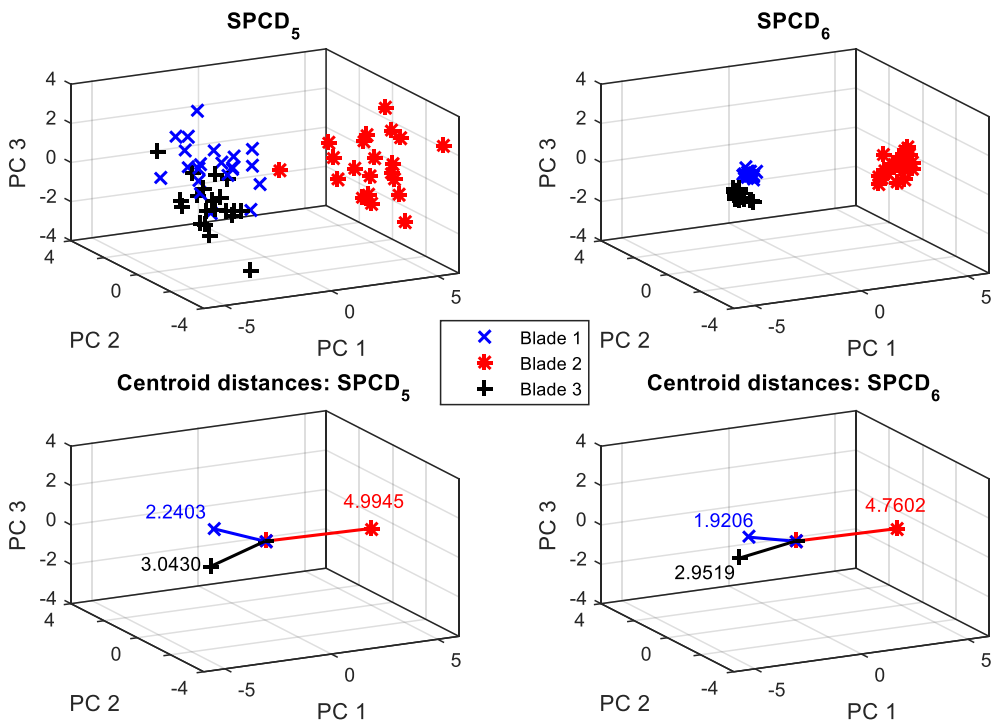


Figure 88: Staggered blades 1000 rpm SPCD₅ and SPCD₆ projected in a 3D feature space

For a particular system, clusters can still be indistinguishable visually as a result of the condition and settings adopted for that system. These settings include the blade orientation, rotational speed, blade condition and camera positioning. In those cases the proposed

approach can still be valuable for monitoring blade dynamics. As the state of the machine changes, the behaviour can be monitored by analysing how the clusters shift from the original (initially undistinguishable) positions. When using this technique, it is necessary to understand the form of the shape under consideration, and how the structural response affects that shape. This will aid in identifying which SPCDs to monitor, and how the data can be transformed for better classification of different responses or damage modes.

As highlighted earlier, the FEA conducted was done for a model that was not modal updated according to the experimental setup. The operational conditions of the two systems also differ. Whilst it is not possible to quantitatively and qualitatively compare the results obtained from the two investigations, concepts surrounding shape-based condition monitoring can be highlighted. The FEA based investigation clearly illustrated that damage progression in a system can be monitored for the blades (Figure 74). This is expected to be applicable in a physical rotor system, and the basis for establishing models describing the relationship between the amount of cluster shift and the level of damage using a modal updated FEA model has been created.

4.8 Application to wind turbines

In this investigation, wind turbines have been adopted as the structures of interest to motivate the study. Being outdoor large structures with significant rigid body motions, they require the use of non-interruptive measurement technologies to capture data that can be used to characterize their behaviour for condition monitoring purposes. Because the investigations conducted in this study were not done on an actual outdoor full scale wind turbine, it is necessary to address the applicability of the technique to an actual wind turbine in terms of feasibility and the form of measurements one would expect in that scenario.

As highlighted in Section 1.2.2.2 describing the use of optical techniques to capture dynamics of rotating structures, photogrammetry has been successfully used to analyse outdoor wind turbines. In the studies done by Winstroth et al. (2014) a 3.2 MW full-scale wind turbine was successfully analysed using DIC. Cameras had to be separated by 105 m and situated about 205 m in front of the turbine blades to capture the data. In another study by Ozbek et al. (2010), a 2.5 MW wind turbine with a diameter of 80 m diameter was analysed using CCD cameras at a stand-off distance of 220 m. Displacements with an accuracy of ± 25 mm could be identified. In both these investigations, prior surface preparation had to be done, and tracking of either a speckle pattern (DIC) or markers (3DPT) conducted. The image processing required to extract the boundary shape of a turbine blade is much less complicated compared to the processing required to track and correlate specific pixels on the surface of a blade. The quality of the images required for the global-natured shape extraction does not have to be as high as the quality of images required for DIC or 3DPT. Taking into account that successful measurements can be captured for DIC and 3DPT, it is reasonable to claim that implementation of a shape-based technique under similar conditions will not only be feasible, but also easier.

The approach proposed in this study considered a 300 mm diameter system being rotated at speeds as high as 1000 rpm in a laboratory setting. A frame rate of 4000 FPS was used for the cameras. Maximum out-of-plane displacements of magnitudes less than 2 mm were translated to usable shape variation data. In the study conducted by Winstroth et al. (2014), the 3.2 MW turbine has a diameter of 80 m, images were captured at 30 FPS, and out-of-plane deflections with amplitudes around 800 mm could be captured. Using the experimental

data in this study as a baseline, a rotor system with a deflection-to-diameter ratio of about 0.007 (2 mm/ 300 mm) can be successfully investigated using the proposed shape analysis approach. A higher deflection-to-diameter ratio means that the shape variations in the system are even more significant for them to be easily detectable. For the 3.2 MW turbine, the deflection-to-diameter ratio can be calculated to be about 0.01 (800 mm/ 80000 mm). This is about 1.4 times the deflection-to-diameter ratio that could be detected and consequently used to successfully classify different blade damage modes. Thus it is reasonable to assume that the proposed approach can be successfully used to analyse full scale wind turbines out-door.

Like all condition monitoring systems, the quality of data captured significantly influence the feasibility of the approach, which in this case are images. In the case of wind turbines where the environmental conditions cannot be controlled, poor lighting conditions might make it be difficult to accurately capture the turbine blade profiles, thereby negatively affecting the accuracy of the results. As the turbine blades rotate, the camera captured blades' profile overlay with the support tower profile at the vertical downward angular position. This can also compromise the captured measurements. Sophisticated image processing techniques such as Artificial Intelligence (AI) methods will have to be employed to reconstruct and fill in possible blade missing edges for incomplete contours, and interpolation techniques will have to be used to compensate for blade angular positions where the cameras do not capture the blades completely. These AI methods such as Active Shape Models (ASM) and Active Appearance Models (AAM) can automatically adjust and fit shapes to imaging data, thus allowing for accurate shape variation capturing and analysis.

4.9 Chapter conclusion

This chapter focused on the extension to a 3D environment, of the 2D shape analysis approach introduced and investigated in Chapters 2 and 3. The determination of 3D shape principal components of a rectangular shape representing the profile of a single blade on a typical axial bladed system is presented. How each V affect the general form of the shape is also demonstrated, and two investigations (numerical and experimental) conducted to illustrate the applicability of a shaped based procedure as a condition monitoring tool for rotating turbine blades.

The FEA based investigation conducted confirmed variations in the natural frequency as the levels of damage in the blades were being increased. SPCDs variation analysis for a system of blades connected together via multipoint constraints and a central node undergoing displacement excitation at a frequency in the range of the system's first bending mode natural frequencies was conducted. Coupled with a clustering approach of the SPCDs' FFTs, it was illustrated that a shape-based approach can be used to classify blades according to their levels of damage. In terms of increasing levels of damage, monitoring the location of the clusters proved to be a viable way to analyse and identify progressing damage in the blades, as the centre of each cluster digresses from the original location with damage.

Whilst the natural frequency is a parameter that is widely and conventionally used to monitor changes in the state of a machine, its applicability in a physical environment where point-wise contact sensors have to employed to capture the data can be limited. In terms of simply being able to detect changes in the behaviour of a structure in a non-intrusive manner applicable whilst a machine is in operation, the potential of a shape-based approach was demonstrated in the numerical investigation presented.

To apply the same concepts in an experimental setting, 3D shape contours extracted from stereoscopic images captured using calibrated high speed cameras were considered. Three blades at different states of health were analysed through investigating variations of their calculated SPCDs. In the experimental investigation where the blades were actually rotating, clustering to classify the blades was conducted via PCA of revolution segmented SPCD data. This was successfully implemented to isolate differently behaving turbine blades. In comparison to point-wise out-of-plane blade responses, it was illustrated that the small amplitude blade responses characterized with low SNRs can better be analysed and classified using the proposed shape order-based approach. The shape-based measurements captured in a contactless manner are multi-dimensional in nature, making it possible to manipulate the data through rotational transformations for example. This was successfully illustrated in the experimental investigation of 30° staggered blades, in which the shape principal components that influence the in-plane geometric mode features could be engaged to better identify blades behaving differently.

In order to accurately determine and verify relationships between damage severity and blade cluster location rate of variation, a finite element modal updated system of the rotor coupled with experimental investigations will have to be employed. The determined parameters can then be incorporated in an analysis to predict blade dynamic behaviour at different stages of damage, and at various operating conditions. This can also be useful in determining the remaining useful life of the blades. Such an investigation remains to be explored in the future as a next phase in adopting shape analysis as a condition monitoring tool.

In terms of the applicability of the proposed measurement technique, preliminary considerations based on the size of a typical full scale turbine point towards a successful implementation of the approach in an out-door setting. It should be highlighted that the proposed clustering technique is expected to be more valuable in those cases where progressing type of faults are an issue. These may include misalignment, unbalance from ice loading for instance, and bolt loosening. In these cases, a digressing cluster identified for a particular blade for measurements taken at different time intervals can be a valuable indicator of progressing damage, and the rate at which the fault is progressing.

CHAPTER 5: A COMPARATIVE STUDY OF THE PERFORMANCE OF PCA AND KPCA

5.1 Introduction

This chapter focuses on investigating ways by which classification of different blade damage modes can be improved. If the technique is to be implemented in the field to investigate full scale wind turbine blades, the system considered should be robust to noise and able to reliably classify blades at various operating conditions. In this chapter, the concept of kernel principal component analysis is evaluated and applied to the time domain SPCDs data. The performance of the system if SPCDs multi-domain statistical features are considered instead of the typical time domain SPCDs is evaluated. Finally, how robust the system is to noise is investigated.

5.2 Data classification performance evaluation

To evaluate how well a technique can distinguish between different behavioural states of a machine, two parameters, namely the intra-class scatter S_w , and inter-class scatter S_b are calculated using Equations (34) and (35), (Gharavian et al., 2013).

$$S_b = \sum_{i=1}^c (\mu_i - \mu)(\mu_i - \mu)^T \quad (34)$$

$$S_w = \sum_{i=1}^c \sum_{f_k \in C_i} (f_k - \mu_i)(f_k - \mu_i)^T \quad (35)$$

In the equations above, μ_i is the average value of a class $C_i = (1, 2, \dots, c)$, μ the total average and f_k the features extracted by PCA or KPCA. Essentially, a smaller intra-class scatter and a larger inter-class scatter represent better clustering classification performance. The quality of the clustering for an investigation can then be defined as the ratio S_b/S_w . In this chapter, because results are included for both the 2D and the 3D feature spaces, attention is focused on inter-class and intra-class properties of the clusters instead of the centroidal locations introduced in Chapter 4.

The results presented in Chapter 4 were determined for 650 rpm and 1000 rpm. For these two rotational speeds, some of their harmonics almost coincided with the bending mode shapes of the blades, which are 108 Hz, 127 Hz and 119 Hz for blades 1, 2 and 3 respectively (Church (2015)). What this means is that the blade out-of-plane responses were quite pronounced and the shape variations more distinct. To evaluate how the approach performs for a rotational speed that has potentially hidden shape variation characteristics, a rotational speed of 1460 rpm was considered.

SPCD₅ and SPCD₆ for the three rotational speeds are displayed in Figure 89. Whilst all SPCDs show clearly isolated clusters for the three blades for 650 rpm and 1000 rpm, the proposed PCA approach cannot classify the blades for SPCD₆ at 1460 rpm. As highlighted in Section 1.2.4, complex system responses typically consists of nonlinearly related features. Being a linearly based transformation approach, PCA can thus result in loss of these features, making system classification impossible. To investigate if this contributes to the poor performance of

the proposed approach at 1460 rpm, KPCA as employed. Non-linear relationships between different SPCDs time segments (per rotation) were expected for all three rotational speeds.

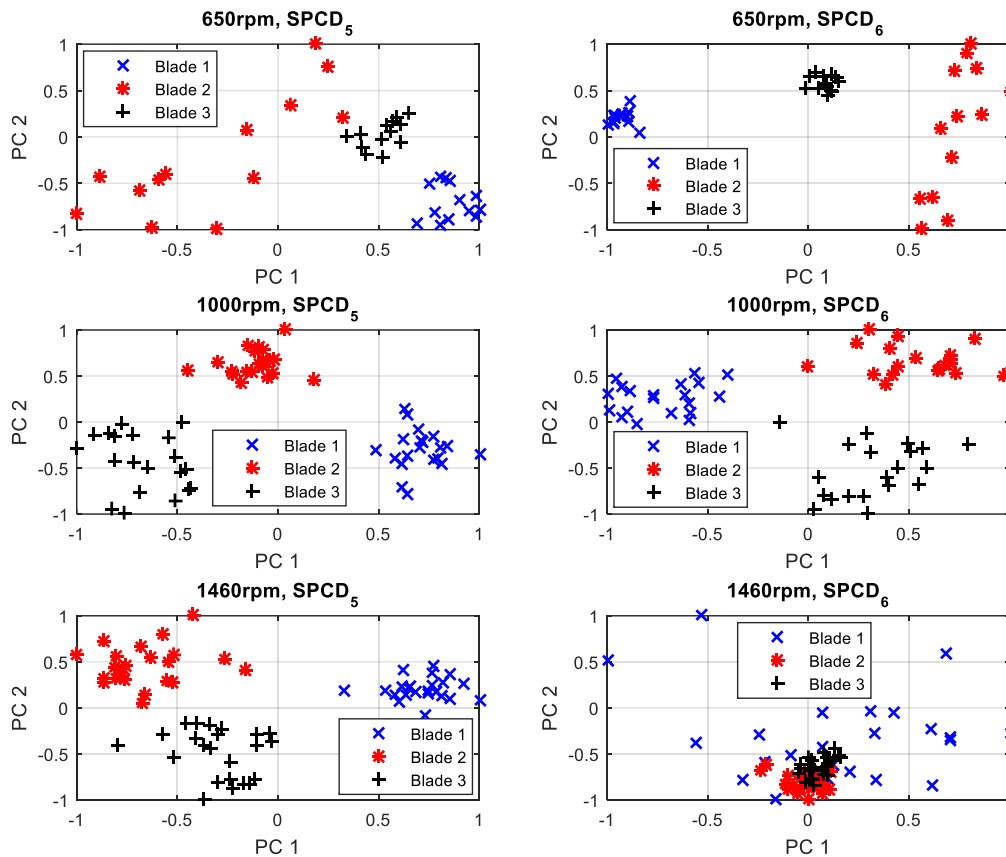


Figure 89: PCA SPCD₅ and SPCD₆ projected in a 2D feature space for 650 rpm, 1000 rpm and 1460 rpm

Three different investigations were conducted to develop post-processing approaches that are more robust and more suitable for processing shape analysis-based data. These are listed below.

- (i) PCA vs KPCA evaluation for time domain SPCDs
- (ii) raw data (time domain SPCDs) analysis vs multi-domain feature-based analysis
- (iii) noise sensitivity evaluation for PCA and KPCA

5.2.1 PCA vs KPCA

The choice of the kernel parameter does influence KPCA results with regards to the contribution of the first principal component. This contribution can be in terms of the percentage of the first eigenvalue variance for instance. According to Nguyen & Golival (2010), the Gaussian kernel function introduced in Equation (22) is known to be flexible when it comes to the choice of the kernel function width. A width less than one or even a much larger value can be adopted. In this investigation, a width of three was arbitrarily chosen for the KPCA. The results obtained for projections in the 2D and 3D feature spaces are given in Figure 90 and Figure 91 for 650 rpm rotational speed.

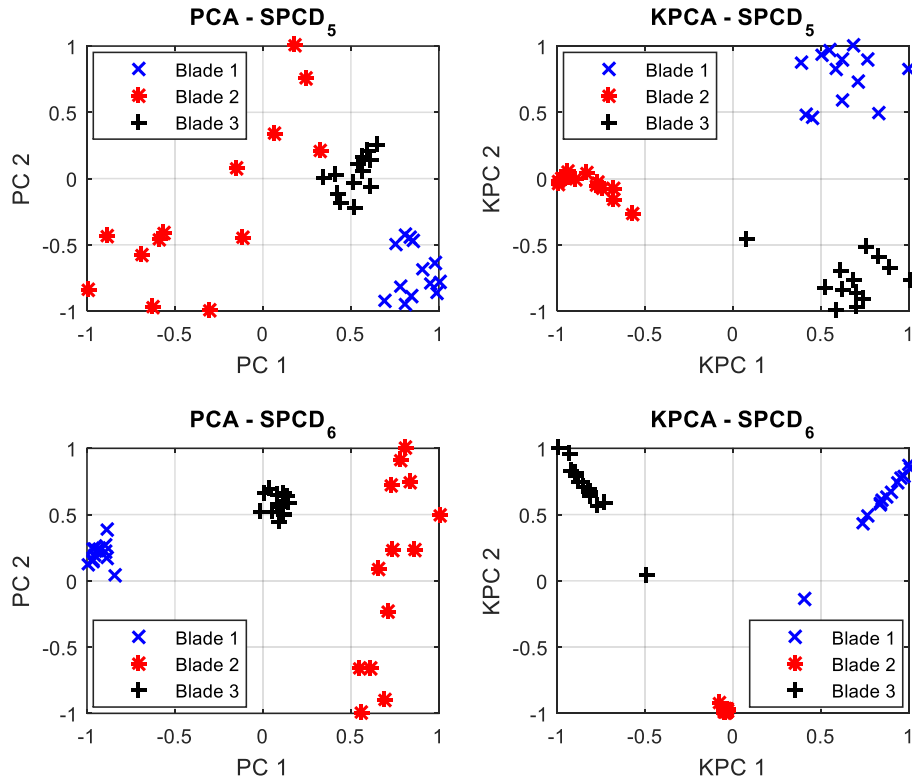


Figure 90: 650 rpm PCA and KPCA SPCD₅ and SPCD₆ projected in a 2D feature space

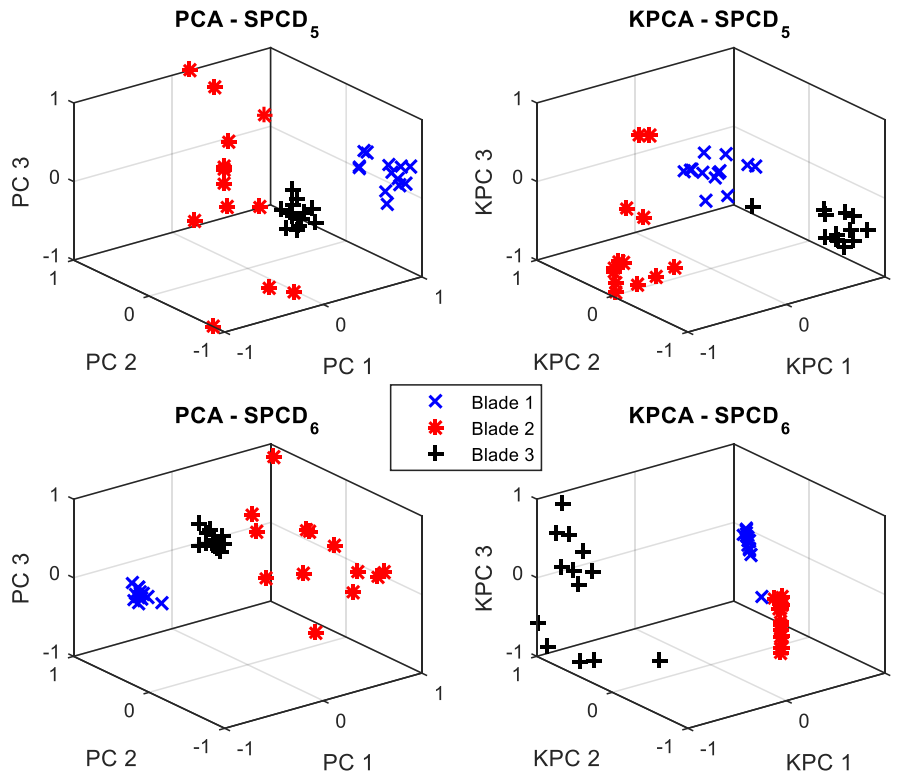


Figure 91: 650 rpm PCA and KPCA SPCD₅ and SPCD₆ projected in a 3D feature space

For 650 rpm, using the non-linear kernel transformation of the SPCDs resulted in more compact clusters in which the data points are arranged in a linear manner (SPCD₆). The improved clustering is better visualized in the 2D feature space (Figure 90).

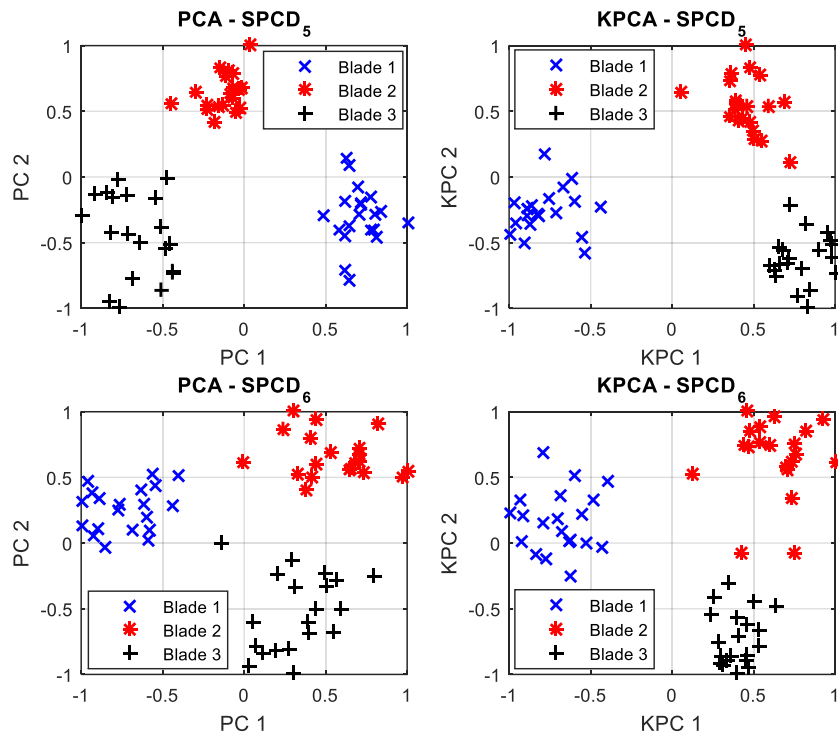


Figure 92: 1000 rpm PCA and KPCA SPCD₅ and SPCD₆ projected in a 2D feature space

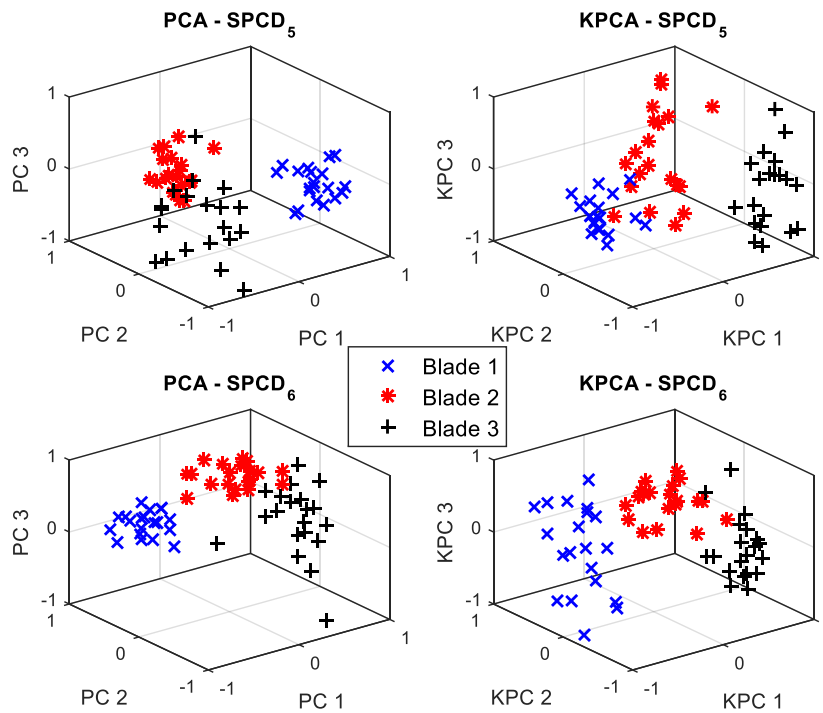


Figure 93: 1000 rpm PCA and KPCA SPCD₅ and SPCD₆ projected in a 3D feature space

Results for the 1000 rpm rotational speed are given in Figure 92 and Figure 93. As illustrated below, at 1000 rpm KPCA does not seem to significantly improve the clustering in the measurements visually. A quantitative analysis presented later on will give a better insight in the performance of PCA and KPCA at 1000 rpm.

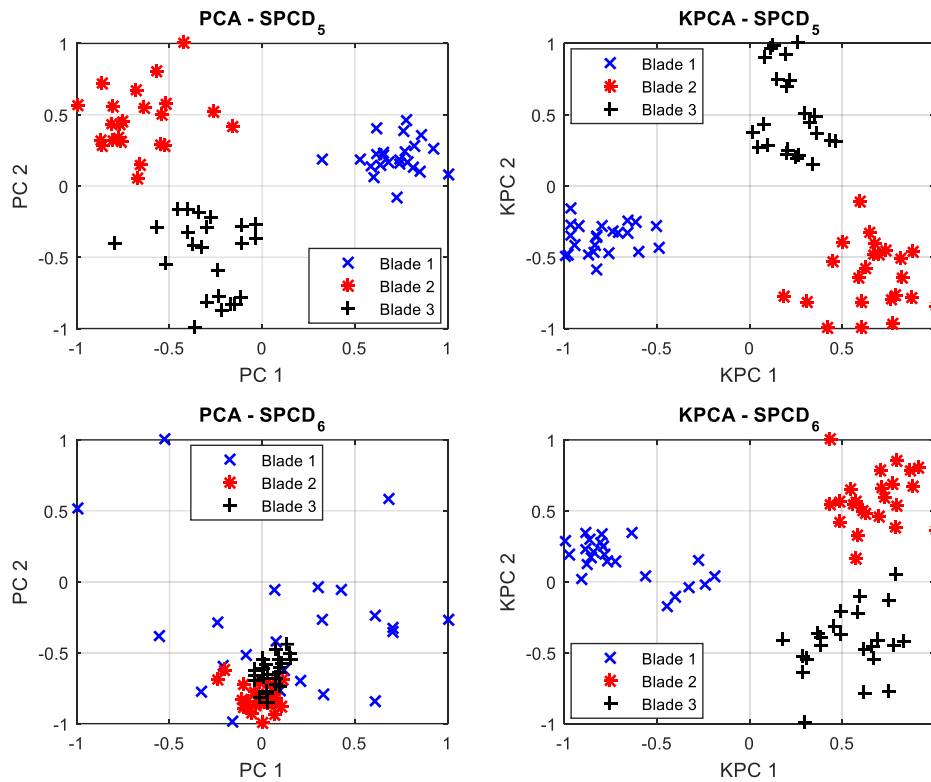


Figure 94: 1460 rpm PCA and KPCA SPCD₅ and SPCD₆ projected in a 2D feature space

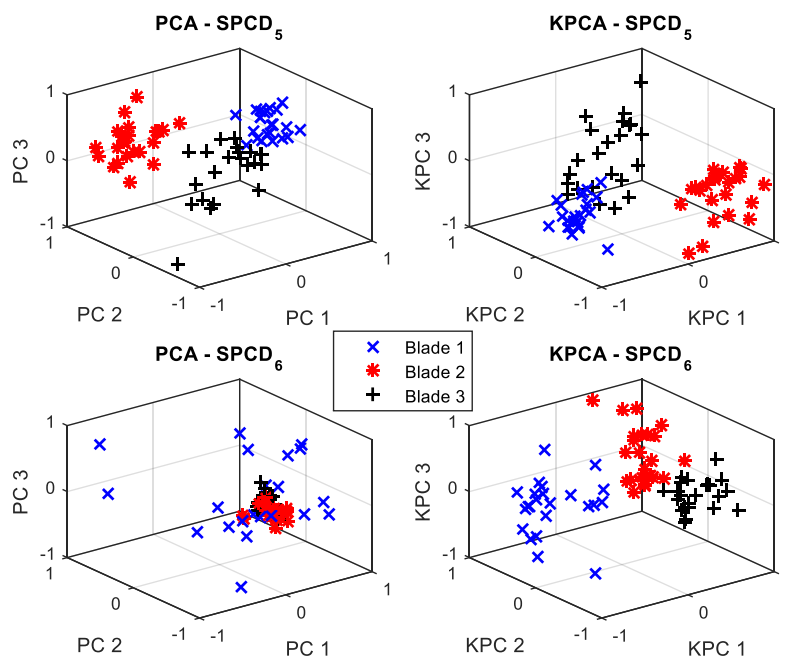


Figure 95: 1460 rpm PCA and KPCA SPCD₅ and SPCD₆ projected in a 3D feature space

Illustrated in Figure 94 and Figure 95 are results for 1460 rpm. At 1460 rpm, it can be observed that KPCA significantly improved blade cluster separation. For $SPCD_6$, PCA is unable to properly cluster the data for blade visual identification. This can be attributed to the low SNR of $SPCD_6$ at that speed. Unlike the rotational speeds at 650 rpm and 1000 rpm that have harmonics that nearly coincide with the out-of-plane blade bending natural frequencies stated above, at 1460 rpm the blade responses are not that well defined. Thus from the results presented, it is evident that the blade behaviour is better characterized by an approach that can capture the nonlinear relationships between the different shaft revolutions.

To better evaluate the performance of PCA vs KPCA, the clustering parameters ratio S_b/S_w was determined for the three rotational speeds investigated. Results obtained are shown in Figure 96.

As can be noted from Figure 96, KPCA outperforms PCA for 650 rpm $SPCD_5$ and $SPCD_6$, and also 1460 rpm $SPCD_6$ in terms of overall clustering. Overall clustering performance considers the intra-class parameter (S_w). In terms of separation of clusters for accurate classification of different blades with varying damage, the inter-class cluster values can be argued to be of more importance than the spread of data points within a cluster. It can be noted that the S_b values are larger for KPCA compared to PCA for all the rotational speeds. This applies to both $SPCD_5$ and $SPCD_6$, as illustrated more clearly in Figure 97.

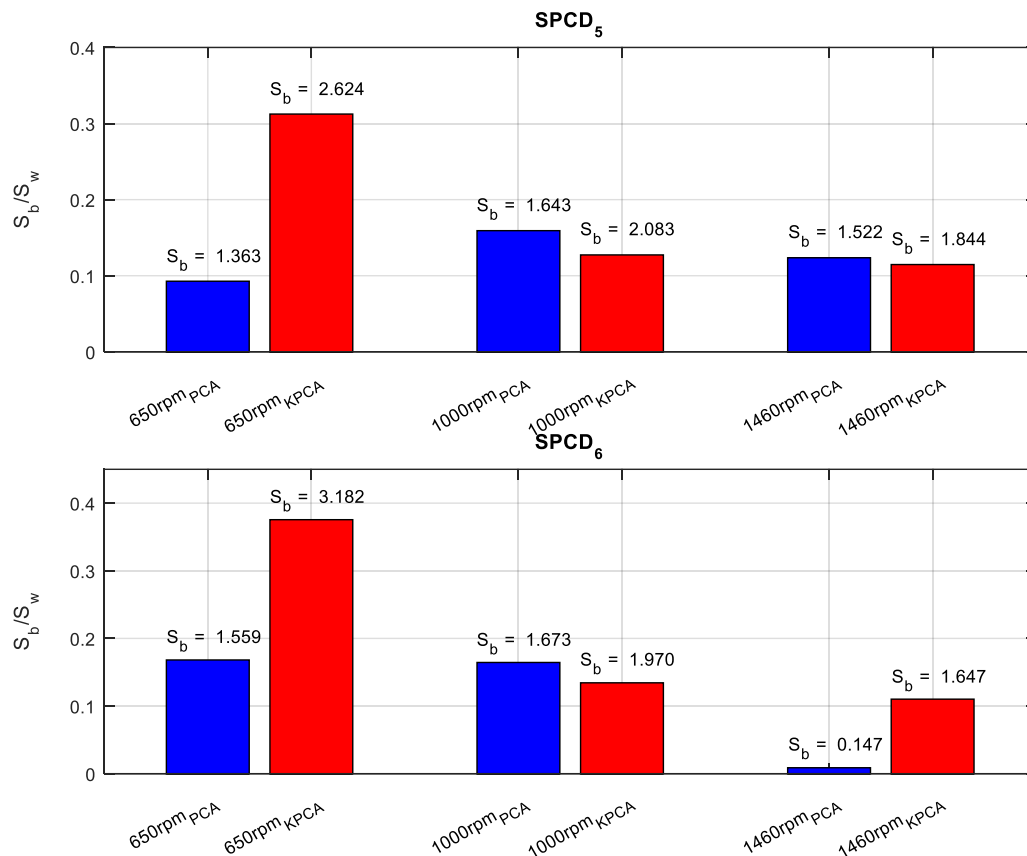


Figure 96: PCA and KPCA clustering performance for time domain SPCDs raw data

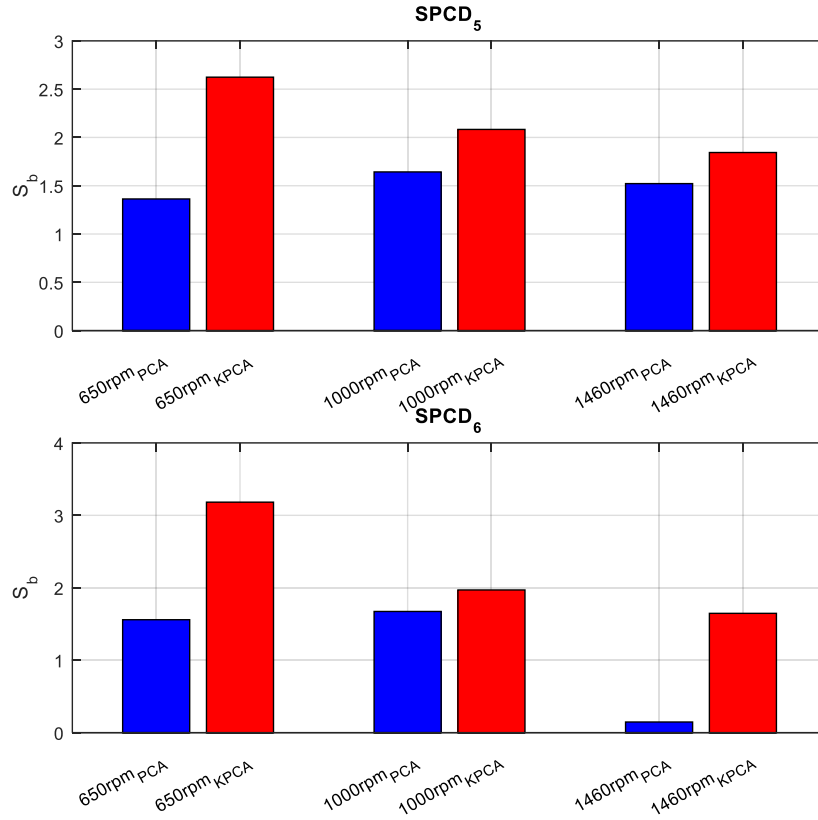


Figure 97: S_b based PCA and KPCA clustering performance for time domain SPCDs raw data

5.2.2 Multi-domain Statistical Features (MSF) based evaluation

Advantages of dealing with statistical features over the raw time signals were discussed in Section 1.2.5. In investigating if these ideas extend to the proposed approach, typical time domain statistical features were extracted from the SPCD raw response data and used as the feature vectors for either PCA or KPCA. These are given in Table 12 (He et al., 2007).

Table 12: Time domain statistical features

Feature	Formula	Feature	Formula
Absolute mean value, $ \bar{x} $	$\frac{1}{N} \sum_{i=1}^N x_i $	Variance, D_x	$\frac{1}{N-1} \sum_{i=1}^N (x_i - \bar{x})^2$
Maximum peak value, x_p	$\max x_i $	Kurtosis, κ_T	$\frac{1}{N} \sum_{i=1}^N x_i^4$
Root mean square, x_{rms}	$\sqrt{\frac{1}{N} \sum_{i=1}^N x_i^2}$	Crest factor, C_f	$\frac{x_p}{x_{rms}}$
Square root value, x_r	$\left(\frac{1}{N} \sum_{i=1}^N \sqrt{ x_i }\right)^2$	Shape factor, S_f	$\frac{x_{rms}}{ \bar{x} }$

Using the instantaneous phase calculated using the Hilbert transform as explained in Section 1.2.5, circular domain features were determined using equations given in Table 13 (Martin et al. (2010)).

Table 13: Circular domain statistical features

Circular statistical feature	Formula
p^{th} -order sample trigonometric moment, μ_p	$\frac{1}{N} \sum_{n=1}^N \exp(jp\theta_n)$
Variance, σ^2	$1 - \mu_1 $
Skewness, γ	$\frac{ \mu_2 \sin(\arg(\mu_2) - 2 \arg(\mu_1))}{(\sigma^2)^{\frac{3}{2}}}$
Kurtosis, κ	$\frac{ \mu_2 \cos(\arg(\mu_2) - 2 \arg(\mu_1)) - \mu_1 ^4}{(\sigma^2)^2}$

Combining the time domain statistical features and the circular domain features, one can calculate a set of multi-domain statistical features (MSFs) that are representative of the properties of a signal. PCA and KPCA can then be used to analyse these features for dynamic behavioural classification purposes. A MSF set consisting of 12 features was considered. Illustrated in Figure 98, Figure 99 and Figure 100 are the determined Normalized Feature Values (NFVs).

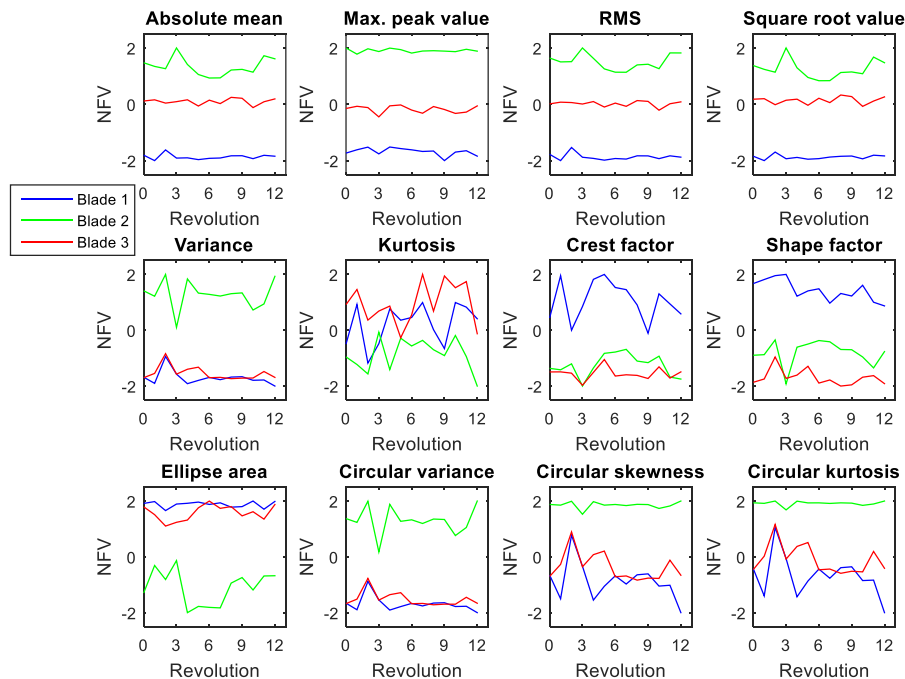


Figure 98: Averaged MSFs, SPCD₆, 650 rpm

Normalization of the feature values is done to make sure that the features fall within a similar range, so that they have equal weightage in the classification process. For 650 rpm, it can be easily observed that the three blades have different statistical features.

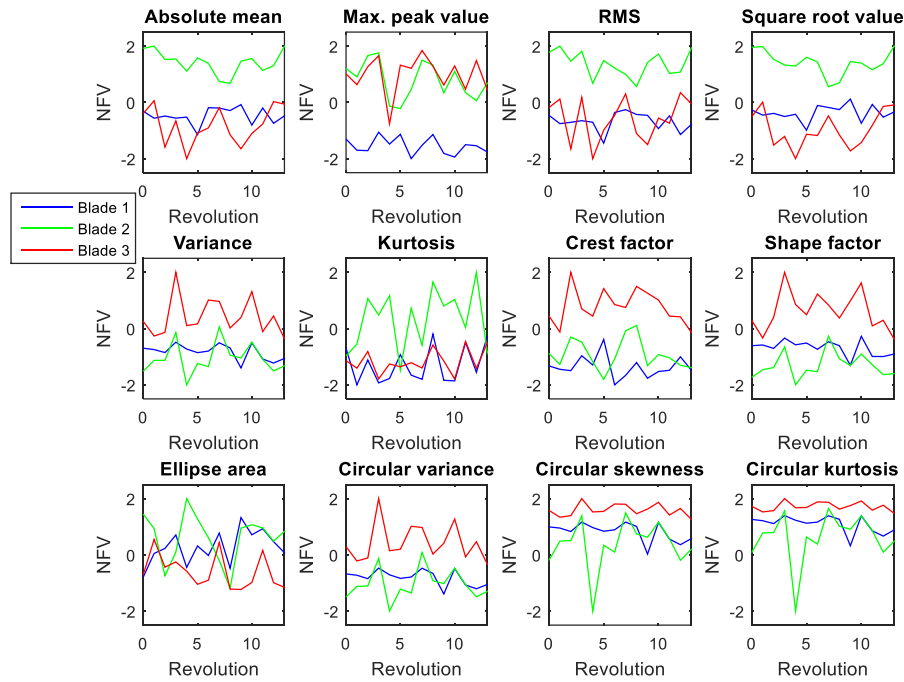


Figure 99: Averaged MSFs, SPCD₆, 1000 rpm

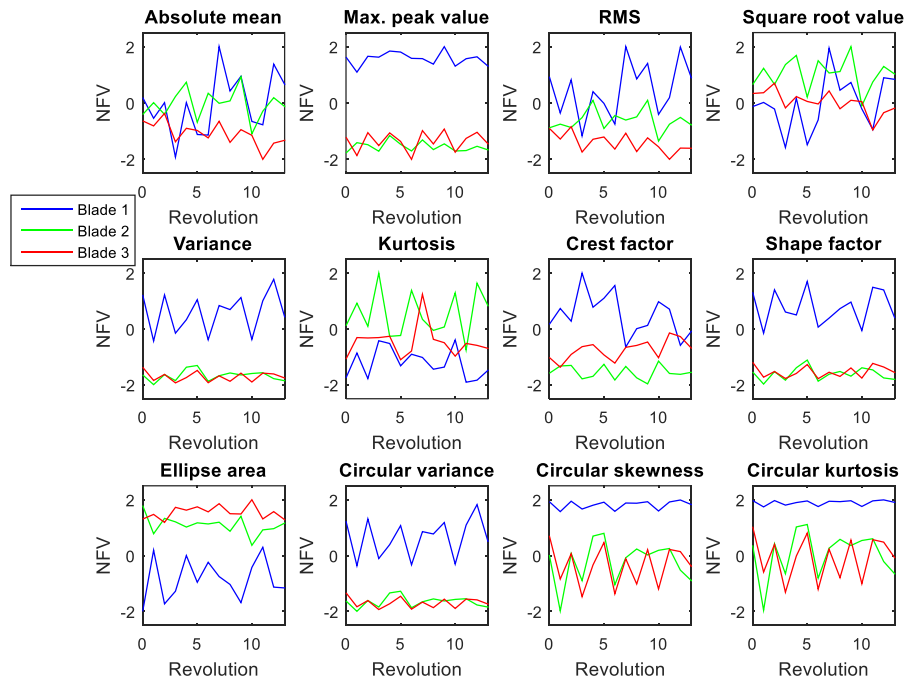


Figure 100: Averaged MSFs, SPCD₆, 1460 rpm

For 1000 rpm, the NFVs illustrated in Figure 99 show that some of features are not significantly different for different blades. These include the variance (blades 1 and 2) and the maximum peak value (blades 2 and 3). The same can be observed for 1460 rpm NFVs illustrated in Figure 100. Application of PCA and KPCA on the 650 rpm MSFs resulted in the results indicated in Figure 101 and Figure 102.

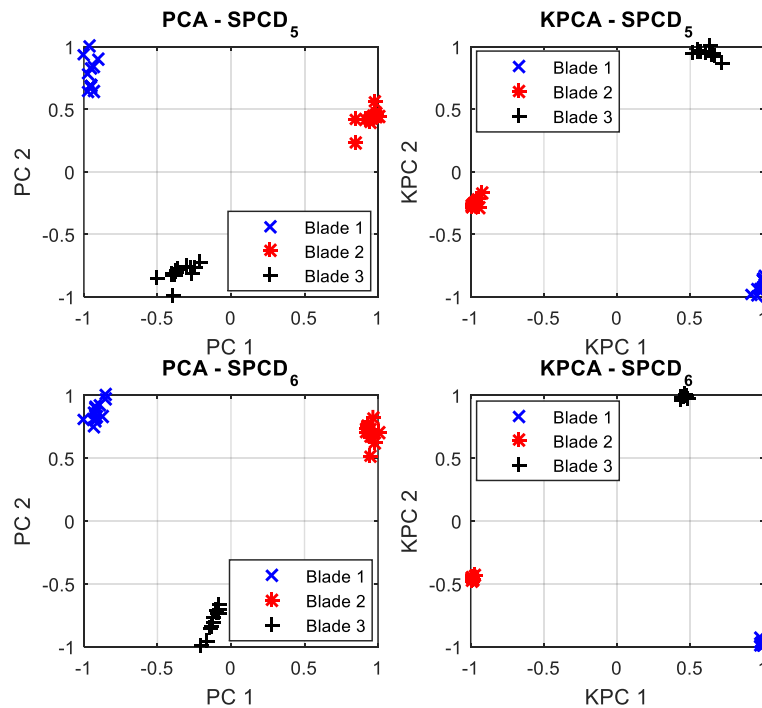


Figure 101: MSFs 650 rpm PCA and KPCA 2D

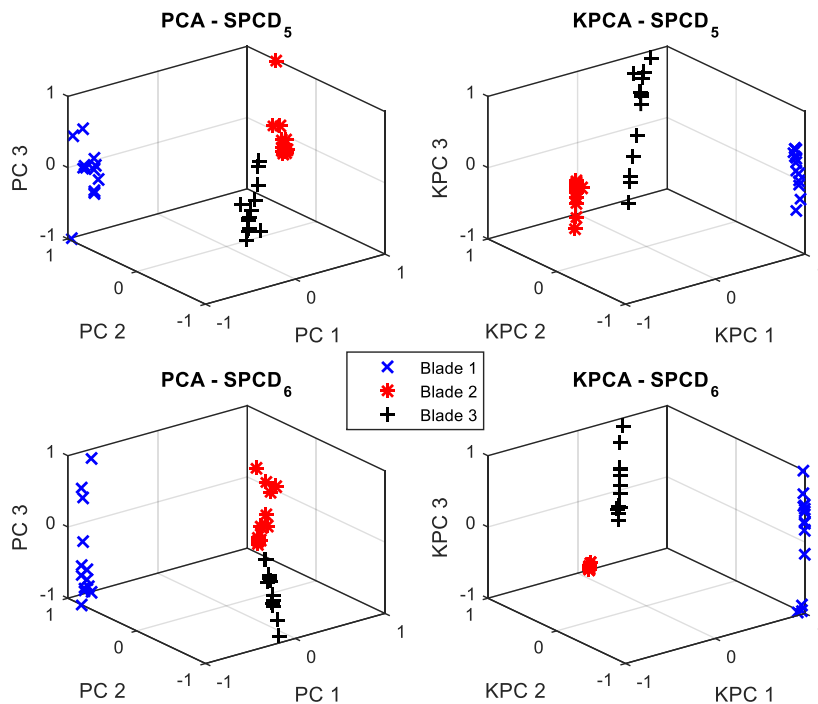


Figure 102: MSFs 650 rpm PCA and KPCA 3D

As can be observed in Figure 101 and Figure 102, MSFs produce clusters that are much more distinguishable, compared to the raw data clusters presented earlier (Figure 90 and Figure 91). The same can be concluded for the 1000 rpm and the 1460 rpm results presented in Figure 103, Figure 104, Figure 105 and Figure 106.

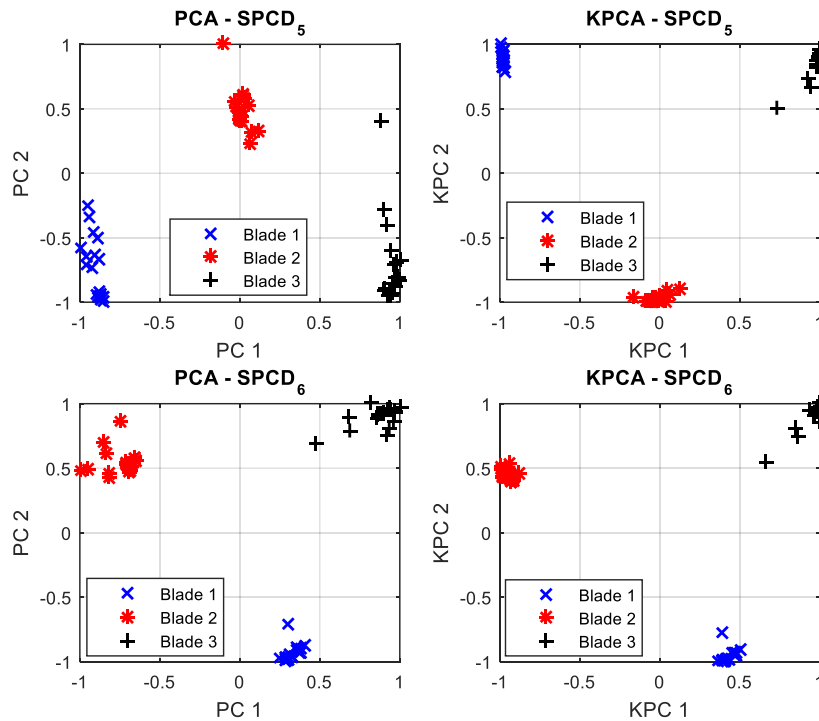


Figure 103: MSFs 1000 rpm PCA and KPCA 2D

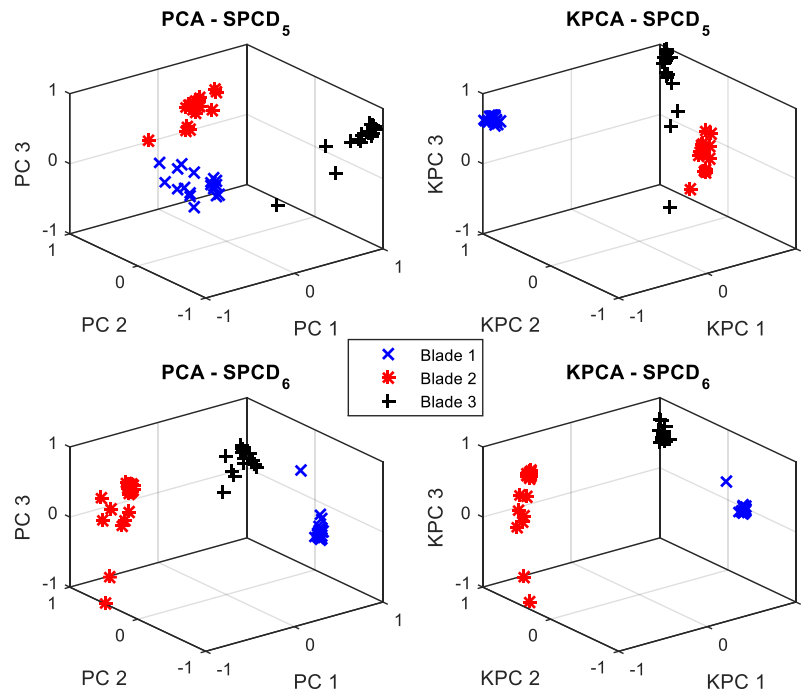


Figure 104: MSFs 1000 rpm PCA and KPCA 3D

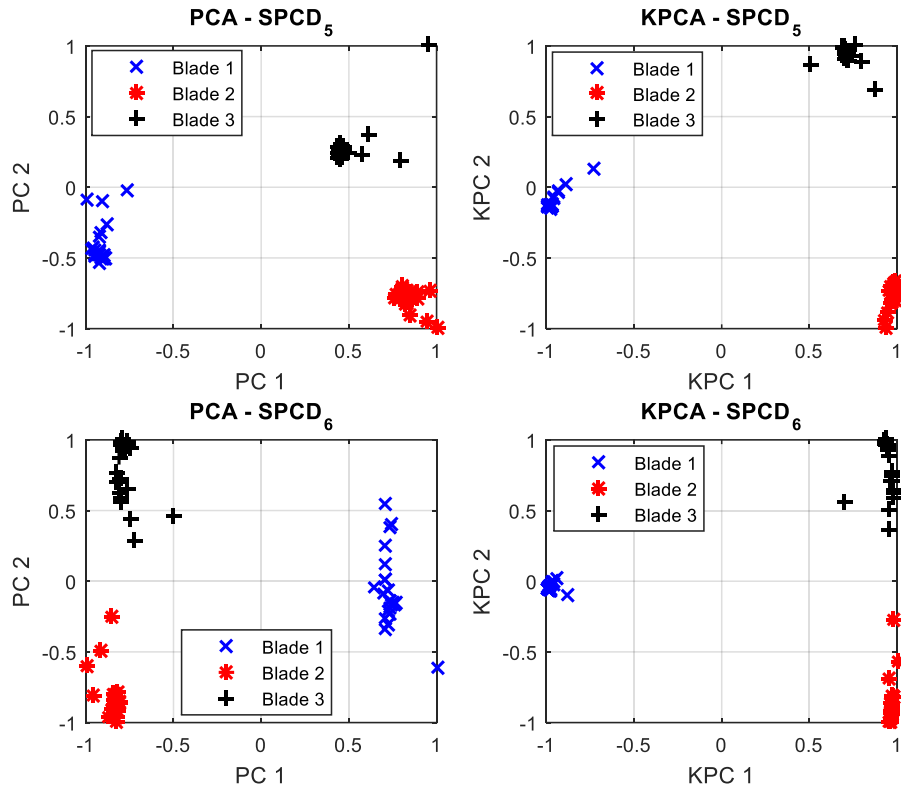


Figure 105: MSFs 1460 rpm PCA and KPCA 2D

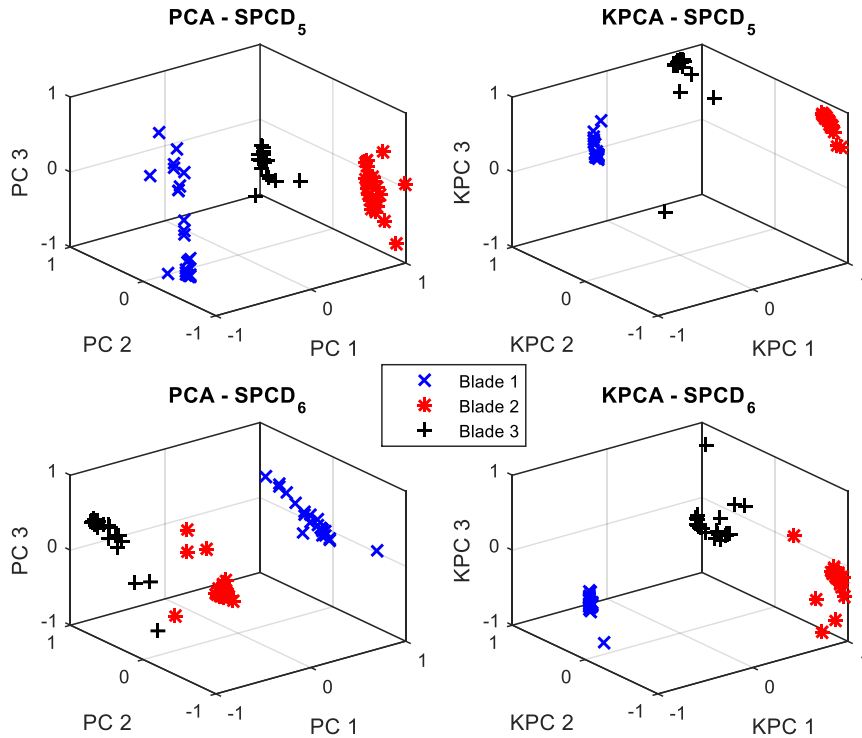


Figure 106: MSFs 1460 rpm PCA and KPCA 3D

Clustering parameter ratio S_b/S_w was also determined for the three rotational speeds investigated, this time for PCA and KPCA data calculated from the multi-domain statistical features. Results obtained are shown in Figure 107.

Figure 107 and Figure 108 illustrate how KPCA also tends to produce better clusters than the PCA approach, in terms of the higher S_b determined for each case analysed. Comparing the range of S_b/S_w for the raw SPCDs data and the multi-domain statistical features calculations (Figure 96 and Figure 107), it can be concluded that using multi-domain features extracted from the raw data provides results that make classification the blades much easier. MSFs S_b/S_w parameters are in the range of 0 to 1. They are only between 0 and 0.4 for the raw SPCDs data.

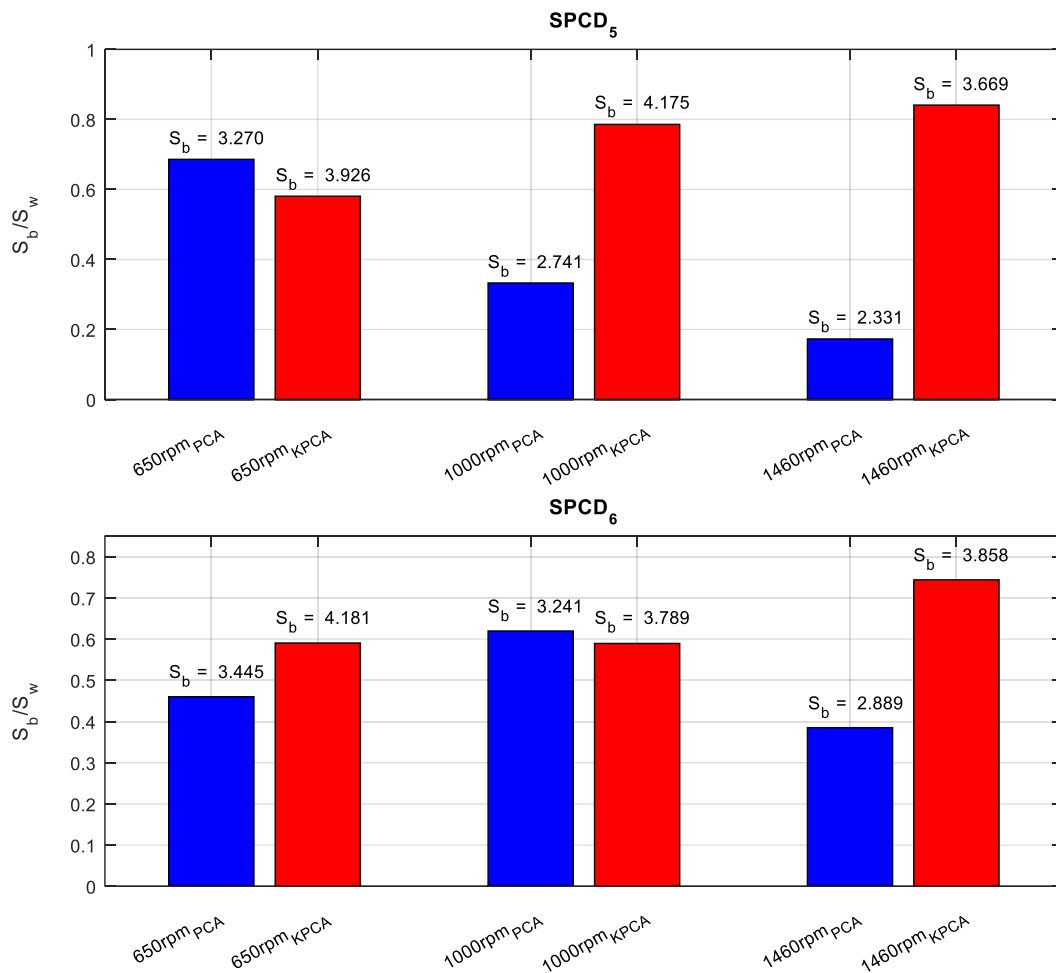


Figure 107: PCA and KPCA clustering performance for MSFs

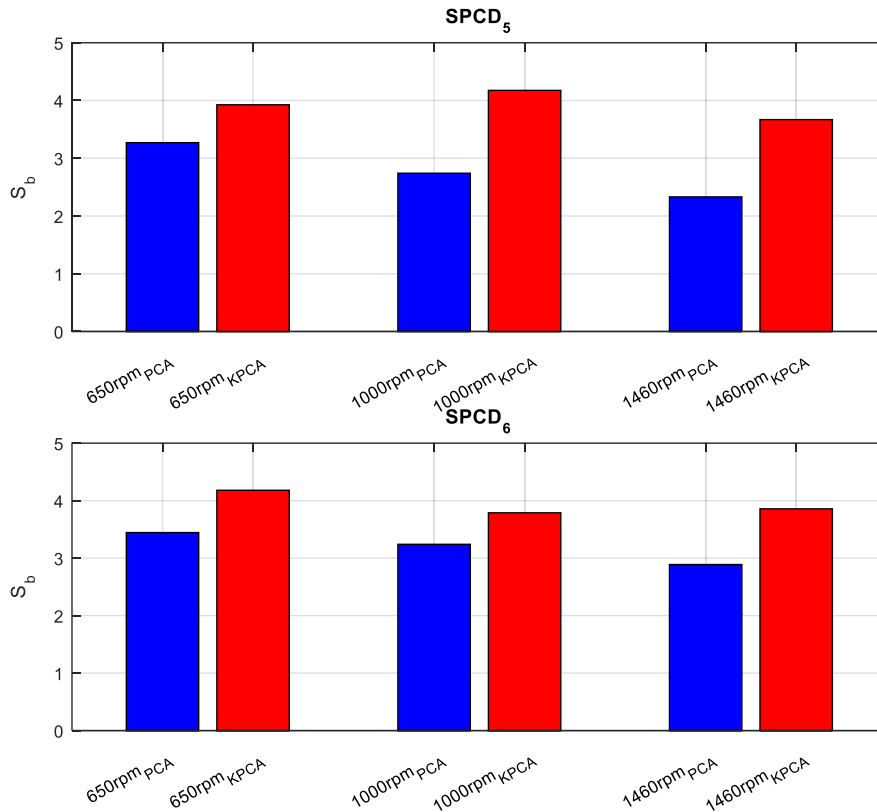


Figure 108: S_b based PCA and KPCA clustering performance for MSFs

5.2.3 Robustness to noise

An investigation was conducted to analyse how sensitive the proposed approaches are to signal noise. The signals were contaminated with pseudorandom Gaussian white noise of zero mean and a variable standard deviation (power). Standard deviation values were varied from 0.1 to 1.5 at 0.1 increments. Figure 109 shows $SPCD_6$ signals contaminated with different levels (standard deviation, σ) of Gaussian white noise for blade 1 measurements at 1000 rpm.

For 1000 rpm, it can be observed in Figure 110 that the SNR is nearly 0 dB for $\sigma = 1$, indicating that the signal and the noise almost have the same energy at that instant.

Illustrated in Figure 111 is the clustering performance of PCA and KPCA applied to the MSFs and the raw data for the $SPCD_6$ at the three rotational speeds considered. Results in Figure 111 indicate that S_b/S_w decreases with decreasing SNR, as the power of the noise introduced increases. The clustering performance of PCA and KPCA applied to the raw data degrades significantly with very little noise introduced into the system. For 1000 rpm for instance, S_b/S_w approaches zero at $\sigma = 0.4$, indicating that distinguishing between the different blades' clusters will not be possible.

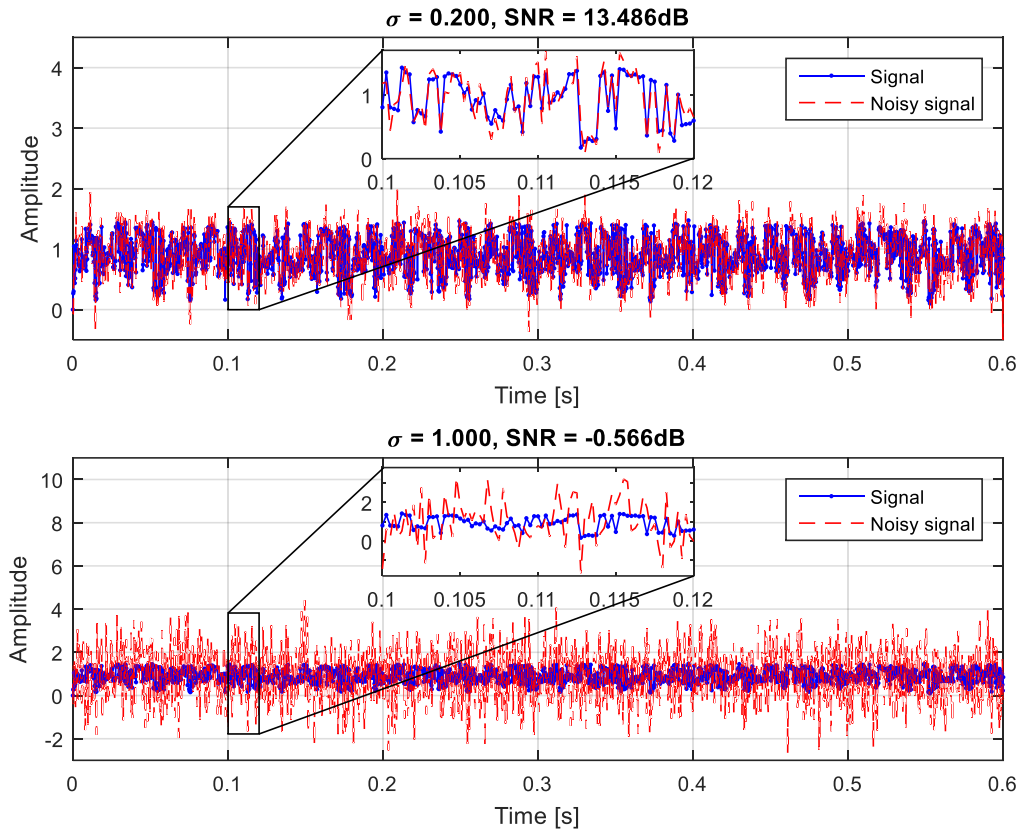


Figure 109: SPCD contamination with Gaussian white noise

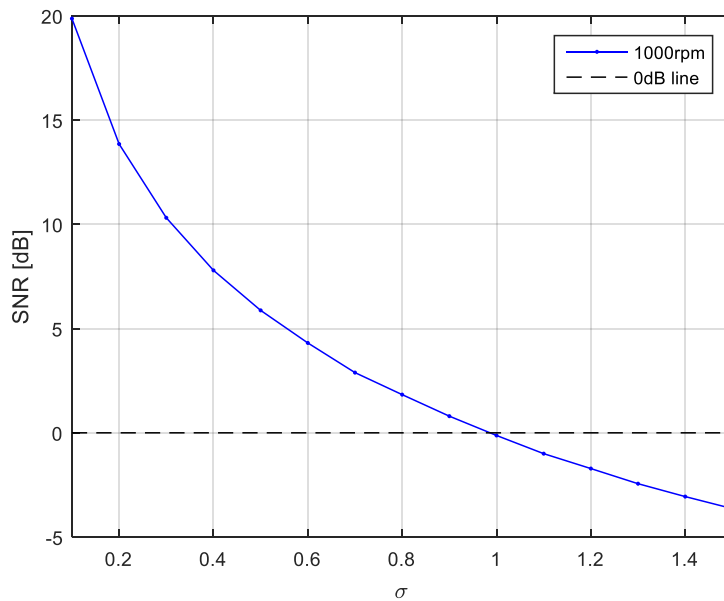


Figure 110: SNR variation with Gaussian noise standard deviation

MSF clustering performance on the other hand is quite robust to noise, and generally degrades substantially when the power of the noise gets closer to $\sigma = 1$. Illustrated in Figure 112 and Figure 113 are results for KPCA projections of MSF values for different levels of noise for SPCD 6 at 1000 rpm.

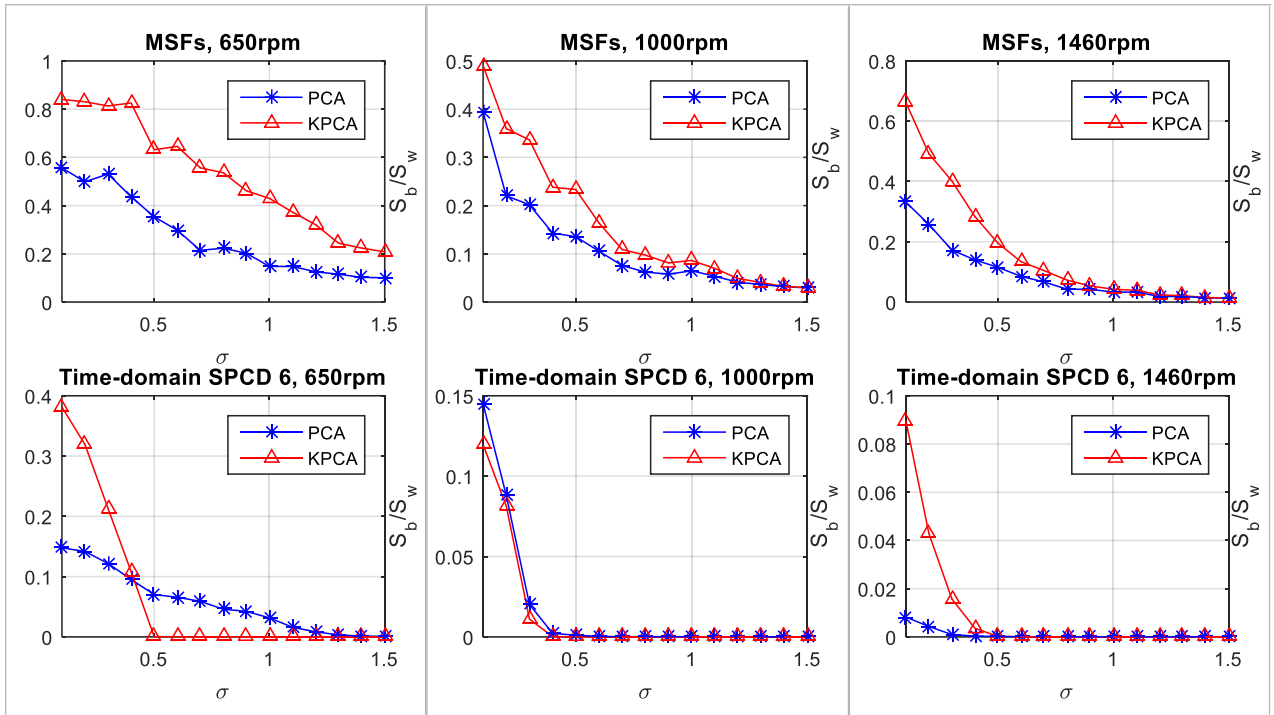


Figure 111: Clustering performance (S_b/S_w) as function of σ

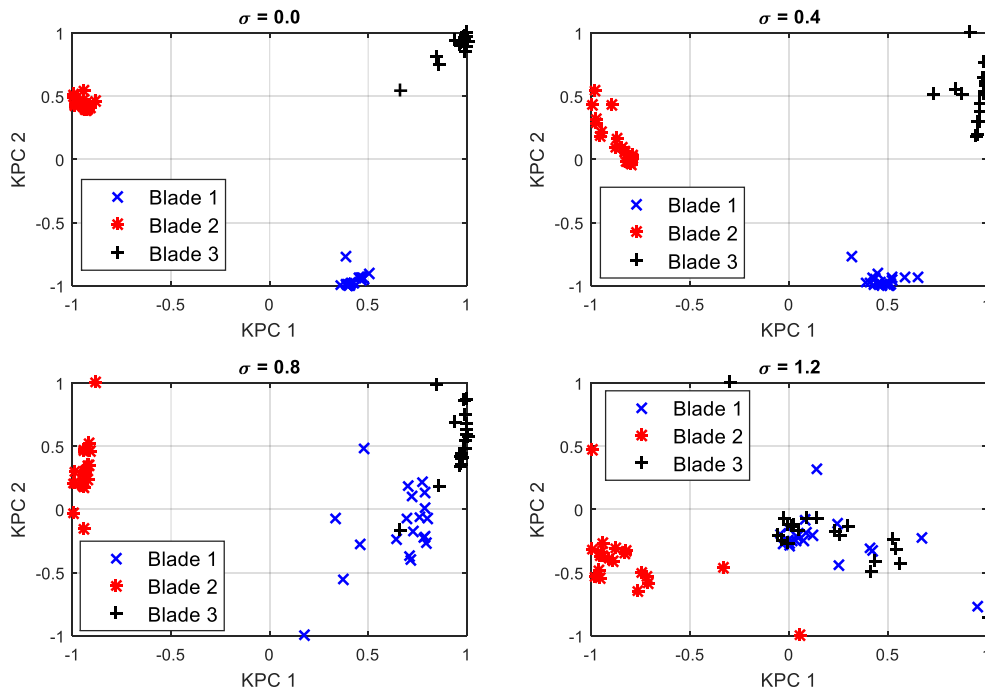


Figure 112: Cluster variation with noise level for KPCA SPCD₆ projected in a 2D feature space

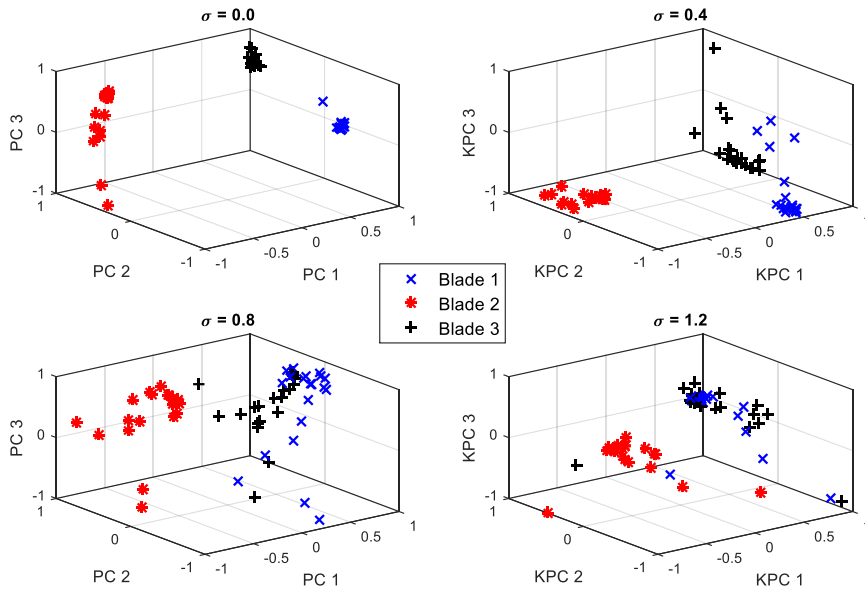


Figure 113: Cluster variation with noise level for KPCA SPCD₆ projected in a 3D feature space

5.3 Chapter conclusion

In this chapter, a comparative study of the performance of principal component analysis and kernel principal component analysis applied to shape principal component descriptors for condition monitoring purposes is conducted. The use of multi-domain statistical features as inputs for data reduction for classification purposes is successfully investigated, and the robustness of the technique to system noise also analysed.

It is illustrated that the data nonlinear transformation using Gaussian kernels in KPCA implementation allows better classification through incorporating the nonlinear relationships that exist in the SPCDs data. Utilizing a multi-domain statistical feature set composed of eight-time domain and four circular domain statistical features proved to also have better blade classification compared to the raw time domain SPCDs. Multi-domain statistical features classification is shown to be significantly robust to noise compared to classification using the raw time domain data. It was noted that raw data classification fails completely at a 0.4 standard deviation noise level, whilst MSFs could still separate the healthy blade from the two damaged blades at 1.5 standard deviation noise level.

CHAPTER 6: CONCLUSIONS AND RECOMMENDATIONS

6.1 Conclusions

This research focused on the development and application of a photogrammetric boundary shape analysis-based condition monitoring technique. The development was done specifically to suit rotating structures that have to be analysed whilst they are in operation. Shape boundaries were characterized by first representing them using the chain code as the shape signature of choice. Elliptical Fourier coefficients of these chain codes were then decomposed using PCA, and four (2D analysis) or six (3D analysis) shape principal components or geometric modes (V) obtained. These uncorrelated geometric modes are unique to the shape, and their relationships to the form of the shape of interest were investigated via scaling of their respective PCA scores. SPCDs were then defined from these shape principal components. SPCDs variation from one image to the next in a sequence of images could then be analysed to provide information in the way the shape changes. Since the way the chosen shapes change was directly associated with the machine responses, the dynamic behaviour of the machines could be characterized and investigated to classify different types and severity of faults.

In the development of this non-contact measurement technique, specific shape characteristics associated with each of the V s were analysed. It was illustrated that each of these components is associated with a unique shape representation. Whilst the physical shape variation resulting from the behaviour of a machine might not exactly mimic a specific geometric mode, it was illustrated different machine behaviour affect the characterising shape principal components differently. This makes it possible to have four or six parameters in the form of SPCDs that one can monitor when investigating the dynamic behaviour of a machine. For a 2D analysis, a sensitivity investigation indicated that the perspective at which images are captured by a camera affect the apparent shape variation that can be observed. It was shown that it is essential to understand the shape whose variation is to be monitored. This is essential when deciding how the system must be set up for better detection of any shape variation resulting from the dynamics of the machine.

In a 2D analysis of a Bently Nevada rotor system, different forms of unbalance in the system could be detected and classified. The measurements were captured using a single sensor (one camera) and the 2D approach was confirmed by conventional proximity probes. It can be concluded that the shape-based approach is very promising in terms of limiting the number of sensors that one has to employ to fully diagnose a rotating machine. The fact that the approach is non-contact and therefore non-intrusive, renders it favourable in some cases. The high sensitivity of shape analysis was also proven to be useful in detecting rotor-stator rub faults. Uniaxial conventional sensors tend to capture signals with low SNR values in those types of cases. On the other hand, the interference of components may result in significant 2D variations of a shape enclosed between a shaft and a bearing housing for instance. It can be concluded from the investigation conducted that for some applications, the proposed technique can detect faults efficiently and accurately.

For the 3D shape analysis, data reduction and classification of the SPCDs was done through PCA of the revolution segmented SPCD. Instead of analysing the SPCDs by transforming them into the frequency domain as done for the 2D shape analysis, it was successfully illustrated that the data reduction approach simplified the classification of different blade

damage modes. Clustering the SPCDs by projecting their PCs in either a 2D (PCs 1 and 2) or a 3D (PCs 1, 2 and 3) feature space provided three parameters in the form of spherical coordinates. These parameters identifying the centroid locations of the SPCDs clusters illustrated how the proposed technique can be utilized for tracking progressing damage. The 3D shape analysis was firstly conducted in a FE controlled environment, before being extended to an actual physical system. The experimental data was correlated to measurements documented by other researchers in terms of size of full-scale turbines and recorded maximum blade responses. This was done to illustrate the feasibility of adopting a shape-based measurement technique as a condition monitoring tool for field applications.

Kernel based PCA was used to reduce the SPCDs. Compared to the linear based PCA, KPCA implementation was proved to be a better fault classification tool. Combining the KPCA data reduction with multi-domain statistical features of the SPCDs, instead of reducing the raw time domain SPCDs, resulted in a more robust better performing system that could classify the blades even in significantly noise contaminated signals.

Whilst the investigations conducted in this study demonstrate the applicability of a shape-based condition monitoring approach, there are some limitations especially when it comes to industrial adaptation of the technique. Being an image-based system, the technique relies on having a clear line of sight of the structure under investigation. In an industrial or workshop setting, machine components of interest might be obscured or located in confined spaces making it impossible to capture images for contour extraction. For visible components, the quality of the images in terms of resolution, blurriness and noise should be such that edges of interest can be isolated from the background accurately. For outdoor applications, shadows, variability in contrast, lighting and uneven illumination can distort boundaries leading to inaccurate measurements.

Computational complexity is also an important limitation to the applicability of the proposed technique. In the 3D investigation conducted, a sampling rate of 4000 FPS was used, and the camera capacity only allowed storage of 5173 images (measurement duration of 1.29 s) per measurement. Thus, the camera capacity and desired measurement duration dictate the sampling frequency that one can use, which in turn can be limiting to the machine's response frequency range that can be captured. Advanced image processing techniques are also required to process the large volumes of captured image and perform the necessary edge detection. The real-time applicability of the technique requires significant computational resources and complex data analytics infrastructure.

It has been highlighted in the previous discussions that one of the advantages of using non-contact measurement techniques is that no machine shutdowns are needed. Without prior knowledge of the shape based dynamic behaviour of a machine, the approach requires that measurements are taken at various stages in the life cycle of a machine. This will be necessary to create a baseline to which deviations from normal behaviour can be compared to. In the case of outdoor measurements, this can be complicated as the measurement equipment cannot be left in harsh operating conditions. Long term continuous condition monitoring strategies using the proposed approach therefore requires complicated planning and implementation.

In the 3D investigation, it was illustrated that corresponding point matching of the stereo captured images is necessary to extract depth response measurements. The investigation

showed that in cases where the out-of-plane responses are too small, the camera resolution has to be of very high quality to ensure that resolution induced contour noise does not make it impossible to match corresponding points accurately. Small response measurements using the proposed technique is therefore limited to high spatial resolution cameras.

6.2 Recommendations and future work

In this investigation, the elliptical Fourier descriptors were applied to the chain code shape signatures in characterising the contours of interest for shape analysis. Whilst this is the most commonly adopted approach for shape analysis in object recognition and shape matching, other forms of shape signatures and shape feature extraction techniques still need to be evaluated and their performance compared to this approach.

Other data reduction techniques such as Independent Component Analysis (ICA) also need to be considered for this type of investigation. PCA and KPCA were utilized as the data reduction techniques as the relevance of the PCs to consider is easily recognised from the calculated variance values. This is not the case for ICA, but researchers have come up with ways to select the most dominant components, such as the variance of a histogram of the projected data. Further investigations still need to be conducted with regards to that matter.

Incorporating progressing damage parameters into an updated finite element model of a machine for predicting remaining life of a damaged component is something that must be conducted. This will be useful in understanding how far shape analysis can be utilized as a tool for extracting information that can be used in designing more durable components. Being a shape-based approach, a better understanding of the way in which the determined geometric modes can be related to a structure's mode shapes is also something of interest. This will aid in basic understanding of the dynamics of structures. Full-scale implementation of this technique in the field must be conducted as well. Photogrammetry on full-scale wind turbine blades using high speed cameras was highlighted in the literature review. The future work entails application of a non-contact optical approach that does not require any form of surface preparation in an actual wind turbine blade analysis.

In the investigation presented, geometric mode shapes were decomposed through the use of vector norms to represent each shape format with four (2D) or six (3D) scalar parameters. This approach results in loss of some of the geometric modes' properties, information which can potentially provide further insights in the dynamic behaviour of the machine. For instance, the use of derivatives of ODS has been known to be efficient when it comes to detecting localized damage. Further investigations in which multidimensional processing of geometric mode shapes is implemented should be explored. This can potentially elevate the applicability of the technique to damage localization, damage quantification and useful remaining life estimation.

Motion magnification has been proven to be a powerful tool for condition monitoring purposes. The accuracy and reliability of the presented shape analysis technique has been shown to be dependent on the extent to which the shape of a structure changes from one captured frame to the next. As part of further investigations, it is necessary to analyse how the use of motion magnification can enhance the quality and applicability of shape analysis as a condition monitoring technique, especially for large structures that might have high frequency dynamic properties in addition to significant rigid body motions.

Research included in the literature review has indicated the feasibility of mounting cameras on drones to capture 3DPT and DIC data for large structures. Ideally, cameras capturing the data must be stationary relative to the static components of the structure under investigation. In the case of offshore wind turbines for example, the ocean current will make this difficult. Any conditions that can disturb the set camera positions/orientation (high speed wind for example), obscure field of view of the cameras or diminish the quality of the captured images will make it difficult to use image-based techniques. Having a reference static point on the structure in the camera field of view means that frame correction through compensation of the camera rig position relative to the 'known' reference static position can be done for each frame captured. Alternatively, the movement of the cameras can be measured in 6 DOFs using Inertial Measurement Unit (IMU) sensors, and that data used to stabilize images captured images as part of the preprocessing analysis. This should also be investigated further.

In terms of validation of the technique and comparison to other measurement approaches, other optical techniques such as SLDV can be employed to extract ODSs of components. Analysis of these ODSs to evaluate how sensitive alternative methods are to different levels of damage will be a good way to benchmark robustness of shape-based condition monitoring. These types of investigations should also be considered as part of the future studies to further develop and verify the proposed technique.

REFERENCES

- Abanto-Bueno, J. & Lambros, J. 2002. Investigation of crack growth in functionally graded materials using digital image correlation. *Engineering Fracture Mechanics*, 69: 1695–1711.
- Adams, L.M. 2010. *Rotating Machinery Vibration From Analysis to Troubleshooting*. 2nd ed. CRC Press.
- Antoniadou, I., Dervilis, N., Papatheou, E., Maguire, A.E., Worden, K. & Sheffield, S. 2015. Aspects of structural health and condition monitoring of offshore wind turbines. *Phil. Trans. R. Soc.*
- Baqersad, J., Niezrecki, C. & Avitabile, P. 2015. Full-field dynamic strain prediction on a wind turbine using displacements of optical targets measured by stereophotogrammetry. *Mechanical Systems and Signal Processing*, 62–63: 284–295.
- Bently, D.E., Hatch, C.T. & Grissom, B. 2003. *Fundamentals of Rotating Machinery Diagnostics*. 1st ed. ASME Press eBooks.
- Bhonsle, S., Klinzmann, A., Park, F. & Esser, E. 2009. Centroid Distance Function and the Fourier Descriptor with Applications to Cancer Cell Clustering. *UC Irvine*.
<http://www.math.uci.edu/icamp/summer/research/klinzmann/cdfd.pdf>.
- Bose, P. 2000. *The encoding and Fourier descriptors of arbitrary curves in 3-dimensional space*. University of Florida.
<http://citeseerx.ist.psu.edu/viewdoc/download?doi=10.1.1.7.1087&rep=rep1&type=pdf>.
- Caesarendra, W., Kosasih, B., Tieu, A.K. & Moodie, C. a S. 2014. Circular domain features based condition monitoring for low speed slewing bearing. *Mechanical Systems and Signal Processing*, 45(1): 114–138.
- Caro-Martín, C.R., Delgado-García, J.M., Gruart, A. & Sánchez-Campusano, R. 2018. Spike sorting based on shape, phase, and distribution features, and K-TOPS clustering with validity and error indices. *Scientific Reports*, 8(1): 33–38.
- Church, C.B. 2015. *Turbomachine Internal Pressure and Blade Response Modelling*. University of Pretoria.
- Ciang, C.C., Lee, J.-R. & Bang, H. 2008. Structural health monitoring for a wind turbine system: a review of damage detection methods. *Measurement Science and Technology*, 19(12): 122001.
- Crammond, G., Boyd, S.W. & Dulieu-Barton, J.M. 2013. Speckle pattern quality assessment for digital image correlation. *Optics and Lasers in Engineering*, 51: 1368–1378.
- Diamond, D.H., Heyns, P.S. & Oberholster, A.J. 2016. Accuracy evaluation of sub-pixel structural vibration measurements through optical flow analysis of a video sequence. *Measurement*: 1–21.

- Ebert, R., Lutzmann, P., Scherer, C., Scherer-Negenborn, N., Göhler, B. & Van Putten, F. 2014. Laser vibrometry for wind turbines inspection. In *Advanced Solid State Lasers, ASSL 2014*. Washington, D.C.: OSA.
- Ertek, G. & Kailas, L. 2021. Analyzing a decade of wind turbine accident news with topic modeling. *Sustainability (Switzerland)*, 13(22).
- Freeman, H. 1974. Computer Processing of Line-Drawing Images. *Computing Surveys*, 6(1): 58–97.
- García Márquez, F.P. & Peco Chacón, A.M. 2020. A review of non-destructive testing on wind turbines blades. *Renewable Energy*, 161: 998–1010.
- Ge, D. & Farina, D. 2013. Spike Sorting. In *Introduction to Neural Engineering for Motor Rehabilitation*. Elsevier: 155–172.
- Gharavian, M.H., Almas Ganj, F., Ohadi, A.R. & Heidari Bafroui, H. 2013. Comparison of FDA-based and PCA-based features in fault diagnosis of automobile gearboxes. *Neurocomputing*, 121: 150–159.
- Grama, S.N. & Subramanian, S.J. 2014. Computation of full-field strains using principal component analysis. *Experimental Mechanics*. 54(6):913–933.
- Guan, B., Su, Z., Yu, Q., Li, Z., Feng, W., Yang, D. & Zhang, D. 2022. Monitoring the blades of a wind turbine by using videogrammetry. *Optics and Lasers in Engineering*, 152: 106901.
- Gwashavanhu, B., Oberholster, A.J. & Heyns, P.S. 2016. Rotating blade vibration analysis using photogrammetry and tracking laser Doppler vibrometry. *Mechanical Systems and Signal Processing*: 174-186.
- GWEC. 2023. Global Wind Energy Council. <https://gwec.net/globalwindreport2023/> [2023, August 15].
- Ha, N.S., Jin, T. & Seo, N. 2013. Modal analysis of an artificial wing mimicking an *Allomyrina dichotoma* beetle's hind wing for flapping-wing micro air vehicles by noncontact measurement techniques, 51: 560–570.
- Hahn, B., Durstewitz, M. & Rohrig, K. 2007. Reliability of Wind Turbines: Experiences of 15 years with 1,500 WTs. *Wind Energy: Proceedings of the Euromech Colloquium*, (July): 329–332.
- Halkon, B.J. & Rothberg, S.J. 2006. Vibration measurements using continuous scanning laser vibrometry: Advanced aspects in rotor applications. *Mechanical Systems and Signal Processing*, 20(6): 1286–1299. <http://www.mendeley.com/catalog/vibration-measurements-using-continuous-scanning-laser-vibrometry-advanced-aspects-rotor-application/> [2014, November 29].
- Hasanen, M., Saarenrinne, P. & Kokko, V. 2013. A New technique for torsional vibration measurements with. In *The 26th International Congress of Condition Monitoring and Diagnostic Engineering Management*. Tampere: 1–6.

- He, Q., Kong, F. & Yan, R. 2007. Subspace-based gearbox condition monitoring by kernel principal component analysis. *Mechanical Systems and Signal Processing*, 21(4): 1755–1772.
- Helfrick, M.N., Niezrecki, C., Avitabile, P. & Schmidt, T. 2011. 3D digital image correlation methods for full-field vibration measurement. *Mechanical Systems and Signal Processing*. 25(3):917-927
- Helfrick, M.N., Pingle, P., Niezrecki, C. & Avitabile, P. 2009. Using Full-Field Vibration Measurement Techniques for Damage Detection. In *Proceedings of the IMAC-XXVII*.
- Iwata, H., Nesumi, H., Ninomiya, S., Takano, Y. & Ukai, Y. 2002. Diallel Analysis of Leaf Shape Variations of Citrus Varieties Based on Elliptic Fourier Descriptors. *Breeding Science*, 52: 89–94.
- Jusoh, N.A. & Zain, J.M. 2009. Application of Freeman Chain Codes: An Alternative Recognition Technique for Malaysian Car Plates. *International Journal of Computer Science and Network Security*, 9(11): 222–227.
- Kazmi, I.K., You, L. & Zhang, J.J. 2013. A Survey of 2D and 3D Shape Descriptors. *2013 10th International Conference Computer Graphics, Imaging and Visualization*: 1–10. <http://ieeexplore.ieee.org/lpdocs/epic03/wrapper.htm?arnumber=6658152>.
- Khadka, A., Fick, B., Afshar, A., Tavakoli, M. & Baqersad, J. 2020. Non-contact vibration monitoring of rotating wind turbines using a semi-autonomous UAV. *Mechanical Systems and Signal Processing*, 138: 106446.
- Kim, D.Y., Kim, H.-B., Jung, W.S., Lim, S., Hwang, J.-H. & Park, C.-W. 2013. Visual testing system for the damaged area detection of wind power plant blade. In *IEEE ISR 2013*. IEEE: 1–5.
- Krüger, A. 2012. Transient Dynamic Finite Element Modelling of Flexible Rotor Systems with Nonlinear Fluid Film Bearings and Faults. University of Pretoria.
- Kuhl, F.P. & Giardina, C.R. 1982. Elliptic Fourier features of a closed contour. *Computer Graphics and Image Processing*, 18(3): 236–258.
- Lado-Roigé, R., Font-Moré, J. & Pérez, M.A. 2023. Learning-based video motion magnification approach for vibration-based damage detection. *Measurement*, 206: 112218.
- LeBlanc, B., Niezrecki, C., Avitabile, P., Chen, J. & Sherwood, J. 2013. Damage detection and full surface characterization of a wind turbine blade using three-dimensional digital image correlation. *Structural Health Monitoring*, 12: 430–439.
- Lecompte, D., Smits, a., Bossuyt, S., Sol, H., Vantomme, J., Van Hemelrijck, D. & Habraken, a. M. 2006. Quality assessment of speckle patterns for digital image correlation. *Optics and Lasers in Engineering*, 44(11): 1132–1145.
- Littrell, N. 2005. Understanding and Mitigating Shaft Runout. *Orbit Magazine*: 5–17.

- Liu, Zhenxing, Wei, Y., Chen, L., Liu, Zhansheng & Wang, X. 2018. Simulation of oil whirl for geared rotor journal bearing system. *Journal of Physics: Conference Series*, 1074: 012045.
- Lomenzo, R.A. 1998. *Static Misalignment Effects in a Self-Tracking Laser Vibrometry System for Rotating Bladed Disks by Static Misalignment Effects in a Self-Tracking Laser Vibrometry System for Rotating Bladed Disks*. Virginia Polytechnic Institute and State University.
- Lu, M., Chai, Y. & Liu, Q. 2019. Observation of tower vibration based on subtle motion magnification. *IFAC-PapersOnLine*, 52(24): 346–350.
- Lundstrom, T., Baqersad, J. & Niezrecki, C. 2016. Monitoring the dynamics of a helicopter main rotor with high-speed stereophotogrammetry. *Experimental Techniques*, 40(3): 907–919.
- MacCamhaoil, M. 1989. Application Note – Static and Dynamic Balancing of Rigid Rotors. Available at: <https://www.bksv.com/media/doc/bo0276.pdf> [2023, November 30].
- Di Maio, D. & Ewins, D.J. 2010. Applications of continuous tracking SLDV measurement methods to axially symmetric rotating structures using different excitation methods. *Mechanical Systems and Signal Processing*, 24(8): 3013–3036.
- Martarelli, M. & Ewins, D.J. 2006. Continuous scanning laser Doppler vibrometry and speckle noise occurrence. *Mechanical Systems and Signal Processing*, 20(8): 2277–2289.
- Martin, S.C., Muster, G.S., Curilem, M., Fuentealba, G., Gallegos, C. & Melgarejo, C. 2010. Feature Extraction Using Circular Statistics Applied to Volcano Monitoring. In *Progress in Pattern Recognition, Image Analysis, Computer Vision, and Applications*. 458–466.
- McFadden, C. 2018. The World's Fastest 10 Trillion FPS Camera is Here And it Can Freeze Time. <https://interestingengineering.com/the-worlds-fastest-10-trillion-fps-camera-is-here-and-it-can-freeze-time> [2019, November 5].
- Mebatsion, Hibru K., Paliwal, J. & Jayas, D.S. 2012. A novel, invariant elliptic Fourier coefficient based classification of cereal grains. *Biosystems Engineering*, 111(4): 422–428.
- Mebatsion, H. K., Paliwal, J. & Jayas, D.S. 2012. Evaluation of variations in the shape of grain types using principal components analysis of the elliptic Fourier descriptors. *Computers and Electronics in Agriculture*, 80: 63–70.
- Mistras Group. 2019. Wind Energy Turbine Inspection, Repair and Monitoring. https://www.google.com/imgres?imgurl=https%3A%2F%2Fmistrasgroup.co.uk%2Fwp-content%2Fuploads%2F2017%2F02%2FBlade-and-Tower-Services.png&imgrefurl=https%3A%2F%2Fmistrasgroup.co.uk%2Fwind-energy%2F&docid=NqnyCfQnsKaBIM&tbnid=HJ_46xZ_UCGjKM%3A&vet=1&w=379&h= [2019, October 24].

- Molina-Viedma, A.J., Felipe-Sesé, L., López-Alba, E. & Díaz, F. 2018. High frequency mode shapes characterisation using Digital Image Correlation and phase-based motion magnification. *Mechanical Systems and Signal Processing*, 102: 245–261.
- Najafi, N. & Vesth, A. 2018. Establishing a robust testing approach for displacement measurement on a rotating horizontal-axis wind turbine. *Wind Energy Science*, 3(1): 301–311.
- National Instruments. 2018. IMAQ Learn Binocular Stereo Calibration VI - NI Vision 2017 for LabVIEW: 2017–2018. http://zone.ni.com/reference/en-XX/help/370281AG-01/imaqvision/imaq_learn_binocular_stereo_calibration/ 20 September 2019.
- Nelson, F.C. 2007. Rotor Dynamics without Equations Rotor Dynamics without Equations Rotor Dynamics without Equations Rotor Dynamics without Equations. *International Journal of COMADEM*, 10(3): 2–10.
- Nguyen, V.H. & Golinval, J.-C. 2010. Fault detection based on Kernel Principal Component Analysis. *Engineering Structures*, 32(11): 3683–3691.
- Oberholster, A.J. & Heyns, P.S. 2011. Eulerian laser Doppler vibrometry: Online blade damage identification on a multi-blade test rotor. *Mechanical Systems and Signal Processing*, 25(1): 344–359.
- Ozbek, M., Rixen, D.J., Erne, O. & Sanow, G. 2010. Feasibility of monitoring large wind turbines using photogrammetry. *Energy*, 35(12): 4802–4811.
- Pan, B. 2010. Recent Progress in Digital Image Correlation. *Experimental Mechanics*, 51(7): 1223–1235. <http://link.springer.com/10.1007/s11340-010-9418-3> [2014, March 24].
- Pasialis, V. & Lampeas, G. 2015. Shape descriptors and mapping methods for full-field comparison of experimental to simulation data. *Applied Mathematics and Computation*, 256: 203–221.
- Patterson, E.A. & Patki, A.S. 2012. On Characterizing Strain Fields in Impact-Damaged Composites using Shape Descriptors. *Procedia IUTAM*, 4: 126–132.
- Russakovsky, O., Deng, J., Su, H., Krause, J., Satheesh, S., Ma, S., Huang, Z., Karpathy, A., Khosla, A., Bernstein, M., Berg, A.C. & Fei-Fei, L. 2015. ImageNet Large Scale Visual Recognition Challenge. *International Journal of Computer Vision*, 115(3): 211–252.
- Sanati, H. & Wood, D. 2018. Condition Monitoring of Wind Turbine Blades Using Active and Passive Thermography. *Applied Sciences*, 8.
- Sarraf, A. & Mao, Z. 2018. Wind Turbine Blade Damage Detection Via 3-Dimensional Phase-Based Motion Estimation. *The 11th International Workshop on Structural Health Monitoring*.
- Scotland Against Spin. 2023. Summary of Wind Turbine Accident Data. <https://scotlandagainstspin.org/turbine-accident-statistics/>. [2023, August 15].

- Shao, R., Hu, W., Wang, Y. & Qi, X. 2014. The fault feature extraction and classification of gear using principal component analysis and kernel principal component analysis based on the wavelet packet transform. *Measurement*, 54: 118–132.
- SKF. 2018. SKF Reliability Systems® Vibration Diagnostic Guide CM5003. http://edge.rit.edu/edge/P14453/public/Research/SKF_VibrationGuide.pdf [2018, January 9].
- Śmieja, M., Mamala, J., Prażnowski, K., Ciepliński, T. & Szumilas, Ł. 2021. Motion magnification of vibration image in estimation of technical object Condition-Review. *Sensors*. 21(19):6572.
- Souza, B.C., Lopes-dos-Santos, V., Bacelo, J. & Tort, A.B.L. 2019. Spike sorting with Gaussian mixture models. *Scientific Reports*, 9(1): 1–14.
- Spranghers, K., Lecompte, D., Sol, H. & Vantomme, J. 2012. Material characterization of blast loaded plates. In *9th National Congress on Theoretical and Applied Mechanics*. http://meca.rma.ac.be/nctam/Experimental_Techniques/4_Spranghers.pdf [2013 August 9].
- Sutton, M.A., Orteu, J.J. & Schreier, H.W. 2009. *Image Correlation for Shape, Motion and Deformation Measurements*. New York, NY: Springer Science and Business Media.
- Tippmann, J.D., Zhu, X. & Lanza di Scalea, F. 2015. Application of damage detection methods using passive reconstruction of impulse response functions. *Philosophical Transactions of the Royal Society A*. 373(2035):20140070.
- Tiwari, V., Sutton, M. a., McNeill, S.R., Xu, S., Deng, X., Fourney, W.L. & Bretall, D. 2009. Application of 3D image correlation for full-field transient plate deformation measurements during blast loading. *International Journal of Impact Engineering*, 36(6): 862–874. <http://linkinghub.elsevier.com/retrieve/pii/S0734743X08002376> [2013, August 18].
- Turnbull, A., McKinnon, C., Carrol, J. & McDonald, A. 2022. On the Development of Offshore Wind Turbine Technology: An Assessment of Reliability Rates and Fault Detection Methods in a Changing Market. *Energies*, 15(9).
- Vanlanduit, S., Vanherzeele, J., Longo, R. & Guillaume, P. 2009. A digital image correlation method for fatigue test experiments. *Optics and Lasers in Engineering*, 47: 371–378.
- Wadhwa, N. & Rubinstein, M. 2013. Phase-based video motion processing. *ACM Transactions on Graphics*, 32(4): 80:1–80:10.
- Wang, W., Mottershead, J.E., Ihle, A., Siebert, T. & Reinhard Schubach, H. 2011. Finite element model updating from full-field vibration measurement using digital image correlation. *Journal of Sound and Vibration*, 330(8): 1599–1620.
- Wang, W, Mottershead, J.E., Siebert, T. & Pipino, a. 2012. Full-field modal identification using image moment descriptors. *Proceedings of the International Conference on Noise and Vibration Engineering ISMA 2012*: 2133–2143.

- Wang, Weizhuo, Mottershead, J.E., Siebert, T. & Pipino, A. 2012. Frequency response functions of shape features from full-field vibration measurements using digital image correlation. *Mechanical Systems and Signal Processing*, 28: 333–347.
- Warren, C., Niezrecki, C. & Avitabile, P. 2010. Optical Non-contacting Vibration Measurement of Rotating Turbine Blades II. In *IMAC-XXVIII*. 39–44.
- Warren, C., Niezrecki, C., Avitabile, P. & Pingle, P. 2011. Comparison of FRF measurements and mode shapes determined using optically image based, laser, and accelerometer measurements. In *Mechanical Systems and Signal Processing*. 2191–2202.
- Winstroth, J., Schoen, L., Ernst, B. & Seume, J.R. 2014. Wind turbine rotor blade monitoring using digital image correlation: a comparison to aeroelastic simulations of a multi-megawatt wind turbine. *Journal of Physics: Conference Series*, 524.
- Wu, H., Rubinstein, M., Shih, E. & Guttag, J. 2012. Eulerian video magnification for revealing subtle changes in the world. *ACM Transactions on Graphics*, 31(4):1–8
- Yang, S. & Allen, M.S. 2012. Output-only Modal Analysis using Continuous-Scan Laser Doppler Vibrometry and application to a 20kW wind turbine. *Mechanical Systems and Signal Processing*, 31: 228–245.
- Yang, Y., Dorn, C., Farrar, C. & Mascareñas, D. 2020. Blind, simultaneous identification of full-field vibration modes and large rigid-body motion of output-only structures from digital video measurements. *Engineering Structures*, 207: 110183.
- Yang, Y., Dorn, C., Mancini, T., Talken, Z., Kenyon, G., Farrar, C. & Mascareñas, D. 2017. Blind identification of full-field vibration modes from video measurements with phase-based video motion magnification. *Mechanical Systems and Signal Processing*, 85:567–590.
- Yao, M. & Wang, H. 2015. On-line monitoring of batch processes using generalized additive kernel principal component analysis. *Journal of Process Control*, 28: 56–72.
- Yu, Y., Cao, H., Yan, X., Wang, T. & Ge, S.S. 2020. Defect identification of wind turbine blades based on defect semantic features with transfer feature extractor. *Neurocomputing*, 376: 1–9.
- Zhang, D. & Lu, G. 2003. A comparative study of curvature scale space and Fourier descriptors for shape-based image retrieval. *Journal of Visual Communication and Image Representation*, 14(1): 39–57.
- Zhang, D. & Lu, G. 2004. Review of shape representation and description techniques. *Pattern Recognition*, 37(1): 1–19.
- Zhou, H.F., Dou, H.Y., Qin, L.Z., Chen, Y., Ni, Y.Q. & Ko, J.M. 2014. A review of full-scale structural testing of wind turbine blades. *Renewable and Sustainable Energy Reviews*, 33: 177–187.
- Zhou, W., Li, H. & Tian, Q. 2017. Recent advance in content-based image retrieval: a literature survey. *arXiv (Cornell University)*. <http://export.arxiv.org/pdf/1706.06064>.

